NOVEL FUNCTIONALIZATION METHODS OF 1D AND 2D MATERIALS AND THEIR APPLICATIONS

Mariano Vera Hidalgo

Madrid, Noviembre, 2019

Memoria presentada para optar al título de Doctor en

Química Orgánica

Director de Tesis:

Prof. Emilio M. Pérez

IMDEA Nanociencia

Chemistry of Low Dimensional Materials Lab

Universidad Autónoma de Madrid

Facultad de Ciencias

Instituto IMDEA Nanociencia

A mis padres y a la familia de Berlín.

AGRADECIMIENTOS

Una etapa de mi camino ha terminado…

Descubro hoy que mi paso por IMDEA Nanociencia ha resultado más corto de lo que tres años atrás pude imaginar; relativo no obstante; es mucho lo acontecido y más lo que me han aportado todos esos días. Ha sido un regalo, sin duda.

Toca ahora corresponder como realmente merece y agradecer a mi director de tesis, Emilio M. Pérez, la confianza que depositó en mí, su apoyo y su supervisión del trabajo que me ha permitido concluir esta tesis. Agradecimiento que hago extensivo al instituto IMDEA Nanociencia y a todo su personal, por el mantenimiento y la gestión.

Ocupan un lugar muy especial en este camino mis estancias en Europa, primero en el instituto LIOS en la Universidad Johannes Kepler en Linz y después en el instituto ZMP en Fürth, Universidad FAU. Mi gratitud al Dr. Dong y al Prof. Saricifti y al Prof. Hirsch quienes, no sólo las hicieron posible financiándolas; hicieron que éstas resultaran tan interesantes como útiles. Mención especial merecen igualmente todos los compañeros en ambas estancias.

¿Pero, qué hubiera sido de todo esto sin los compañeros del grupo EMP?

Hemos pasado tantos desde entonces…a todos ellos GRACIAS en mayúsculas: Alex, fan de Dani Martín, con lo poco que coincidimos y todo lo que hemos hablado y seguimos hablando…; hubiese estado muy bien hacer la tesis juntos.

A los primeros Postdocs: Emerson, la tranquilidad y el psicopato, por tu ayuda y por todo lo que me has enseñado; Matías, por todo tu trabajo. A los últimos PhDs: Teresa, por traer la alegría al laboratorio; Leire, por toda tu paciencia, lo más fuerte del IMDEA.

A todos los que desde entonces siguen aún: Enrique, por toda tu ayuda durante estos años y enseñarme ciencia tan distinta; Zulay, por enseñarme a usar el equipo de RMN y regañarme por mis malas etiquetas; Edu, no me podía olvidar de ti, me alegro de haberte conocido más.

A los de la UAM: no podían ser otros!!, Luis y David. No estábais sólo para dejarnos material. ¡¡Cómo me gusta pasar por vuestro laboratorio a saludar y echar un rato!! Y a Nico, que aunque haya llegado al final también incluyo; Antonio, Eider, Sara, Silvia

y Alicia, nuevos integrantes, no ha sido mucho el tiempo que he estado con vosotros, pero aun así el tiempo que os he conocido ha merecido la pena; Antonio, tenemos que hablar más de anime y manga; Sara, aguanta y no acabes con Tomás y Ramiro, son jóvenes aún; Eider, la vasca, me alegro haberte conocido en la bienal y poder haber seguido en contacto en IMDEA; Silvia, hemos coincidido poco tiempo, agradezco tu compañía; Alicia, la manchega, la nueva, que todo te vaya genial en tu tesis en EMP; el gallego (Manuel), el murciano (Tomás) y los asturianos, doble ración!!, (Ramiro y Álvaro), vosotros habéis sido el aire fresco este último año, un aire que me ha venido genial, por eso y por mucho más, quiero agradeceros especialmente vuestro apoyo incondicional y todas las risas y buenos momentos que me habéis regalado dentro y fuera del laboratorio. Claro que no puedo dejar de recordar la primera posición en las pachangas de la UAM (Manu, tu entrenador forever); Anita, otra veterana que acaba, durante estos tres años tus visitas, que te pasaras a saludar, han dado vida al día a día del laboratorio; finalmente Julia y Sofía, con quienes he podido compartir Congreso en dos ocasiones, geniales!! Los tres más veteranos del grupo acabamos juntos, gracias por vuestra entrañable compañía y por vuestro apoyo cordial y sincero durante todo este tiempo.

A los madrileños/villalbinos: Beloki, Edu, Pablo, Diego, Álvaro, Vladi y Losa, los de siempre, mi agradecimiento más especial por estar siempre ahí.

A los de la Uni: Alberto, Laura, Edu y Sistemas, gracias. Qué buenos esos viajes a Manchester.

Andrea, el apoyo que he tenido de ti estos años ha sido fundamental para que pudiera seguir adelante, en lo bueno y en lo malo. Siempre te lo agradeceré.

… el buen vino, para el final.

A mi familia. A mis padres primero, por todo lo que nadie ve; tan simple como profundo, el auténtico pilar. A mis hermanos María José y Carlos, inmediatamente después, con Alma y la sobrinita que ya estamos deseando conocer, siempre conmigo, aún en la distancia; cómo os echamos de menos!!

Gracias a todos.

Mariano.

otra comienza…

Eso desean quienes viven estos tiempos,

pero no les toca a ellos decidir,

solo tú puedes decidir,

qué hacer con el tiempo que se te ha dado.

Gandalf, La Comunidad del Anillo.

CONTENTS

LIST OF ABBREVIATIONS AND NOTES

Bibliographic citations have been placed as footnotes in the pages where they were first cited in the section and at the end of this thesis.

ACN	Acetonitrile
AcOEt	Ethyl acetate
ADMP	Acyclic Diene Metathesis Polymerization
AFM	Atomic Force Microscopy
Ant	anthracene
AQ	anthraquinone
AuNP	Gold Nanoparticle
BDS	Bisdiazonium salts
Bn	Benzyl
Bn-mal	*N*-benzylmaleimide
BP	Black Phosphorus
CCPA	cycloparaphenyleneacetylene
CE	chemical exfoliated
CNTs	Carbon Nanotubes
CP	Counterpoise
CPMAS-^{13}C-NMR	Solid state Cross-polarization ^{13}C nuclear magnetic resonance
cs-MoS_2	control sample-MoS_2
CV	Cyclic Voltammetry
CVD	Chemical vapor deposition
DCM	Dichloromethane
DFT	Density functional theory
DIC	Diiodo Compounds
DMPA	2,2-dimethoxy2-phenylacetophenone
DMSO	dimethyl sulfoxide

DNA	Deoxyribonucleic acid
exTTF	2-[9-(1,3-dithiol-2-ylidene)anthracen-10(9*H*)-ylidene]-1,3-dithiole
f-MoS_2	functionalized-MoS_2
FT-ATR-IR	Fourier-transform infrared spectroscopy
GO	Graphene oxide
h-BN	Boron nitride
HER	Electrocatalytic hydrogen evolution
Hex	Hexane
HRTEM	High-Resolution Transmission Electronic Microscopy
I	Current
LPE	Liquid-phase Exfoliation
Mac	macrocycle
Me	Methyl
MIMs	Molecular Interlocked Molecules
MWNTs	Multi-Walled Carbon Nanotubes
Napth	naphtalene
nBuLi	n-butyl lithium
NMP	1-methyl-2-pyrrolidinone
ORR	Oxygen reduction reaction
PEG	Polyethyleneglycol
Ph	phenyl
PLE	Photoluminescence excitation
p-MoS_2	pristine-MoS_2
Polysucc	polysuccinimide
PTFE	Polytetrafluoroethylene
Pyr	pyrene
QRE	Quasi-reference electrode
RCM	Ring Closing Metathesis
RDE	Rotating Disk Electrode
RE	Reference electrode
rGO	Reduced graphene oxide

rt	room temperature
SAM	Self-Assembled Monolayer
SDS	Sodium dodecylsulfate
SHE	Standard Hydrogen electrode
Succ	Succinimide
SWNT/SWCNT	Single-Walled Carbon Nanotubes
t	time
$TBAPF_6$	Tetrabutylammonium hexafluorophosphate
TCNQ	Tetracyanoquinodimethane
TEM	Transmission Electronic Microscopy
TEMPO	(2,2,6,6-Tetramethylpiperidin-1-yl)oxyl
TGA	Thermogravimetric analysis
TLC	Thin-layer chromatography
TMDCs	Transition Metal Dichalcogenides
UV-Vis	Ultra-Violet-Visible
UV-Vis-NIR	Ultra-Violet-Visible near Infrared
WE	Working electrode
XPS	X-ray photoelectron spectroscopy
XRD	X-ray Powder Diffracation

RESUMEN

En las últimas décadas se han descubierto y estudiado nuevos materiales con excelentes propiedades electrónicas, mecánicas, ópticas etc., como por ejemplo los nanotubos de carbono de una pared (SWNTs), formados por átomos de carbono dispuestos en una red hexagonal cilíndrica, y los dicalcogenuros de metales de transición (TMDCs), formados por capas de un metal de transición y dos átomos del grupo de los anfígenos (normalmente S, Se y Te) unidos covalentemente, conectadas por interacciones de van der Waals. Estos materiales poseen propiedades únicas: en el caso de los SWNTs, algunos son semiconductores perfectos para dispositivos. Por otro lado, los TMDCs como por ejemplo: WS_2 y MoS_2, son fotoluminiscentes y usados como fotodetectores. Sin embargo, en ambos casos obtener estas propiedades y aplicarlas es problemático debido a su difícil manipulación y/u obtención: por ejemplo los SWNTs son insolubles en cualquier disolvente y tienden a agregarse unos con otros; y los TMDCs, es necesario exfoliarlos porque sus propiedades únicamente se obtienen cuando son monocapas. Para aprovechar todas estas increíbles propiedades es necesario modificar y mejorar los métodos de manipulación de dichos materiales. En este punto es donde entra la química. Este campo se encarga de la funcionalización química de los materiales para mejorar las propiedades y aumentar la manejabilidad. En términos generales, la química ha tenido dos maneras de funcionalizar los materiales: mediante interacciones no covalentes, por ejemplo van der Waals como interacciones π-π; y la funcionalización covalente creando enlaces covalentes.

Los *capítulos 1* y *2* se centran en los SWNTs y su funcionalización mediante enlace mecánico (formando especies llamadas MINTs) y su aplicabilidad en catálisis, debido a su carácter dador de electrones al medio de reacción y su gran superficie activa. En primer lugar, Mechanically Interlocked Nanotubes (MINTs) son especies creadas mediante la encapsulación de SWNTs con macrociclos mediante la reacción de metátesis entre dos alquenos, formando así un enlace mecánico entre ellos. Es un procedimiento donde se aprovechan las ventajas de los dos métodos tradicionales de funcionalización, creando especies estables sin modificar la estructura del nanotubo, es decir, mantiene sus propiedades intrínsecas intactas.

Concretamente, en el *capítulo 1*, mediante la síntesis de diferentes MINTs (AQ, exTTF y pyr) y su uso como catalizadores de la reacción de reducción de nitroarenos, es posible ver el efecto electrónico que tiene el macrociclo sobre los SWNTs y la regulación de la actividad catalítica en la reacción: mejorándola (dopaje tipo n, exTTF) o ralentizándola (dopaje tipo p, AQ). Con estos resultados, es posible regular el comportamiento catalítico de los SWNTs mediante la encapsulación de macrociclos por enlace mecánico (MINT) sin modificar sus propiedades intrínsecas y de manera no alostérica.

En el *capítulo 2*, se muestran las ventajas de juntar dos especies activas electroquímicamente, como son la antraquinona (AQ) y los SWNT mediante enlace mecánico (MINT-AQ). Usar MINT-AQ como electrodo revela una gran estabilidad electroquímica tanto en medio acuosa como orgánica respecto a la especie aislada de AQ. Además, MINT-AQ ofrece una mejora en la reacción de reducción de oxigeno (ORR) respecto a los SWNTs.

Los *capítulos 3* y *4* se centran en la funcionalización de TMDCs (MoS_2 y WS_2) con maleimidas, mediante la reacción tiol-eno "click". La reacción tiol-eno es una reacción tipo "click" en donde participan un grupo tiol y una olefina para dar enlaces S-C. Al ser una reacción "click" se caracteriza por ser ortogonal, robusta y eficiente. Además, son reacciones versátiles donde las condiciones de reacción son suaves. Reuniendo todas estas condiciones, es muy usada en múltiples campos como en síntesis orgánica, bioorgánica, polímeros y en química de materiales. Hay varios tipos de reacción tiol-eno según como se rompa el enlace S-H del tiol, pero nos centraremos en la nucleófila donde se genera tiolatos mediante la acción de una base. Concretamente, usando carbonilos α,β insaturados (dobles enlaces pobres en electrones) recibe el nombre de tiol-Adición de Michael. Un ejemplo de este tipo de moléculas es el grupo maleimida. Esta molécula se caracteriza por tener un doble enlace muy pobre en electrones que es capaz de reaccionar con nucleófilos suaves como los tioles. De hecho, estas moléculas reaccionan de manera ortogonal y especifica con grupos tioles, ofreciendo una gran aplicabilidad en biología con grupos cisteína y en la química de polímeros.

En el *capítulo 3* desarrollamos un método sencillo de funcionalización covalente entre MoS_2/WS_2 y maleimidas vía tiol- Adición de Michael en condiciones suaves donde la estructura del TMDCs se conserva, aprovechando la nucleofilia del azufre. El producto

es ampliamente caracterizado para probar la funcionalización (TGA, espectroscopia Raman, UV-vis, XPS…).

En el *capítulo 4* hemos descrito un estudio exhaustivo de la funcionalización covalente de MoS_2 con maleimidas vía tiol-Adición de Michael, previamente descrito en el *capítulo 3*. Durante el estudio de las condiciones, hemos descubierto que, en presencia de base, MoS_2 es funcionalizado covalentemente con un polímero generado a partir de *N*-benzylmaleimida. En cambio, en ausencia de base se funcionaliza con moléculas aisladas de *N*-benzylmaleimida. Ademas, se llevo a cabo un estudio completo de la reacción cambiando la temperatura, el tiempo de reacción, tipo de disolventes, y usando diferentes maleimidas

.

ABSTRACT

In the last decades, new materials with excellent electronic, mechanical and optical properties have been discovered and studied, such as single-walled carbon nanotubes (SWNTs), formed by carbon atoms arrange in a cylindrical hexagonal network and Transition Metal Dichalcogenides (TMDCs), constituted by layers connected by Van der Waals interactions of a transition metal with two chalcogenide atoms (usually S, Se and Te) covalently bonded. These materials have unique properties: in the case of SWNTs, some of them are semiconductors and used in devices. Likewise, TMDCs, such as WS_2 and MoS_2, is photoluminescence and used as photodetectors. However, in both cases obtaining these properties and applying them is a problem due to the difficulty to handle and/or obtaining: for instance, SWNTs are insoluble in any solvent and tend to aggregate with each other; and TMDC, it is necessary to exfoliate them because the most important properties are only obtained in the monolayer form. To take advantage of all these incredible properties, it is necessary to modify and improve the methods of handling them. In this point the chemistry field appears. This field is responsible for the chemical functionalization in order to improve the properties and increase the manageability. In general terms, the chemistry has had two methods to functionalize materials: through non-covalent interaction, for instance Van der Waals interaction as π-π interactions, and covalent functionalization with covalent bonds.

Chapters 1 and *2* focus on carbon nanotubes and their functionalization through mechanical bond (forming species called MINTs) and their applicability in catalysis, due to their electron-giving character and their long active surface. First of all, Mechanically Interlocked Nanotubes (MINTs) are species created by encapsulating SWNTs with macrocycles by ring closing metathesis (RCM) between two alkenes, thus forming a mechanical bond between them. This procedure takes advantages of the two methods of functionalization, forming stable species without modifying the structure of the nanotube.

Specifically in *chapter 1*, with the synthesis of different MINTs (AQ, exTTF and pyr) and their use as catalysts for the nitroarenes reduction reaction, is possible to appreciate an electronic effect of the macrocycle in the SWNTs and a regulation of the catalytic activity: either enhancing it (n-doping) or slowing it down (p-doping). With

these results, it is possible to regulate the catalytic behaviour of SWNTs by encapsulating macrocycles by mechanical bond (MINT) without damaging their structure and in non-allosteric pathway.

In the *chapter 2* the advantages of joining together two electrochemically active species, such as AQ and SWNT by mechanical bonding (MINT-AQ) are shown. Using MINT-AQ as an electrode reveals great electrochemical stability in both aqueous and organic solvents with respect to the isolated species of AQ. In addition, MINT-AQ offers an improvement in the oxygen reduction reaction (ORR) over SWNT.

Chapters 3 and *4* focus on the functionalization of TMDCs (MoS_2 and WS_2) with maleimides through thiol-ene "click" reaction. The thiol-ene reaction is a "click" reaction between thiol group and olefin yielding S-C bond. This reaction is characterized by being robust, efficient and orthogonal. In addition, they are versatile reactions which the reaction conditions are mild. Bring together all of these characteristics, it is widely used in multiple fields such as organic synthesis, biochemistry, polymers and chemistry of materials. There are several kinds of thiol-ene reaction depending on how the bond S-H from thiol is broken, but we will focus on the nucleophile method where thiolate are generated thanks to a base. Specifically, using α,β- unsaturated carbonyls (electron poor enes) is called thiol-Michael Addition. An example of these molecules is the maleimide group. This molecule is characterized by having a electron poor double bond capable of reacting with soft nucleophiles such as thiols. In fact, these molecules react orthogonally and specifically with these groups, offering a great applicability in biology field with cysteine groups and in polymer chemistry.

In the *chapter 3* we have developed a simple method of covalent functionalization between TMDCs (MoS_2 and WS_2) and maleimides via thiol-Michael Addition in mild conditions where the structure of TMDCs is preserved, exploiting the soft nucleophilicity of sulfur atom. Extensive characterization proves that the reaction occurs through Michael addition.

In the *chapter 4*, we have described an exhaustive study of the covalent functionalization of MoS_2 with maleimides via thiol-Michael Addition, previously described in the *chapter 3*. During this study of conditions, we have discovered that, in the presence of base, MoS_2 is functionalized with a polymer generated from *N*-

benzylmaleimide. In contrast, in the absence of base, it is functionalized with isolated *N*-benzylmaleimide molecules. In addition, we have performed a complete study of the reaction changing temperature, time, different kind of solvent and using different maleimides derivatives.

1. Introduction. Applications of Modified Carbon Nanotubes: Mechanically Interlocked Nanotubes (MINTs) in Catalysis

1.1. Single-Walled Carbon Nanotubes (SWNTs).

Carbon nanotubes (CNTs) are an allotrope of carbon like fullerene, graphite/graphene and diamond. CNTs are cylindrical structures and they are made of rolled-up graphene sheets. Their first appearance was in 1991 through a report of the observation of multi-walled carbon nanotubes (MWNTs) on the cathode of a carbon arc discharge experiment used to produce fullerenes.[1] Those tubes contained at least two or more C layers and they had a diameter from 3 nm to 30 nm. However, single-walled carbon nanotubes (SWNTs),[2] produced by gas phase and with diameters in the range 1-2 nm, are the most widely studied form of CNTs because slight changes in tube diameter (d_t) and chiral angle (θ), defined by the chirality indices (n,m) (Figure 1), will shift their electronic properties. SWNTs can be metallic if |n-m| is 0 (armchair SWNTs) or a multiple of 3, or semiconductors showing a well-defined bandgap for any other values of the chiral indices.[3] Since their emergence, SWNTs have evolved into one of the most studied nanomaterials.

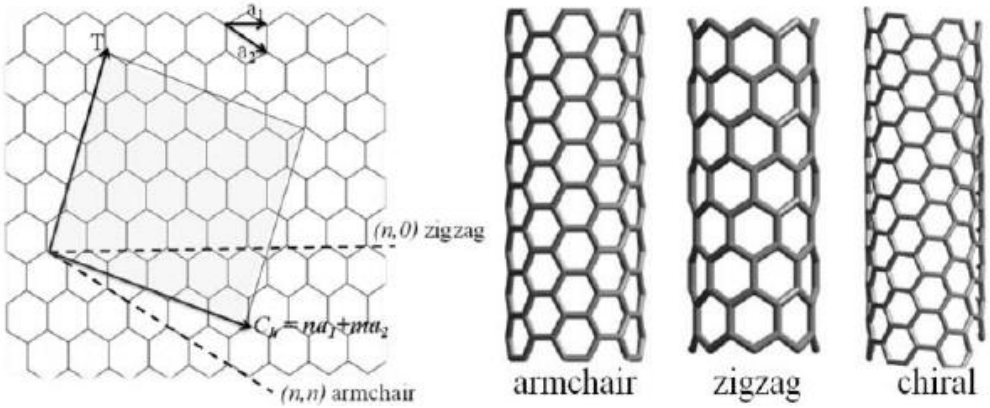

Figure 1. The construction of SWNTs from a graphene sheet along the chiral vector $C_h = na_1 + ma_2$, where a_1 and a_2 are the graphene lattice vectors and n and m are integers (n,m) which define the dimensions of SWNT.

[1] Iijima, S. *Nature* **1991,** *354* (6348), 56-58.

[2] Iijima, S.; Ichihashi, T. *Nature* **1993,** *363* (6430), 603-605.

[3] Odom, T. W.; Huang, J.-L.; Kim, P.; Lieber, C. M., *Nature* **1998,** *391* (6662), 62-64.

The great interest in the fundamental properties of SWNTs and in their exploitation through a wide range of applications is due to their unique structural, chemical, mechanical, thermal, optical and electronic properties.[3,4,5,6,7,8,9,10] However, due to the large surface ratio, SWNTs tends to create insoluble aggregates. Due to the formation of these big bundles held strongly together, SWNTs are very difficult to disperse homogeneously in solution, which makes them difficult to manipulate. For this, an important goal is the manipulation of SWNTs through chemical funcionalization with molecules. Throughout all this introduction, we will show different ways to functionalize SWNTs.

With respect to the characterization of SWNTs, the most commonly used spectroscopic methods include Raman spectroscopy, absorption and photoluminescence (PL) (Figure 2). Raman spectroscopy is a versatile method capable of giving structural and electronic information of SWNTs. The most important bands are G, D, 2D and lower frequency breathing mode (RMB). The G-band is related to the graphite optical mode, around ~1580 cm^{-1} and is typically the most intense band in the Raman spectra of SWNTs. It represents the fundamental vibration of tangential elongation. The D-band (ca. 1400 cm^{-1}) is related to defects in the structure of the SWNTs. This band is very useful in the covalent modification of SWNTs: the relative intensity of the D and G bands shows the type of functionalization. Covalent functionalization methods induce sp^3 defects, and therefore result in an increased I_D/I_G while noncovalent modifications do not change the I_D/I_G ratio. Raman shifts of 2D band, around ~2700 cm^{-1}, together with shifts in the G band frequency, are usually considered the best indication of doping in SWNTs. Finally, RBMs are around 100-500 cm^{-1} and correspond to a bond-stretching out-of-plane mode in which all the carbon atoms move coherently in the radial direction. The RBM frequency is proportional to the tube diameter.

Regarding UV-vis-NIR, SWNT have a unique, chirality-dependent optical absorption spectrum which shows the energy band structure and the number of electronic

[4] Javey, A.; Guo, J.; Wang, Q.; Lundstrom, M.; Dai, H., *Nature* **2003,** *424* (6949), 654-657.

[5] Berber, S.; Kwon, Y.-K.; Tománek, D., *Phys. Rev. Lett.* **2000,** *84* (20), 4613-4616.

[6] Tans, S. J.; Devoret, M. H.; Dai, H.; Thess, A.; Smalley, R. E.; Geerligs, L. J.; Dekker, C., *Nature* **1997,** *386* (6624), 474-477.

[7] Cao, L.; Meziani, M. J.; Sahu, S.; Sun, Y.-P., *Acc. Chem. Res.* **2013,** *46* (1), 171-180.

[8] Singh, P.; Campidelli, S.; Giordani, S.; Bonifazi, D.; Bianco, A.; Prato, M., *Chem. Soc. Rev.* **2009,** *38* (8), 2214-2230.

[9] Zhao, Y.-L.; Stoddart, J. F., *Acc. Chem. Res.* **2009,** *42* (8), 1161-1171.

[10] Dai, H., *Acc. Chem. Res.* **2002,** *35* (12), 1035-1044.

transitions. For instance, in the case of (6,5)-SWNT, there are two possible transitions: S_{11} (~990 nm) and S_{22} (~570 nm). Finally, an alternative probe of this energy band structure is photoluminescence excitation (PLE). In PLE, the PL intensity is recorded while the excitation wavelength is changed. A maximum in intensity is found when the excitation energy equals an absorption resonance from which relaxation to a PL-emitting transitions occurs. The map is represented with luminescent intensity (Z axis) vs. emission (X axis) and excitation wavelength (Y axis). With a PLE map, also called "fingerprint", it is possible to difference chirality number (*n*,*m*) of SWNTs due to each kind of tube has an specific signal.

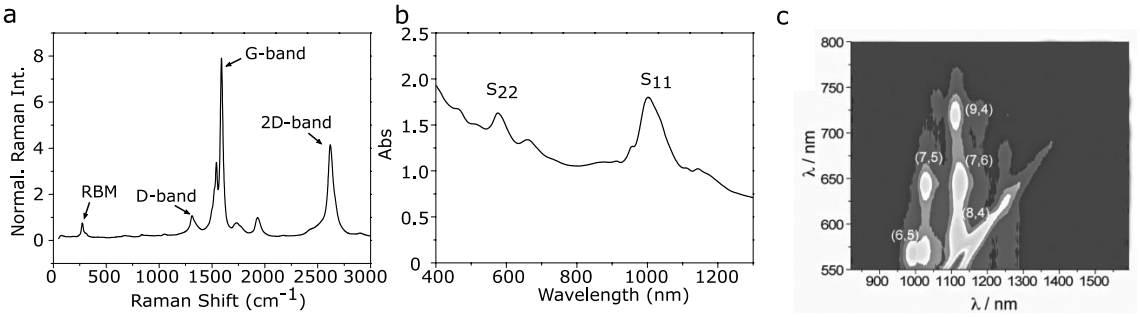

Figure 2. Example of characterization of SWNT: **a.** Raman spectroscopy (532nm) of (6,5)-SWNT. **b.** UV-vis-NIR of (6,5)-SWNT with the two electronic transitions (S_{11} and S_{22}). **c.** PLE map of a mixture (*n*,*m*)-SWNT in a surfactant solution. Rayleigh scattering has not been filtered in this image.

Finally, the applications of CNTs[11,12,13] are very varied due to their properties. Regarding the electronic properties, semiconductor SWNTs, have been used in transistors,[14] devices[15] and even prototype computers.[16] Also, due to the large industrial production of CNTs, are incorporated in diverse commercial products[17] ranging from batteries, automotive parts, water filters etc. as well in the biologic field,[18] natural

[11] Rao, R. *et.al. ACS Nano* **2018,** *12* (12), 11756-11784.
[12] Appenzeller, J., *Proceedings of the IEEE* **2008,** *96* (2), 201-211.
[13] Marcaccio, M.; Paolucci, F., *Making and exploiting fullerenes, graphene, and carbon nanotubes*. Springer: 2014.
[14] LeMieux, M. C.; Roberts, M.; Barman, S.; Jin, Y. W.; Kim, J. M.; Bao, Z., *Science* **2008,** *321* (5885), 101-104.
[15] Avouris, P.; Chen, Z.; Perebeinos, V., *Nat. Nanotechnol.* **2007,** *2* (10), 605-615.
[16] Shulaker, M. M.; Hills, G.; Patil, N.; Wei, H.; Chen, H.-Y.; Wong, H. S. P. *Nature* **2013,** *501*, 526.
[17] De Volder, M. F. L.; Tawfick, S. H.; Baughman, R. H.; Hart, A. J., *Science* **2013,** *339* (6119), 535-539.
[18] Aurand, E. R.; Usmani, S.; Medelin, M.; Scaini, D.; Bosi, S.; Rosselli, F. B. *Adv. Funct. Mater.* **2018,** *28* (12), 1700550.

receptors,[19] sensors[20] and they are used in heterogeneous catalysis,[21] for instance as electrocatalyst on the oxygen reduction reaction (ORR).[22]

1.2. **Functionalization of SWNTs.**

In terms of applications, in order to take advantage of all the outstanding properties of SWNTs already mentioned, the chemical functionalization is a main point. This functionalization is used enhance their properties, such as solubility, electronic properties or combine the properties of SWNTs with others materials. There are two main strategies to functionalize SWNTs: non-covalent and covalent functionalization. In this part, we will discuss both methods and provide some examples of them.

1.2.1. **Non-covalent functionalization.**

The non-covalent functionalization is based on van der Waals interactions or π-π stacking, for instance with unsaturated (poly)cyclic molecules. In this kind of forces, the main point is the surface area available for interactions.[23,24] This method is attractive because it offers the possibility of attaching chemical molecules, such as polymers,[25] DNA,[26] pyrene derivatives[27,28] or surfactants[29,30] without affecting the electronic network of the SWNTs and maintaining their properties. However, these interactions are weak and the products typically lack kinetic stability.

An example of non-covalent functionalization with pyrene derivatives was reported by Chen *et al.*[27] They developed a controlled and easy method for immobilizing proteins onto SWNTs through anchored succinimidyl pyrene derivative (Figure 3). The

[19] Kwon, O. S.; Song, H. S.; Park, T. H.; Jang, J., *Chem. Rev.* **2019,** *119* (1), 36-93.

[20] Schroeder, V.; Savagatrup, S.; He, M.; Lin, S.; Swager, T. M., *Chem. Rev.* **2019,** *119* (1), 599-663.

[21] Melchionna, M.; Marchesan, S.; Prato, M.; Fornasiero, P., *Catal. Sci. Technol.* **2015,** *5* (8), 3859-3875.

[22] Dai, L.; Xue, Y.; Qu, L.; Choi, H.-J.; Baek, J.-B., *Chem. Rev.* **2015,** *115* (11), 4823-4892.

[23] Gavrel, G.; Jousselme, B.; Filoramo, A.; Campidelli, S., Supramolecular Chemistry of Carbon Nanotubes. In *Making and Exploiting Fullerenes, Graphene, and Carbon Nanotubes*, Marcaccio, M.; Paolucci, F., Eds. Springer Berlin Heidelberg: Berlin, Heidelberg, 2014; pp 95-126.

[24] Pérez, E. M.; Martín, N., *Chem. Soc. Rev.* **2015,** *44* (18), 6425-6433.

[25] Tuncel, D., *Nanoscale* **2011,** *3* (9), 3545-3554.

[26] Zheng, M.; Jagota, A.; Semke, E. D.; Diner, B. A.; McLean, R. S.; Lustig, S. R.; Richardson, R. E.; Tassi, N. G., *Nat. Mater.* **2003,** *2*, 338.

[27] Chen, R. J.; Zhang, Y.; Wang, D.; Dai, H., *J. Am. Chem. Soc.* **2001,** *123* (16), 3838-3839.

[28] Naotoshi, N.; Yasuhiko, T.; Hiroto, M., *Chem. Lett.* **2002,** *31* (6), 638-639.

[29] Fagan, J. A., *Nanoscale Adv.* **2019,** *1* (9), 3307-3324.

[30] Moore, V. C.; Strano, M. S.; Haroz, E. H.; Hauge, R. H.; Smalley, R. E.; Schmidt, J.; Talmon, Y., *Nano Lett.* **2003,** *3* (10), 1379-1382.

amine groups on a protein react with succinimidyl ester to form amide bonds for protein immobilization.

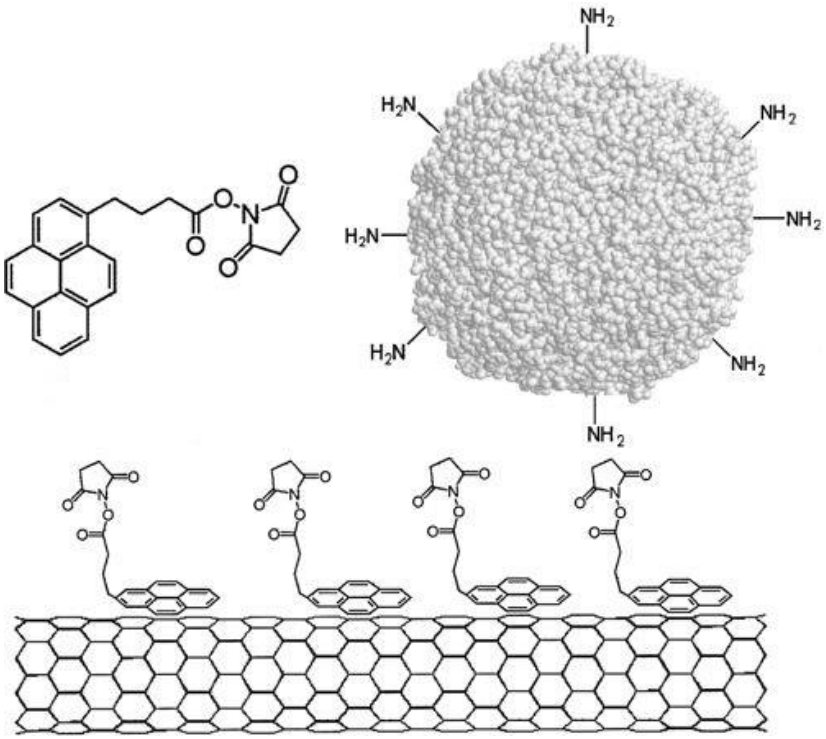

Figure 3. 1-pyrenebutanoic acid onto the sidewall of SWNT. Adapted with permission from *J. Am. Chem. Soc.* **2001,** *123* (16), 3838-3839. Copyright (2001) American Chemical Society.

Another example using anchored pyrene with SWNTs was reported by Nakashima *et al.*[28] (Figure 4). Through the mixture of a pyrene salt and SWNTs and sonication, they obtained a transparent dispersion/solution of the nanotubes in water. This is a perfect example of improving properties using non-covalent functionalization.

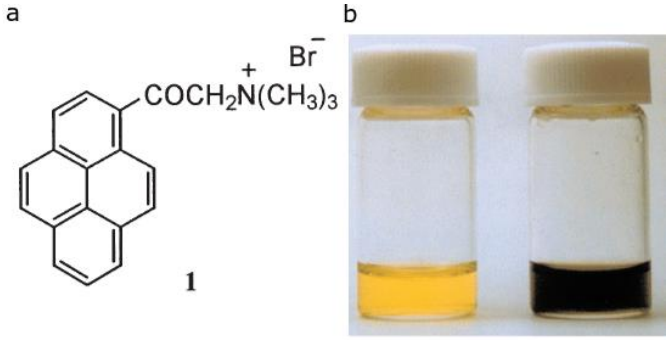

Figure 4. **a.** Anchor pyrene salt molecule (**1**). **b.** Aqueous solutions of **1** (first bottle) and SWNTs-**1** (second bottle), as described by Nakashima *et al.*[28]

1.2.2. **Covalent functionalization.**

The covalent functionalization of SWNTs has been widely studied.[8] Although the products are characterized by the large kinetic stability characteristic of covalent bonds, this covalent bond produces an alteration of the structure of SWNTs due to the saturation of some sp^2 C atoms. Therefore, the intrinsic properties of the SWNTs change, which might be detrimental in some cases. There are two pathways to functionalize SWNTs covalently: i) oxidation of SWNTs and amidation or esterification of the carboxilic groups and ii) addition chemistry to SWNTs.

i) Amidation and esterification of oxidized SWNTs.

The first step is the strong oxidation of pristine SWNTs (Scheme 1). This procedure preferentially breaks the end sides of the tube. Normally these conditions are concentrated nitric acid or hydrogen peroxide with sulfuric acid. The product is oxidized SWNTs (o-SWNTs) with carboxylic groups. After that, the functionalization of o-SWNTs is performed through standard carboxylic acid chemistry: amidation and esterification.

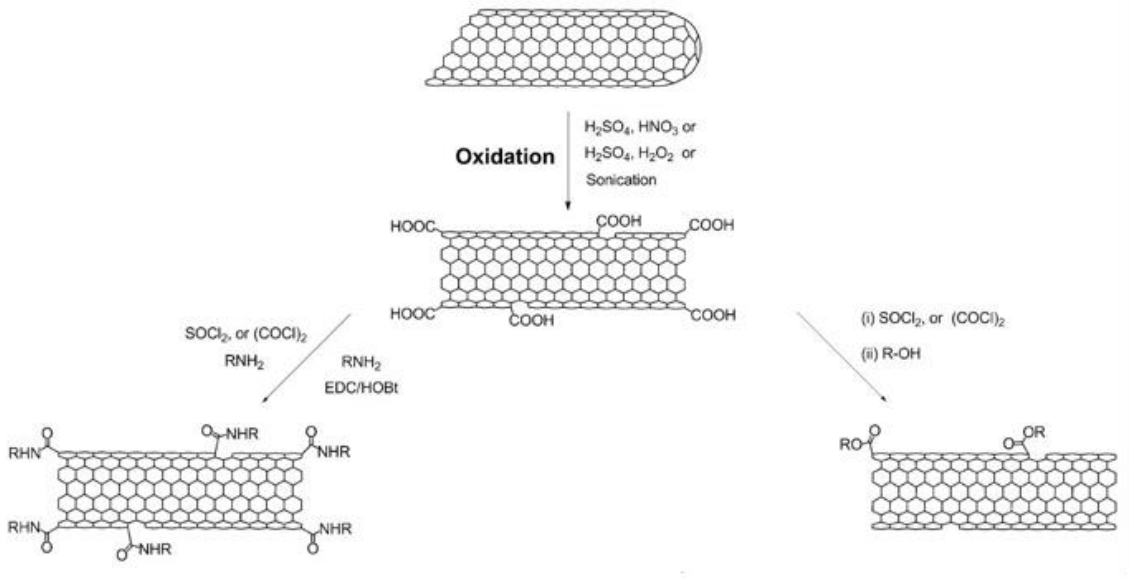

Scheme 1. Schematic procedure of oxidation of SWNTs and amidation or esterification reactions. The amidation strategy has been used to link SWNTs to: fullerenes,[31]

[31] Delgado, J. L.; de la Cruz, P.; Urbina, A.; López Navarrete, J. T.; Casado, J.; Langa, F., *Carbon* **2007,** *45* (11), 2250-2252.

glucosamine[32] and DNA,[33] for example. Likewise, esterification has been used to link, porphyrins[34] and alkyl pyrrole derivatives,[35] among many others.

ii) Addition chemistry to SWNTs.

This method consists in the direct organic reaction with the double bonds of the SWNTs which highly reactive species are necessary. Inside of this methodology there are multiple kinds of reactions such as fluorination,[36] addition of carbenes[37] and nitrenes,[19] 1,3-dipolar cycloaddition[38] (Scheme 2), Diels-Alder reaction,[39] nucleophilic[40] and free radical[41] additions and reduction and reductive alkylation, such as Birch reduction.[42]

[32] Pompeo, F.; Resasco, D. E., *Nano Lett.* **2002,** *2* (4), 369-373.

[33] Baker, S. E.; Cai, W.; Lasseter, T. L.; Weidkamp, K. P.; Hamers, R. J., *Nano Lett.* **2002,** *2* (12), 1413-1417.

[34] Baskaran, D.; Mays, J. W.; Zhang, X. P.; Bratcher, M. S., *J. Am. Chem. Soc.* **2005,** *127* (19), 6916-6917.

[35] Cosnier, S.; Holzinger, M., *Electrochim. Acta* **2008,** *53* (11), 3948-3954.

[36] Mickelson, E. T.; Huffman, C. B.; Rinzler, A. G.; Smalley, R. E.; Hauge, R. H.; Margrave, J. L., *Chem. Phys. Lett.* **1998,** *296* (1), 188-194.

[37] Hu, H.; Zhao, B.; Hamon, M. A.; Kamaras, K.; Itkis, M. E.; Haddon, R. C., *J. Am. Chem. Soc.* **2003,** *125* (48), 14893-14900.

[38] Guldi, D. M.; Marcaccio, M.; Paolucci, D.; Paolucci, F.; Tagmatarchis, N.; Tasis, D.; Vázquez, E.; Prato, M., *Angew. Chem. Int. Ed.* **2003,** *42* (35), 4206-4209.

[39] Delgado, J. L.; de la Cruz, P.; Langa, F.; Urbina, A.; Casado, J.; López Navarrete, J. T., *Chem. Commun.* **2004,** (15), 1734-1735.

[40] Coleman, K. S.; Bailey, S. R.; Fogden, S.; Green, M. L. H., *J. Am. Chem. Soc.* **2003,** *125* (29), 8722-8723.

[41] Ying, Y.; Saini, R. K.; Liang, F.; Sadana, A. K.; Billups, W. E., Functionalization of Carbon Nanotubes by Free Radicals. *Org. Lett.* **2003,** *5* (9), 1471-1473.

[42] Pénicaud, A.; Poulin, P.; Derré, A.; Anglaret, E.; Petit, P., *J. Am. Chem. Soc.* **2005,** *127* (1), 8-9.

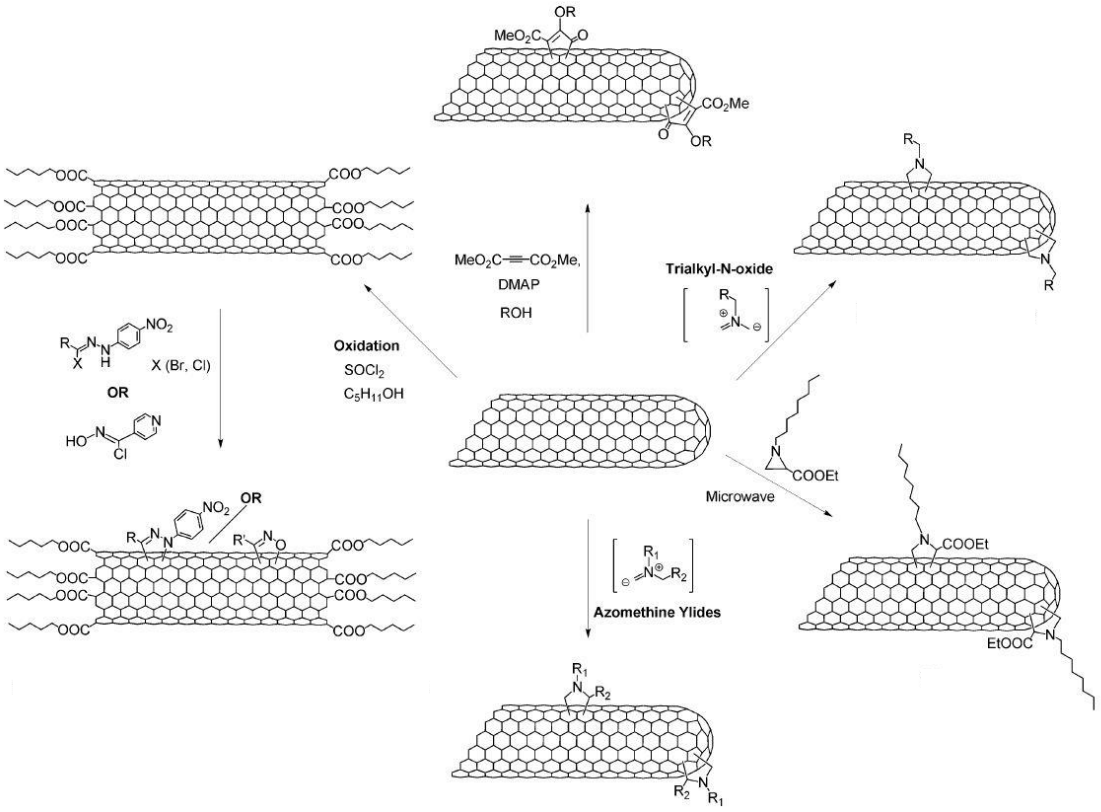

Scheme 2. 1,3-dipolar cycloaddition reactions of SWNTs.

One recent example of via reductive alkylation of SWNTs was reported by Hirsch[43] and co-workers. They synthesised a covalently cross-linked SWNT network starting from negatively charged carbon nanotubides (KC_4). In addition, they compared the molecule and the functional group of the molecule added iodides and diazonium salts (Scheme 3) showing the best results with iodides phenylene molecule in terms of degree of functionalization and biphenyl in thermal stability and improving in the oxygen reduction reaction (ORR).

[43] Schirowski, M.; Abellán, G.; Nuin, E.; Pampel, J.; Dolle, C.; Wedler, V.; Fellinger, T.-P.; Spiecker, E.; Hauke, F.; Hirsch, A., *J. Am. Chem. Soc.* **2018,** *140* (9), 3352-3360.

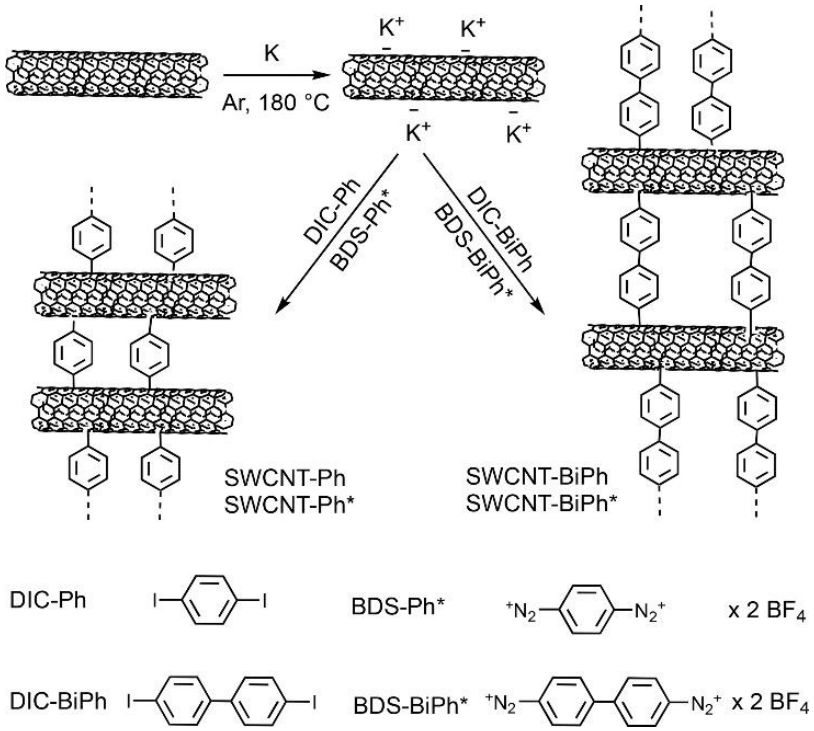

Scheme 3. Schematic procedure of covalently cross-linked with phenylene and biphenylene molecules (Bisdiazonium Salts (BDS) and Diiodo Compounds (DIC)) in SWNTs. Reprinted with permission from *J. Am. Chem. Soc.* **2018**, *140* (9), 3352-3360. Copyright (2018) American Chemical Society.

1.3. **Mechanically Interlocked Nanotubes (MINTs).**

Mechanically interlocked molecules (MIMs) are molecules that are connected as a consequence of their topology. These molecule are not directly connected with covalent bonds, yet they cannot be separated without breaking a covalent bond. Examples of MIMs include catenanes, rotaxanes and molecular knots. For the design and synthesis of molecular machines, was recognized with Nobel Prize in Chemistry in 2016[44] to Fraser Stoddart,[45] Jean-Pierre Sauvage[46] and Ben Feringa.[47]

[44] Leigh, D. A., *Angew. Chem. Int. Ed.* **2016,** *55* (47), 14506-14508.

[45] Stoddart, J. F., *Angew. Chem. Int. Ed.* **2017,** *56* (37), 11094-11125.

[46] Sauvage, J.-P., *Angew. Chem. Int. Ed.* **2017,** *56* (37), 11080-11093.

[47] Feringa, B. L., *Angew. Chem. Int. Ed.* **2017,** *56* (37), 11060-11078.

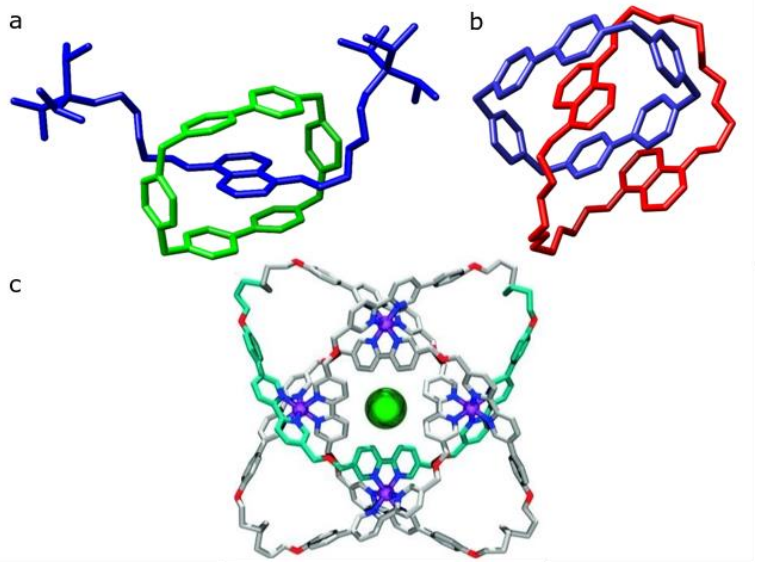

Figure 5. Examples of **a.** rotaxane, **b.** catenane and **c.** molecular knot.

An example of MIMs are rotaxanes. Very briefly, a rotaxane is a MIM in which a rod-like fragment is threaded through the macrocyclic component and the bulky groups located on both ends of the axle preventing de-threading (Figure 5a). Very recently, von Delius and co-workers have described a beautiful example of a rotaxane in which fullerene derivatives were used both as station for the macrocycle and as stoppers[48,49] (Figure 6). Examples of MIM compounds comprising carbon nanotubes have also been described.[49]

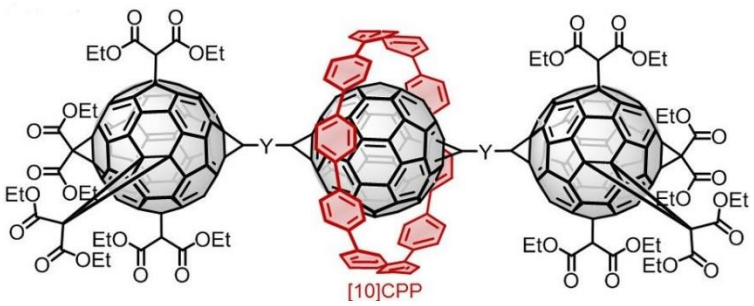

Figure 6. Cycloparaphenylene-fullerene rotaxane synthesised by Xu *et al*.[48] Adapted with permission from *J. Am. Chem. Soc.* **2018,** *140* (41), 13413-13420. Copyright (2018) American Chemical Society.

[48] Xu, Y.; Kaur, R.; Wang, B.; Minameyer, M. B.; Gsänger, S.; Meyer, B.; Drewello, T.; Guldi, D. M.; von Delius, M., *J. Am. Chem. Soc.* **2018,** *140* (41), 13413-13420.

[49] Barrejón, M.; Mateo-Alonso, A.; Prato, M., *Eur. J. Org. Chem.* **2019,** *2019* (21), 3371-3383.

Regarding the carbon nanotubes, an example of combination with MIMs was reported by Stoddart and co-workers.[50] They used a non-covalent functionalization of semiconducting SWNT (as the bottom electrode) with a monolayer of bistable, nondegenerate [2]catenane tetracations, self- organized by their supporting amphiphilic dimyristoyl phosphatidyl anions which shield the mechanically switchable tetracations (Figure 7). Active and remnant current–voltage measurements demonstrated that these devices can be reconfigurable switched and repeatedly cycled under ambient conditions.

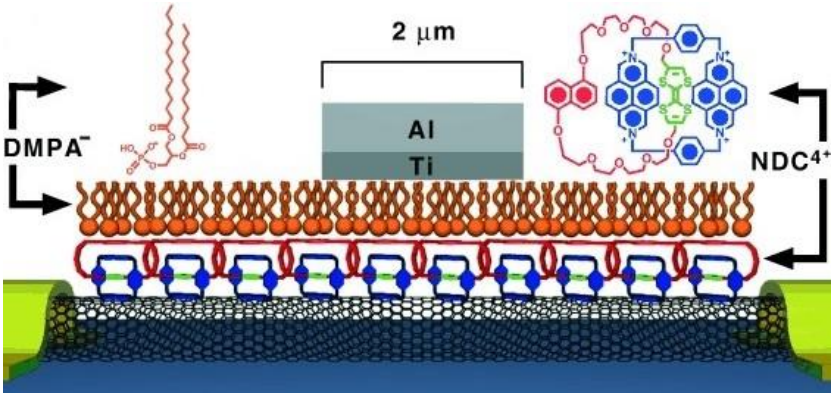

Figure 7. Representation of SWNT- two-terminal molecular switch tunnel junctions (MSTJ) device.

In order to find a functionalization method of SWNTs which not implies the saturation of C sp^2 (covalent functionalization) but in which the product is kinetically stable (non-covalent functionalization), our group has developed a new method of chemical manipulation of SWNTs through the synthesis of Mechanically Interlocked derivatives of SWNTs (MINTs).[51,52,53,54,55] The strategy is to use a U-shape macrocycle equipped with two SWNT recognition units and terminated with bisalkenes that were closed around the nanotubes through ring-closing metathesis (RCM) (Figure 8a, b).

[50] Diehl, M. R.; Steuerman, D. W.; Tseng, H.-R.; Vignon, S. A.; Star, A.; Celestre, P. C.; Stoddart, J. F.; Heath, J. R., *ChemPhysChem* **2003,** *4* (12), 1335-1339.

[51] Pérez, E. M., *Chem. Eur. J.* **2017,** *23* (52), 12681-12689.

[52] López-Moreno, A.; Pérez, E. M., *Chem. Commun.* **2015,** *51* (25), 5421-5424.

[53] Leret, S.; Pouillon, Y.; Casado, S.; Navío, C.; Rubio, Á.; Pérez, E. M., *Chem. Sci.* **2017,** *8* (3), 1927-1935.

[54] de Juan, A.; Pouillon, Y.; Ruiz-González, L.; Torres-Pardo, A.; Casado, S.; Martín, N.; Rubio, Á.; Pérez, E. M., *Angew. Chem. Int. Ed.* **2014,** *53* (21), 5394-5400.

[55] de Juan-Fernández, L.; Münich, P. W.; Puthiyedath, A.; Nieto-Ortega, B.; Casado, S.; Ruiz-González, L.; Pérez, E. M.; Guldi, D. M., *Chem. Sci.* **2018,** *9* (33), 6779-6784.

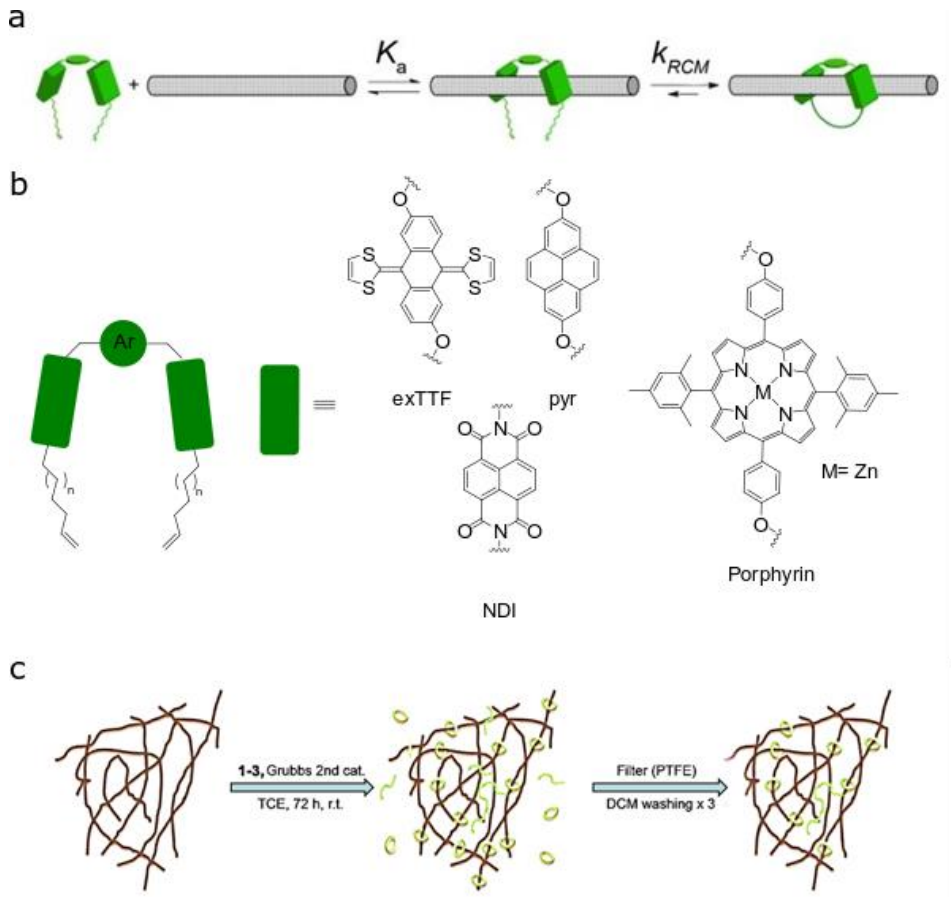

Figure 8. **a.** Clipping strategy for the synthesis of MINTs. Equilibrium due to the interaction between the macrocycle and the carbon nanotube (K_a) and organic RCM reaction through pseudo-first order kinetics (k_{RCM}) **b.** Structure of U-shape molecules with different units of recognition: π-extended tetrathiafulvalene derivative (exTTF), pyrene derivative (pyr), naphthalene diimide (NDI) derivative and porphyirin derivative. **c.** Schematic representation of the experimental procedure of MINTs reaction.

The experimental procedure is simple (Figure 8c): A suspension of SWNTs is made in an adequate solvent (normally tetrachloroethane) using ultrasonication and then, U-shape molecule and 2nd generation Grubs catalyst are added. The mixture is left stirring at room temperature during 72 hours, and then is filtered through polytetrafluoroethylene membrane of 0.2 μm pore. The product is washed and filtered three times with dichloromethane. These MINTs were fully characterized by analytical, spectroscopic, and microscopic techniques, as well as by appropriate control experiments. In addition, these macrocycles are stable even heating at reflux in tetrachloroethane (147ºC) during 30 min.

In fact, the only way to remove these macrocycles is calcination of the sample at 360ºC for 30 min. (Thermogravimetric analysis (TGA)).

Regarding the kinetics of the reaction, the MINT formation is performed in two steps: non-covalent association between U-shape-SWNT and covalent reaction through RCM (Figure 8a). The first one is a supramolecular binding equilibrium. In a chemical equilibrium, the association constant K_a determines the direction of the reaction. Although there was not standard method to measure K_a to nanotubes, our group[56] developed an easy method to measure through the mixture of host-SWNT, filtration and calculation of host-bound with the values in TGA. We also measured U-shapes for MINTs reaction and we obtained a values of K_a in order of 10^4 M^{-1}. Hence, these values indicates a high and favourable interaction between U-shape-SWNT. In the second step (covalent bond, RCM reaction) there are two possible products: reaction between bisalkenes to form the macrocycle around the tube (RCM) and reaction between U-shapes through acyclic diene metathesis polymerization (ADMP). The difference of these two products is the kinetic profile. In the case of RCM is well known to be pseudo-first order kinetic, while ADMP is expected to be second order.[57] This also was studied, showing that RCM is the rate-determining step, and hence MINTs the major product.[53]

In summary, our group has developed a versatile methodology of functionalization of SWNTs through mechanical bond, using different recognition motifs in the U-shape molecules, including exTTFs,[54] pyrenes,[52] NDIs[53] and porphyrins[55] (Figure 8b).

More recently, Miki *et al.*[58] reported another method to obtain supramolecular complexes in carbon nanotubes through "ring toss" based on the strong inclusion ability of carbon nanoring (Figure 9b). They synthesized different π-conjugated carbon nanorings, such as cycloparaphenyleneacetylene (CCPA), which have high affinity to the nanotube and directly mixed this macrocycles with the tubes. Finally, they studied and compared different diameter of CCPA compounds with different SWNT diameters with TGA.

[56] de Juan, A.; López-Moreno, A.; Calbo, J.; Ortí, E.; Pérez, E. M., *Chem. Sci.* **2015,** *6* (12), 7008-7014.
[57] Dias, E. L.; Nguyen, S. T.; Grubbs, R. H., *J. Am. Chem. Soc.* **1997,** *119* (17), 3887-3897.
[58] Miki, K.; Saiki, K.; Umeyama, T.; Baek, J.; Noda, T.; Imahori, H.; Sato, Y.; Suenaga, K.; Ohe, K., *Small* **2018,** *14* (26), 1800720.

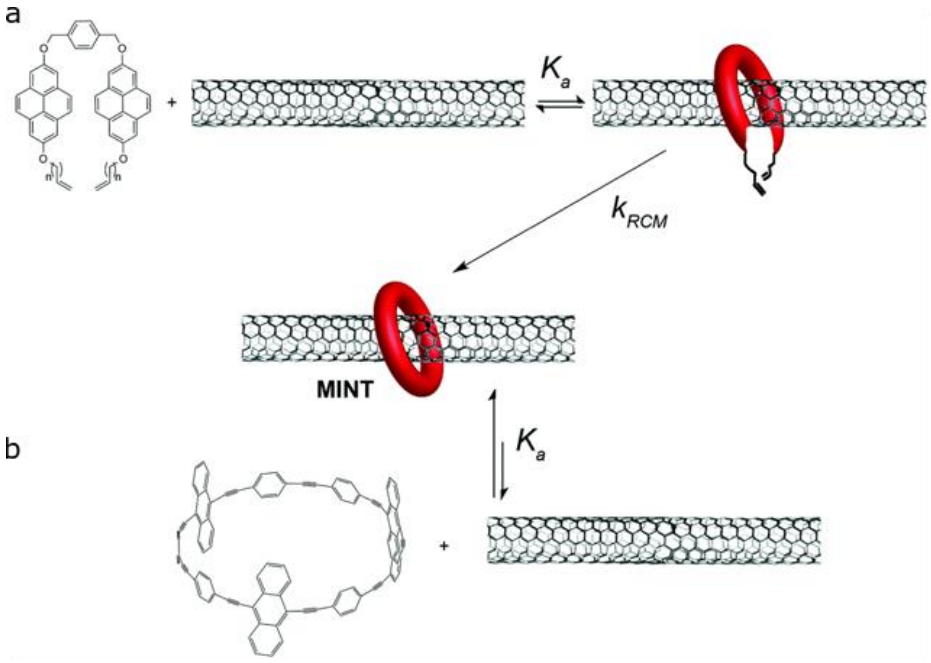

Figure 9. **a.** Ring Closing Metathesis (RCM) strategy developed by our group. **b.** "Ring toss" method by Miki *et al*. The difference between these two methods is Miki *et al* directly mixed the closed-macrocycle with the tube and our group the U-shape first is associated with the tube and secondly the macrocycle is create through RCM around the tube.

Regarding the applications of MINTs, Lopez-Moreno in our group[59] reported a reinforcement of polymers (polystyrene) using MINTs. With very low loading (0.01% of MINTs) resulted in improvement of the Young's modulus and tensile strength of the fibers of over 200% (Figure 10).With computational calculations, they showed this improvement is due to the ability of the MINTs to induce extended conformation in the polystyrene, which allows for an optimized transfer of stress between matrix and SWNTs. In these results, they used three kinds of nanotubes (plasma-purified SWNT (pp-SWNT), (6,5)-SWNT and shorter COOH functionalized SWNT (o-SWNT)), two macrocycles (exTTF and pyr) and the corresponding supramolecular controls.

[59] López-Moreno, A.; Nieto-Ortega, B.; Moffa, M.; de Juan, A.; Bernal, M. M.; Fernández-Blázquez, J. P.; Vilatela, J. J.; Pisignano, D.; Pérez, E. M., *ACS Nano* **2016,** *10* (8), 8012-8018.

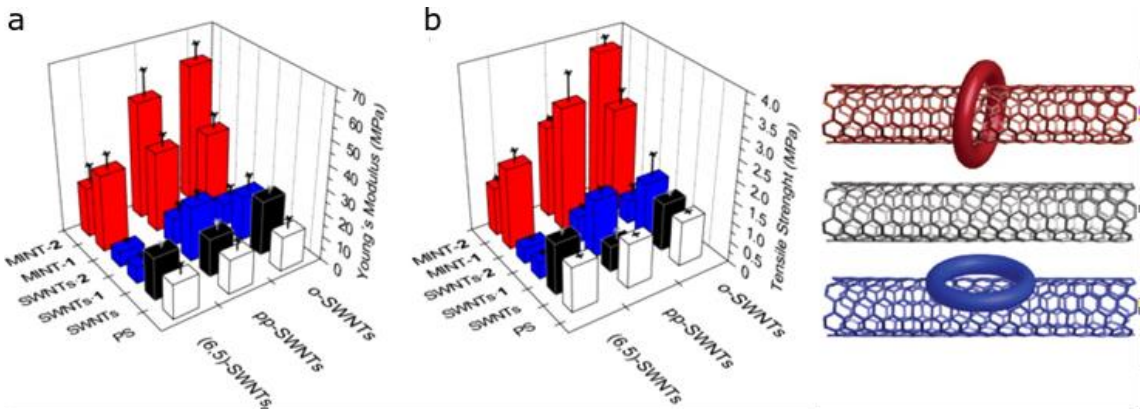

Figure 10. **a.** Young's modulus of polystyrene (PS) (white), SWNTs (black), supramolecular complexes (blue), and MINTs (red) with (6,5)-SWNTs (left), pp-SWNTs (center), and o-SWNTs (right). **b.** Tensile strength of polystyrene (PS) (white), SWNTs (black), supramolecular complexes (blue), and MINTs (red) with (6,5)-SWNTs (left), pp-SWNTs (center), and o-SWNTs (right).

1.4. **Carbon Nanotubes in Catalysis.**

As we mentioned before, one of the applications of SWNTs is in catalysis.[13,21] In general, SWNTs show large specific surface areas, which makes them extremely attractive supports for heterogeneous catalysts. In fact, all atoms in a SWNT are surface atoms, and the surface area is only limited due to aggregation. Another advantage is their relatively high oxidation stability which is induced by their chemical inertness. All these properties make SWNTs a promising support material for heterogeneous catalysis. In this section, we focus on the catalysis putting some examples according to the modification of the CNTs (non-covalent and covalent functionalization) and the type of catalysis (organic reactions and electrochemistry).

Regarding the covalent modification of carbon nanotubes with applications in organic catalysis, an example was reported by Matias Blanco *et al.*[60] In this case, they catalysed the reduction of cyclohexanone to cyclohexanol with 2-propanol/KOH as hydrogen source under air conditions. (Figure 11). They functionalized oxidized CNTs with imidazolium derivative followed by the incorporation of Ir-complex via carbene

[60] Blanco, M.; Álvarez, P.; Blanco, C.; Jiménez, M. V.; Fernández-Tornos, J.; Pérez-Torrente, J. J.; Oro, L. A.; Menéndez, R., *ACS Catal*. **2013,** *3* (6), 1307-1317.

chemistry. As a heterogeneous catalyst, no leaching was observed and they obtained a good recyclability without any loss of activity.

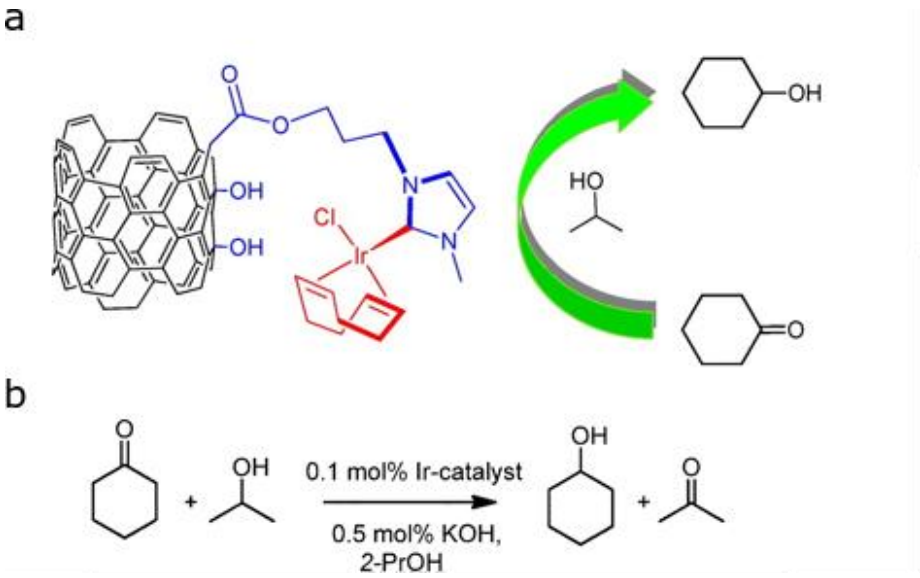

Figure 11. **a.** Schematic representation of the reaction with the Ir-oxidized CNTs. **b.** Conditions of reduction reaction of cyclohexanone to cyclohexanol with 2-propanol/KOH. Adapted with permission from *ACS Catal.* **2013,** *3* (6), 1307-1317. Copyright (2013) American Chemical Society.

More recently, an example of electrocatalysis using non-covalent functionalization CNTs was reported by Reuillard *et al.*[61] They performed the reduction of CO_2 to CO using a Mn-catalyst complex anchored via a pyrene unit to CNTs electrode (Scheme 4). They observed that with difference loading of Mn-catalyst they can be tunable the product selectivity: with high loading of Mn-catalyst, the main product is CO; and with low loading of Mn-catalyst, the main products are hydrogen and formic acid. Through UV-vis and IR spectrosocopy, they could observe two different intermediates depending of the loading of Mn-catalyst: with high loading, this intermediate is a dimeric Mn^0 species and with low loading, monomeric Mn^1-H specie.

[61] Reuillard, B.; Ly, K. H.; Rosser, T. E.; Kuehnel, M. F.; Zebger, I.; Reisner, E., *J. Am. Chem. Soc.* **2017,** *139* (41), 14425-14435.

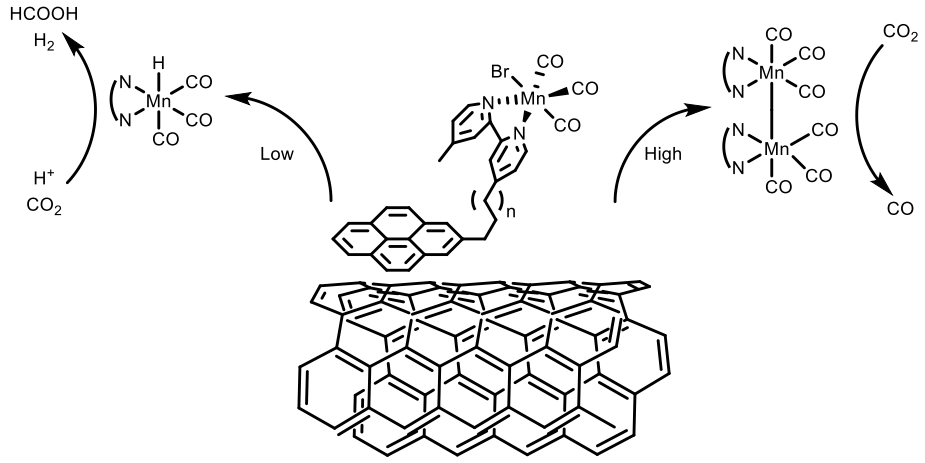

Scheme 4. Schematic representation of [MnBr(bpy$_{pyr}$)(CO)$_3$](Mn$_{pyr}$) immobilized on a CNT sidewall, concentration-dependent dimerization or Mn-H formation, and intermediate-Dependent (Dimeric Mn^0) reduction of CO_2 to CO.

As we have shown, CNTs are usually used in oxidation-reduction catalysis due to their electronic properties. Specifically, they are very used in electrocatalysis[62] with non-covalent functionalization[63,64] due to their high surface area and excellent conductivity, which allow to anchor large amount of electrocatalytic species while retaining good electron transfer properties. For this reason, normally the covalent functionalization is avoided. As we have seen in Scheme 4, the immobilization of unsaturated (poly)cyclic molecules-catalyst (such as pyrene) via π-π interactions with the CNTs has emerged as an important strategy.[65,66] The immobilization of catalyst species onto electrodes gives an enhancement of the catalytic activity.[67,68] Other advantages of this methodology include the need for less catalyst, avoidance of decomposition pathways and easier determination

[62] Sgobba, V.; Guldi, D. M., *Chem. Soc. Rev.* **2009,** *38* (1), 165-184.

[63] Hijazi, I.; Bourgeteau, T.; Cornut, R.; Morozan, A.; Filoramo, A.; Leroy, J.; Derycke, V.; Jousselme, B.; Campidelli, S., *J. Am. Chem. Soc.* **2014,** *136* (17), 6348-6354.

[64] Murakami, N.; Miyake, H.; Tajima, T.; Nishikawa, K.; Hirayama, R.; Takaguchi, Y., *J. Am. Chem. Soc.* **2018,** *140* (11), 3821-3824.

[65] Tran, P. D.; Le Goff, A.; Heidkamp, J.; Jousselme, B.; Guillet, N.; Palacin, S.; Dau, H.; Fontecave, M.; Artero, V., *Angew. Chem. Int. Ed.* **2011,** *50* (6), 1371-1374.

[66] Li, F.; Zhang, B.; Li, X.; Jiang, Y.; Chen, L.; Li, Y.; Sun, L., *Angew. Chem. Int. Ed.* **2011,** *50* (51), 12276-12279.

[67] Kramer, W. W.; McCrory, C. C. L., *Chem. Sci.* **2016,** *7* (4), 2506-2515.

[68] Rosser, T. E.; Windle, C. D.; Reisner, E., *Angew. Chem. Int. Ed.* **2016,** *55* (26), 7388-7392.

of catalyst lifetime. Likewise, the immobilization could change the solubility and behaviour of the catalyst in different solvent, for example water.[69,70]

Also, another common used unsaturated (poly)cyclic molecules is the anthraquinone (AQ) molecule. AQ is an electron-acceptor molecule, cheap and it is a good substituent to metal catalysis in electrocatalysis. As regards in applications, AQ is widely used as electrocatalyst for oxygen reduction reaction (ORR),[71,72] batteries,[73] and capture and release CO_2.[74]

The same as pyrene, the AQ can be anchored to CNTs in order to enhance the characteristics of the molecule with the properties of CNTs.[22] Gong *et al*[75] reported a nanohybrid AQ-CNTs in glassy carbon electrodes proving an increasing of electrocatalytic activity in ORR process.

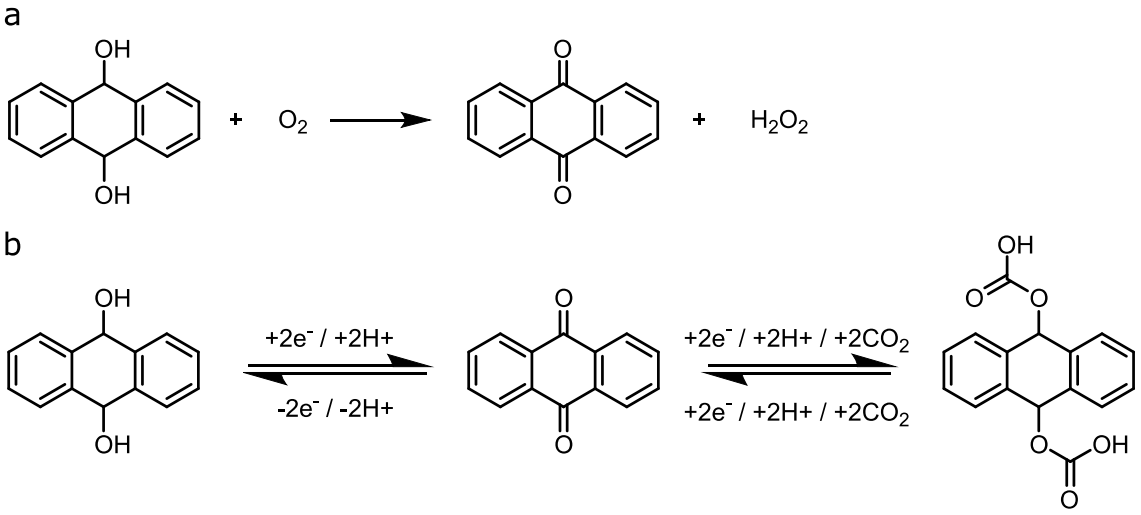

Figure 12. **a.** Simple oxidation reaction of 9, 10-dihydroanthracene-9, 10-diol (AHQ) with oxygen to obtain AQ and H_2O_2. **b.** Electrochemistry of AQ.[74] To reduction to AHQ and capture and release CO_2.

[69] Maurin, A.; Robert, M., *Chem. Commun.* **2016,** *52* (81), 12084-12087.

[70] Lin, S.; Diercks, C. S.; Zhang, Y.-B.; Kornienko, N.; Nichols, E. M.; Zhao, Y.; Paris, A. R.; Kim, D.; Yang, P.; Yaghi, O. M.; Chang, C. J., *Science* **2015,** *349* (6253), 1208-1213.

[71] Mirkhalaf, F.; Tammeveski, K.; Schiffrin, D. J., *Phys. Chem. Chem. Phys.* **2004,** *6* (6), 1321-1327.

[72] Campos-Martin, J. M.; Blanco-Brieva, G.; Fierro, J. L. G., *Angew. Chem. Int. Ed.* **2006,** *45* (42), 6962-6984.

[73] Werner, D.; Apaydin, D. H.; Portenkirchner, E., *Batteries Supercaps* **2018,** *1* (4), 160-168.

[74] Wielend, D.; Apaydin, D. H.; Sariciftci, N. S., *J. Mater. Chem.* **2018,** *6* (31), 15095-15101.

[75] Gong, Z.; Zhang, G.; Wang, S., *J. Chem.* **2013,** *2013*, 9.

2. Objectives

With all these premises, part of this thesis aims to functionalize SWNTs through mechanical bond in order to obtain MINTs samples with different macrocycles. Then, we shall search applications in heterogeneous catalysis and electrochemistry of these MINT samples. In electrochemistry, we will try to combine the properties of anthraquinone and SWNT through mechanically interlocked derivatives carbon nanotubes (MINTs).

With all of this, the specific objectives are:

1) **Synthesis of MINT based on anthraquinone (MINT-AQ).**

2) **Influence of the macrocycle (pyr, exTTF and AQ) in the MINT used as catalyst in the nitro-arene reduction reaction.**

3) **Electrocatalysis using MINT-AQ in the oxygen reduction reaction (ORR).**

Chapter 1.

3. Positive and Negative Regulation of Carbon Nanotube Catalyst through Encapsulation within Macrocycles

The work described in this chapter is published on *Nature Communications* **2018**, *9*, 2671.

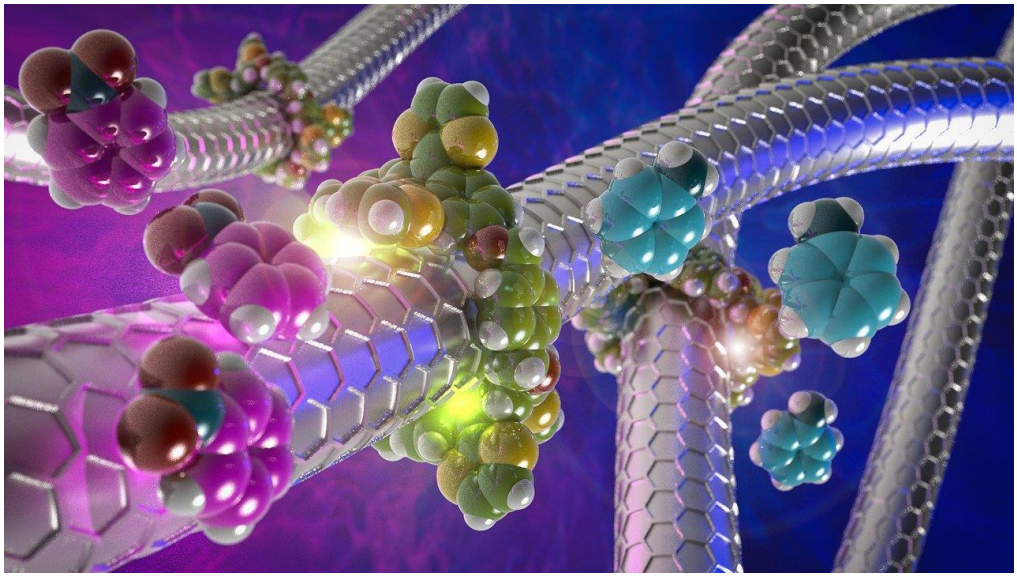

One of the most attractive applications of carbon nanomaterials is as catalysts, due to their extreme surface-to-volume ratio. The substitution of C with heteroatoms (typically B and N as p- and n-dopants) has been explored to enhance their catalytic activity. Here we show that encapsulation within weakly doping macrocycles can be used to modify the catalytic properties of the nanotubes towards the reduction of nitroarenes, either enhancing it (n-doping) or slowing it down (p-doping). This artificial regulation strategy presents a unique combination of features found in the natural regulation of enzymes: binding of the effectors (the macrocycles) is noncovalent, yet stable thanks to the mechanical link, and their effect is remote, but not allosteric, since it does not affect the structure of the active site. By careful design of the macrocycles' structure, we expect that this strategy will contribute to overcome the major hurdles in SWNT-based catalysts: activity, aggregation, and specificity.

3.1. **Introduction.**

Nature uses a variety of strategies to regulate the activity of enzymes. Mechanisms include complex multimolecular approaches, such as compartmentalization within specific organelles or increasing the concentration of enzyme within a protein scaffold, but the most general methods imply the supramolecular or covalent modification of the enzyme's structure. Direct competition for the active site is the simplest supramolecular regulatory mechanism. Allosteric regulation implies a conformational change in the three-dimensional (3D) structure of the enzyme's active site in response to the noncovalent binding of an effector to a regulatory site located far from it. Phosphorylation, the hydrolysis of GTP to GDP by GTP-binding proteins, and (poly)ubiquitination are the most general methods of regulation based on the making and breaking of covalent bonds.[76]

Metal-free catalysis is one of the most attractive applications of carbon nanomaterials.[77,78,79,80] However, the mechanisms explored to regulate their catalytic activity are limited to positive regulation via covalent modification of their native structure, mostly by including heteroatoms.[81,82,83,84]

We, and subsequently Miki *et al*., have recently reported strategies to form rotaxane-like mechanically interlocked nanotube (MINT) derivatives.[51,58] The native structure of single walled carbon nanotubes (SWNTs) is preserved upon formation of MINTs, while the addition of the macrocycles can prevent bundling at the nanoscale.[52,53,54,85] We have shown that these unique features make MINTs superior polymer fillers[59] and are in principle very appealing for their application in catalysis. The carbon surface of nanomaterials acts as both adsorbent and facilitator of the electron-

[76] Alberts, B., *Molecular Biology of the Cell*. CRC Press: 2017.

[77] Zhou, M.; Wang, H.-L.; Guo, S., *Chem. Soc. Rev.* **2016,** *45* (5), 1273-1307.

[78] Shi, H.; Shen, Y.; He, F.; Li, Y.; Liu, A.; Liu, S.; Zhang, Y., *J. Mater. Chem.* **2014,** *2* (38), 15704-15716.

[79] Schaetz, A.; Zeltner, M.; Stark, W. J., *ACS Catal.* **2012,** *2* (6), 1267-1284.

[80] Yu, D.; Nagelli, E.; Du, F.; Dai, L., *J. Phys. Chem. Lett.* **2010,** *1* (14), 2165-2173.

[81] Shui, J.; Wang, M.; Du, F.; Dai, L., *Sci. Adv.* **2015,** *1* (1), e1400129.

[82] Zhang, S.; Kang, P.; Ubnoske, S.; Brennaman, M. K.; Song, N.; House, R. L.; Glass, J. T.; Meyer, T. J., *J. Am. Chem. Soc.* **2014,** *136* (22), 7845-7848.

[83] Lee, W. J.; Maiti, U. N.; Lee, J. M.; Lim, J.; Han, T. H.; Kim, S. O., *Chem. Commun.* **2014,** *50* (52), 6818-6830.

[84] Zhao, Y.; Yang, L.; Chen, S.; Wang, X.; Ma, Y.; Wu, Q.; Jiang, Y.; Qian, W.; Hu, Z., *J. Am. Chem. Soc.* **2013,** *135* (4), 1201-1204.

[85] Martínez-Periñán, E.; de Juan, A.; Pouillon, Y.; Schierl, C.; Strauss, V.; Martín, N.; Rubio, Á.; Guldi, D. M.; Lorenzo, E.; Pérez, E. M., *Nanoscale* **2016,** *8* (17), 9254-9264.

transfer process in nitroarene reductions,[86] while the modification of the electronic properties of SWNTs through supramolecular modification with electroactive molecules is a well-documented phenomenon.[87,88] Moreover, mechanically interlocked molecules have shown distinctive advantages in the regulation of catalytic activity.[89,90,91] Based on these facts, we expected that the catalytic activity of SWNTs would be controlled remotely by encapsulation with suitable n- or p-doping macrocycles. Here we show that encapsulation of SWNTs within electroactive macrocycles to form MINTs is a valid strategy for the positive and negative regulation of the catalytic activity of SWNTs.

3.2. **Results.**

Synthesis and characterization. We used (6,5)-enriched SWNTs ((6,5)-SWNTs; 0.7–0.9 nm in diameter, length >700 nm, 95% purity) in all experiments. The structures of all macrocycles and density functional theory (DFT) optimized geometries of MINTs with (6, 5)-SWNTs are shown in Figure 1a and b, respectively. Mac-exTTF and mac-pyr and their corresponding MINTs were synthesized as previously reported and fully characterized using thermogravimetric analysis (TGA), Raman spectroscopy, ultraviolet–visible–near infrared absorption spectroscopy (UV-Vis- NIR), photoluminescence excitation/emission spectroscopy (PLE) maps, high-resolution transmission electron (HRTEM), and atomic force microscopies (AFM) and, most importantly, adequate control experiments.[52,54]

[86] Larsen, J. W.; Freund, M.; Kim, K. Y.; Sidovar, M.; Stuart, J. L., *Carbon* **2000,** *38* (5), 655-661.

[87] Anaya-Plaza, E.; Oliva, M. M.; Kunzmann, A.; Romero-Nieto, C.; Costa, R. D.; de la Escosura, A.; Guldi, D. M.; Torres, T., *Adv. Funct. Mater.* **2015,** *25* (48), 7418-7427.

[88] Mollahosseini, M.; Karunaratne, E.; Gibson, G. N.; Gascón, J. A.; Papadimitrakopoulos, F., *J. Am. Chem. Soc.* **2016,** *138* (18), 5904-5915.

[89] Blanco, V.; Leigh, D. A.; Marcos, V.; Morales-Serna, J. A.; Nussbaumer, A. L., *J. Am. Chem. Soc.* **2014,** *136* (13), 4905-4908.

[90] Marcos, V.; Stephens, A. J.; Jaramillo-Garcia, J.; Nussbaumer, A. L.; Woltering, S. L.; Valero, A.; Lemonnier, J.-F.; Vitorica-Yrezabal, I. J.; Leigh, D. A., *Science* **2016,** *352* (6293), 1555-1559.

[91] Zhu, K.; Baggi, G.; Vukotic, V. N.; Loeb, S. J., *Chem. Sci.* **2017,** *8* (5), 3898-3904.

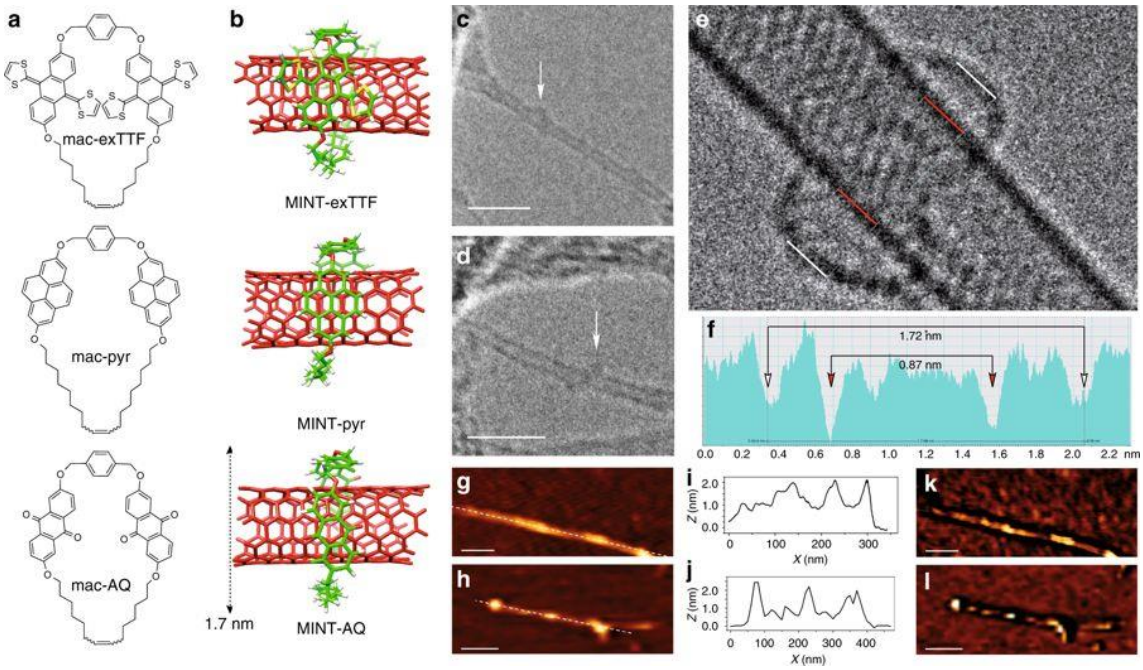

Figure. 1 Structures and microscopy. **a.** Chemical structure of the macrocycles and **b.** minimum energy (DFT) geometries of the corresponding MINTs with (6,5)-SWNTs. The calculated diameter of MINT-AQ is shown for comparison with the microscopy images. **c, d.** Representative TEM images of MINT-AQ, showing SWNTs surrounded objects of adequate size (ca. 2 nm) and shape to be mac-AQ. Scale bars are 5 nm. **e.** ac-HRTEM image of a single MINT-AQ, and **f.** its corresponding analysis along the box depicted with thin white and red lines. **g–l.** AFM characterization of MINT-AQ. We observe isolated SWNTs with protrusions of around 2 nm (**g, h**), as shown in the profiles along the white dashed lines (**i, j**). The phase images (**k, l**) show energy dissipation contrast at the protrusions. Scale bars are 50 nm (**g, k**) and 100 nm (**h, l**).

Mac-AQ shows identical structure to mac-exTTF but features the well-known electron acceptor AQ[72] (see Figures S1-4). For the synthesis of MINT-AQ, we used a clipping strategy in which the SWNTs serve as template for the formation of mac-AQ around the nanotubes, to yield MINT-AQ. Analysis of the kinetics of formation of MINT-AQ confirms that ring-closing metathesis around the SWNTs is the major reaction pathway, with negligible participation of oligomerization. Control experiments using C_{60} as soluble template for RCM are also in agreement with this picture (Figure S8). After the MINT-forming reaction, the SWNTs showed a loading of macrocycle of 35–37% for MINT-exTTF, 24–28% for MINT-pyr, and 31–33% for MINT-AQ by TGA analysis

(Figure S5). This degree of functionalization remains stable even after reflux in tetrachloroethane for 30 min, which demonstrates the extreme stability of MINTs. A preliminary TEM study performed in conventional equipment at 200 kV allows for the visualization of contrasts of adequate size and shape to be individual macrocycles around the SWNTs (or their decomposition products after reaction with the electron beam).[92] Figure 1c, d show representative examples of conventional TEM images of isolated SWNTs (diameter 0.8–0.9 nm) around which we can observe circular objects of ca. 2.0 nm diameter, marked at the images. In order to get more precise structural information, atomically resolved images were acquired in an aberration-corrected microscope at low voltage, 60 kV, in order to minimize the electron beam damage. A characteristic aberration-corrected HRTEM image is shown in Figure 1e. The image shows a macrocycle of diameter 1.7–1.8 nm around a SWNT of 0.9 nm in diameter. Remarkably, the distances between mac-AQ and the walls of the SWNT (see contrast profile in Figure 1f) correspond to nearly ideal (0.35 nm, top) or very close (0.42 nm, bottom) van der Waals contacts, indicating a very strong interaction between mac-AQ and the SWNT, which justifies the template effect during the synthesis of MINT-AQ. The experimental distances observed in between the dark contrasts that compose the macrocycle are around 0.12 nm, in agreement with the average theoretical carbon–carbon distances. The AFM images obtained upon exploration of a drop-casted suspension of MINT-AQ on mica are also consistent with the proposed rotaxane-like structure. Figure 1g, h show AFM topographic images of individualized SWNTs of height around 0.6–1.0 nm, which show protuberances of approximately 2 nm height (see profiles in Figures 1i and j). In the phase images (Figures 1k and l), these objects show different contrast compared to the SWNTs, demonstrating that they are not carbon nanotube protrusions or deformations. We have previously shown that mac-exTTF behaves as an electron donor toward (6,5)-SWNTs.[85] The steady-state photophysical characterization of MINT-AQ (UV-vis-NIR and PLE) confirms that mac-AQ acts as an electron acceptor toward SWNTs, at least upon photoexcitation (Figures S6 and S7).

[92] Chamberlain, T. W.; Biskupek, J.; Skowron, S. T.; Markevich, A. V.; Kurasch, S.; Reimer, O.; Walker, K. E.; Rance, G. A.; Feng, X.; Müllen, K.; Turchanin, A.; Lebedeva, M. A.; Majouga, A. G.; Nenajdenko, V. G.; Kaiser, U.; Besley, E.; Khlobystov, A. N., *ACS Nano* **2017,** *11* (3), 2509-2520.

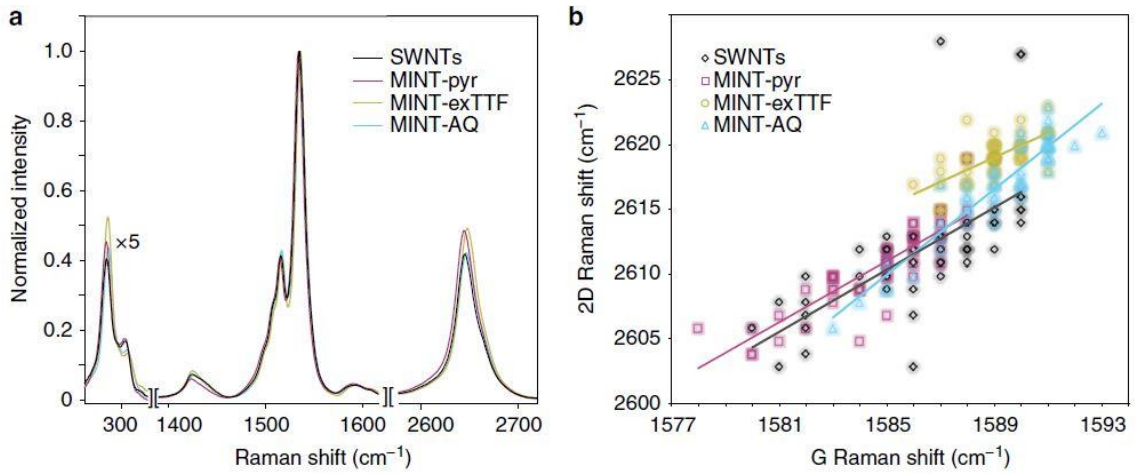

Figure. 2 Raman spectroscopy. **a.** Average (N = 50) Raman spectra of SWNT (black), MINT-exTTF (yellow), MINT-pyr (purple), and MINT-AQ (cyan). **b.** Plot of the Raman shift of 2D band vs G band for each of the 50 different spectra (λ_{exc} = 532 nm) of SWNT (black rhombi), MINT-exTTF (yellow circles), MINT-pyr (purple squares), and MINT-AQ (cyan triangles), data points are shaded to indicate the frequency of occurrence.

Raman spectroscopy is particularly useful in characterizing the electronic properties of SWNTs. Figure 2a displays the average of 50 Raman spectra (λ_{exc} = 532 nm) of MINT-exTTF (yellow), MINT-pyr (purple), MINT-AQ (cyan), and pristine (6,5)-SWNT (black). All spectra are very similar, with no increase in the relative intensity of the D band, proving that the covalent structure of the SWNT is preserved upon formation of MINTs. Analysis of the Raman shifts of the G and 2D bands is usually considered the best indication of doping in SWNTs. For direct and strong doping of SWNTs via electrochemical or electronic means, the expected direction and magnitude: large (up to 10 cm^{-1}) blue shift for p-doping, moderate (<5 cm^{-1}) red shift for n-doping, of the Raman shifts for the G band is well stablished.[93] Unfortunately, the case is not so clear for molecular dopants, since the Raman shifts are affected by other factors such as aggregation or mechanical strain that can change during the chemical treatment, and moderate blue shifts have been related to an increase in conductivity that can be found for both types of dopants.[94] In our case, both MINT-exTTF (1589 ± 2 and 2616 ± 4 cm^{-1}) and MINT-AQ (1589 ± 1 and 2619 ± 2 cm^{-1}) showed small hypsochromic shifts in the

[93] Sumanasekera, G. U.; Allen, J. L.; Fang, S. L.; Loper, A. L.; Rao, A. M.; Eklund, P. C., *J. Phys. Chem.* **1999,** *103* (21), 4292-4297.
[94] Skákalová, V.; Kaiser, A. B.; Dettlaff-Weglikowska, U.; Hrnčariková, K.; Roth, S., *J. Phys. Chem.* **2005,** *109* (15), 7174-7181.

frequency of the G and 2D bands with regards to pristine SWNTs (1587 ± 2 and 2612 ± 5 cm^{-1}), while MINT-pyr shows smaller bathochromic shifts (1585 ± 2 and 2611 ± 3 cm^{-1}). Recently, Ryu and coworkers have shown that the mechanical strain and charge doping components of the Raman shifts can be separated for graphene by plotting the Raman shift of the G band against that of the 2D band, whereby variations due to mechanical strain fall along a straight line of known slope while effects due to doping deviate from this behavior.[95] Since the origin of the G and 2D bands in SWNTs is identical to that of graphene,[96] we reasoned that a similar analysis would help us shed light on the origin of the Raman shifts. Figure 2b shows the corresponding plot. For SWNTs (black) and MINT-pyr (purple), the data show nearly identical linear tendencies, following a straight line of slope 1.2. In contrast, the data for MINT-AQ (cyan) shows a significantly larger slope of 1.65, while the MINT-exTTF data are closely grouped and show a significantly smaller (0.95) slope. By comparison with graphene,[95] both MINT-exTTF and MINT-AQ data fall into the doping-affected quadrant, while MINT-pyr does not. Taken together, the Raman data are a solid experimental indication of the electronic effects of each type of macrocycle on the SWNTs: weak n-doping for mac-exTTF, weak p-doping for mac-AQ, no doping for mac-pyr, supporting the initial design. An analysis of Mülliken population confirms that there is a charge transfer between the macrocycle and SWNTs in the expected directions. For MINT-AQ, the charge transfer is from SWNT to mac-AQ leaving the SWNT with +0.011e (p-doping), while for the formation of the MINT-exTTF the charge transfer takes place from mac-exTTF to SWNT, leaving the latter with −0.043e (n-doping). This is consistent with the nature of electron-accepting tendency of AQ and electron-donor tendency of exTTF. For the MINT-pyr, the calculated charge transfer is +0.005e, one order of magnitude lower, and cannot be unambiguously identified as a charge transfer between the macrocycle and the SWNT. Furthermore, analysis of the localization and energy of the frontier molecular orbitals of energy-minimized (DFT, b97d/3-21g*) MINT models sufficiently large to reproduce the Raman results supports the predicted electronic effects (Figures S10 and S11). These theoretical results are in good agreement with the experimental Raman tendencies in Figure 2b.

[95] Lee, J. E.; Ahn, G.; Shim, J.; Lee, Y. S.; Ryu, S., *Nat. Commun.* **2012,** *3*, 1024.

[96] Dresselhaus, M. S.; Jorio, A.; Hofmann, M.; Dresselhaus, G.; Saito, R., *Nano Lett.* **2010,** *10* (3), 751-758.

Catalysts activity and recyclability.

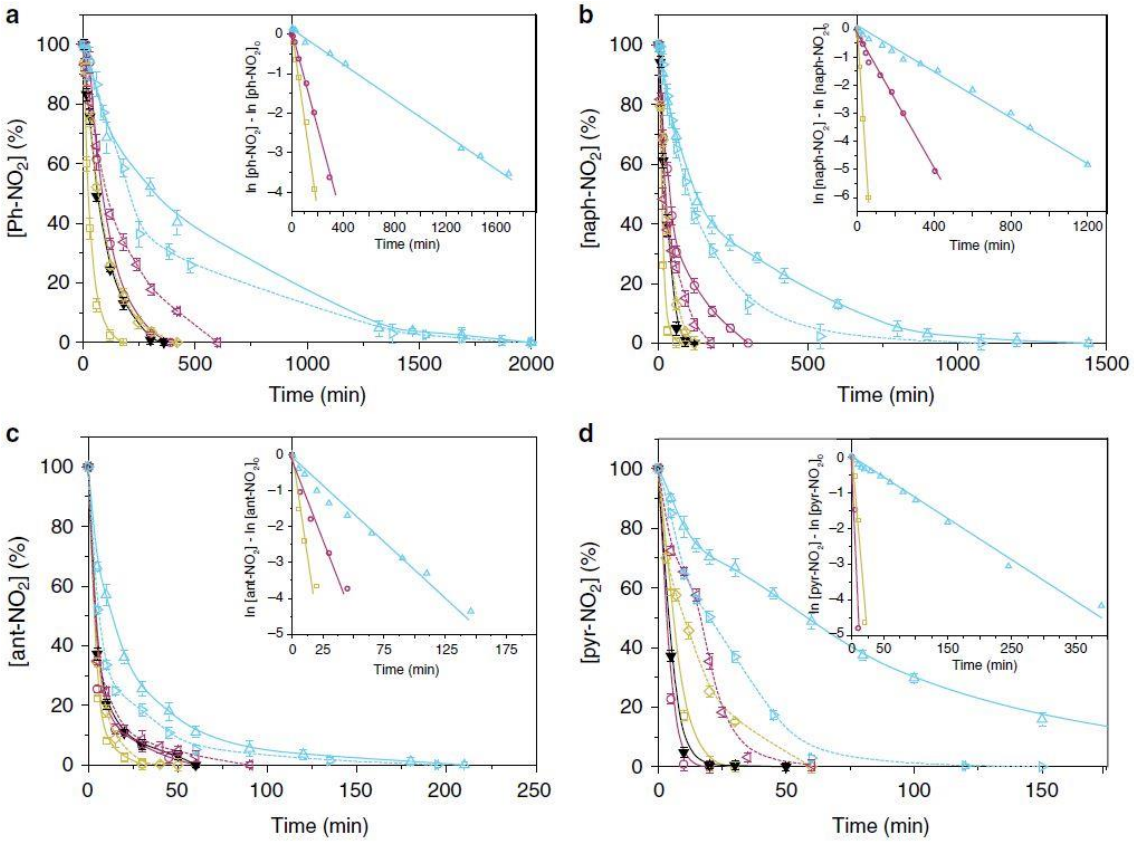

Figure. 3 Catalysts activity. Kinetics of the reduction of **a.** Ph-NO_2, **b.** naph-NO_2, **c** ant-NO_2, **d.** pyr-NO_2 catalyzed by MINT-exTTF (yellow solid line), MINT-pyr (purple solid line), MINT-AQ (cyan solid line), 6,5-SWNT (black solid line), SWNT-exTTF (yellow dashed line), SWNT-pyr (purple dashed line), and SWNT-AQ (cyan dashed line). Error bars are standard deviation from three separate experiments.

With the different influence of the macrocycles on the electronic properties of the MINT samples established, we went on to test its effects on the catalytic reduction of nitroarenes. Supramolecular complexes resulting from the direct mixing of SWNTs and mac-exTTF, mac-pyr, or mac-AQ were used as reference samples. A series of aromatic compounds with increasing conjugated aromatic rings: nitrobenzene (ph-NO_2), 1-nitronaphthalene (naph-NO_2), 9- nitroanthracene (ant-NO_2), and 1-nitropyrene (pyr-NO_2), were selected as substrates to be reduced. Very briefly, the SWNT catalyst (5 mg) was mixed with 4.1 mmol of substrate in 2mL of d_6-DMSO as solvent (selected after optimization of the reaction conditions) (Figure S13). Finally, 31.8 mmol of hydrazine were added as reducing agent, and the progress of the reaction was monitored by ^{1}H-

nuclear magnetic resonance (NMR) spectroscopy. In order to confirm that the active sites corresponded only to the nanotube walls, we conducted total reflection X-ray fluorescence (TRXF) measurements, and only ppm-level of metallic impurities were detected (Figures S15-18). More importantly, we used the same batch of SWNTs for all experiments and the synthesis of all MINTs, so any changes in catalytic activity can only be ascribed to modifications in the SWNT material. The reactions proceed smoothly with no induction period detected, yielding the aniline reduction products almost exclusively, with the corresponding hydroxylamines as only detectable intermediates (Figure S14). In Figure 3, we compare the activity of all catalysts under study. In the absence of catalyst, the reduction of Ph-NO_2 proceeded to a conversion of only ca. 50% after 24 h of reaction (Figure S14). The first observation is that conversions >95% with selectivity >95% to the target aniline were achieved in all catalyzed reactions. Some noticeable tendencies are clear across the different substrates. For example, for Ph-NO_2, MINT-exTTF converted 95% of the starting material in 120 ± 5 min, while MINT-pyr needed more than twice as much time to reach the same conversion (300 ± 6 min); finally the reaction catalyzed by MINT-AQ required over 1800 ± 20 min to achieve 95% conversion. For comparison, the pristine (6,5)-SWNT showed an intermediate catalytic activity and required 260 ± 7 min to consume 95% of the starting material. This last observation confirms that the possible decrease in available SWNT catalytic sites due to the encapsulation with the macrocycles does not result in a significant decrease in the catalytic activity. An electronic effect, however, is clear. Larsen et al. showed that the carbon nanomaterial extracts electrons from the medium, stocks them as an electronic reservoir, and provides them for the reacting molecules.[86] According to this picture, the electron–donor behavior of mac-exTTF moiety should be beneficial, either by supplying additional electrons to the nanotube or, most likely, by decreasing the energy barrier toward release of the electrons. Following the same argument, the electronically "neutral" character of the mac-pyr should not influence the reactivity, and the electron-acceptor nature of mac-AQ should withdraw electron density from the nanotube, which would result in decreased activity. This is exactly the picture that emerges for the reduction of Ph-NO_2 and is conserved for all other substrates, except the largest pyr-NO_2, where the catalytic activity of (6,5)-SWNT, MINT-exTTF, and MINT-pyr is approximately equal. The detrimental effect of the electronwithdrawing mac-AQ is patent in all cases. Interestingly, the same relative

tendencies are qualitatively reproduced in the supramolecular control experiments (mac-exTTF > mac-pyr > mac-AQ), but all supramolecular models show lower catalytic activity than the pristine SWNTs, except in the case of mac-exTTF for the reduction of ant-NO_2 (dashed lines, Figure 3). It has been argued that residual carbonyl groups are responsible for the catalytic effect of SWNTs in the reduction of nitroaromatics;[97] our results contradict such hypothesis and support the picture provided by Larsen *et al*.[86] The effect of the substrate on the catalytic reduction was also investigated. The reaction becomes progressively faster as the size of the aromatic nitroarene increases. For naph-NO_2, we needed 45 ± 2, 260 ± 4, and 1080 ± 10 min to achieve complete conversión using MINT-exTTF, MINT-pyr, and MINT-AQ, respectively. Shorter times were required to reduce ant-NO_2 (20 ± 4, 45 ± 5, and 120 ± 3 min) and even shorter for pyr-NO_2 (16 ± 1, 8 ± 1 and 240 ± 5 min). DFT calculations were performed to evaluate the binding energy between the nitroaromatic molecules and the nanotube walls.[56,98] The calculations revealed a progressively more favorable binding energy between the nitroaromatic molecule and the carbon nanomaterial: −15.45 Kcal mol^{-1} for Ph-NO_2, −21.73 Kcal mol^{-1} for naph-NO_2, −26.54 Kcalmol^{-1} for ant-NO_2, and −31.38 Kcalmol^{-1} in the case of pyr-NO_2, as expected due to the increase in available surface of the nitroaromatic system.

Table 1 First-order kinetic constants (k values in $s^{-1} \times 10^{-3}$) as obtained from the fits shown in the insets of Figure 3.

	ph-NO_2	*naph-NO_2*	*ant-NO_2*	*pyr-NO_2*
MINT-exTTF	0.36	1.71	2.93	3.98
MINT-pyr	0.20	0.36	1.28	7.98
MINT-AQ	0.03	0.06	0.47	0.18
(6,5)-SWNT	0.27	0.88	1.27	4.67
SWNT-exTTF	0.19	0.60	2.83	1.10
SWNT-pyr	0.07	0.45	0.86	3.98
SWNT-AQ	0.08	0.12	0.48	0.72

[97] Wu, S.; Wen, G.; Wang, J.; Rong, J.; Zong, B.; Schlögl, R.; Su, D. S., *Catal. Sci. Technol.* **2014,** *4* (12), 4183-4187.
[98] Calbo, J.; López-Moreno, A.; de Juan, A.; Comer, J.; Ortí, E.; Pérez, E. M., *Chem. Eur. J.* **2017,** *23* (52), 12909-12916.

Therefore, the increase in reduction rate is directly related to an increase in SWNT–substrate binding energy. Analysis of the first-order kinetic constants (insets of Figure 3, and Table 1) allows for a more quantitative comparison of the results. MINT-exTTF is consistently the best catalyst and k progressively increases with the number of condensed rings in the substrate. Meanwhile, the constants of the MINT-pyr are very similar to those obtained for the pristine (6,5)-SWNT and consistently smaller than those obtained for MINT-exTTF, with the exception of the pyr-NO_2 substrate. We interpret this exception in light of the strong tendency of pyrene to selfassociate and the presence of two pyrene moieties in mac-pyr, which probably facilitates the adsorption of pyr-NO_2 on the catalyst surface. Finally, MINT-AQ consistently shows significantly smaller k in all cases, reflecting the electron-acceptor character of mac-AQ. Supramolecular control samples show the same tendencies and comparable but slower reaction rates for the first round of reactions, ruling out a direct catalytic effect of the macrocycle (Figure 3). Remarkably, the supramolecular catalysts cannot be recycled, as they recover the basal activity of pristine (6,5)-SWNTs upon purification after the first reaction cycle (Figures S26 and S27). In comparison, recycling of the MINT-based catalysts MINT-exTTF, MINT-pyr, and MINT-AQ, without any detectable loss in the macrocycle effects for up to 12 cycles was straightforward. In line with this recyclability results, the structural integrity of the MINT catalysts under the reaction conditions was probed by Raman spectroscopy (Figure S28).

3.3. **Conclusions.**

In conclusion, we have shown that encapsulation within p- or n-doping macrocycles is a valid strategy for the regulation of the catalytic activity of SWNTs. As a test bed, we have chosen the reduction of nitroaromatic compounds. The effect of the macrocycles on the catalytic activity is most likely due to a combination of factors, including changes in the degree of aggregation, binding site availability, etc., but the electronic effect is clearly predominant. Electron-donating exTTF macrocycles lead to a higher activity, while electron-accepting mac-AQ moieties significantly slow the reaction rates. Meanwhile, SWNTs modified with the electronically neutral mac-pyr show very similar activity to pristine SWNTs. Crucially, mechanical interlocking of the macrocycles around the SWNTs to form MINTs results in stable catalysts that can be recycled, as

opposed to classic supramolecular model compounds, which lose the effect of the macrocycle after the first reaction cycle. To achieve these conclusions, we purposely designed, synthesized, and fully characterized MINTs based on mac-AQ. We have also carried out DFT calculations on all MINTs, which support the picture provided by the experimental data. This new artificial regulation strategy presents a combination of the features found in the natural regulation of enzymes that make it unique: it can be used for both positive and negative regulation, the effector (macrocycle) is associated with the catalyst (SWNT) via noncovalent yet stable mechanical bonds, and its effect is remote but not allosteric, since it does not affect the 3D structure of the catalyst active site. We have focused here on the regulation of activity of SWNT catalysts, but we anticipate that structural variations on the macrocycles could make this strategy of general interest to help overcome the problems of aggregation and substrate specificity in one-dimensional catalysts.

3.4. **Supplementary Information.**

3.4.1. **General Information.**

Materials. (6,5)-Enriched single walled nanotubes ((6,5)-SWNT) were purchased from Sigma-Aldrich (0.7−0.9 nm in diameter, length ≥700 nm, mostly semiconducting, 95% purity). Reagents were used as purchased. All solvents were dried according to standard procedures. All air-sensitive reactions were carried out under N_2 atmosphere. *Characterization methods.* Analytical thin layer chromatographies (TLC) were performed using aluminium-coated Merck Kieselgel 60 F254 plates. NMR spectra were recorded on a Bruker Avance 400 (1H: 400 MHz; 13C: 100 MHz) spectrometers at 298 K, using partially deuterated solvents as internal standards. Coupling constants (*J*) are denoted in Hz and chemical shifts (δ) in ppm. Electrospray ionization mass spectrometry (ESI-MS) and Matrix-assisted Laser desorption ionization (coupled to a Time-Of-Flight analyzer) experiments (MALDITOF) were recorded on a HP1100MSD spectrometer and a Bruker REFLEX. Thermogravimetric analyses (TGA) were performed using a TA Instruments TGAQ500 with a ramp of 10 °C min^{-1} under air from 100 to 1000 °C. Transmission electron microscopy (TEM) images were obtained with JEOL-JEM 2100F instrument or a JEOL-JEM GRAND ARM300cF (ac-HRTEM). Atomic Force

Microscopy (AFM) images were acquired using a JPK NanoWizard II AFM working in dynamic mode. NT-MDT NSG01 silicon cantilevers, with typical values of 5.1 N m^{-1} spring constant and 150 kHz resonant frequency, were employed under ambient conditions in air. Total reflection X Ray Fluorescence analyses (TRXF) were performed on a TXRF 8030c - FEI Spectrometer. Raman spectra were acquired with a Bruker Senterra confocal Raman microscope instrument equipped with 532, 633 and 785 nm excitation lasers. UV-vis-NIR spectra were performed using a Shimadzu 3 UV-VIS-NIR Spectrophotometer UV-3600. Photoluminescence excitation intensity maps (PLE) were obtained with NanoLog 4 HORIBA instrument.

3.4.2. **Experimental Procedures.**

Synthesis and characterization of macrocycle mac-AQ. A catalytic amount of Grubb's 1st generation catalyst was added to a solution of the corresponding linear precursor[99] in dry and degassed DCM, and the mixture was stirred at room temperature. The progress of the reaction was monitored by TLC. When the starting linear precursor was consumed, the reaction was stopped by filtration through a pad of celite. Solvent was evaporated under reduced pressure, and the crude was purified by flash chromatography (Hex:AcOEt 3:1) to obtain the product in 70% yield. ^{1}H NMR (400 MHz, $CDCl_3$, 298 K) δ 7.93 – 7.89 (m, 4H, Hi), 7.40 – 7.28 (m, 8H, 4Hj+4Hl), 7.03 – 6.99 (m, 4H, Hh), 5.39 (t, *J* = 3.9 Hz, 2H, Ha), 5.33 (s, 4H, Hk), 4.07 (t, *J* = 6.8 Hz, 4H, Hg), 2.07 (dd, *J* = 15.6, 5.9 Hz, 4H, Hf), 1.87 – 1.80 (m, 4H, Hb), 1.49 – 1.38 (m, 12H, Hc-He).^{13}C NMR (101 MHz, $CDCl_3$) δ 181.7, 181.2, 163.8, 162.6, 137.2, 135.5, 135.4, 131.1, 129.5, 127.1, 126.7, 126.0, 124.3, 121.1, 120.5, 111.8, 110.8, 69.6, 68.7, 32.0, 29.4, 29.0, 28.1, 25.7. HRMS-MALDI calculated for $C_{50}H_{46}NaO_8$ $[M+Na]^+$: 797.3085; found 797.3114.

[99] Canevet, D.; Gallego, M.; Isla, H.; de Juan, A.; Pérez, E. M.; Martín, N., *J. Am. Chem. Soc.* **2011,** *133* (9), 3184-3190.

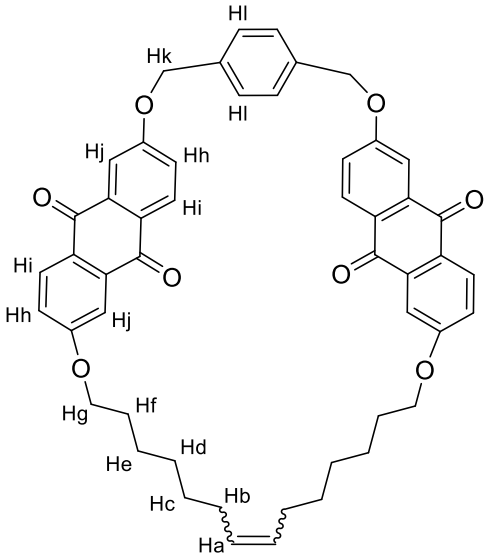

Figure S1. Proposed structure of mac-AQ with the assignation.

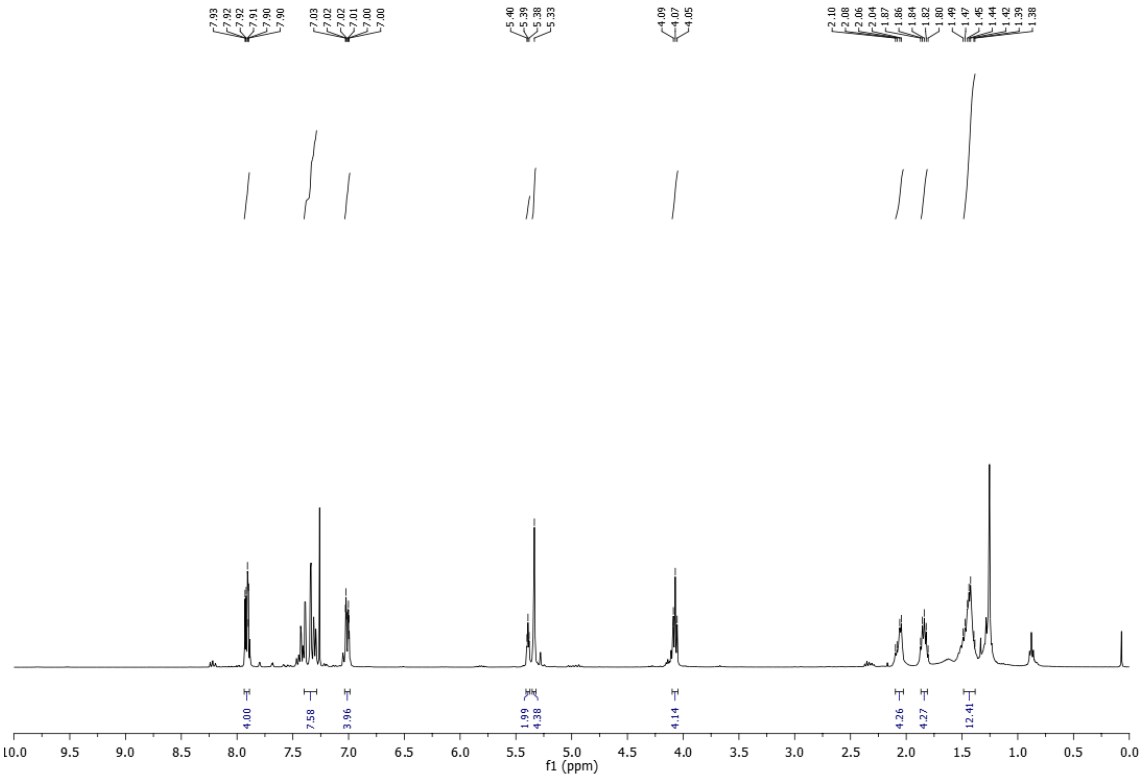

Figure S2. ^{1}H-NMR spectrum of mac-AQ ($CDCl_3$, 298 K).

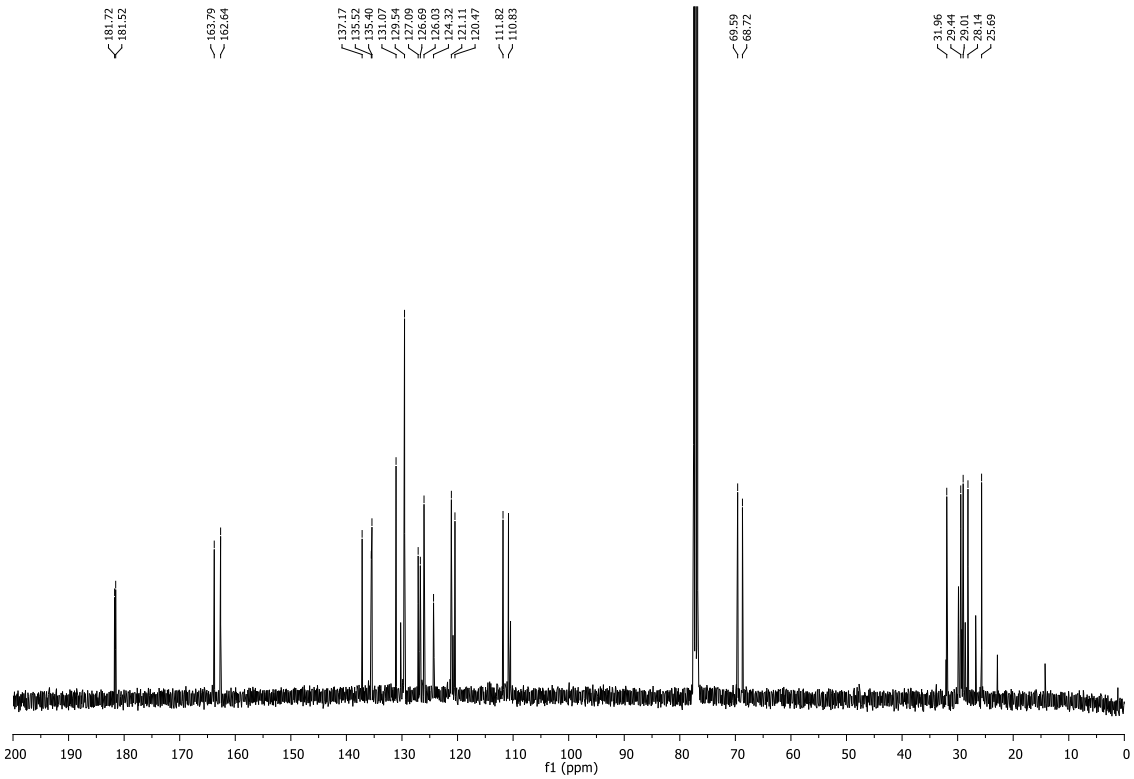

Figure S3. ^{13}C-NMR spectrum of mac-AQ ($CDCl_3$, 298 K).

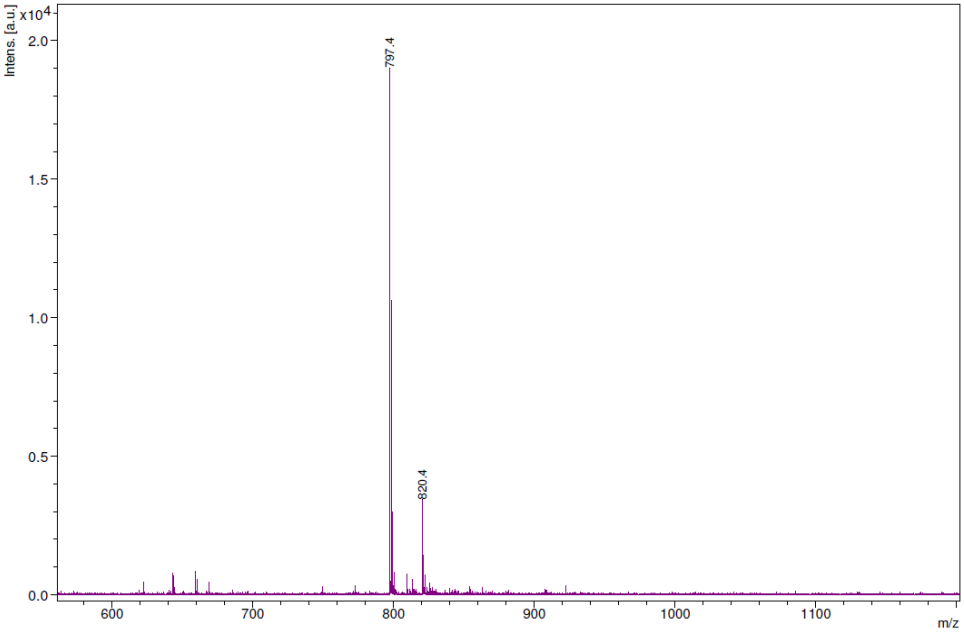

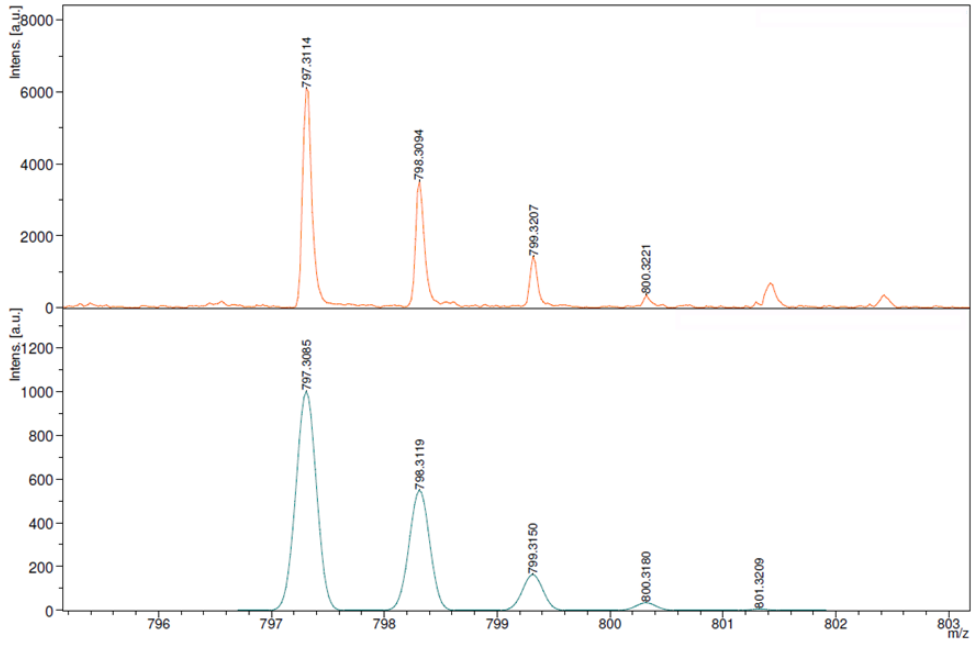

Figure S4. MALDI-TOF spectra of mac-AQ.

Synthesis and characterization of MINTs. The general method for the synthesis of MINTs has been reported elsewhere.[52, 54] Briefly, the nanotubes (10 mg) were suspended in 10 mL of tetrachloroethane through sonication (10 min) and mixed with 0.01 mmol of linear bisalkene U-shaped precursors of the macrocycles mac-exTTF, mac-pyr or mac-AQ, and Grubbs' second-generation catalyst at room temperature for 72 h. After this time, the suspension was filtered through a PTFE membrane of 0.2 μm pore size and the solid washed profusely with DCM. The solid was resuspended in 10 mL of DCM through sonication for 10 min and filtered through a PTFE membrane of 0.2 μm 4 pore size again. This washing procedure was repeated three times. Samples obtained were denoted as MINT-exTTF, MINT-pyr or MINT-AQ as a function of the threading macrocycle around the nanotubes. The synthesis of the supramolecular complexes denoted as SWNT-exTTF, SWNT-pyr and SWNT-AQ was performed by the direct mixing of the adequate amounts of (6,5)-SWNT and the corresponding macrocycle without catalyst to achieve the same functionalization loading of organic material over the nanotube compared to their respective MINT sample.

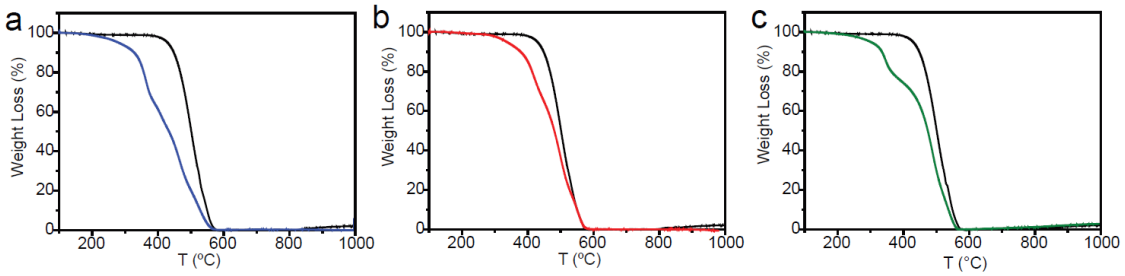

Figure S5. TGA plots (ramp of 10 °C min^{-1} under air from 100 to 1000 °C) of **a.** MINT-exTTF (blue), **b.** MINT-pyr (red) and **c.** MINT-AQ (green) compared with (6,5)-SWNT (black).

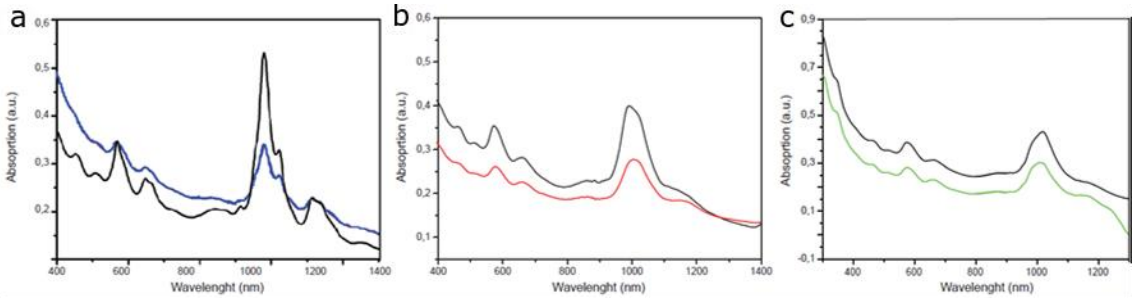

Figure S6. UV-Vis spectra (D_2O / SDS (1 wt%) at room temperature) of **a.** MINT-exTTF (blue), **b.** MINT-pyr (red) and **c.** MINT-AQ (green) compared with (6,5)-SWNT (black).

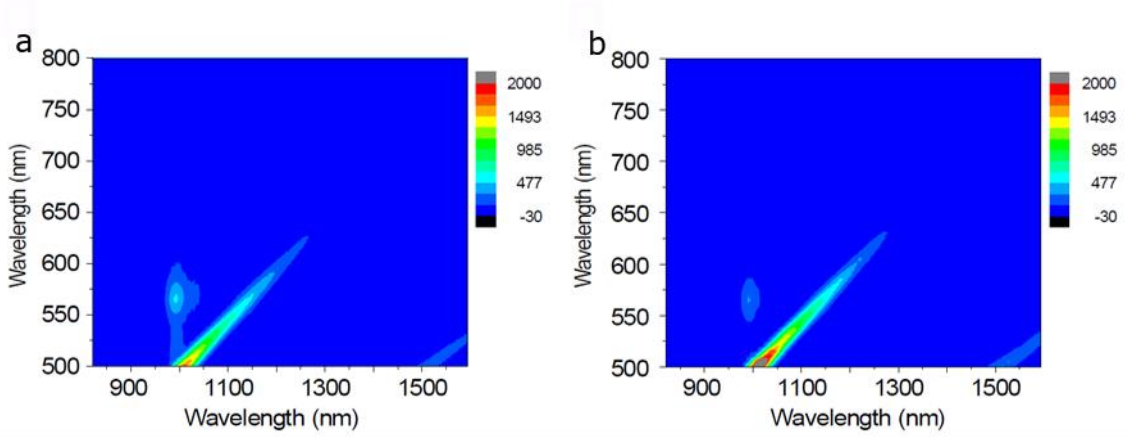

Figure S7. PLE map of **a.** (6,5)-SWNT and **b.** MINT-AQ. Rayleigh scattering has not been filtered in this image.

Analysis of the MINT-forming reaction. We have previously observed that under the MINT-forming reaction conditions, besides MINTs, oligomers of the bisalkene macrocycle precursors can be formed in-situ through acyclic diene metathesis polymerization (ADMP) and wrap around SWNTs forming supramolecular associates that are stable enough to survive our purification process.[53] To unambigously discard a significant participation of oligomer-wrapped SWNTs in our final MINT product we analysed the kinetics of formation of MINT-AQ. To that end, we extracted aliquots at different reaction times and performed TGA of the products after purification. If Ring-Closing Metathesis (RCM) is the rate-determining step, the kinetics of the reaction must be of pseudo first order and the final products are MINTs. However, if ADMP were the main reaction pathway, the kinetics would correspond to a bimolecular reaction and follow second order kinetics. The data from the formation of MINT-AQ fit very well (r^2 = 0.988) to a pseudo-first order model with kinetic constant of $2.2 \times 10{-}3\ s^{-1}$. Therefore, the main path for functionalization of SWNTs is by macrocyclization around them, to form MINTs, with negligible contribution from supramolecularly attached oligomers (Supplementary Figure 8). For comparison, we also studied the use of fullerene C_{60} as soluble template for the RCM, since its diameter (0.7 nm) is very similar to that of (6,5)-SWNTs. To follow the reaction in real time by ^{1}H-NMR, we performed the experiment using 1,1,2,2-tetrachloroethane-d_2 as solvent and recorded spectra at different times. As the reaction progresses, the signal at 4.19 ppm that corresponds to the -CH_2 group next to the oxygen ether group in the bisalkene precursor decreases and a new signal a 4.13 ppm, which corresponds to the macrocycle, appears. The data obtained from this experiment also fit well (r^2 = 0.982) to a pseudo-first order reaction kinetics, in this case with $k = 5.6 \pm 0.5 \times 10{-}4\ s^{-1}$. Since in this case we can unambiguously identify mac-AQ as the sole product of the reaction detectable by NMR, these data strongly support the formation of MINTs by analogy. Moreover, (6,5)-SWNTs are found better templates for the RCM than C_{60}, as the RCM reaction is approximately twice as fast with the nanotubes as templates.

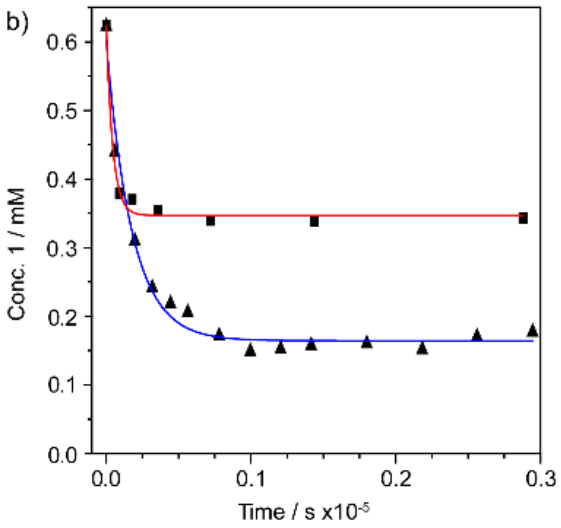

Figure S8. Data from kinetic experiment of MINT-AQ (squares) and RCM templated with C_{60} (triangles). The fit to a mono-exponential decay are shown in red and blue respectively.

DFT calculations: All theoretical DFT calculations were carried out within the density functional theory (DFT) approach by using the C.01 revision of the Gaussian 09 program package. Optimization and molecular orbitals calculations of MINT derivative were performed using the long-range corrected B97D density functional,[100] which are able to incorporate the dispersion effects by means of a pair-wise London-type potential. The B97D density functional has emerged as a robust and powerful density functional able to provide accurate structures in large supramolecular aggregates dominated by non-covalent interactions of different nature. Raman spectra and analysis of Mülliken population were simulated by using the Coulomb-attenuated hybrid exchange-correlation functional (CAM-B3LYP) functional. This functional was develop by Yanai *et al.*[101] which includes the Hartree-Fock and the Becke exchanges as a variable ratio depending of the intermolecular distance. Both functional were combined with the Pople's 3-21G* basis set.[102] The dimension of the MINT-exTTF (Figure S9) is an example of the size of our systems.

[100] Grimme, S., *J. Comput. Chem.* **2006,** *27* (15), 1787-1799.
[101] Yanai, T.; Tew, D. P.; Handy, N. C., *Chem. Phys. Lett.* **2004,** *393* (1), 51-57.
[102] Binkley, J. S.; Pople, J. A.; Hehre, W. J., *J. Am. Chem. Soc.* **1980,** *102* (3), 939-947.

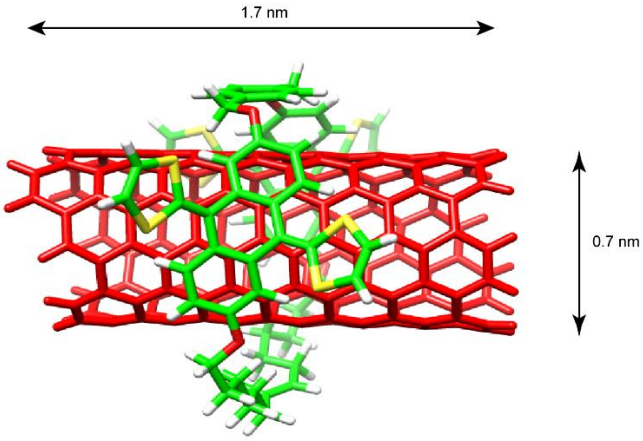

Figure S9. Optimized structure of MINT-exTTF. Dimension of the modelled carbon nanotubes are indicated in the figure.

Binding energies. The interaction energy between the macrocycles or the substrates (E_{int}) (*Equation S1*) and the carbon nanotube (Table S1 and S2) and MINT-AQ (Table S3) is defined as the energy difference between the two fully optimized monomers from the fully optimized dimer complex in the geometry of the dimer complex, where E_x^y is the energy of fragment X at the geometry of Y. The basis set superposition error (BSSE) was half-corrected according to the counterpoise (CP) scheme of Boyd and Bernardi for the single-point interaction energies.[103] Otherwise, the binding energy (E_{bind}) (*Equation S2*) was calculated taking into account the relaxation of the separate monomers and, therefore, considering the deformation energy required to transform the both moieties from their minimum-energy geometries to the geometry acquired in the assembly.

$$E_{int}(AB) = E_{AB}^{\alpha\beta} - E_A^{\alpha\beta} - E_B^{\alpha\beta} \qquad \textit{Equation S1}$$

$$E_{bind} = E_{def} + E_{int} \qquad \textit{Equation S2}$$

[103] Boys, S. F.; Bernardi, F., *Mol. Phys.* **1970,** *19* (4), 553-566.

Table S1. Energy parameters (kcal mol^{-1}) of the interaction between macrocyles and guest SWNTs at the B97-D/3-21G* level.

	E_{int}	E_{def}	$E_{bind} = E_{int} + E_{def}$
MINT-AQ	-97.74	22.81	-74.93
MINT-pyr	-108.61	40.74	-67.88
MINT-exTTF	-103.58	12.01	-91.57

Table S2. Energy parameters (kcal mol^{-1}) of the interaction between the nitroaromatic molecules and the (6,5)-SWNT at the B97-D/3-21G* level.

	E_{int}	E_{def}	$E_{bind} = E_{int} + E_{def}$
Nitrobenzene	-16.05	0.59	-15.45
1-Nitronaphtalene	-22.22	0.49	-21.73
9-Nitroanthracene	-28.06	1.52	-26.54
1-Nitropyrene	-32.03	0.65	-31.38

Table S3. Energy parameters (kcal mol^{-1}) of the interaction between the nitroaromatic molecules and the MINT-AQ at the B97-D/3-21G* level.

	E_{int}	E_{def}	$E_{bind} = E_{int} + E_{def}$
Nitrobenzene	-16.11	0.30	-15.81
1-Nitronaphtalene	-22.66	0.61	-22.04
9-Nitroanthracene	-28.56	1.48	-27.08
1-Nitropyrene	-33.09	1.07	-32.02

Mülliken population. The analysis of Mülliken population was carried out at CAMB3LYP/ 3-21g* level of theory (Table S4). An extra example at CAMB3LYP/ 6-31g* level for the case of MINT-AQ has been included to support that a change in the basis set does not modify the sense of the charge transfer.

This analysis suggests that there is charge transfer between the macrocycles and SWNT. For MINT-AQ, the extent of electron transfer upon the formation of the MINT in the SWNT is found to be +0.011 e (p-doping), while for the formation of the MINT-exTTF

the value is -0.043 e (n-doping), higher and with opposite sign. This is consistent with the nature of electronwithdrawing tendency of the AQ and electron-donor tendency of exTTF. For the MINTpyr, the calculated charge transfer is +0.005 e, one order the magnitude lower and it is not a charge transference between the two moieties. These theoretical results are in relay good agreement with the Raman experimental tendencies (Figure 2b in the main text) and with our interpretation of the catalysis data.

Table S4. Calculated charge transfer from macrocycle to nanotube.

	Charge transfer [e]
MINT-AQ (3-21g*)	+0.011
MINT-AQ (6-31g*)	+0.087
MINT-pyr	+0.005
MINT-exTTF	-0.043

Raman Calculations. Raman spectra of MINT-exTTF, MINT-pyr and MINT-AQ along with the Raman spectrum of pristine (6,5)-SWNT (Figure S10a). All spectra are very similar, proving that the covalent structure of the SWNT is preserved upon formation of MINTs, with no increase in the relative intensity of the D band. However, the intensity of the radial breathing modes of all three MINT samples decreases with respect to (6,5)-SWNT, in accordance with the type of functionalization.[85] Some variations were observed in the frequency of the G band, too. For instance, in the cases of MINT-exTTF and MINT-AQ we observe a small blue shift of 2-5 cm^{-1}, but with MINT-pyr we do not observe remarkable variations. The fact that both the electron donor mac-exTTF and acceptor mac-AQ cause blue shifts[104] and that these are quantitatively small, suggests that the degree of charge-transfer in the ground state is small. To shed light on the underlying causes of these spectroscopic changes, we performed DFT calculations at the CAM-B3LYP/3-21g* level of theory (Figure 1b of the main text). All three macrocycles are a good fit for (6,5)-SWNTs and show sizeable binding energies towards them (−103.58, −108.61 and −97.74 Kcal mol^{-1} for MINT-exTTF, MINT-Pyr and MINT-AQ, respectively). The calculated Raman spectra (Figure S10b) showed the same blue shift of

[104] Rao, C. N. R.; Voggu, R., *Mater. Today* **2010,** *13* (9), 34-40.

5 cm^{-1} upon formation of MINT-exTTF and MINT-AQ, in very good correlation with our experimental results. However, we also observe a blue shift for the MINT-pyr that we do not see experimentally.

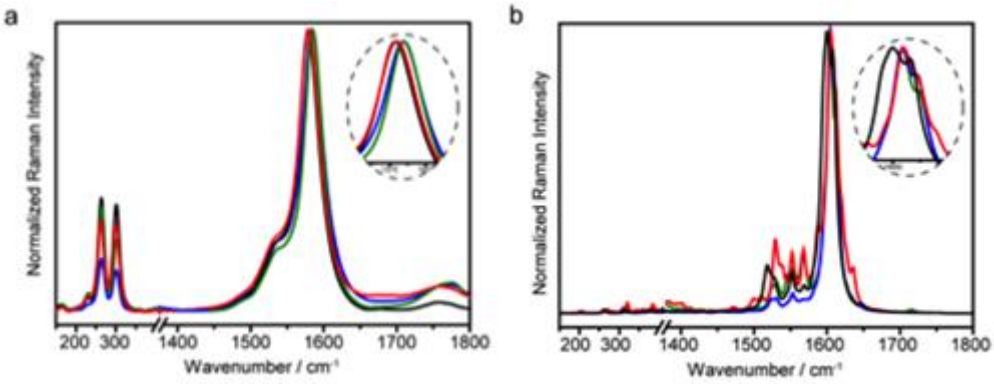

Figure S10. **a.** Experimental Raman spectra of SWNT (black), MINT-exTTF (blue), MINT-pyr (red) and MINT-AQ (green). **b.** Calculated Raman spectra at CAM-B3LYP/3-21g* level of theory. Same color code.

HOMO-LOMO calculations: The energy gap between the highest occupied molecular orbital (HOMO) and the lowest unoccupied molecular orbital (LUMO) plays an important role in the charge transport properties of any organic molecule (Figure S11). Specifically, in semiconducting SWNTs the HOMO-LUMO gap corresponds to absorption or luminescence of the lowest-energy transition (S_{11}). The calculations show that the degenerated HOMO/HOMO-1 of MINT-exTTF is mainly formed from a combination of the molecular orbitals (MOs) of the macrocycle threaded along the nanotube and the carbon scaffold, whereas its LUMO/LUMO+1 is formed only by 6,5-SWNT MOs (Figure S11). The opposite trend is observed for MINT-AQ, where the HOMO/HOMO-1 reside exclusively on the SWNT, while the LUMO/LUMO+1 are located on mac-AQ. Interestingly, for MINT-pyr, both HOMO and LUMO are located on the SWNT, without any participation of mac-pyr. These changes in the nature of MOs confirm the different electronic characteristics of each MINT sample. The HOMO of MINT-exTTF is significantly higher in energy than that of MINT-pyr, in correspondence with the donor behavior of mac-exTTF compared to mac-pyr. On the other hand, the LUMO of MINT-AQ is lower in energy than the corresponding LUMO of MINT-pyr, as is expected for an acceptor. The energy gap between the HOMO and the LUMO (ΔE

HOMO-LUMO) can be correlated with the conductivity of the complex. Experimentally, by spectrofluorimetric measurements, (6,5)-SWNTs have a ΔE HOMO-LUMO of 1.27 eV,[105] in good correlation with our calculated value of 1.22 eV, which support our theoretical data. This value decreases to 0.63 eV for MINT-exTTF, while is increased to 1.29 eV and 1.26 eV for MINT-pyr and MINT-AQ respectively (Figure S11). For MINT-exTTF, the first orbital with electronic density that resides mainly on the carbon nanotube moiety is found at 4.29 eV in the HOMO-4, at a significantly higher value that for MINT-pyr and MINT-AQ. All these theoretical results, together with the experimental findings, indicate that the electronic character of our MINT samples can be modulated changing the recognition motifs of U-shape precursors.

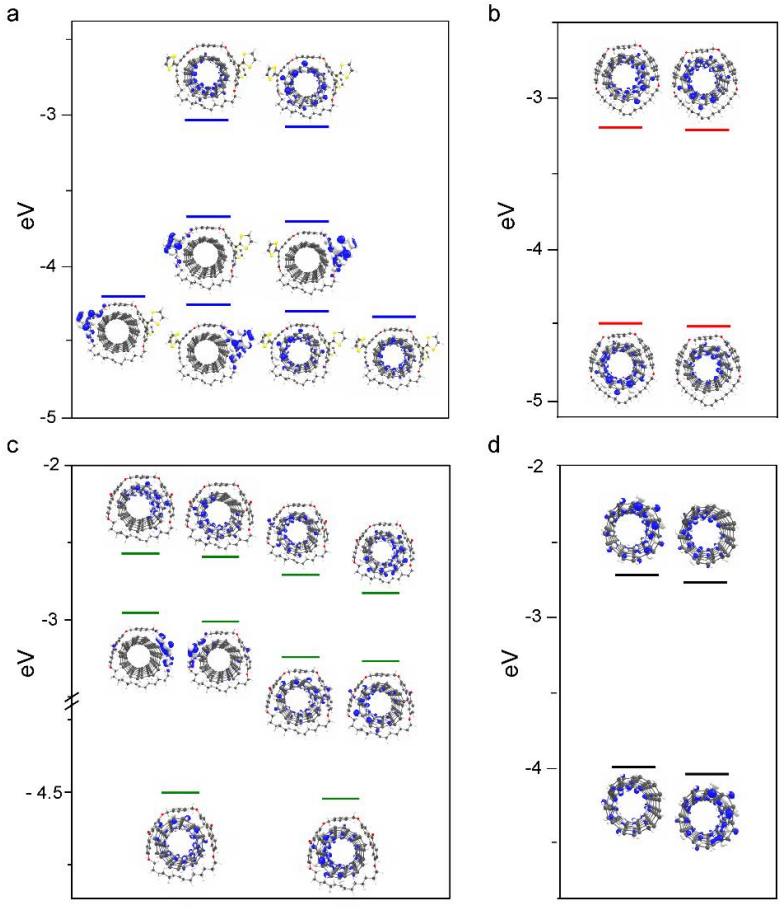

Figure S11. Energy diagrams and topologies of the frontier molecular orbitals of, **a.** MINT-exTTF (blue), **b.** MINT-pyr (red), **c.** MINT-AQ (green) and **d.** (6,5)-SWNT (black) calculated at B97D/3-21G* level of theory.

[105] Bachilo, S. M.; Strano, M. S.; Kittrell, C.; Hauge, R. H.; Smalley, R. E.; Weisman, R. B., *Science* **2002,** *298* (5602), 2361-2366.

Catalytic activity. The typical catalytic experiment was performed as follows: a certainamount of nanotube-containing material (5 mg) was mixed with 4.1 mmol of nitroaromatic substrate in 2 mL of DMSO-d_6 as solvent (selected after reaction condition optimizations, Figure S13) in a round botton flask under N_2 atmosphere. Finally, 31.8 mmol of hydrazine (acting as hydrogen source)[106] were added and the reaction was stirred magnetically and held at 85 ºC for a desired time. At regular intervals, aliquots were withdrawn from the reaction and subjected to NMR spectroscopy analysis to follow the catalytic evolution (Figures S19-25). Once the reaction was complete, the crude mixture was diluted with 15 mL of DCM and the MINT-containing solid catalysts MINT-exTTF, MINT-pyr and MINT-AQ were recovered by filtration through a PTFE membrane of 0.2 μm pore-size and washed profusely with DCM. The solid was re-suspended in 10 mL of DCM through sonication for 10 min and filtered through a PTFE membrane of 0.2 μm pore size again. This washing procedure was repeated three times. After drying, the material was submitted to another catalytic run without adding in any case new catalyst precursor. To isolate the pure products, the organic phase was washed three times with water. Then, organic fractions were dried over anhydrous $MgSO_4$ and concentrated under reduced pressure. Crude product was purified by flash chromatography in silica (hexane: ethyl acetate 3:1) yielding the final product.

Aniline.

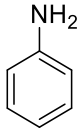

Prepared according to the general procedure. ^{1}H-NMR (400.16 MHz, DMSO-d_6, δ ppm): 7.02 (t, J = 7.3 Hz, 2H), 6.56 (d, J = 7.2 Hz, 1H), 6.49 (t, J = 7.3 Hz 2H), 4.99 (s, 2H).

1-aminonaphthalene.

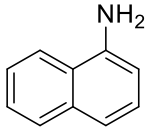

Prepared according to the general procedure. ^{1}H-NMR (400.16 MHz, DMSO-d_6, δ ppm): 8.05 (d, J = 8.3 Hz, 1H), 7.73 (d, J = 8.2 Hz, 1H), 7.37 (m, 2H), 7.19 (t, J = 7.7 Hz, 2H), 7.07 (d, J = 8.0 Hz, 1H), 6.67 (d, J = 7.3 Hz 2H), 5.68 (s, 2H).

[106] Gao, Y.; Ma, D.; Wang, C.; Guan, J.; Bao, X., *Chem. Commun.* **2011,** *47* (8), 2432-2434.

9-aminoanthracene.

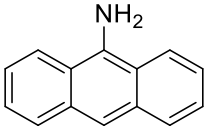

Prepared according to the general procedure. ^{1}H-NMR (400.16 MHz, DMSO-d_6, δ ppm): 8.59 (s, 1H), 8.13 – 8.06 (m, 4H), 7.53 (dd, J = 6.6, 3.2 Hz, 4H), 6.87 (s, 2H).

1-Aminopyrene.

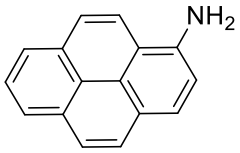

Prepared according to the general procedure. ^{1}H-NMR (400.16 MHz, DMSO-d_6, δ ppm): 8.26 (d, J = 9.2 Hz, 1H), 8.02 – 7.84 (m, 6H), 7.72 (d, *J* = 8.8 Hz, 1H), 7.36 (d, *J* = 8.3 Hz, 1H), 6.32 (s, 2H).

The evolution of the ^{1}H-NMR spectra during the reduction of ph- NO_2 with MINT-exTTF as catalyst (Figure S14a) proceeds smoothly with no induction period detected, yielding the aniline reduction product almost exclusively, with phenylhydroxylamine as only detectable intermediate. The transformation can be easily monitored by the disappearance of the up-shielded protons of the starting material at ~ δ 8.25-7.75 ppm and the increase of the signals downshielded at ~ δ 6.75–6.25 ppm as a consequence of the increase in electron density of the aromatic ring caused by the aniline nitrogen, and the characteristic 2-proton singlet of the aniline group at ~ δ 5.0 ppm. The reduction proceeds to completion in approximately 2 hours. Compared to a blank non-catalyzed reaction, which saturated after 24 h with ~50% of conversion (Figure S14b), and resulted in an approximately equimolar mixture of phenylhydroxylamine and aniline, MINT-exTTF showed remarkably activity.

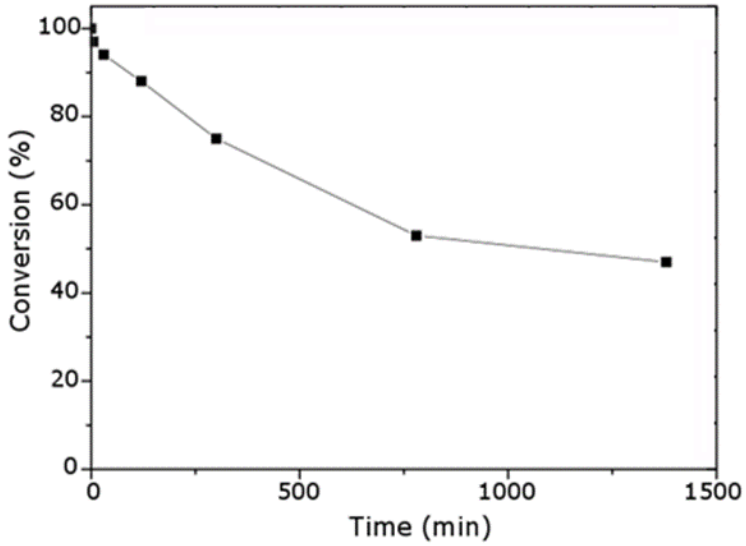

Figure S12. Reduction of 1-nitronaphtalene without catalyst.

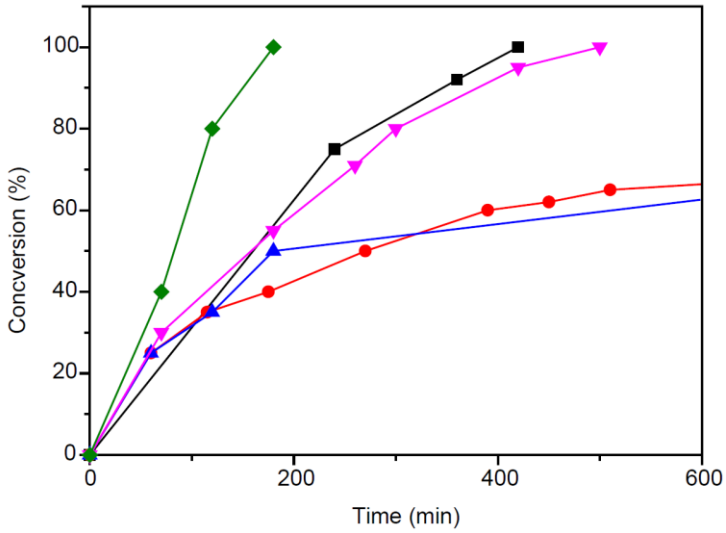

Figure S13. Solvent optimization on the reduction of 1-nitronaphtalene catalyzed by (6,5)-SWNT (green: DMSO; black: Ethanol; purple: Methanol; blue: H_2O; red: $CHCl_3$).

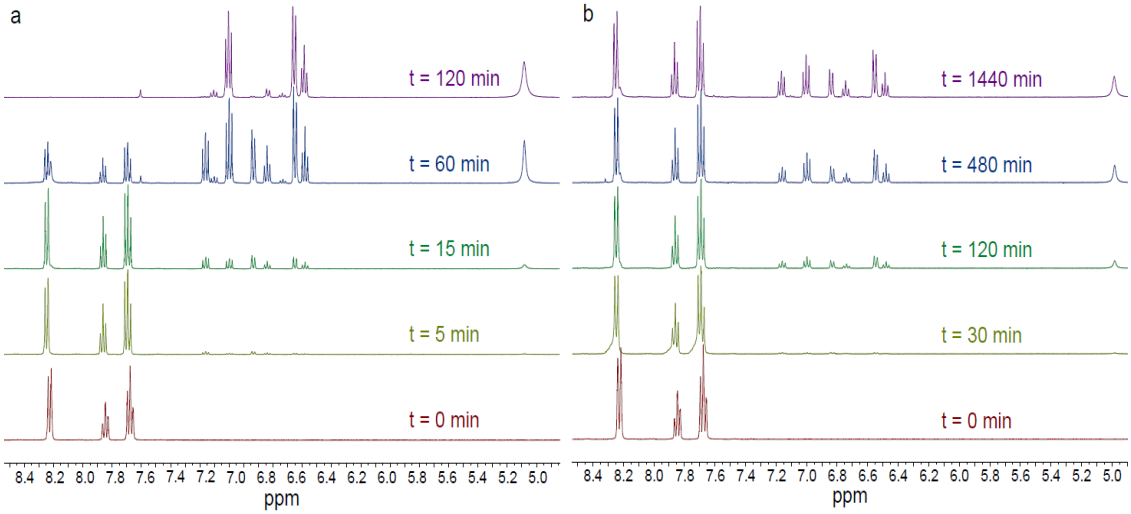

Figure S14. Partial ^{1}H-NMR (400 MHz, DMSO-d_6) spectra of the reduction of ph-NO_2 **a.** catalyzed by sample MINT-exTTF and **b.** without catalyst.

Analysis of X-Ray Fluorescence (TRXF). In order to confirm that the active sites corresponded only to the nanotube walls, we conducted total reflected X-ray fluorescence (TRXF) measurements, and only ppm-level of metallic impurities were detected (Figures S15- 18 and Table S5).

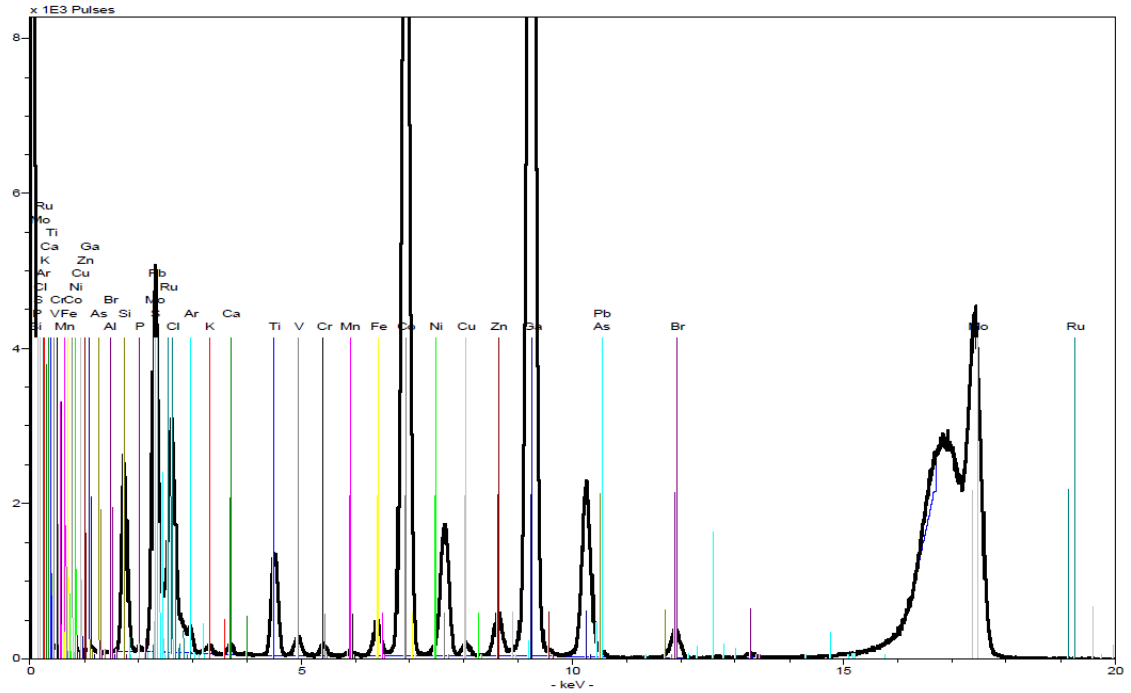

Figure S15. FTRX spectrum of MINT-exTTF sample.

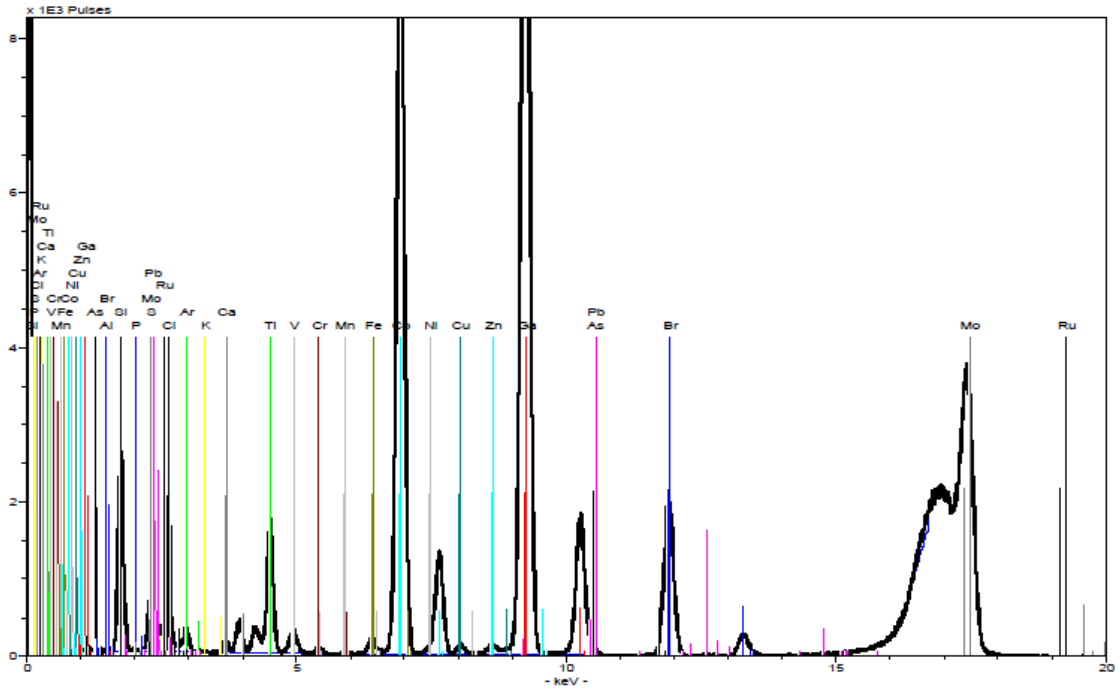

Figure S16. FTRX spectrum of MINT-pyr sample.

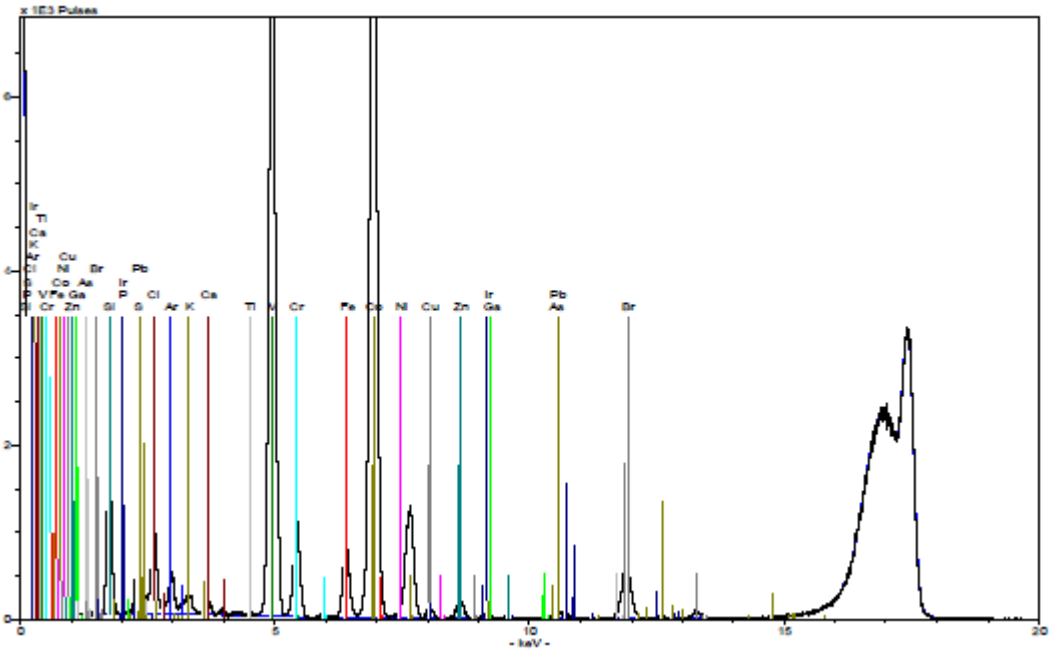

Figure S17. FTRX spectrum of MINT-AQ sample.

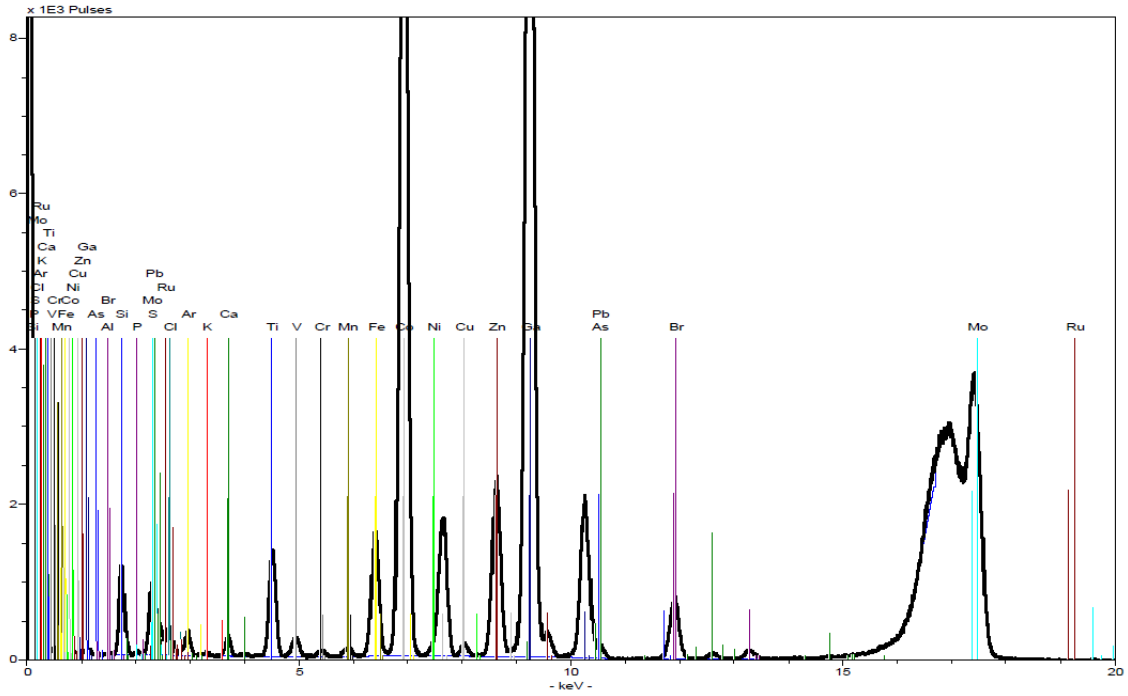

Figure S18. FTRX spectrum of (6,5)-SWNT sample.

Table S5. Metal analysis by TRXF.

Element	*MINT-exTTF*[a]	*MINT-pyr*[a]	*MINT-AQ*[a]	*6,5-SWNT*[a]
Al	-	-	-	-
Si	146.72	191.56	129.9	78.06
P	-	-	0.44	-
S	70.26	2.125	10.12	2.084
Cl	28.06	11.879	12.906	4.055
K	0.509	-	1.214	0.142
Ca	0.534	2.488	0.894	1.119
Ti	3.233	5.763	0.1	3.713
V	0.111	0.172	0.124	0.139
Cr	0.200	0.145	0.011	0.122
Mn	0.040	-	-	0.153
Fe	0.505	0.289	1.079	2.053
Co	13.435	12.748	11.285	15.438
Ni	0.032	0.023	0.015	0.063

Cu	0.117	0.101	0.071	0.127
Zn	0.340	0.084	0.147	1.620
Ga[b]	10.000	10.000	10.000	10.000
As	0.027	0.028	0.035	0.049
Br	0.168	1.185	0.315	0.396
Mo	17.82	25.69	20.48	29.68
Ru	17.02	0.494	0.941	-
Pb	0.017	0.006	-	0.086

[a]Concentrations in mg L^{-1}, [b]Internal standard

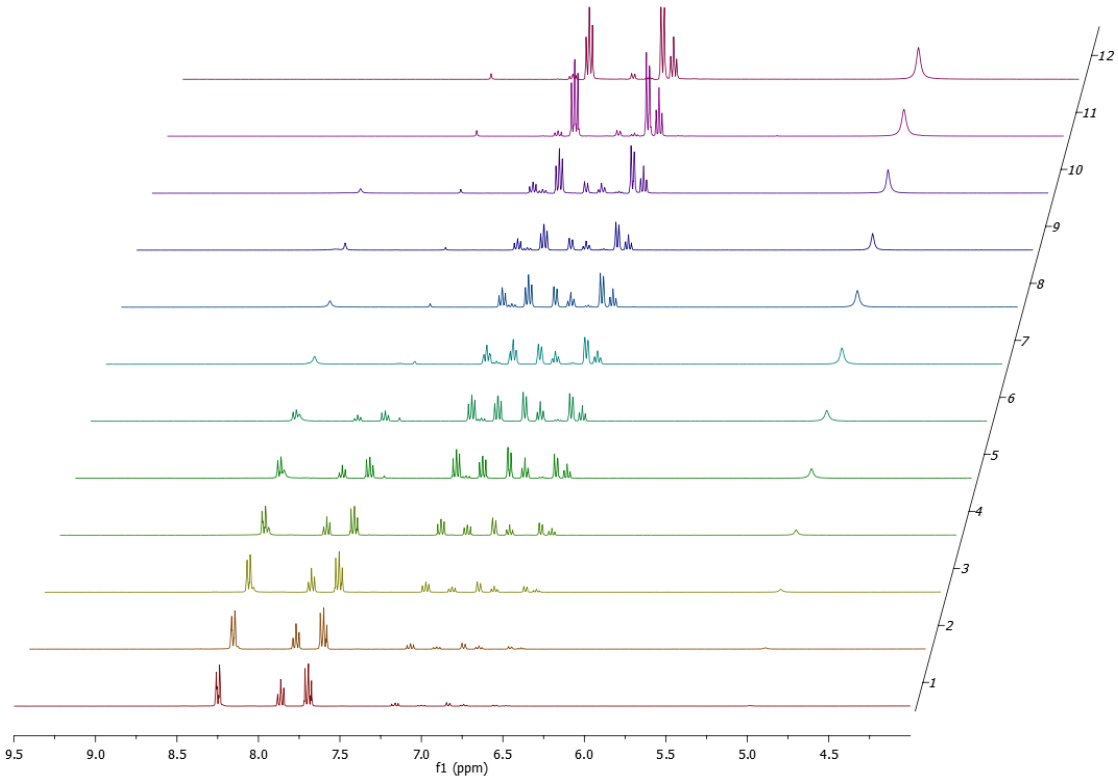

Figure S19. Nitrobenzene reduction catalyzed by catalyst MINT-exTTF.

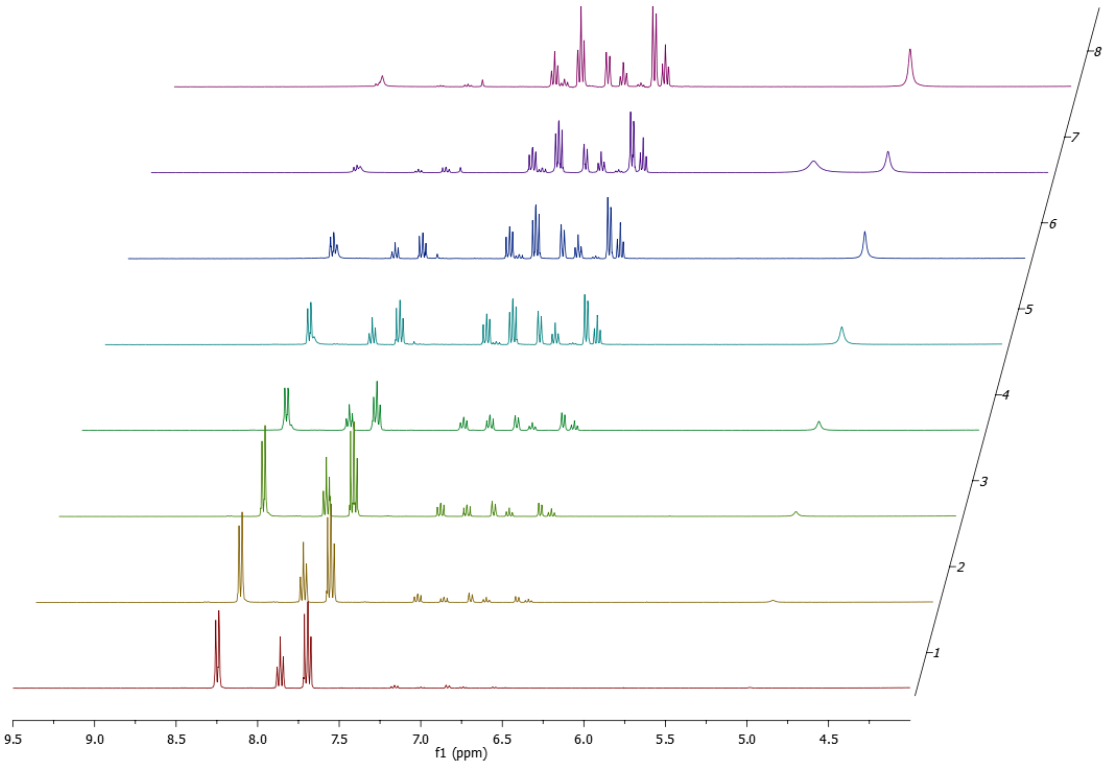

Figure S20. Nitrobenzene reduction catalyzed by catalyst MINT-pyr.

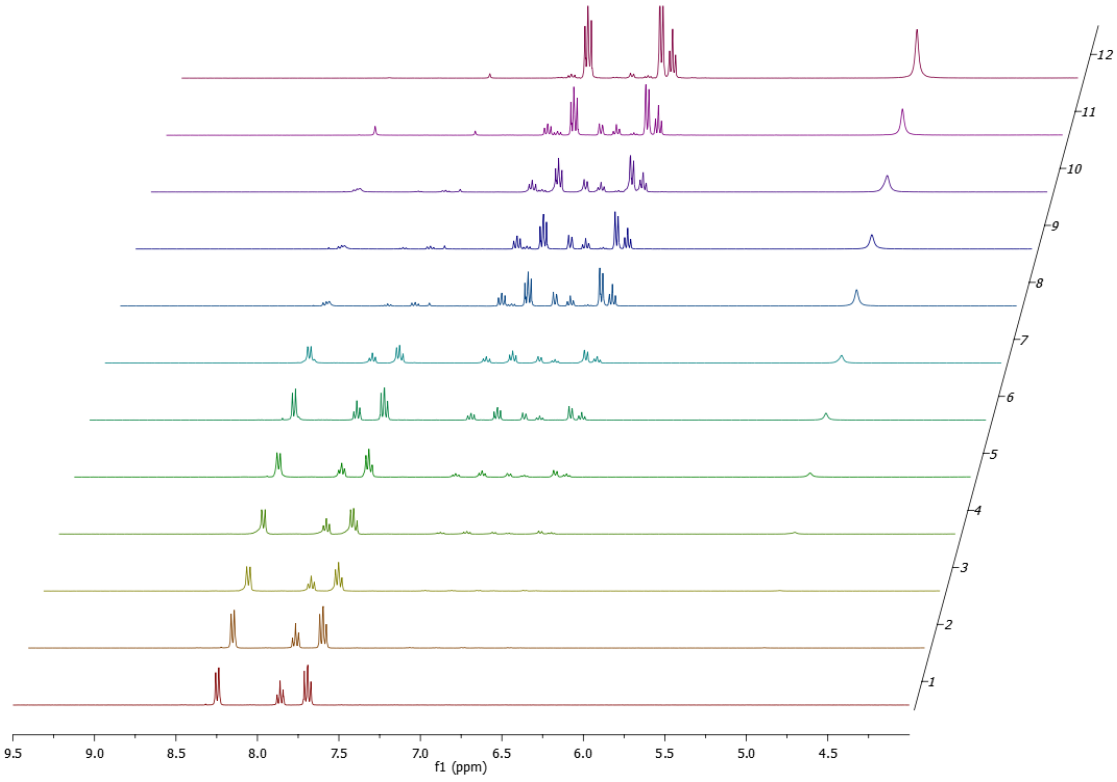

Figure S21. Nitrobenzene reduction catalyzed by catalyst MINT-AQ.

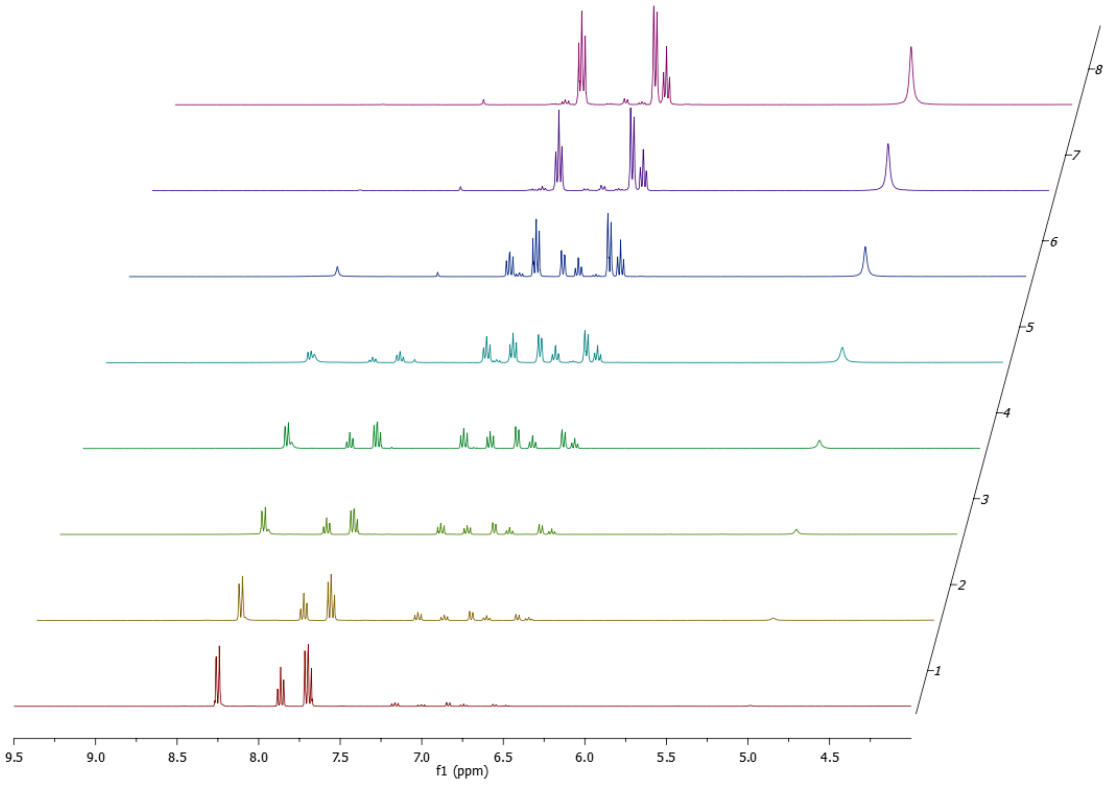

Figure S22. Nitrobenzene reduction catalyzed by catalyst (6,5)-SWNT.

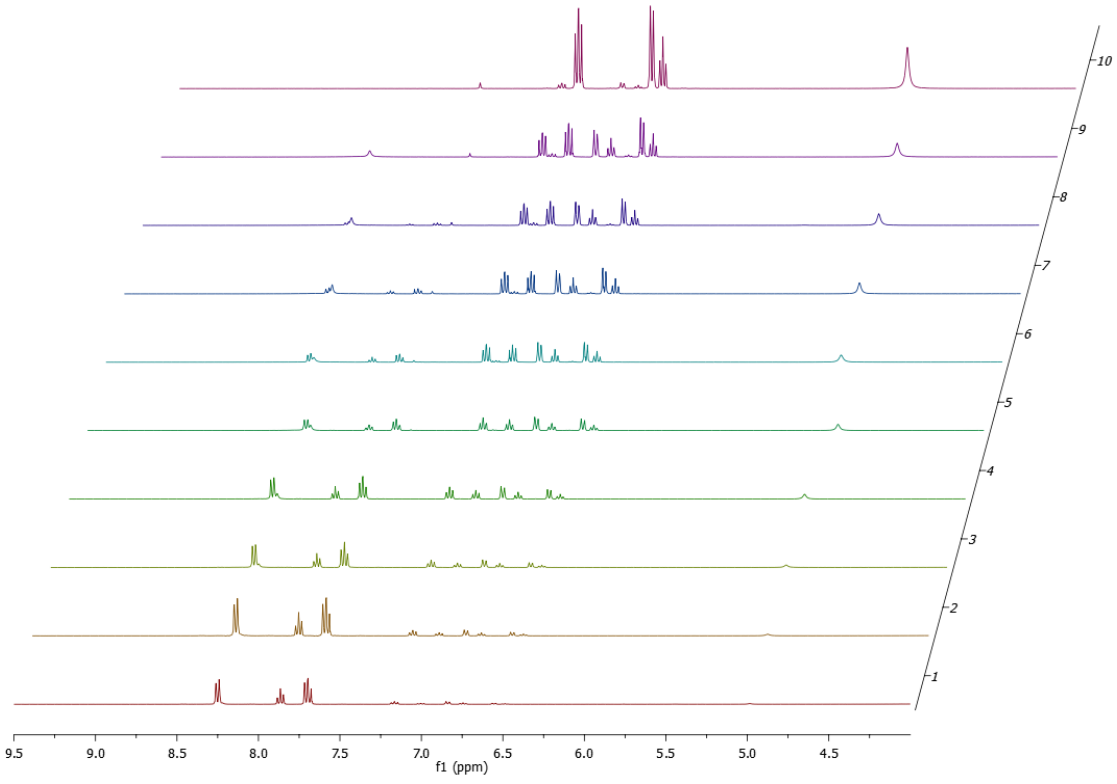

Figure S23. Nitrobenzene reduction catalyzed by catalyst SWNT-exTTF.

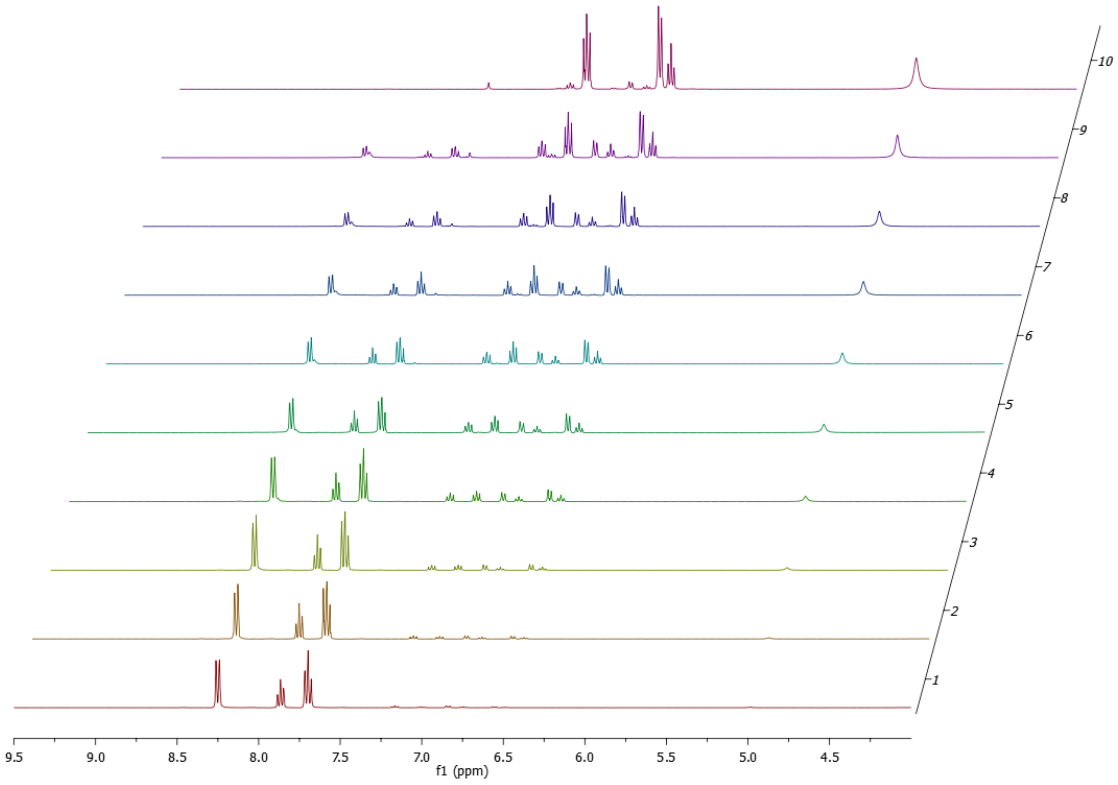

Figure S24. Nitrobenzene reduction catalyzed by catalyst SWNT-pyr.

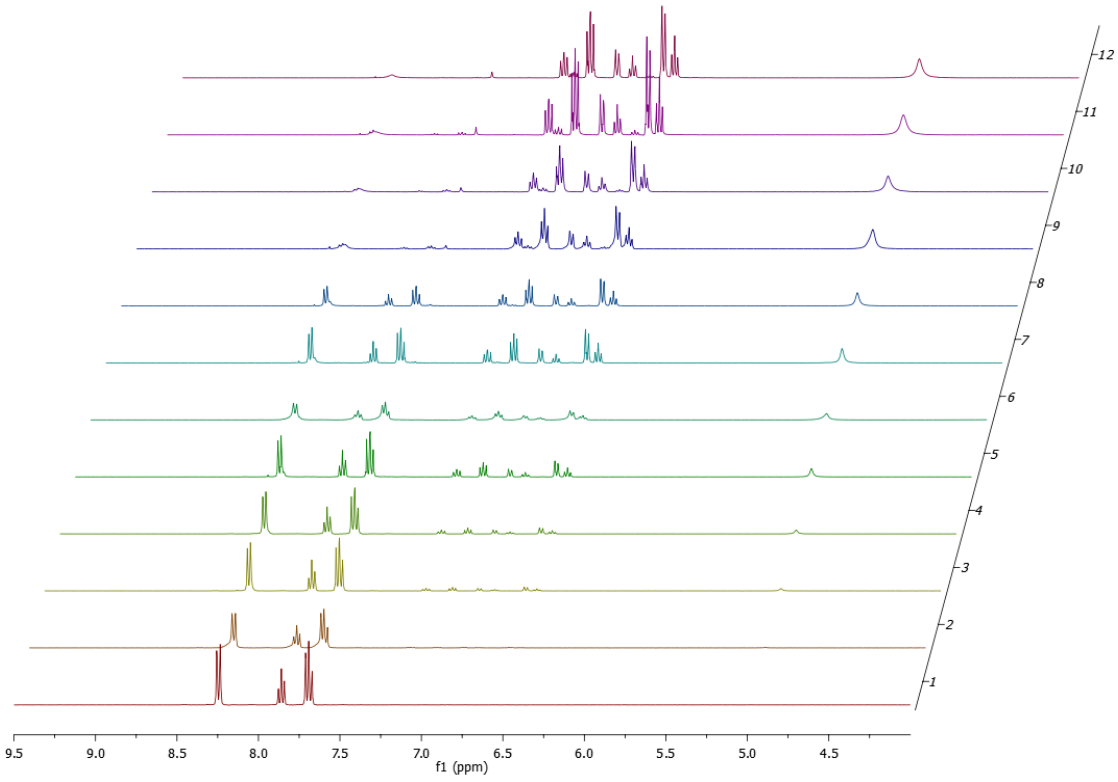

Figure S25. Nitrobenzene reduction catalyzed by catalyst SWNT-AQ.

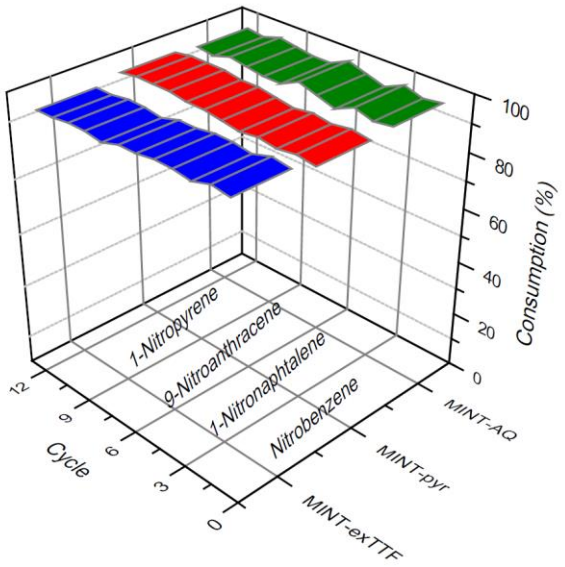

Figure S26. Recycling studies of the MINT-exTTF (blue), MINT-pyr (red) and MINT-AQ (green) catalysts.

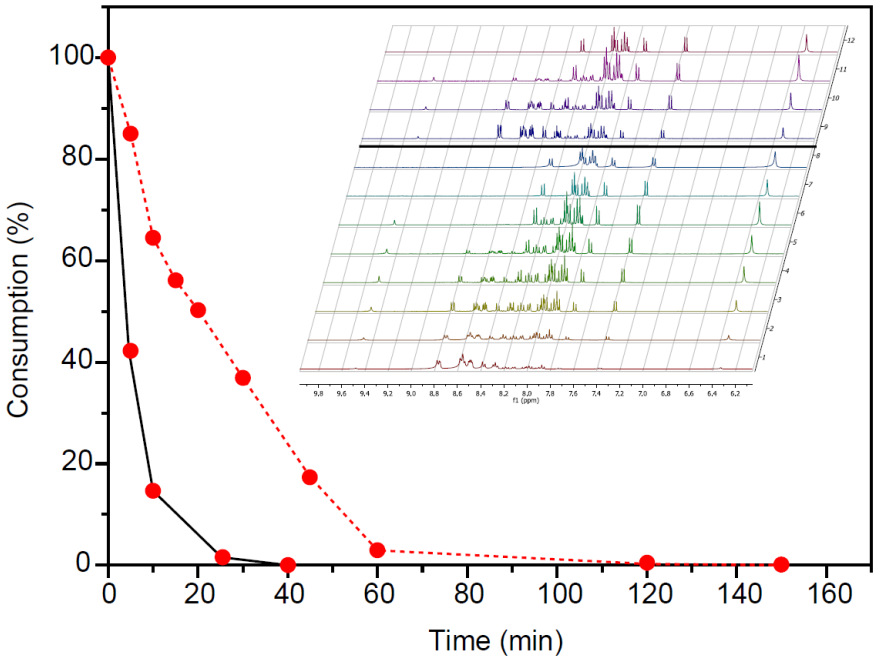

Figure S27. Recycling study of the reduction of 1-nitropyrene catalyzed by SWNT-pyr (red dots) on the first cycle (red pointed line) and on the second cycle (black line). Inset: NMR kinetic profile of the first and second cycle.

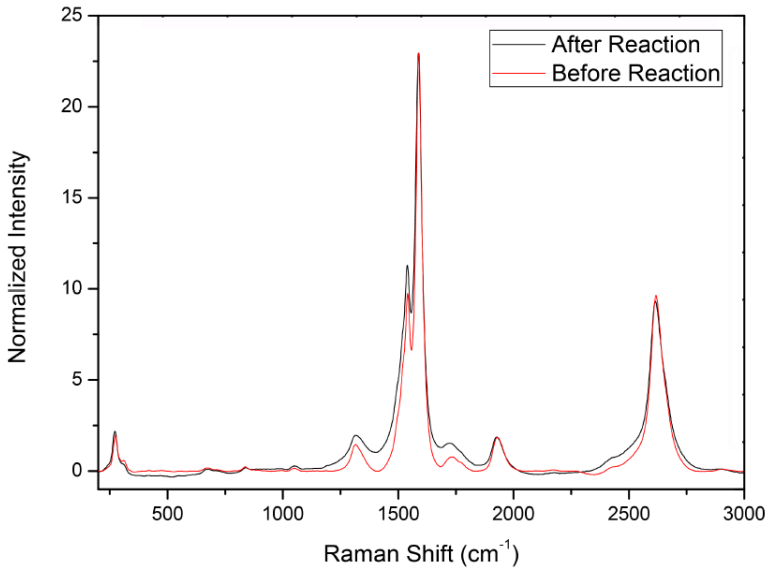

Figure S28. Raman spectra of MINT-AQ before and after the reduction reaction, showing its structural integrity.

Chapter 2.

4. Mechanically Interlocked Nanotubes (MINTs) as a Stable Electrochemical Platform

The work described in this chapter has been performed in collaboration with LIOS Institute[a] of Johannes Kepler Unviersität (JKU) in Linz, Austria. This chapter is not already published.

Dominik Wielend [a] †, Mariano Vera-Hidalgo †, Hathaichanok Seelajaroen [a], Niyazi Serdar Sariciftci [a], Emilio M. Pérez* and Dong Ryeol Whang*[a].

[†] These authors contributed equally to this work.

Mechanically interlocking a redox-active anthraquinone (AQ) onto SWNT (MINT-AQ) gives a new, advanced example of a supramolecular architecture for an electrochemical platform. Electrochemical studies using MINT-AQ as an electrode reveal enhanced electrochemical stability in both aqueous and organic solvents compared to the physically coated AQ-based electrodes. While maintaining the electrochemical properties of the parent molecule, we observed a stable oxygen reduction reaction (ORR) to produce hydrogen peroxide (H_2O_2). Using such MINT-AQ electrodes we got 7 and 2 µmoles H_2O_2 produced over 8 h in basic and neutral conditions, while the control system of SWNT showed 2.2 and 0.5 µmoles respectively. Those catalytic results further substantiate the potential of this rotaxane-type immobilization approach for heterogenized electrocatalysis.

4.1. **Introduction.**

Great effort is made worldwide on investigations of appropriate electrocatalysts for energy storage-devices such as batteries,[107,108,109] supercapacitors,[110] electrolysis[111,112] of water[113,114] and/or recycling of carbon dioxide (CO_2).[115,116,117,118]

Due to their high efficiency, noble and rare metals, like platinum, palladium or rhenium, serve as state-of-the-art electrocatalysts for various energy storage reactions, like reduction of protons,[119,120] CO_2[121] and oxygen (O_2).[22,122,123] However, as these metals are costly, one approach is to substitute those metals with cheap and more abundant metals like nickel,[124] iron,[125] manganese[126] or to use fully metal-free systems.[127] Specially regarding the oxygen reduction reaction (ORR), numerous reports on organic catalysts[128,129] and even small molecules[130,131] can be found in literature.[22] Anthraquinone (AQ) and their derivatives have been widely explored as a pure molecular electrocatalyst for ORR, since AQ is cheap,[132] has chemical functionality[71] and high selectivity for

[107] Etacheri, V.; Marom, R.; Elazari, R.; Salitra, G.; Aurbach, D., *Energ. Environ. Sci.* **2011,** *4* (9), 3243-3262.
[108] Häupler, B.; Wild, A.; Schubert, U. S., *Adv. Energ. Mater.* **2015,** *5* (11), 1402034.
[109] Alotto, P.; Guarnieri, M.; Moro, F., *Renew. Sustain. Energ. Rev.* **2014,** *29*, 325-335.
[110] González, A.; Goikolea, E.; Barrena, J. A.; Mysyk, R., *Renew. Sustain. Energ. Rev.* **2016,** *58*, 1189-1206.
[111] Dalle, K. E.; Warnan, J.; Leung, J. J.; Reuillard, B.; Karmel, I. S.; Reisner, E., *Chem. Rev.* **2019,** *119* (4), 2752-2875.
[112] Kalyanasundaram, K.; Graetzel, M., *Curr. Opin. Biotech.* **2010,** *21* (3), 298-310.
[113] Eftekhari, A., *Int J Hydrog Energ.* **2017,** *42* (16), 11053-11077.
[114] Safizadeh, F.; Ghali, E.; Houlachi, G., *Int. J. Hydrog. Energ.* **2015,** *40* (1), 256-274.
[115] Apaydin, D. H.; Schlager, S.; Portenkirchner, E.; Sariciftci, N. S., Organic, *ChemPhysChem* **2017,** *18* (22), 3094-3116.
[116] Aresta, M., *Carbon dioxide recovery and utilization*. Springer Science & Business Media: 2013.
[117] Benson, E. E.; Kubiak, C. P.; Sathrum, A. J.; Smieja, J. M., *Chem. Soc. Rev.* **2009,** *38* (1), 89-99.
[118] Aresta, M., *Carbon dioxide as chemical feedstock*. Wiley Online Library: 2010; Vol. 416.
[119] Nocera, D. G., *Acc. Chem. Res.* **2012,** *45* (5), 767-776.
[120] Berardi, S.; Drouet, S.; Francàs, L.; Gimbert-Suriñach, C.; Guttentag, M.; Richmond, C.; Stoll, T.; Llobet, A., *Chem. Soc. Rev.* **2014,** *43* (22), 7501-7519.
[121] Francke, R.; Schille, B.; Roemelt, M., *Chem. Rev.* **2018,** *118* (9), 4631-4701.
[122] Martinez, U.; Komini Babu, S.; Holby, E. F.; Zelenay, P., *Curr. Opin. Electrochem.* **2018,** *9*, 224-232.
[123] Fukuzumi, S., *Biochim. Biophys. Acta.* **2016,** *1857* (5), 604-611.
[124] Rosser, T. E.; Gross, M. A.; Lai, Y.-H.; Reisner, E., *Chem. Sci.* **2016,** *7* (7), 4024-4035.
[125] Hammouche, M.; Lexa, D.; Savéant, J. M.; Momenteau, M., *J. Electroanal. Chem. Interf. Electrochem.* **1988,** *249* (1), 347-351.
[126] Steinlechner, C. *et al*. *ACS Catal.* **2019,** *9* (3), 2091-2100.
[127] Coskun, H.; Aljabour, A.; De Luna, P.; Farka, D.; Greunz, T.; Stifter, D.; Kus, M.; Zheng, X.; Liu, M.; Hassel, A. W.; Schöfberger, W.; Sargent, E. H.; Sariciftci, N. S.; Stadler, P., *Sci. Adv.* **2017,** *3* (8), e1700686.
[128] Yu, H.; Shang, L.; Bian, T.; Shi, R.; Waterhouse, G. I. N.; Zhao, Y.; Zhou, C.; Wu, L.-Z.; Tung, C.-H.; Zhang, T., *Adv. Mater.* **2016,** *28* (25), 5080-5086.
[129] Dey, S.; Mondal, B.; Chatterjee, S.; Rana, A.; Amanullah, S.; Dey, A., *Nat. Rev. Chem.* **2017,** *1*, 0098.
[130] Warczak, M.; Gryszel, M.; Jakešová, M.; Đerek, V.; Głowacki, E. D., *Chem. Commun.* **2018,** *54* (16), 1960-1963.
[131] Jakešová, M.; Apaydin, D. H.; Sytnyk, M.; Oppelt, K.; Heiss, W.; Sariciftci, N. S.; Głowacki, E. D., *Adv. Funct. Mater.* **2016,** *26* (29), 5248-5254.
[132] Goor, G.; Glenneberg, J.; Jacobi, S., *Ullmann's encyclopedia of industrial chemistry* **2000**.

H_2O_2.[133,134] However, hence physical deposition of the AQ-derivatives on electrodes suffered from low stability and slow reaction kinetics[133] for long-term applications, an immobilization of the molecules at the electrode is a main point.

Accordingly, to overcome this problem, various attempts were already introduced, like for example, covalently linking to glassy carbon (GC) electrodes,[135] using insoluble polymers[136] or covalent linking to carbon nanotubes (CNT).[137] Regarding a broader scope in organic electronics, organic molecules like AQ are also investigated in battery research[73,108,138] as well as using them for non-covalent enzyme linking.[139]

Due to their attractive properties of being mechanically robust, having high electrical conductivity and tuneability upon synthesis,[10,22] CNTs are favourable immobilization platforms. There are examples of antioxidant-linked CNTs in polymer additives[140] and as they are supposingly bio-compatible[139] also CNTs for medical applications.[141] A report by Park and co-workers[138] investigated nanohybrids of organic molecules adsorbed onto SWNTs for battery application and reported significant improvement of electrical and electrochemical properties. Gong, Zhang and Wang[75] investigated similar adsorbed AQ on multi-walled CNTs (MWNT) for electrochemical ORR in neutral solution. Like the previous examples, in general direct covalent modification of CNTs is avoided. In general, SWNTs have more uniform shapes and properties,[142] but their conductivities are lowering upon covalent modification compared to multi-walled CNTs (MWNT).[143] Combining both, high conductivity by non-covalently binding to the SWNT and still achieving close catalytic sites, Pérez and co-workers developed an advanced supramolecular rotaxane systems using SWNTs.[51,53] The recent catalytic study by the Pérez-Group[144] inspired us to test those molecules for electrocatalytic application. In general, supramolecular architectures towards molecular machines are of high interest in

[133] Sarapuu, A.; Helstein, K.; Vaik, K.; Schiffrin, D. J.; Tammeveski, K., *Electrochim. Acta* **2010,** *55* (22), 6376-6382.

[134] Tammeveski, K.; Kontturi, K.; Nichols, R. J.; Potter, R. J.; Schiffrin, D. J., *J. Electroanal. Chem.* **2001,** *515* (1), 101-112.

[135] Vaik, K.; Mäeorg, U.; Maschion, F. C.; Maia, G.; Schiffrin, D. J.; Tammeveski, K., *Electrochim. Acta* **2005,** *50* (25), 5126-5131.

[136] P. M. Hoang, S. H., and B. Lionel Funt, *J. Electrochem. Soc.* **1985,** *132* (9), 2129-2133.

[137] Mooste, M.; Kibena-Põldsepp, E.; Matisen, L.; Tammeveski, K., Oxygen *Electroanal.* **2017,** *29* (2), 548-558.

[138] Lee, M.; Hong, J.; Kim, H.; Lim, H.-D.; Cho, S. B.; Kang, K.; Park, C. B., *Adv. Mater.* **2014,** *26* (16), 2558-2565.

[139] Bourourou, M.; Elouarzaki, K.; Lalaoui, N.; Agnès, C.; Le Goff, A.; Holzinger, M.; Maaref, A.; Cosnier, S., *Chem. Eur. J.* **2013,** *19* (28), 9371-9375.

[140] Weigl, S.; Bretterbauer, K.; Hesser, G.; Schöfberger, W.; Paulik, C., *Carbon* **2015,** *81*, 305-313.

[141] Constanze, L.; Huzil, J. T.; Marina, V. I.; Marianna, F., *Drug Delivery Lett.* **2011,** *1* (1), 45-57.

[142] Belin, T.; Epron, F., *Mater. Sci. Eng.* **2005,** *119* (2), 105-118.

[143] Zhang, W.; Shaikh, A. U.; Tsui, E. Y.; Swager, T. M., *Chem. Mater.* **2009**, *21* (14), 3234-3241.

[144] Blanco, M.; Nieto-Ortega, B.; de Juan, A.; Vera-Hidalgo, M.; López-Moreno, A.; Casado, S.; González, L. R.; Sawada, H.; González-Calbet, J. M.; Pérez, E. M., *Nat. Commun.* **2018,** *9* (1), 2671.

the scientific community due to the Nobel prizes in 1987 for D. J. Cram, J-M. Lehn and C. J. Pederson[145,146] as well as recently in 2016 for J.-P. Sauvage, J. F. Stoddart and B. Feringa.[147,148,149,150]

The main motivation of this work has two aspects: the first task was to investigate the electrochemical behaviour of a mechanically interlocked anthraquinone on SWNTs (MINT-AQ) and compare it with an adsorbed AQ analogue (supramolecular form, AQ@SWNT) as well as with a pure homogeneous AQ analogue cases. In order to do so, AQ as redox-active species on SWNTs in aqueous solution and in organic solvents were compared with the properties of adsorbed and pure AQ cases, like reported in a similar way with a metal complex.[61] The second task was to demonstrate the application of this immobilized AQ platform for electrochemical ORR.

4.2. **Results.**

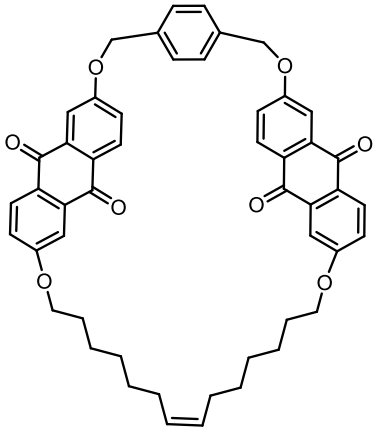

Figure 1. Chemical structure of mac-AQ.

The characterization of mac-AQ[99] and MINT-AQ[144] were synthesized as previously reported.[52,53,54,55] After the MINT-forming reaction, the SWNTs showed a

[145] Lehn, J., *Science* **1993,** *260* (5115), 1762-1763.

[146] Huang, F.; Anslyn, E. V., *Chem. Rev.* **2015,** *115* (15), 6999-7000.

[147] Liu, Z.; Nalluri, S. K. M.; Stoddart, J. F., *Chem. Soc. Rev.* **2017,** *46* (9), 2459-2478.

[148] Amabilino, D. B.; Gale, P. A., *Chem. Soc. Rev.* **2017,** *46* (9), 2376-2377.

[149] Kassem, S.; van Leeuwen, T.; Lubbe, A. S.; Wilson, M. R.; Feringa, B. L.; Leigh, D. A., *Chem. Soc. Rev.* **2017,** *46* (9), 2592-2621.

[150] Stoddart, J. F., *Acc. Chem. Res.* **2001,** *34* (6), 410-411.

loading of macrocycle of 13% and 15% under nitrogen, for MINT-AQ and AQ@SWNT respectively, by TGA analysis (Figure S4 and S5). Regarding the Raman spectroscopy (Figure. S7), a shift showed in the G/2D bands in the MINT-AQ and AQ@SWNT samples, due to the presence of electron acceptor anthraquinone macrocycles. We also synthesized MINT-AQ and AQ@SWNT samples with less loading of macrocycle in order to see the effect of the quantity of anthraquinone moieties (Figure S4 and S5). In the case of synthesis of MINT-AQ and AQ@SWNT with low loading, were 4.3% and 5.8% respectively (under nitrogen).

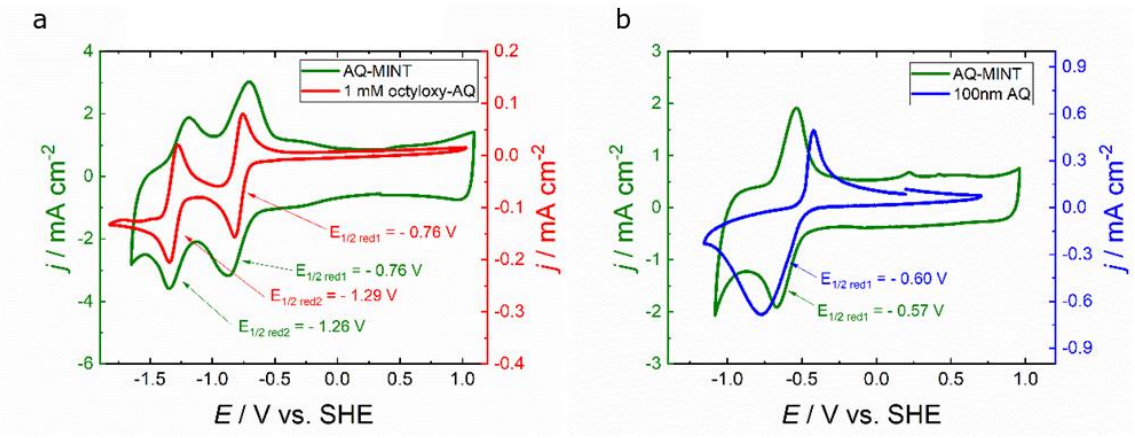

Figure 2. Cyclic voltammograms of **a.** MINT-AQ (green line) and 1 mM octyloxy-AQ (red line) ACN containing in 0.1 M $TBAPF_6$ and **b.** dropcasted MINT-AQ (green line) and 100 nm thin-film of AQ in 0.1 M Na_2SO_4 aqueous solution. The cyclic voltammograms were recorded under N_2 saturated conditions at a scan rate of 20 mV s^{-1}.

The electrochemical behaviour of MINT-AQ was investigated via cyclic voltammetry (CV) either in organic solvent (acetonitrile, ACN) or in aqueous solution as shown in Figure 2. For comparison with non-immobilized anthraquinone, a dissolved octyloxy-anthraquinone derivative (see Figure S10 for more information) as well as an evaporated film of pure AQ were studied. Figure 2a presents the electrochemical features of drop-casted MINT-AQ samples in ACN and dissolved octyloxy-AQ with the concentration of 1 mM. Both cyclic voltammograms are comparable excluding large capacitive current from SWNT carrier observed in the case of the immobilized MINT-AQ (Figure S15 for SWNT CV curves). The graphs show two separated reversible one-electron reduction features of anthraquinone at virtually identical $E_{1/2}$ of -0.76 and -1.26 /

-1.29 V.[151] The electrochemical features of MINT-AQ and evaporated thin-film of AQ in aqueous solution were shown in Figure 2b. The graphs present one reversible and concerted two-electron reduction feature. However, the reduction potential of MINT-AQ with $E_{1/2}$ = -0.57 V is 30 mV less negative as well as its peak separation (ΔE_P) is smaller, as compared to those of thin-film AQ. This smaller ΔE_P in case of MINT-AQ together with the reported delamination of hydroquinone in case of the evaporated AQ[74] shows that MINT-AQ system offers a more versatile redox system. This is in accordance to literature[138] of adsorbed species on SWNTs that stacking induced faster charge-transfer kinetics and smaller ΔE_P.

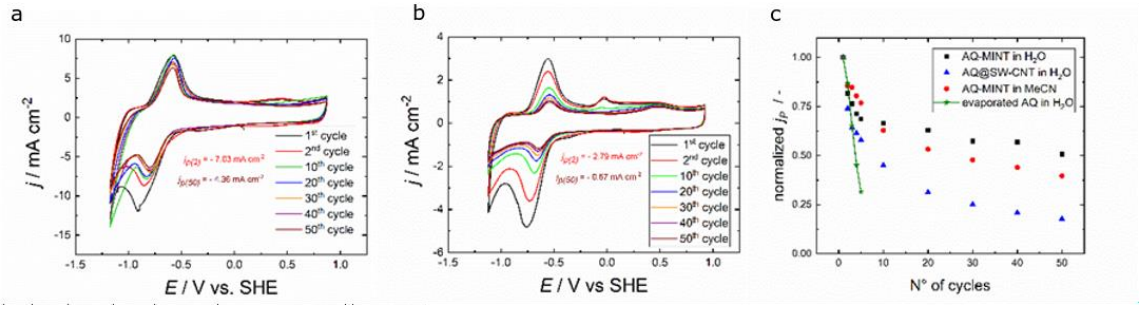

Figure 3. Cyclic voltammograms of **a.** MINT-AQ and **b.** AQ@SWNT in 0.1M Na_2SO_4 upon 50 cycles. **c.** The normalized peak current densities of the first reduction peak are compared.

The stability study of the immobilized MINT-AQ was performed with 50 CV cycles, as shown in Figure 3. The supramolecular adsorbed form (AQ@SWNT) as well as the evaporated AQ film were investigated in a similar manner. Figure 3 shows that MINT-AQ is more stable due to less decrease in reductive peak current compared to the supramolecular form. This observation was strengthened by the comparison of the relative loss of peak current density (j_P) upon 50 cycles. For the calculation of the j_P, the peak height by subtracting a baseline was determined. In MINT-AQ case, the j_P decreased by 38% from the 2nd to the 50th cycles, whereas in the AQ@SWNT case, the loss roughly doubled with 76%. These decreases were exponentially decaying while the evaporated AQ thin-film decayed linearly by 68% within the first 5 cycles (Figure 3c). Moreover, cycle stability was also performed in ACN solution. Similar behaviour was observed with less pronounced decrease from the 1st to the 2nd cycle (Figure S13). According to

[151] Babaei, A.; Connor, P. A.; McQuillan, A. J.; Umapathy, S., *J. Chem. Educ.* **1997,** *74* (10), 1200.

literature[75] kinetic studies performing CV at different scan rates were performed which showed, as expected for immobilized materials, a linear relation between the scan rate (v) and j_P for both, the MINT-AQ and the supramolecular sample (Figure S11).

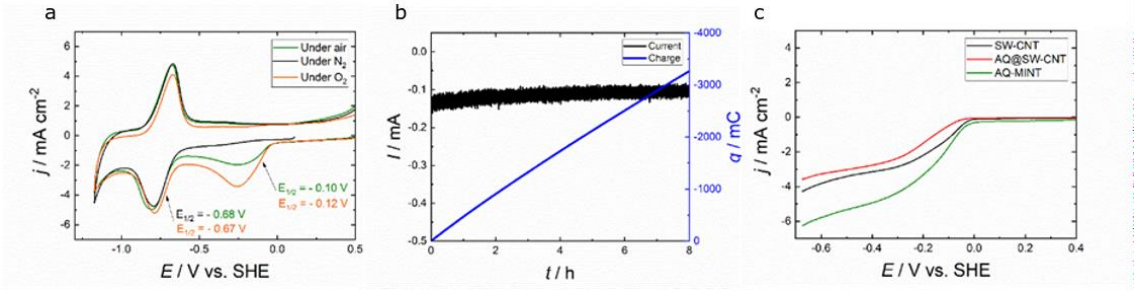

Figure 4. **a.** Cyclic voltammograms of MINT-AQ were recorded in 0.1 M NaOH under air (green line), N_2 (black line) and O_2 (orange line) saturated conditions. **b.** Chronoamperograms and accumulated charges of MINT-AQ was measured by applying a constant potential of -0.33 V vs. SHE in 0.1 M NaOH solution over 8h. **c.** RDE-LSV results of MINT-AQ, AQ@SWNT and SWNT in 0.1M NaOH at a rotation speed of 1200 rpm.

As anthraquinone derivatives are known as chemical[72,132] as well as electrochemical[133,135,137] catalysts for the oxygen (O_2) reduction to hydrogen peroxide (H_2O_2) vide supra, the MINT-AQ was investigated for its electrocatalytic activity under O_2-saturated condition. AQ@SWNT and pristine SWNT were also tested as controls. Figure 4a shows that the characteristic AQ peak[152] at around -0.68 V was observed in all conditions. Upon O_2 saturation, a reduction broad peak around -0.10/-0.12 V as a result of oxygen reduction was observed. Starting from +0.50 V on, some oxidative processes on the SWNT occurred. Bare SWNTs only showed the broad, capacitive current with a small reductive step upon O_2 reduction (Figure S15a). In order to prove the catalytic activities of MINT-AQ, AQ@SWNT and SWNT towards the reduction of O_2 to H_2O_2, a constant potential was applied for 8 h distinguishing the two conditions: neutral (0.1 M Na_2SO_4) and basic (0.1 M NaOH) aqueous solutions. (See Supporting Information for full details). The transient curves in Figure 4 b show that the current in MINT-AQ case was stable over the 8 h period whereas the AQ@SWNT sample (Figure S16) revealed a drastic decrease in current from -0.24 mA cm^{-2} to -0.05 mA cm^{-2} within

[152] J. Revenga, F. R. a. J. T., *J. Electrochem. Soc.* **1994,** *141* (2), 330-333.

8 h reaction. This decrease was attributed to the delamination of the AQ electroactive species, which is in accordance to the cycle stability experiments in Figure 3b. Further, the CV curves of MINT-AQ before and after the electrolysis showed nearly no difference in terms of electroactive AQ peaks which underlines the stable transient curve (Figure S17).

Table 1. Comparison of the total amounts of H_2O_2 produced over 8 h electrolysis reaction time.

	In 0.1 M Na_2SO_4		**In 0.1 M NaOH**	
	$n_{(H2O2)}$ over 8h / µmol	TON	$n_{(H2O2)}$ over 8h / µmol	TON
MINT-AQ	1.9	116	7.0	417
AQ@SWNT	1.4	75	4.4	236
SWNT	0.5	-	2.2	-

Table 1 reveals that basic conditions are more favourable for oxygen reduction, as compared to neutral pH, which is in accordance to literature.[72,153] In case of MINT-AQ, the amount produced was increased from 1.9 µmol in neutral conditions to 7.0 µmol in alkaline conditions. As observed in control experiments, the pristine SWNT also showed small catalytic effect, which was also already reported in literature.[22,154] This effect we attributed to traces of catalytically active metals or small defects as a result of the SWNT production process[22,155] as well as also some intrinsic catalytic activity of GC.[156] However, both AQ modified samples presented enhanced catalytic activity over SWNTs also with the supramolecular sample showing slight enhancement by a factor of 2 under basic conditions. The MINT-AQ even showed superior performance by increasing the activity by a factor of 3 in basic conditions. Considering the amount of AQ molecules in MINT as well as supramolecular case, turnover numbers (TON) were calculated in Table 1, which also substantiate the improved catalysis. Including the total mass of the MINT

[153] Vikkisk, M.; Kruusenberg, I.; Joost, U.; Shulga, E.; Kink, I.; Tammeveski, K., *Appl. Catal. Environ.* **2014,** *147*, 369-376.
[154] Qu, J.; Shen, Y.; Qu, X.; Dong, S., *Electroanal.* **2004,** *16* (17), 1444-1450.
[155] Kruusenberg, I.; Alexeyeva, N.; Tammeveski, K.; Kozlova, J.; Matisen, L.; Sammelselg, V.; Solla-Gullón, J.; Feliu, J. M., *Carbon* **2011,** *49* (12), 4031-4039.
[156] Šljukić, B.; Banks, C. E.; Compton, R. G., *J. Iran. Chem. Soc.* **2005,** *2* (1), 1-25.

and the activity from the supporting material, the average H_2O_2 production rate per mass was found to be 8.8 µmol mg^{-1} h^{-1} for MINT-AQ in basic aqueous solution. For the outstanding reports, the direct synthesis from the elements on Pd nanoparticles[72] was shown with 1100 µmol mg^{-1} h^{-1} and the photo-electrocatalysis with epindolidione[131] was presented with the rate of 120 µmol mg^{-1} h^{-1}. For direct comparison to our system, one has to keep in mind, that in the MINT or supramolecular form also the SWNTs were counted towards the total mass.

In order to perform further electrocatalytic studies on the oxygen reduction process, rotating disc electrode (RDE) experiments were performed with SWNT, AQ@SWNT and MINT-AQ at various rotation speeds. The goal was to get preliminary mechanistic insights by determination of the number of transferred electrons per process. As expected, increasing the rotation speed (ω) resulted in increasing currents as well as the MINT-AQ sample showed a more pronounced behaviour (Figure 4c). The Koutecki-Levich-Analysis revealed that upon drop-casting the samples, we substantially underestimate our electroactive electrode surface area by considering only the geometrical one. As this increase in electrode surface area was related to the organization of the SWNTs on the surface, we suspect different ways of organization between the samples, caused by the attachments, which would be in accordance to the reported reorganization through hybridisation by Lee *et al.*[138] Nevertheless, the intercepts of the Koutecki-Levich analysis revealed that comparing those as-casted films MINT-AQ shows the highest i_K compared to SWNT and AQ@SWNT (Figure S18b).To proof this suspicion of organization, advanced studies with higher resolution SEM facilities than we have would be necessary.

4.3. **Conclusions.**

In this work, we explored the approach of interlocking the organic molecule anthraquinone around carbon nanotubes (MINTs) as efficient way of immobilization. Such advanced supramolecular architectures could solve the problem of dissolution-instability of physically adsorbed organic molecules upon electrochemical reduction. Besides the enhancement in stability while retaining the electrochemical properties of the pristine molecule, also an efficient immobilization towards electrochemistry could be demonstrated by a linear relation of j_P vs. v plots. Further, a proof of concept for

electrocatalytic application of MINT-AQ towards oxygen reduction was explored. In addition to the superior stability, an improvement in H_2O_2 production rate in MINT-AQ systems revealed promising properties of MINTs as immobilization carrier. The promising results described in this work revealed that there is still room for further investigation of different MINT type materials on other catalytic applications.

4.4. **Supplementary Information.**

4.4.1. **Supplementary Methods.**

Characterization methods of SWNT and MINT. (6,5)-Enriched single walled nanotubes (6,5-SWNT) were purchased from Sigma-Aldrich (0.7−0.9 nm in diameter, length ≥700 nm, mostly semiconducting, 95% purity). Analytical thin layer chromatographies (TLC) were performed using aluminium-coated Merck Kieselgel 60 F254 plates. NMR spectra were recorded on a Bruker Avance 400 (^{1}H: 400 MHz; ^{13}C: 100 MHz) spectrometers at 298 K, using partially deuterated solvents as internal standards. Coupling constants (*J*) are denoted in Hz and chemical shifts (δ) in ppm. Electrospray ionization mass spectrometry (ESI-MS) and Matrix-assisted Laser desorption ionization (coupled to a Time-Of-Flight analyzer) experiments (MALDITOF) were recorded on a HP1100MSD spectrometer and a Bruker REFLEX. Thermogravimetric analyses (TGA) were performed using a TA Instruments TGAQ500 with a ramp of 10 °C min^{-1} under air from 100 to 900 °C. Transmission electron microscopy (TEM) images were obtained with JEOL-JEM 2100F instrument or a JEOL-JEM GRAND ARM300cF (AC-HRTEM). Raman spectra were acquired with a Bruker Senterra confocal Raman microscope instrument equipped with 532 excitation laser. UV-vis-NIR spectra were performed using an Agilent Technologies equipment – Cary Series UV-Vis-NIR Spectrophotometer. Photoluminescence excitation intensity maps (PLE) were obtained with NanoLog 4 HORIBA instrument.

Electrode preparation. A 3 mm diameter GC disc-type electrode (BASi, US) was used in all experiments as a working electrode (WE) and prior use polished for 30 s each with a Buehler Micropolish II deagglomerated alumina in decreasing particle sizes from 1.0 to 0.3 to 0.05 µm. In between, the surface was rinsed with 18MΩ water (MQ water) and *iso*-propanol (VWR Chemicals, AnalaR Normapur) to remove excess alumina. To deposit single-walled nanotubes (SWNTs) sample onto the WE, SWNTs suspensions in

iso-propanol with loadings of 5.0 mg mL^{-1} were prepared and sonicated for 2 h prior use. 20 µL aliquots were drop-casted onto the glassy carbon WE and dried for 30 min under ambient conditions.

Platinum plates (Pt) were used as counter electrode together with either commercially available Ag/AgCl/3M KCl (from BASi, US) reference electrodes (RE) in aqueous solutions or Ag/AgCl quasi-reference electrodes (QRE) in organic solutions for electrochemical investigations. In case of the QRE, the calibration towards standard hydrogen electrode (SHE) was done by addition of ferrocene (Sigma Aldrich, >98%) and determination the position of this redox potential.

Electrochemical experiments. All electrochemical measurements were done on a Jaissle Potentiostat-Galvanostat PGU10V-100mA. A three-electrode one-compartment (for organic solution) or two-compartment (for aqueous solution) electrochemical cells were used. The mentioned glassy carbon (GC) was equipped as WE. Platinum plates (Pt) were used as a counter electrode. In aqueous solution, a Ag/AgCl (3 M KCl) reference electrodes (RE) was equipped in the system while in organic solutions, a Ag/AgCl quasi-reference electrodes (QRE) was used. The QRE was prepared by anodization in 1 M HCl solution and the calibration towards standard hydrogen electrode (SHE) was determined by testing with ferrocene.

Throughout this whole work, all potentials mentioned refer to the SHE.
For cyclic voltammetry (CV) experiments in organic solvents, 15.0 mL of acetonitrile (ACN) (Roth, >99.9%) containing 0.1 M $TBAPF_6$ (Sigma Aldrich, >99.0%) was used as electrolyte solution. In aqueous solution, CV experiments were done in 20.0 mL of 0.1 M Na_2SO_4 (Sigma Aldrich, >99.0%) or 0.1 M NaOH (Alfa Aesar) as electrolyte solution. Prior measurement in N_2-saturated condition, the cell was purged with N_2 for 30 min and 60 min for ACN and aqueous solutions, respectively. In case of O_2-saturated case, the solutions were purged with O_2 (Linde Gas GmbH 5.0) for 30 min.

For the RDE measurements, an IPS Rotator 2016 rotating unit with IPS PI-ControllerTouch and an IPS Jaissle PGU BI-1000 Bipotentiostat/Galvanostat was used. An 8 mm diameter GC disc in polychlorotrifluoroethylene (PCTFE) was used as WE and polished like mentioned above. A platinized electrode and Ag/AgCl (3 M KCl) (Messtechnik Meinsberg, Germany) were used as counter electrode and reference electrodes. In order to achieve comparable surface loading, 141 µL of the 5 mg mL^{-1} nanotube suspensions were drop-casted and dried prior use.

Determination of hydrogen hydroxide (H_2O_2) production. The detection of H_2O_2 was done accordingly to recent literature reports.[157,158] Mixtures in a 1:1 ratio of 4 mM *p*-nitrophenyl boronic acid (*p*NBA, Sigma Aldrich, >95%) in DMSO (VWR, technical) and a 150 mM Na_2CO_3/$NaHCO_3$ (Fluka, >99.5%; Sigma Aldrich, 99.7-100.3%)) buffer solution pH 9 were mixed with the sample. After 36 min incubation at room temperature under dark condition, the absorbance at 411 nm was recorded using a Thermo Fischer Multiskan Go Microplate Spectrophotometer. The amount of H_2O_2 was determined using a calibration curve made from H_2O_2 standard solution (Merck, 30%, stabilized for synthesis) (Figure S9). The measured absorbance was subtracted with the absorbance of blank sample (incubation of deionized water with chromophore). The subtracted value, Δabsorbance, was used for the quantification.

4.4.2. Synthesis and characterization of 2,6-bis(oct-7-en-1-yloxy)anthracene-9,10-dione (C_8-AQ-C_8).

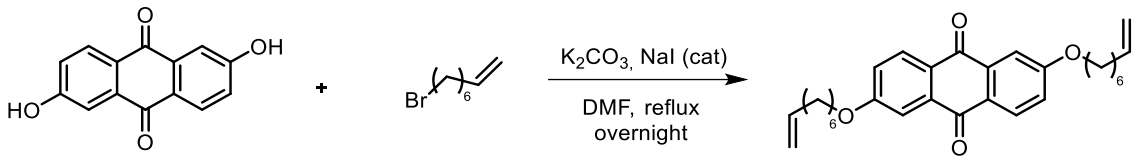

Anthraflavic Acid (0.5 g, 2.08 mmol, 1 eq) was dispersed with sonication in dry dimethylformamide (DMF) (21 mL, 0.1 M). Then, dry carbonate potassium (K_2CO_3) (0.86g, 6.24 mmol, 3eq), 8-Bromo-1-octene (0.7 mL, 4.16 mmol, 2 eq) and catalytic amount of sodium iodide (NaI) were added and the mixture was refluxed overnight under N_2 atmosphere. The next day, the crude of the reaction was allowed to rt and was poured into ice-cold 1M HCl and the precipitate was filtered. The solid was redissolved in dicloromethane (DCM) and washed with water twice times. The organic phase was dried over Na_2SO_4 and the solvent was evaporated under reduced pressure. Finally, the crude was purified by flash chromatography (DCM) to obtain the product in 86% yield. ^{1}H NMR (400 MHz, $CDCl_3$) δ 8.22 (d, *J* = 8.7 Hz, 2H), 7.70 (d, *J* = 2.6 Hz, 2H), 7.21 (dd, *J* = 8.7, 2.7 Hz, 2H), 5.82 (ddt, *J* = 16.9, 10.2, 6.7 Hz, 2H), 5.07 – 4.90 (m, 4H), 4.14 (t, *J* = 6.5 Hz, 4H), 2.07 (q, *J* = 6.9 Hz, 4H), 1.90 – 1.78 (m, 4H), 1.55 – 1.32 (m, 12H). ^{13}C

[157] G. Su, Y. W. a. M. G., *Am. J. Anal. Chem.* **2011,** *2* (8), 879-884.

[158] Apaydin, D. H.; Seelajaroen, H.; Pengsakul, O.; Thamyongkit, P.; Sariciftci, N. S.; Kunze-Liebhäuser, J.; Portenkirchner, E., *ChemCatChem* **2018,** *10* (8), 1793-1797.

NMR (101 MHz, $CDCl_3$) δ 182.5, 164.2, 139.1, 136.0, 129.8, 127.1, 121.1, 114.5, 110.7, 68.9, 33.8, 29.1, 28.9, 26.0. MALDI calculated for $C_{30}H_{36}NaO_4$ $[M+Na]^+$: 483.2506; found 483.2522.

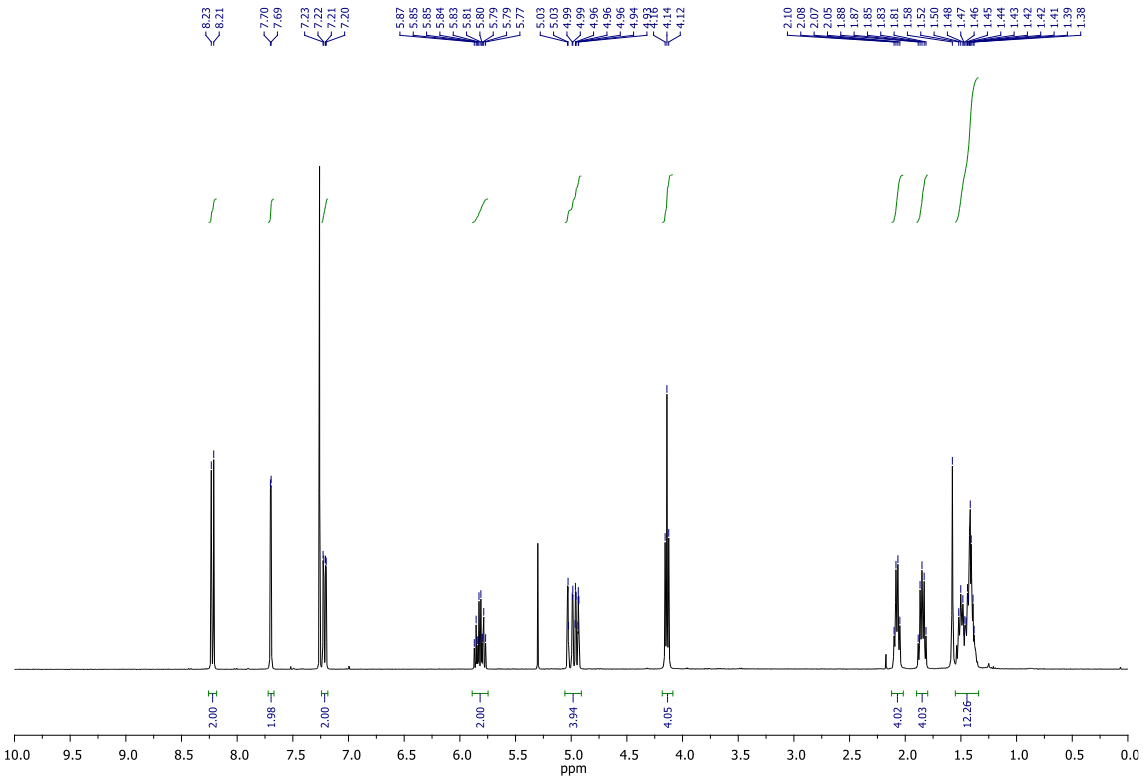

Figure S1. ^{1}H-NMR spectrum of C_8-AQ-C_8 ($CDCl_3$, 298 K).

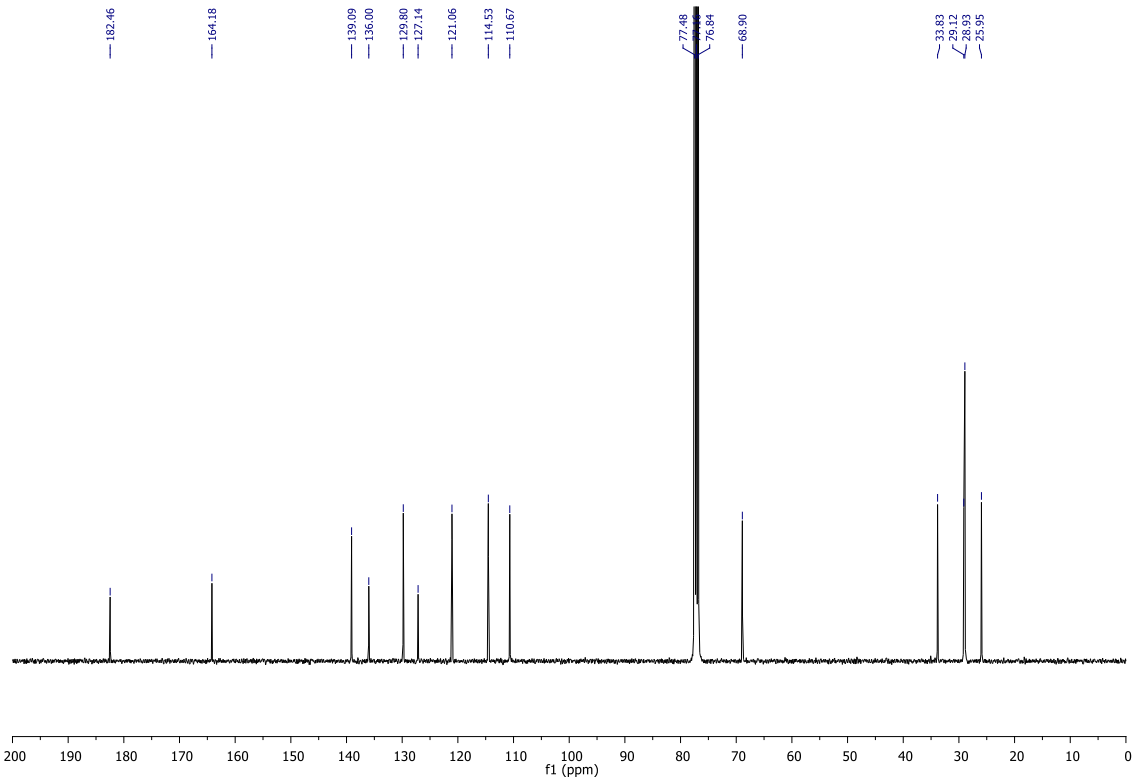

Figure S2. ^{13}C-NMR spectrum of C_8-AQ-C_8 ($CDCl_3$, 298 K).

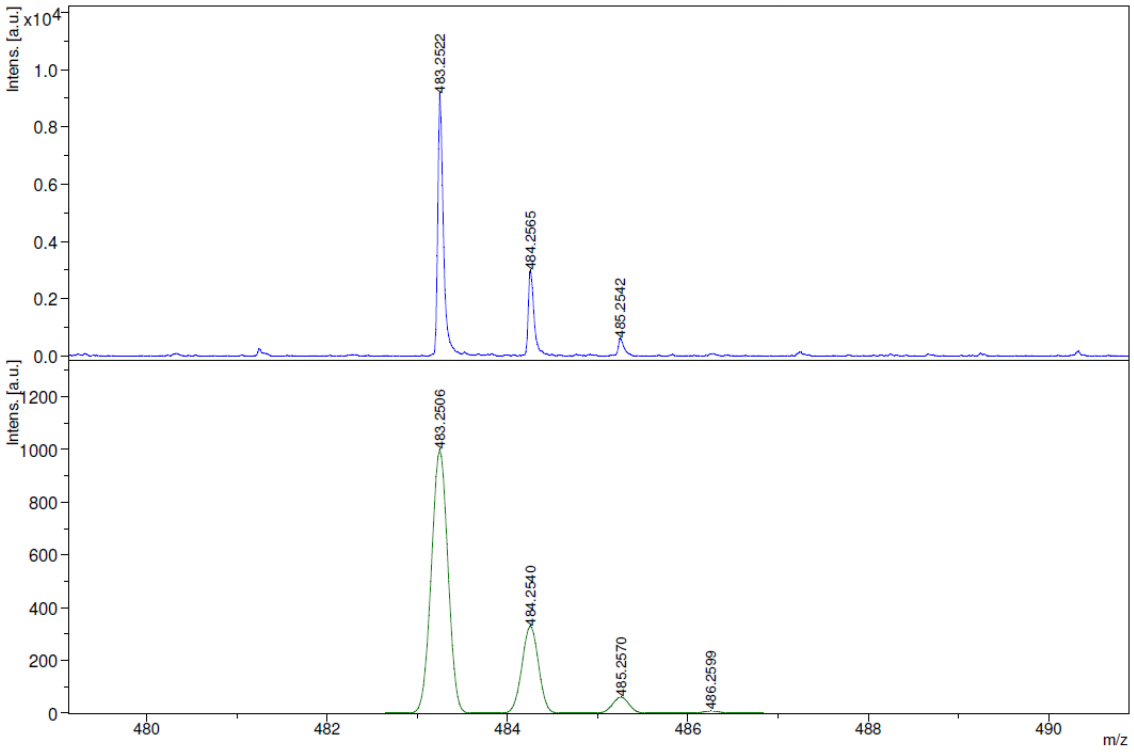

Figure S3. MALDI spectra of C_8-AQ-C_8.

4.4.3. **Synthesis and characterization of MINT.**

The (6,5)- enriched SWNTs purchased from Sigma Aldrich were purified previously. 100 mg of SWNTs were suspended in 70 mL of 35 % HCl, and sonicated for 10 min. The mixture was poured in 200 mL of MQ water and filtered through a polycarbonate membrane of 0.2 μm pore size. The solid was washed with water to neutral pH and then dried in an oven at 350 ºC for 30 min. Pristine plasma-purified SWNTs were used without previous purification.

The pristine (10 mg) were suspended in 10 mL of tetrachloroethane through sonication (10 min) and mixed with 0.01 mmol of linear bisalkene U-shaped AQ,[99] and Grubbs' second-generation catalyst at room temperature for 72 h under N_2 atmosphere. After this time, the suspension was filtered through a PTFE membrane of 0.2 μm pore size and the solid washed profusely with DCM. The solid was re-suspended in 10 mL of DCM through sonication for 10 min and filtered through a PTFE membrane of 0.2 μm 4 pore size again. This washing procedure was repeated three times. The sample obtained was denoted as MINT-AQ.[144] The synthesis of the supramolecular complex was denoted as AQ@SWNT and was performed by the direct mixing of the adequate amounts of (6,5)-SWNT and the corresponding macrocycle without catalyst to achieve the same functionalization loading of organic material over the nanotube compared to their respective MINT sample. Two samples with different loading of the macrocycle have been synthesized.

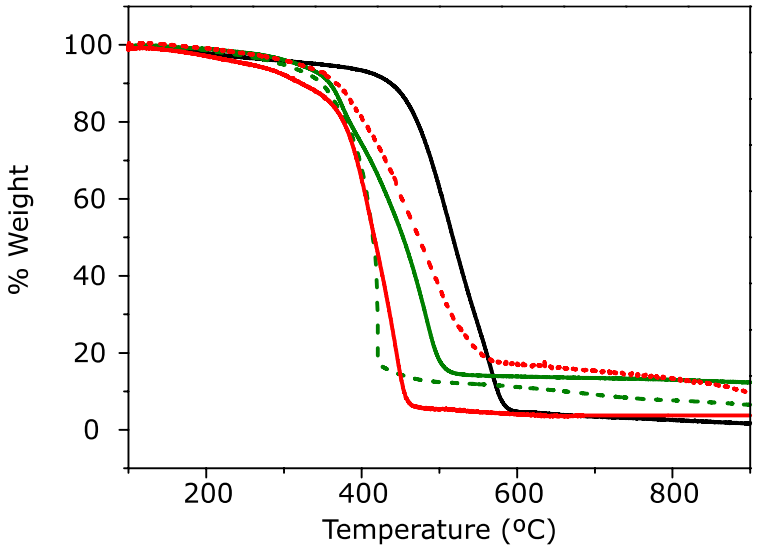

Figure S4. TGA plots (ramp of 10 °C min^{-1} under air from 100 to 900 °C) of SWNT (black), MINT-AQ (green), AQ@SWNT (red), MINT-AQ with low loading (green dashed line) and AQ@SWNT with low loading (red dashed line).

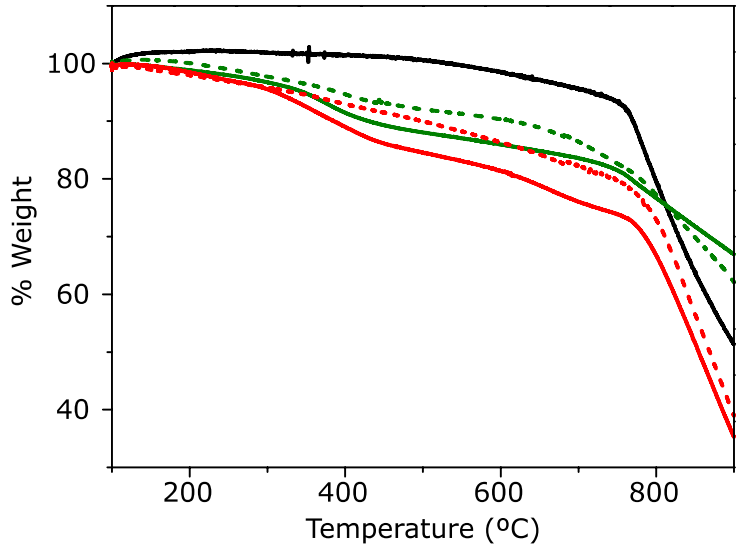

Figure S5. TGA plots (ramp of 10 °C min^{-1} under N_2 from 100 to 900 °C) of SWNT (black), MINT-AQ (green), AQ@SWNT (red), MINT-AQ with low loading (green dashed line) and AQ@SWNT with low loading (red dashed line).

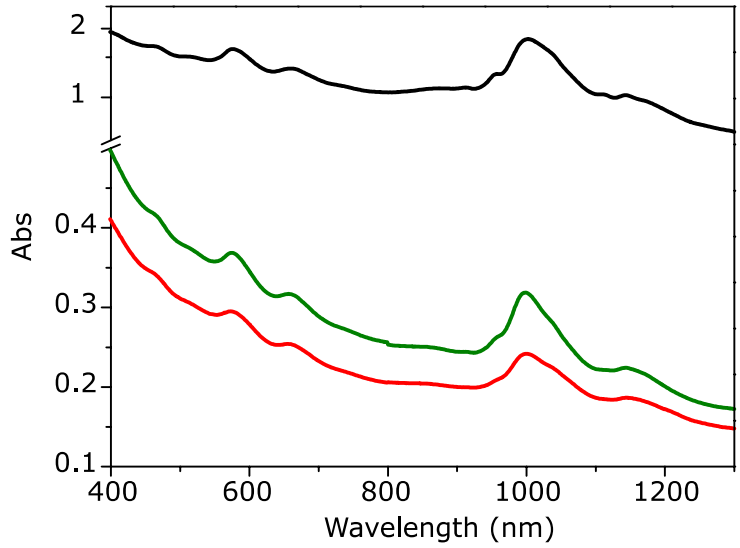

Figure S6. UV-Vis spectra (D_2O / SDS (1 wt. %) at room temperature) of SWNT (black), MINT-AQ (green) and AQ@SWNT (red).

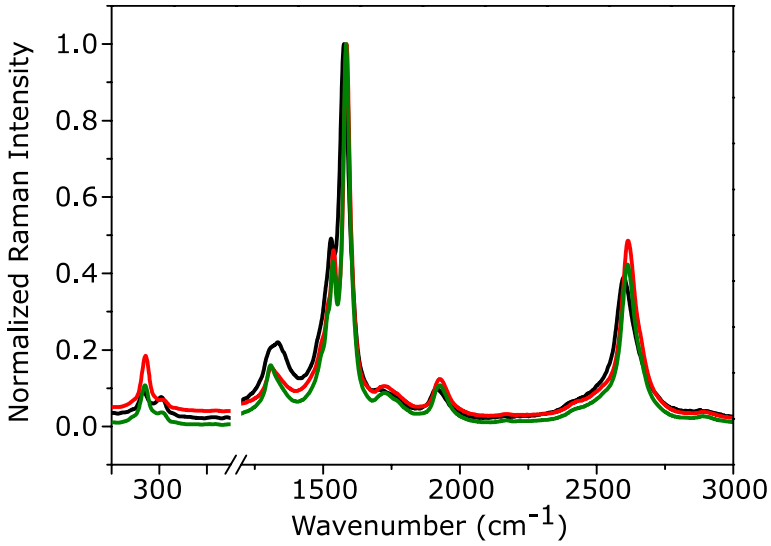

Figure S7. Raman spectroscopy. Average (N = 25). Raman spectra of SWNT (black), MINT-AQ (green) and AQ@SWNT (red).

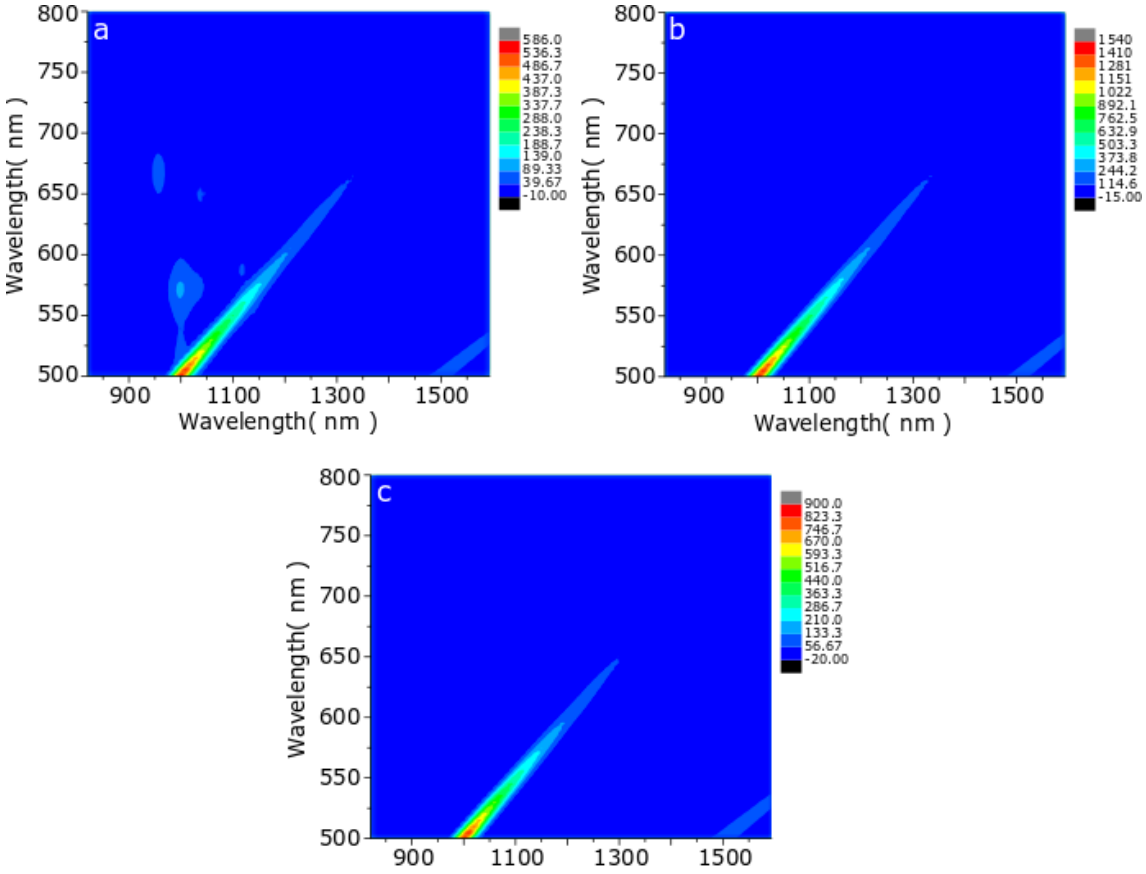

Figure S8. PLE map of **a.** (6,5)-SWNT, **b.** MINT-AQ and **c.** AQ@SWNT. Rayleigh scattering has not been filtered in this image.

4.4.4. H_2O_2 calibration curve.

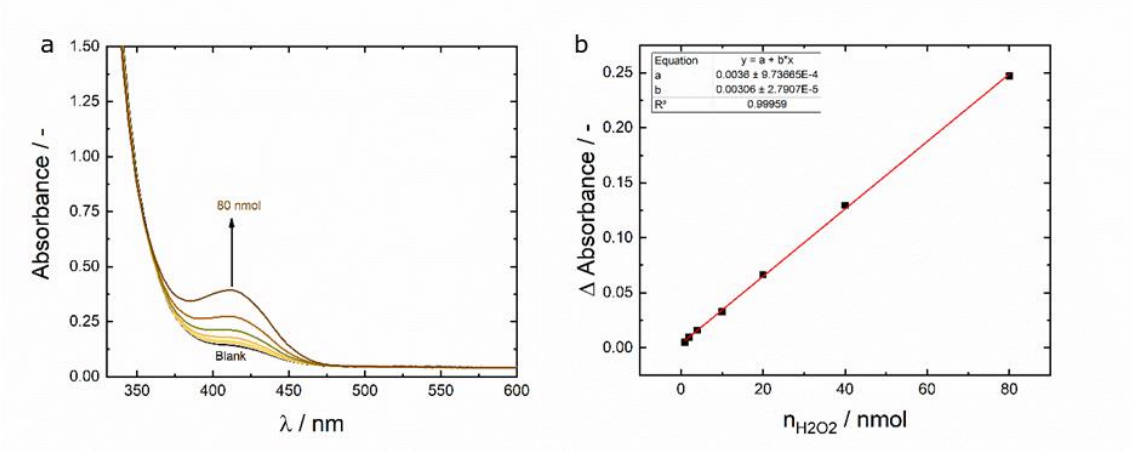

Figure S9. **a.** Absorption spectra of standard H_2O_2 solution at various concentrations and **b.** calibration curves of the H_2O_2 quantification including the formula.

4.4.5. **Homogeneous investigations.**

As mentioned in the article, an octyloxy-AQ derivative was chosen to compare it to the MINT-AQ electrochemical experiments. In the following Figure S10 the CV of 2.5 mM AQ is compared with the CV of 1 mM octyloxy-AQ in 0.1M $TBAPF_6$ in ACN solution.

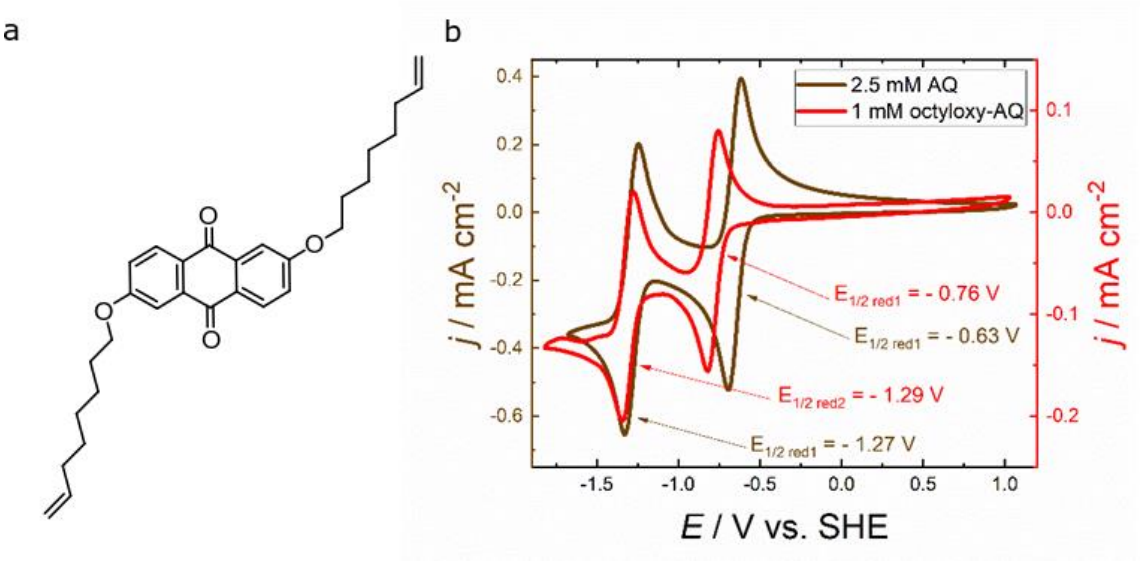

Figure S10. **a.** Structure of the (bis)octyloxy-AQ and **b.** cyclic voltammograms of 2.5 mM AQ and 1 mM octyloxy-AQ recorded in ACN containing 0.1 M $TBAPF_6$ with scan rates of 20 mV s^{-1}.

The CV curves shown in Figure S10 show, that the alkoxy substituents shift the first reduction wave cathodically by 130 mV whereas the second reduction wave is nearly unaffected.

4.4.6. **Kinetic Investigations.**

Regarding the cycle stability test, MINT-AQ was reasonably stable, while AQ@SWNT suffered from severe loss of j_P over 50 cycles. Nevertheless, kinetic studies of both MINT-AQ and AQ@SWNT were performed by CV with varied scan rate (Figure 3a and b). Due to the fact that especially the AQ@SWNT sample with the 15 % loading (and also the MINT-AQ sample with 13 %) suffered from significant loss of j_P during the kinetic studies (Figure S12b and d), from continuous delamination over the experiment time, no further kinetic data could be extracted thereof. The investigation of samples with lower loadings proved sufficient stability (Figure S12a and c), the mentioned kinetic studies and analysis could be determined.

In the following Figure S11 all the CV's of MINT-AQ (4 % m/m) as well as AQ@SWNT (6 % m/m) on GC electrodes in 0.1M Na_2SO_4 in H_2O are shown.

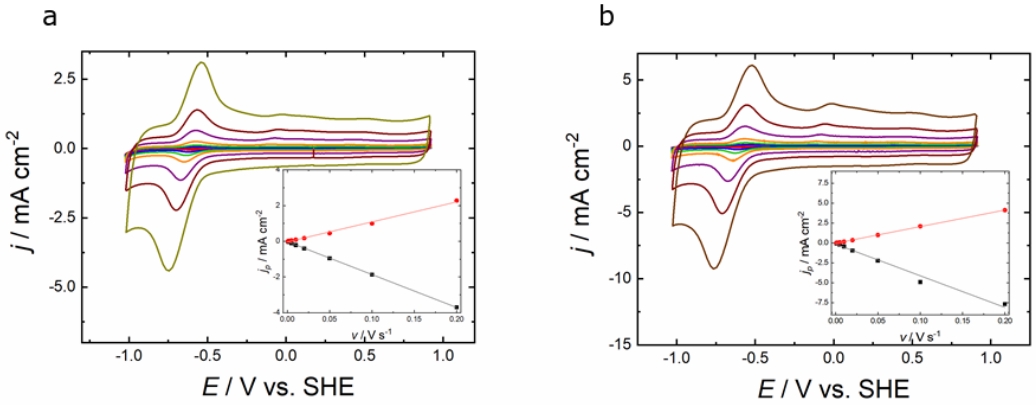

Figure S11. Cyclic voltammograms of **a.** MINT-AQ and **b.** AQ@SWNT recorded in 0.1 M Na_2SO_4 aqueous solution with various scan rates of 1, 2, 5, 10, 20, 50, 100 and 200 mV s^{-1}. The insets show plots of j_p vs the scan rate.

The curves shown in Figure S11 were analysed concerning peak currents j_P's and the resulting plots as are shown as insets. In both cases, a linear correlation of the j_P with the scan rate (v) was observed.

Also, the integrated peak charges were calculated where in case of both MINT-AQ batches quite stable values of, in case of both AQ@SWNT due to degradation over the cycles only decreasing values were observed. This decreasing of the peak currents over the time-scale of the scan rate dependence experiments is shown in the following Figure S12 where in all cases "fast" scans at 200 mV s^{-1} were done before, during and after the experiment.

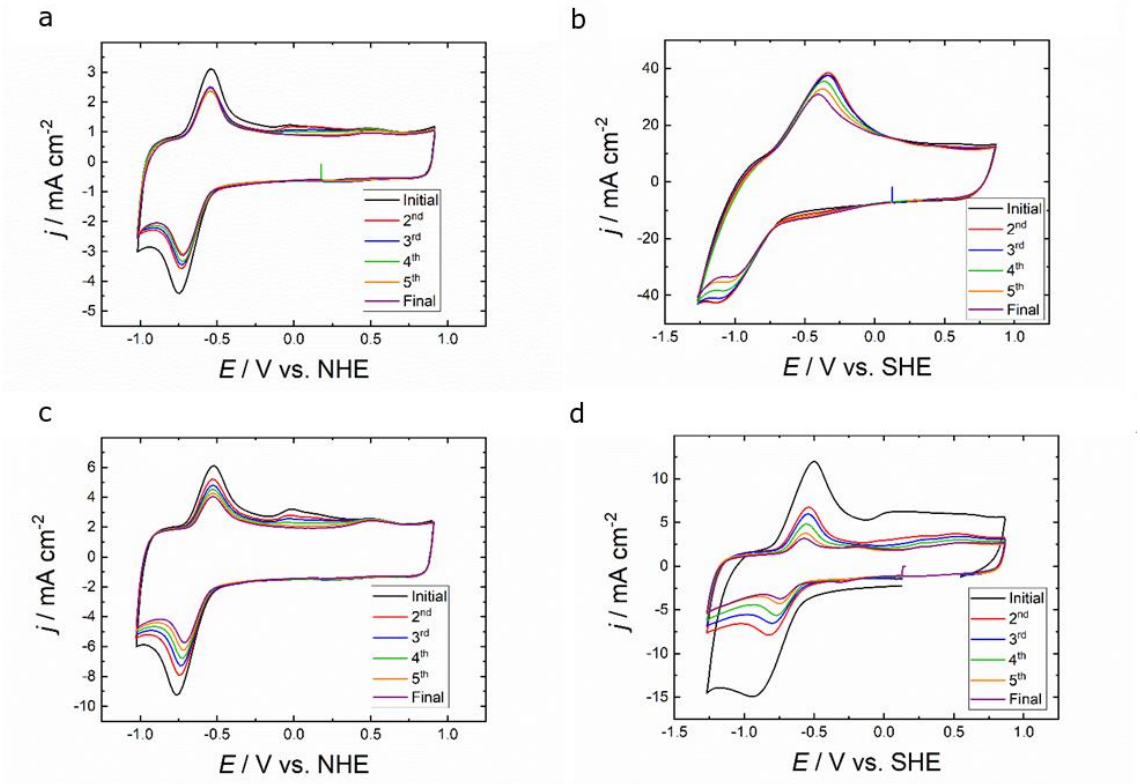

Figure S12. Cyclic voltammograms of **a.** MINT-AQ with low loading (4% m/m), **b.** MINT-AQ with high loading (13% m/m), **c.** AQ@SWNT with low loading (6% m/m) **d.** AQ@SWNT with high loading (15% m/m) (all recorded at 200 mV s^{-1}).

Besides the strong j_P dependence on the loading, a moderate decrease of j_P in case of both MINT-AQ samples was observed in Figure S12. In case of the AQ@SWNT sample with low loading, this j_P drop was still acceptable, although also as reported above the integrated peak charges decrease by 50 % over the experiment. The AQ@SWNT sample with high loading showed a significant decrease in j_P over this experiment, which does not allow a scientific analysis of the scan rate dependence of j_p.

In the following Figure S13, the cycle stability of MINT-AQ in the organic conditions of 0.1M $TBAPF_6$ in ACN is shown.

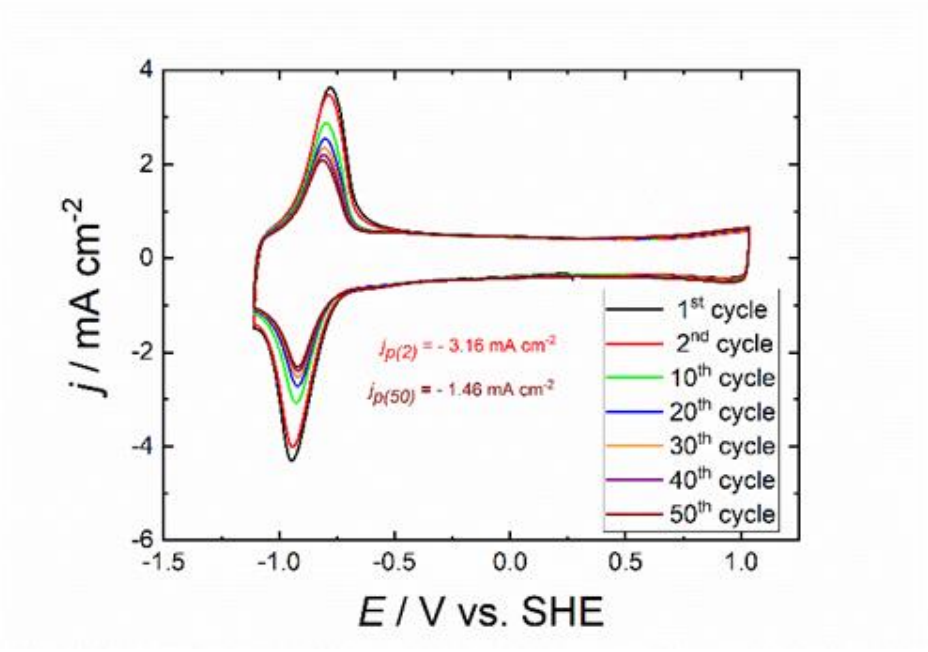

Figure S13. CV curve of MINT-AQ in ACN containing 0.1M $TBAPF_6$ upon 50 sweeping cycles.

In general, a similar behaviour like in aqueous solution (see Figure 3) was observed. The lower j_P can be explained by the fact that, in organic solvents in this potential range only a 1-electron reduction process is taking place.

4.4.7. **Investigations on oxygen reduction reaction with MINT-AQ and SWNT.**

In order to provide a full comparison between the MINT-AQ in 0.1M NaOH (Figure 4a), also in the following Figure S14 cyclic voltammetry of MINT-AQ and AQ@SWNT recorded in 0.1M Na_2SO_4 under air, N_2 and O_2 is compared.

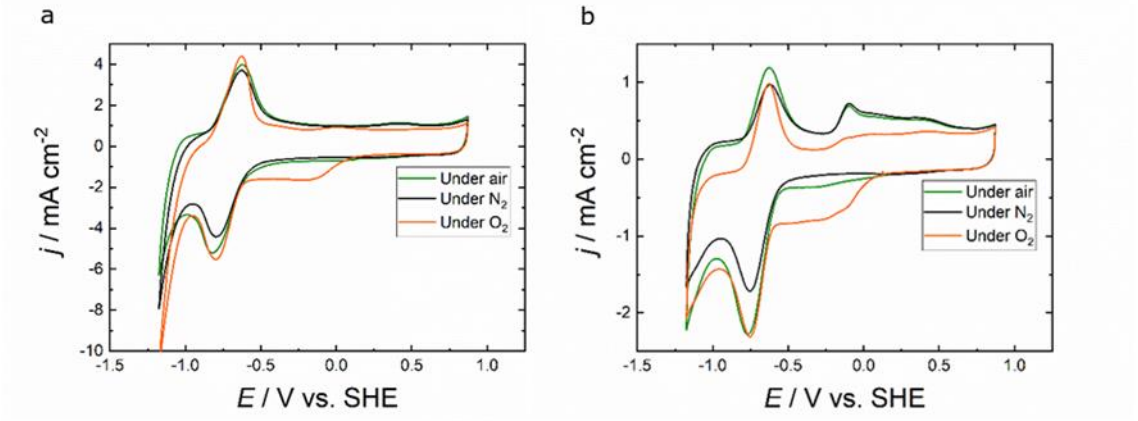

Figure S14. Cyclic voltammograms of **a**. MINT-AQ and **b.** AQ@SWNT recorded in 0.1 M Na_2SO_4 aqueous solution under air, N_2- and O_2-saturated conditions.

Like in the previous samples, upon O_2 present in the electrolyte solution, a reductive peak around 0.0 V vs. SHE was observed. Besides, in accordance to Figure 3b and Figure S12c, in case of AQ@SWNT at -0.15 V an oxidative feature appeared, which decreased in height upon O_2 addition.

Complementary to Figure 4a in the main text as well as Figure S14, the following Figure S15 shows a SWNT sample in 0.1M Na_2SO_4 under N_2 and O_2 as well as the chronoamperometry I/t curve of SWNT at -0.33 V for 8 h.

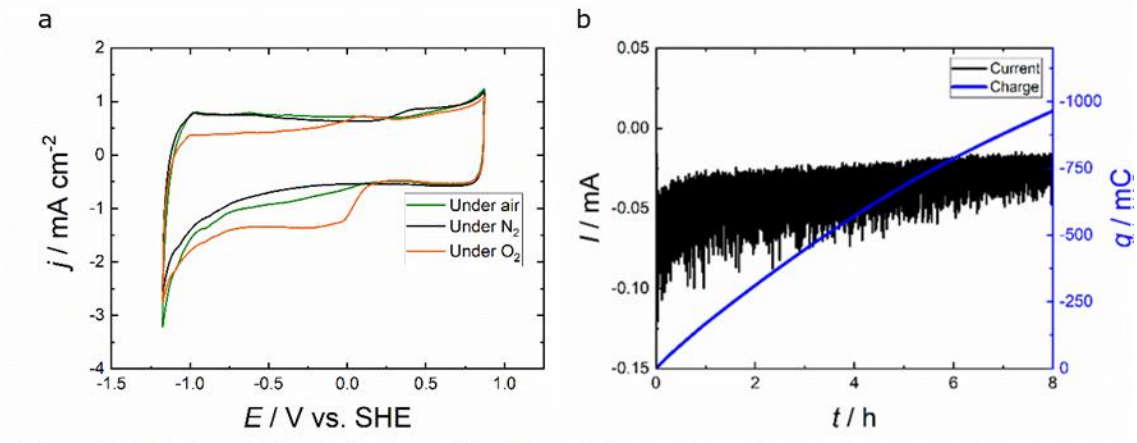

Figure S15. **a.** Cyclic voltammograms of SWNT in 0.1 M Na_2SO_4 aqueous solution under N_2 and O_2-saturated conditions. **b.** Chronoamperometry curve and cumulative charges of SWNT were recorded at -0.33 V in 0.1 M NaOH aqueous solution over 8-h electrolysis.

As can be seen from Figure S15a, also pristine SWNT show a reductive step upon O_2 addition, which is already a hint for oxygen reduction. The I/t curve shows a lower current compared to the MINT-AQ case in Figure 4 with just slight decrease over time.

In addition to the chronoamperogram of MINT-AQ in Figure 4b, in this following Figure S16 the chronoamperogram of AQ@SWNT under elsewise identical conditions is shown.

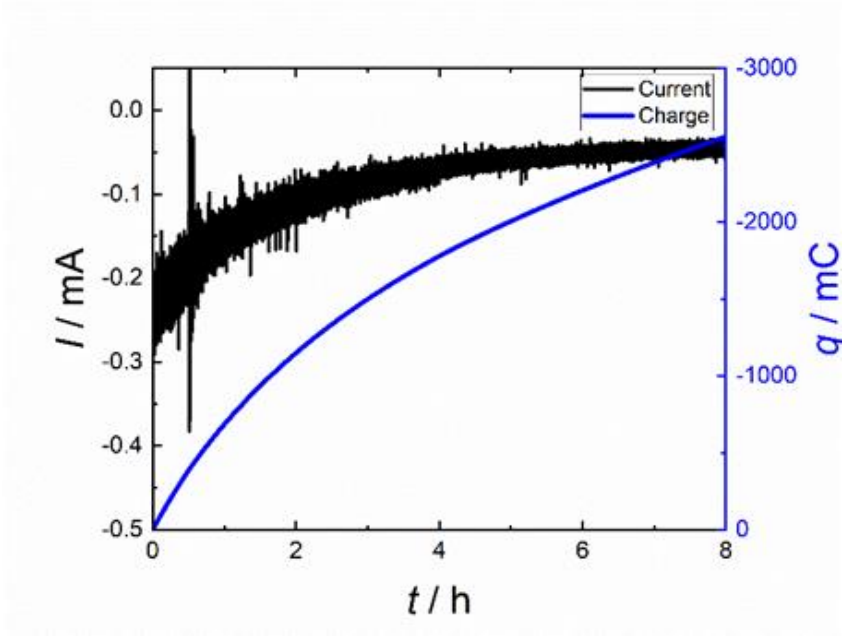

Figure S16. Chronoamperogram and accumulated charges of AQ@SWNT was measured by applying a constant potential of -0.33 V in 0.1 M NaOH solution over 8h.

In order to prove, that the MINT-AQ is stable on the electrode over the time of the electrolysis, in the following Figure S17, CV curves before and after were compared:

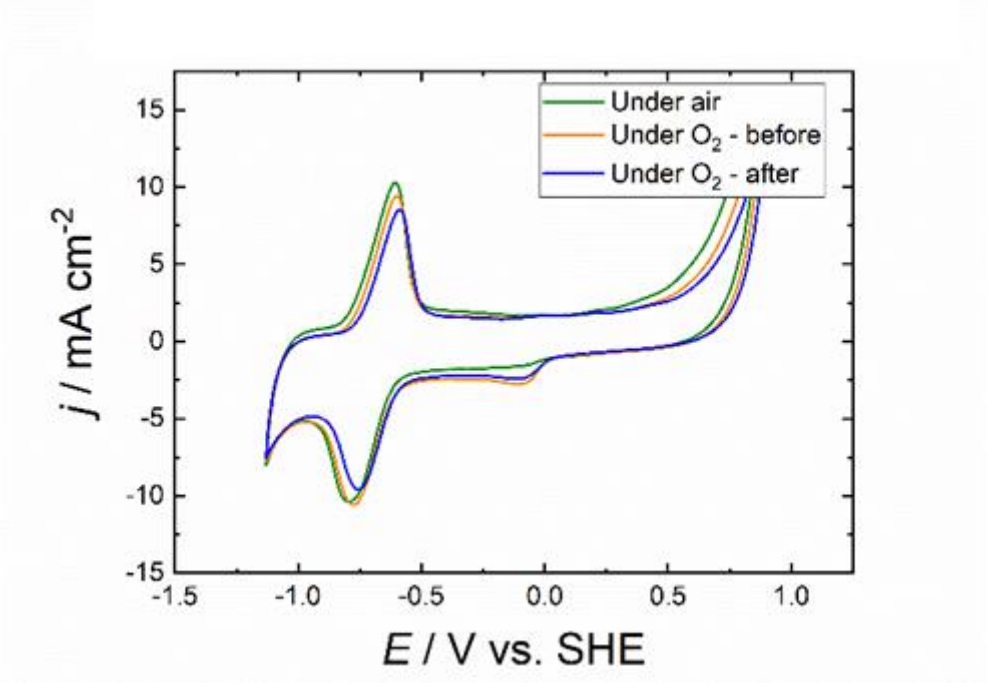

Figure S17. Cyclic voltammograms of MINT-AQ recorded in 0.1 M NaOH under air and O_2-saturated conditions before and after 8-h electrolysis.

From the CV in Figure S17 it can be stated, that the MINT-AQ is very stable under the conditions of electrolysis and shows just a slight decrease in j_P of 6.3 %.
All details on the kinetic parameters like the total moles of H_2O_2 produced, the rate and the Faradaic efficiency (FE) of oxygen reduction electrolysis at different conditions are displayed in the following Table S1:

Table S2. Electrocatalytic activities of SWNT, MINT-AQ and AQ@SWNT in 0.1 M Na_2SO_4 and 0.1 M NaOH for 8-h electrolysis at -330 mV vs. SHE at room temperature. 0.1 mg of the compound was drop-casted in each case.

SWNT

	In 0.1M Na_2SO_4			In 0.1M NaOH		
Time / h	$n_{(H2O2)}$[a] / µmol	H_2O_2 production rate[b] / μmol_{H2O2} mg^{-1} h^{-1}	FE[b] / %	$n_{(H2O2)}$[a] / µmol	H_2O_2 production rate[b] / μmol_{H2O2} mg^{-1} h^{-11}	FE[b] / %
Initial	0.94	n. d.	n. d.	0.16	n. d.	n. d.
1	0.85	n. d.	n. d.	0.29	1.28	14.7
2	0.80	n. d.	n. d.	0.60	3.19	43.0
4	1.09	1.46	17.4	1.09	2.42	36.0
6	1.35	1.33	19.9	1.97	4.39	78.6
8	1.41	0.26	4.7	2.37	2.02	43.7

MINT-AQ

	In 0.1M Na_2SO_4			In 0.1M NaOH		
Time / h	$n(H_2O_2)$[a] / µmol	H_2O_2 production rate[b] / μmol_{H2O2} mg^{-1} h^{-1}	FE[b] / %	$n(H_2O_2)$[a] / µmol	H_2O_2 production rate[b] / μmol_{H2O2} mg^{-1} h^{-11}	FE[b] / %
Initial	0.20	n. d.	n. d.	0.46	n. d.	n. d.
1	0.29	0.86	2.5	1.69	12.31	50.7
2	0.48	1.91	5.4	2.85	11.66	51.6
4	1.24	3.81	11.2	4.34	7.44	34.8
6	1.50	1.32	3.8	6.02	8.38	41.5
8	2.14	3.19	9.6	7.46	7.20	36.7

AQ@SWNT

	In 0.1M Na_2SO_4			In 0.1M NaOH		
Time / h	$n(H_2O_2)$[a] / µmol	H_2O_2 production rate[b] / μmol_{H2O2} mg^{-1} h^{-1}	FE[b] / %	$n(H_2O_2)$[a] / µmol	H_2O_2 production rate[b] / μmol_{H2O2} mg^{-1} h^{-11}	FE[b] / %
Initial	0.39	n. d.	n. d.	1.54	n. d.	n. d.
1	0.48	0.86	4.4	2.06	5.18	14.6
2	0.67	1.89	10.8	2.47	4.13	17.2
4	0.98	1.57	8.1	3.36	4.48	27.4
6	1.38	1.97	10.1	4.41	5.25	47.5
8	1.80	2.15	11.7	5.95	7.68	84.6

[a] Cumulative, absolute amount of H_2O_2 detected by spectrophotometer.

[b] Calculated per time interval

4.4.8. **RDE Experiments.**

Samples of SWNT, MINT-AQ and AQ@SWNT were drop-casted onto RDE electrodes with the same loading and tested under O_2 saturation in 0.1M NaOH solution. The rotation speed was varied between 100 and 3600 rpm. In order to show ORR, linear sweep voltammograms (LSV) of an intermediate and representative speed of 1200 rpm was chosen to compare the three samples in Figure 4c.

Comparing the current densities of the three samples revealed that MINT-AQ shows the highest catalytic current. Nevertheless, performing Koutecki-Levich-Analysis[159] using eq. 1 showed that assuming the geometric electrode surface area is significantly underestimating the real electrode surface area with the CNT structure.

$$\frac{1}{i} = \frac{1}{i_K} + \frac{1}{0.62\, n\, F\, A\, D^{2/3}\, \upsilon^{-1/6}\, c_0} \cdot \frac{1}{\omega^{1/2}} \tag{1}$$

Although the lack of the exact electrode area hinders further analysis of the slope in Koutecki-Levich-Plot, still the values of i_K correlate with the rate constant k, as shown in eq. 2:

$$i_K = n\, F\, A\, k_f(E) c_0 \tag{2}$$

As those values of i_K refer to the exchange current without any convection effects, it can still be regarded as value for comparing the three systems as they arrange on the electrode surface.

[159] Bard, A. J.; Faulkner, L. R., *Electrochem. Methods* **2001,** *2*, 482.

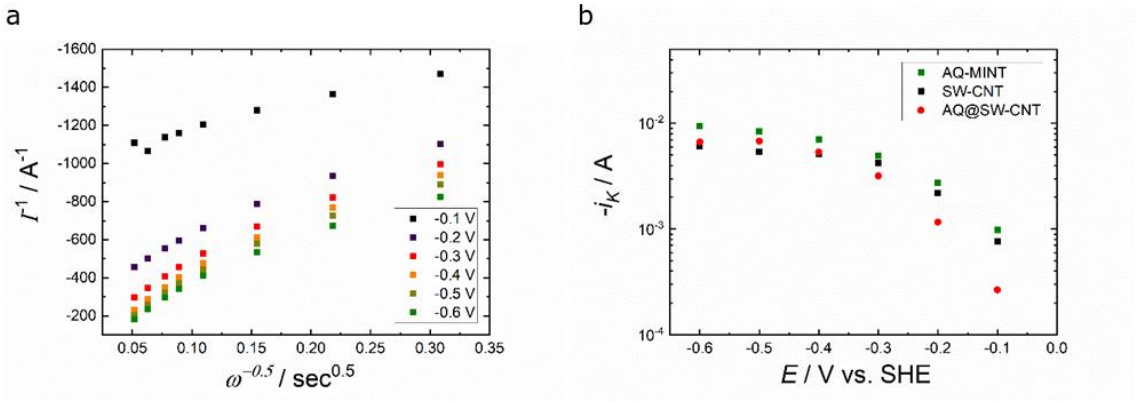

Figure S18. **a.** Koutecki-Levich plots of MINT-AQ in 0.1M NaOH at potentials between -0.1 and -0.6 V. **b.** i_K values of MINT-AQ, AQ@SWNT and SWNT determined from the intercept of the Koutecki-Levich plots depending on the potential applied.

As can be seen from Figure S18a, the Koutecki-Levich plots for MINT-AQ show a reasonable linear trend for those potentials applied. Plotting the i_K values of MINT-AQ, AQ@SWNT and SWNT from the Koutecki-Levich plots show that at more positive potentials AQ@SWNT and SWNT differ but come to quite close values at more negative potentials. In all potentials regarded, MINT-AQ shows the highest i_K which can be regarded as a hint for a higher electrocatalytic activity.

As a result, we propose that the different CNT samples with and without AQ modification arrange in a different way on the GC surface, which also affects the real, electroactive surface area.

5. Introduction. Chemistry of Thiol-ene "Click" Reaction on Materials

5.1. Introduction of "Click" Reaction.

The concept of "Click Reaction" was introduced by Sharpless and co-workers in 2001.[160] This concept refers to a group of reactions which have specific characteristics: a) stereospecific, b) orthogonality, c) simple reaction conditions, d) no or inoffensive subproducts, e) wide range of starting materials and f) tolerance for polar solvents, even water or sometimes even solventless. In summary, click reactions are robust, efficient and orthogonal tools in synthesis.[161] These reactions have been widely used in a range of fields, such as chemistry of materials, metal surfaces or organic synthesis.[161,162,163,164] In Figure 1 is possible to see some examples of click reactions.

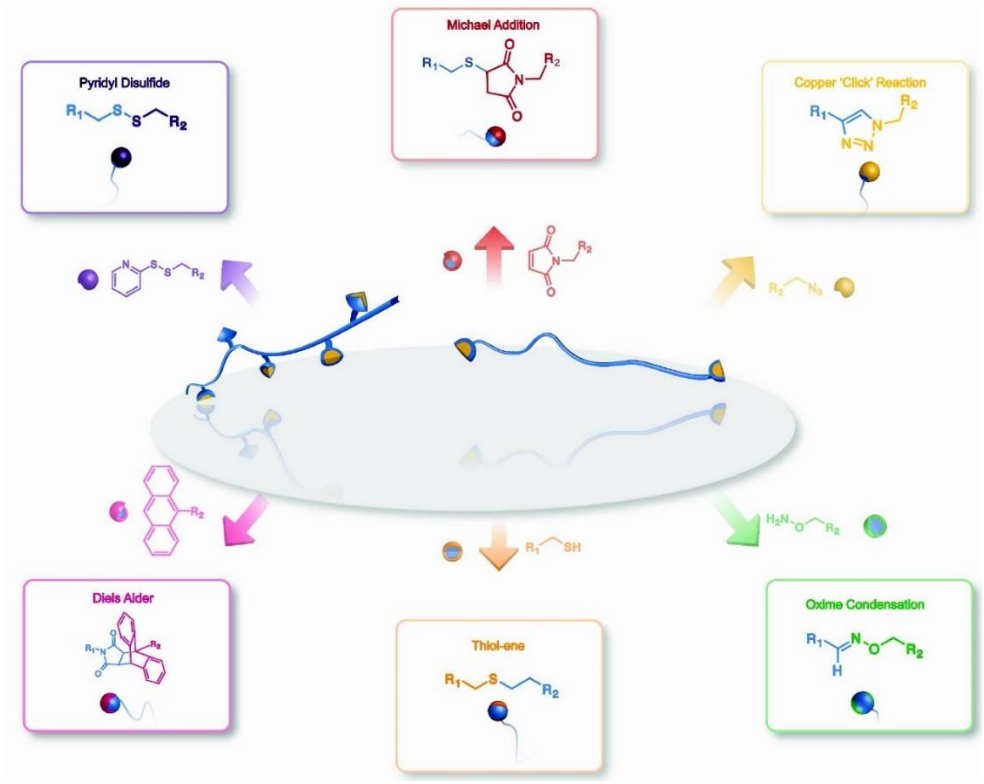

Figure 1. Different kinds of click reactions. Adapted with permission from *Chem. Rev.* **2009**, *109* (11), 5620-5686. Copyright (2009) American Chemical Society.

[160] Kolb, H. C.; Finn, M. G.; Sharpless, K. B., *Angew. Chem. Int. Ed.* **2001,** *40* (11), 2004-2021.
[161] Iha, R. K.; Wooley, K. L.; Nyström, A. M.; Burke, D. J.; Kade, M. J.; Hawker, C. J., *Chem. Rev.* **2009,** *109* (11), 5620-5686.
[162] Tunca, U., *Macromol. Chem. Phys.* **2018,** *219* (16), 1800163.
[163] Collman, J. P.; Devaraj, N. K.; Eberspacher, T. P. A.; Chidsey, C. E. D., *Langmuir* **2006,** *22* (6), 2457-2464.
[164] Xu, Z.; Bratlie, K. M., *ACS Biomater. Sci. Eng.* **2018,** *4* (7), 2276-2291.

The powerful click reaction become even more powerful when used in combination. For example, in the modification of Self-Assembled Monolayers (SAMs), Lamping *et al.*[165] functionalized a surface with different organic functional click groups via "microcontact chemistry" (Figure 2a). Microcontact chemistry consists in a functionalized ink deposited on a suitable substrate using a microstructured elastomer stamp, which delivers the ink exclusively in the area of contact between the stamp and substrate. This ink fixes with the SAM and using different inks and patterns, they obtained a SAM capable to functionalize in different ways. Then, with different click chemistry reactions, and thanks to their orthogonality, they functionalized selectively different patterns because each pattern reacts only with a specific functional group: azide-alkyne, thiol-olefin, amine- carboxylic acid and hydroxyimine –oxime.

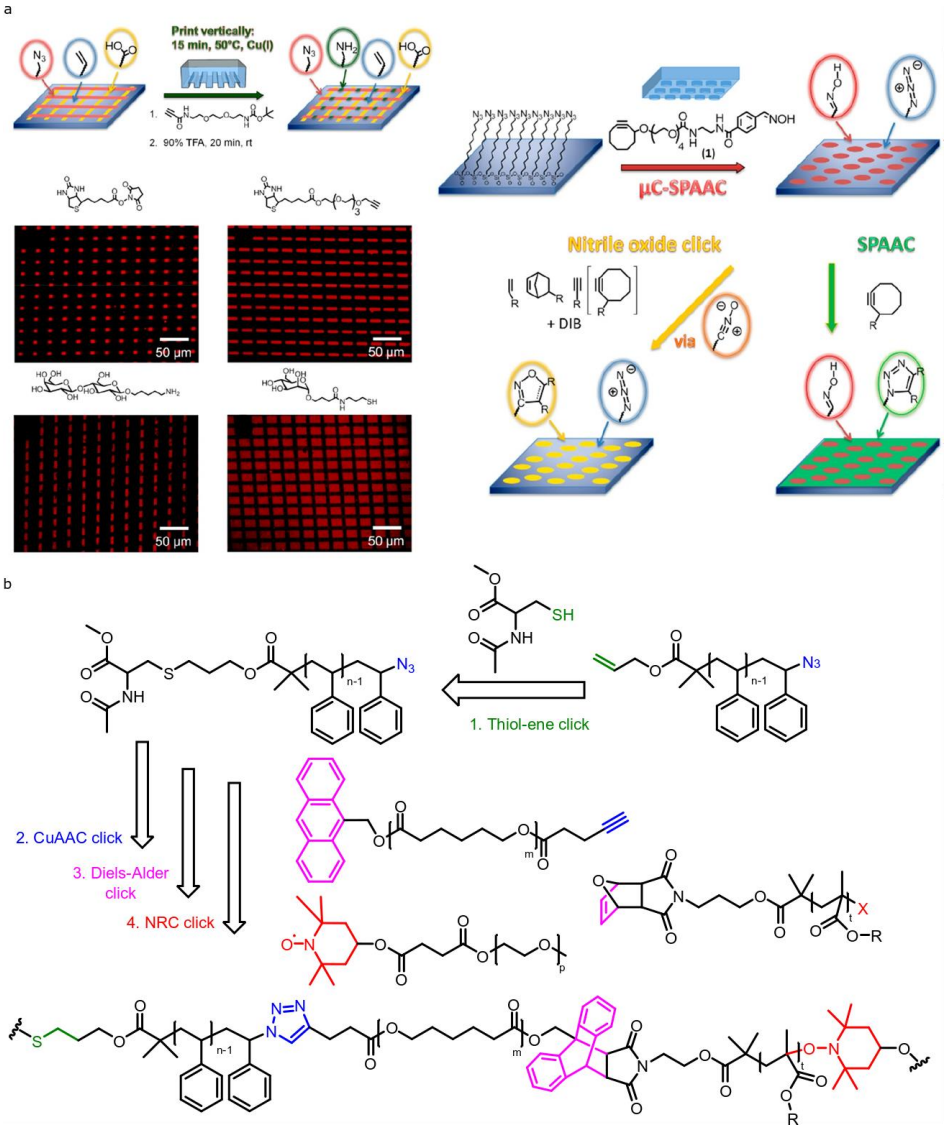

[165] Lamping, S.; Buten, C.; Ravoo, B. J., *Acc. Chem. Res.* **2019,** *52* (5), 1336-1346.

Figure 2. **a.** Different examples of modification of SAMs (left, tetrafunctional alkene/ azide/acid/amine SAM; right, difunctional azide/ nitrile oxide) through microcontact chemistry with different functionalized ink. Each pattern could be functionalized with different click reaction: CuAAC, thiol-ene and oxime condensation. Adapted with permission from *Acc. Chem. Res.* **2019,** *52* (5), 1336-1346. Copyright (2019) American Chemical Society. **b.** Synthesis of cysteine-terminated linear polystyrene through quadruple click reaction.

Another example of the power of combined click chemistry reaction was reported by Tunca and co-workers[166] in the synthesis of polymers. They synthesised a cysteine-terminated linear polystyrene through quadruple click reaction: thiol-ene reaction, CuAAC click, Diels-Alder click and nitro radical coupling click (Figure 2b).

Among all of click reactions, we will focus on thiol-ene reaction (thiol-double bond) and thiol-Michael Addition (thiol and carbonyl α,β-unsaturated), in both cases yielding C-S bond. This chemistry[167,168,169,170] is widely found within in polymer chemistry,[171] organic synthesis[172] and materials, such as hydrogels[164] or photolithographic patterning of a substrate.[173]

5.2. **Thiol-ene "Click" Reaction.**

Since the introduction of the click reaction concept, these reactions have been more developed and studied. One of the most used and important click reactions has been the thiol-ene reaction. This reaction consists in a coupling between a thiol and an olefin to form alkyl sulphide. Thiols are soft nucleophiles characterized by a weak sulfur-hydrogen bond which promotes easy deprotonation of the thiol. The breaking of the sulfur-hydrogen bond can be done through two pathways. These are free radical and base catalysed methods:

[166] Candan, O. A.; Durmaz, H.; Hizal, G.; Tunca, U., *J. Polym. Sci. Polym. Chem.* **2012,** *50* (14), 2863-2870.
[167] Hoyle, C. E.; Bowman, C. N., *Angew. Chem. Int. Ed.* **2010,** *49* (9), 1540-1573.
[168] Nair, D. P.; Podgórski, M.; Chatani, S.; Gong, T.; Xi, W.; Fenoli, C. R.; Bowman, C. N., *Chem. Mater.* **2014,** *26* (1), 724-744.
[169] Lowe, A. B., *Polym. Chem.* **2014,** *5* (17), 4820-4870.
[170] Mather, B. D.; Viswanathan, K.; Miller, K. M.; Long, T. E., *Prog. Polym. Sci.* **2006,** *31* (5), 487-531.
[171] Hoyle, C. E.; Lowe, A. B.; Bowman, C. N., *Chem. Soc. Rev.* **2010,** *39* (4), 1355-1387.
[172] Sinha, A. K.; Equbal, D., *Asian J. Org. Chem.* **2019,** *8* (1), 32-47.
[173] Jonkheijm, P. *et al*., *Angew. Chem.* **2008,** *120* (23), 4493-4496.

a) *Free radical*. In this case, the sulfur-hydrogen bond breaks homolytically, generating **S·** radicals. As a radical method, it is sensitive to oxygen.

The mechanism (Scheme 1) proceeds through the three steps of a radical reaction: initiation, propagation and termination. In the initiation step, a catalyst or photo-initiator generates a thiyl radical. This radical goes to propagation step which involves the addition to an olefin group. This addition generates a second radical which takes a proton from the initial thiol in order to obtain the product. This process generates again the thiyl radical which is the responsible to start again the cycle.

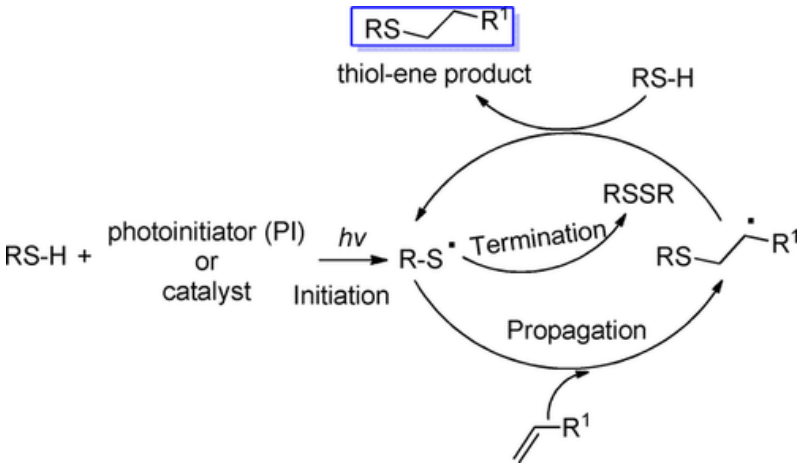

Scheme 1. Radical mechanism for thiol-ene reaction.

According to the reactivity of the thiol molecule, there are four basic groups of thiol groups: alkyl thiols, thiolpropionate thiols, thiolglycolate (thiolacetate) thiols and aromatic thiols. In the free radical method, the reactivity decreases as the pKa increases (Figure 3).

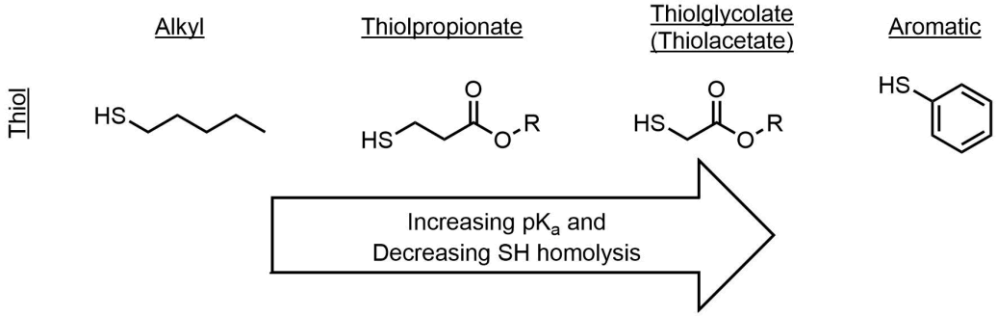

Figure 3. Reactivity of different thiols in the free radical mechanism.

An example of thiol-ene reaction through free radical mechanism in chemistry of materials was reported by Taubert and co-workers.[174] They performed a heterogeneous thiol-ene click photoaddition reaction using mesoporous silica gel functionalized with vinyl groups without photo-initiator. The functionalized mesoporous silica was synthesised previously through a sol-gel hydrolysis-polycondensation reaction from tetramethyl orthosilicate, vinyltriethoxysilane and trimethoxysilane respectively.

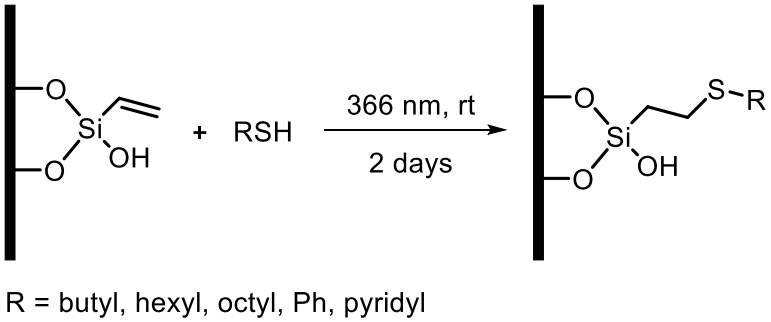

R = butyl, hexyl, octyl, Ph, pyridyl

Figure 4. Surface modification of mesoporous silica monoliths through thiol-ene chemistry.

b) *Base catalysed* method. The sulfur-hydrogen bond breaks using a base, normally tertiary amine, to obtain the thiolate anion (**S-**).

The base (in this case triethylamine, Et_3N) takes a proton from a thiol molecule generating thiolate anion. This thiolate attacks the double bond creating an intermediate specie which takes a proton from a new thiol molecule in order to obtain the product. This process generates again the thiolate anion which is the responsible to start again the cycle.

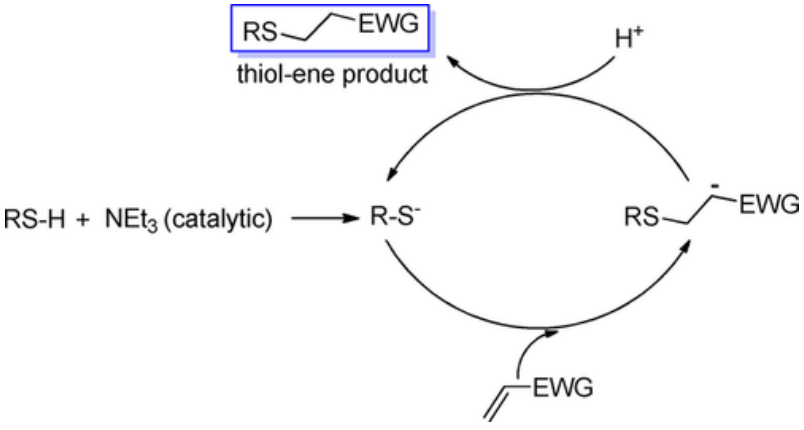

Scheme 2. Base catalysed mechanistic pathway for thiol-ene reaction.

[174] Göbel, R.; Hesemann, P.; Friedrich, A.; Rothe, R.; Schlaad, H.; Taubert, A., *Chem. Eur. J.* **2014,** *20* (52), 17579-17589.

In this kind of catalysis, the reactivity increases with the nucleophilicity of the thiolate. (Figure 5) favouring the attack to electron poor enes.

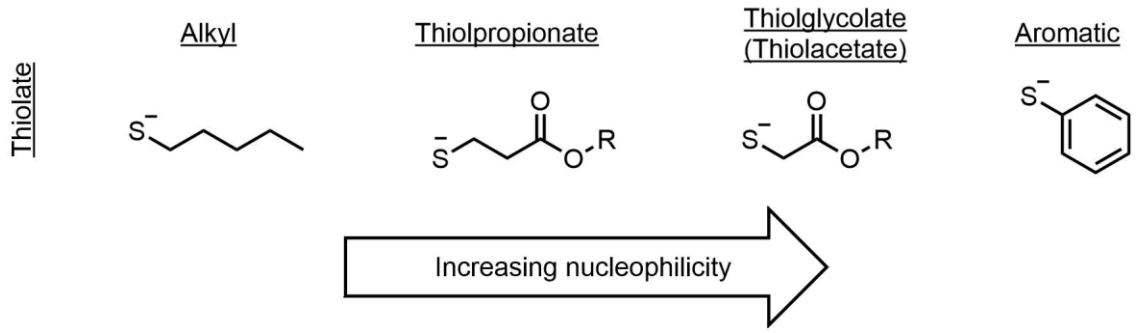

Figure 5. Reactivity of the thiolate molecule in the based-catalysed method.

An interesting example of comparison between the radical and the base catalysed methods was published in 2013 by Stolz *et al.*[175] They studied the regioselectivity of the thiol-ene reaction of *N*-allyl maleimide between free radical method and base catalysed method, specifically in the thiol-Michael Addition.

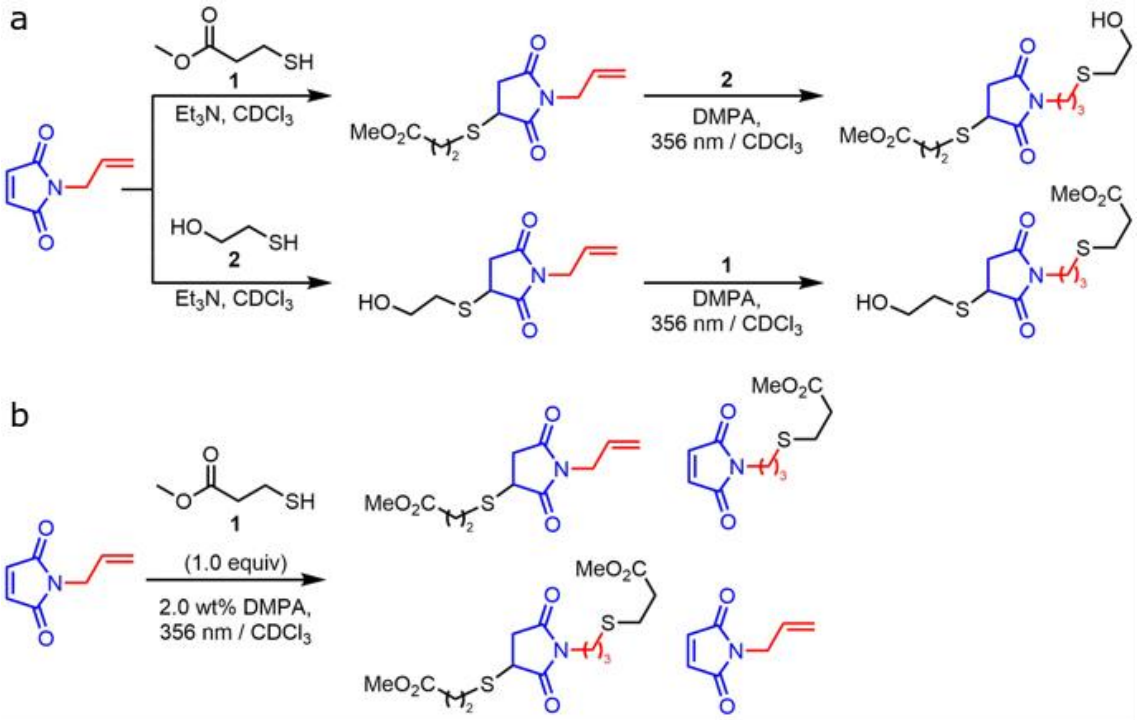

Figure 6. **a.** Regioselectivity of thiol-ene reaction. First step is via base catalysed thiol-Michael Addition with **1** and **2**. The second step by free radical method. **b.** Competitive

[175] Stolz, R. M.; Northrop, B. H., *J. Org. Chem.* **2013,** *78* (16), 8105-8116.

between allyl and maleimide double bonds through free radical method. *DMPA: 2,2-dimethoxy-2-phenylacetophenone. Adapted with permission from *J. Org. Chem.* **2013**, *78* (16), 8105-8116. Copyright (2013) American Chemical Society.

In the based catalysed conditions (thiol-Michael Addition), the regioselectivity remains obtaining succinimide adducts as only product. (Figure 6a). However, if free radical conditions are used, the authors obtained a complex mixture of products (Figure 6b) without total conversion (with 1.0 equiv. of **1**). The authors supported these experimental results with computational studies. There are significant differences in the energetics of thiolate (CH_3S^-) addition to the maleimide versus allyl underlie their absolute selectivity in thiol-Michael reactions. The energetics of thiyl ($CH_3S^{\bullet}$) addition to the maleimide versus allyl are much more similar and, therefore, competitive.

5.2.1. **Thiol-Michael Addition.**

As we have mentioned in the last section, there is a great affinity between thiols and maleimides through thiol-Michael Addition.[168] In the last years it is common to use another kind of bases in this kind of reaction, more nucleophilic, such as primary and secondary amines and alkyl phosphines.[168] With this nucleophilic character, the mechanism must change due to the decreasing of basic character[176] (Figure 7c).

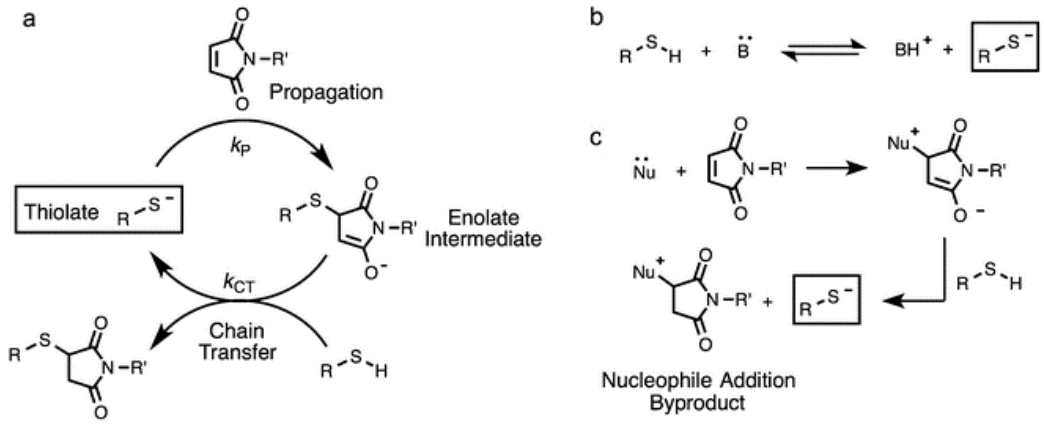

Figure 7. **a**. Mechanism for base catalysed thiol-ene Michael Addition reaction of thiols to an *N*-substituted malemides. **b**. Acid-base equilibrium between base and thiol-thiolate anion. **c**. Mechanism for nucleophile catalysed.

[176] Northrop, B. H.; Frayne, S. H.; Choudhary, U., *Polym. Chem.* **2015,** *6* (18), 3415-3430.

The nucleophile (primary, secondary amines or alkyl phosphines) attacks to π-bond of maleimide to give a zwitterionic enolate intermediate. This enolate deprotonates the thiol to give a thiolate anion, which performed the same catalytic pathway as when initiated by a base. It is important to note that this pathway results in the formation of inconsequential amount of nucleophile addition byproduct. However, as most nucleophile-initiated agent reacts rapidly to the thiol-Michael Addition product even of < 1% of molecule.

The high affinity between thiol-maleimide leads to do multiple studies of the reaction: type of thiol based on pKa, solvent, base/nucleophile and different kinds of electron poor enes.[168,176]

5.2.2. **Maleimide as a Soft Electrophile.**

The popularity of maleimide chemistry has been growing over the years due to his applicability in different field such chemistry of materials, bioorganic and organic synthesis.[177,178] This can be attributed to the great characteristics of this molecule, for instance the unique reactivity. Besides of thiol-ene reaction, it is well known Diels-Alder "click" between maleimides and aromatic rings, such as furan. Moreover, this Diels-Alder "click" can be used as protecting group of double bond maleimide because this reaction is reversible,[179] just by heating. This flexibility has become an important strategy to the elaboration of novel macromolecular materials.[180] These two orthogonal reaction confer variety of applications, for instance, hydrogels[181] or bioconjugation.[182] Another characteristic is the great stability towards air, water and heat, ideal for bioconjugation, materials and organic synthesis. Finally, another characteristic is the large number of commercially available maleimides and easy, low-cost and scalable synthesis of maleimide derivatives. There are some examples in Figure 8.

[177] Oz, Y.; Sanyal, A., *Chem. Rec.* **2018,** *18* (6), 570-586.
[178] Ravasco, J. M. J. M.; Faustino, H.; Trindade, A.; Gois, P. M. P., *Chem. Eur. J.* **2019,** *25* (1), 43-59.
[179] Sanyal, A., *Macromol. Chem. Phys.* **2010,** *211* (13), 1417-1425.
[180] Gandini, A.; Carvalho, A. J. F.; Trovatti, E.; Kramer, R. K.; Lacerda, T. M., *Eur. J. Lipid Sci. Technol.* **2018,** *120* (1), 1700091.
[181] Koehler, K. C.; Anseth, K. S.; Bowman, C. N., *Biomacromolecules* **2013,** *14* (2), 538-547.
[182] Renault, K.; Fredy, J. W.; Renard, P.-Y.; Sabot, C., *Bioconjugate Chem.* **2018,** *29* (8), 2497-2513.

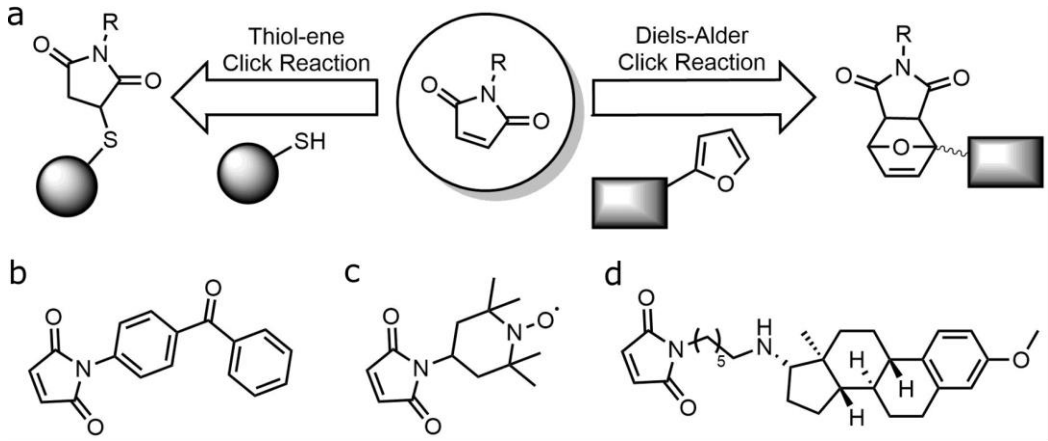

Figure 8. **a.** Maleimide functional group: An ideal “click” substrate. Maleimide *N*-functionaliased with **b.** photoactive group, benzophenone, **c.** spin labels, (2,2,6,6-tetramethylpiperidin-1-yl)oxyl (TEMPO) and **d.** pharmacological inhibitor, U-73122, an inhibitor of phospholipase C-dependent processes.

In the following figure there are multiple examples of using maleimide group. This figure shows the great versatility of its chemistry.

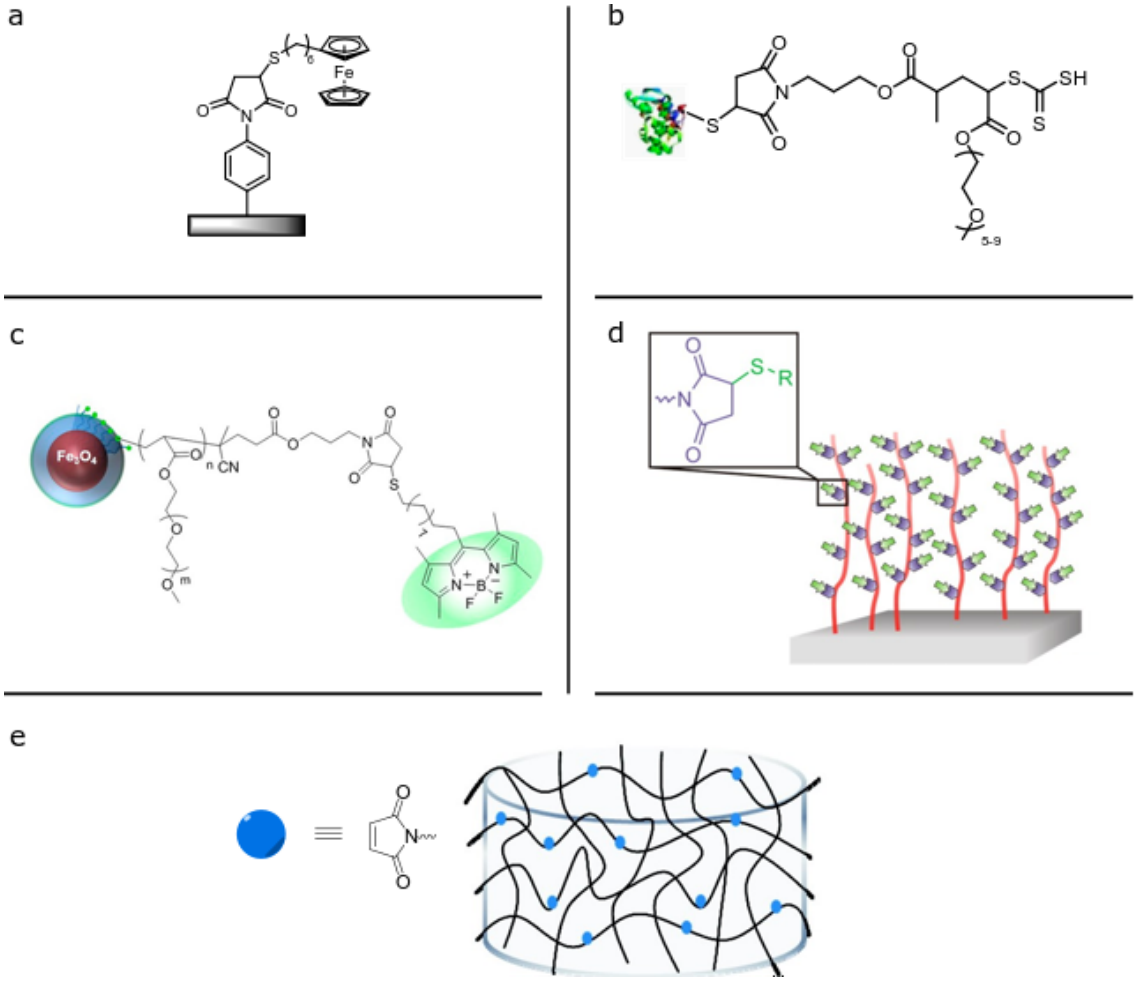

Figure 9. Maleimide containing in different fields as **a.** gold/carbon surfaces for electrochemistry[183] (adapted with permission from *Langmuir*. **2008**, *24* (5), 2206-2211. Copyright (2008) American Chemical Society), **b.** bioorganic with T4L protein[184] (adapted with permission from *Biomacromolecules*. **2009**, *10* (7), 1777-1781. Copyright (2009) American Chemical Society), **c.** nanoparticles coating[185] (adapted with permission from *ACS Appl. Mater. Interfaces.* **2016**, *8* (30), 19813-19826. Copyright (2016) American Chemical Society), **d.** planar surface coating[186] (adapted with permission from *Macromolecules* **2014**, *47* (22), 7842-7851. Copyright (2014) American Chemical

[183] Harper, J. C.; Polsky, R.; Wheeler, D. R.; Brozik, S. M., *Langmuir* **2008,** *24* (5), 2206-2211.
[184] Bays, E.; Tao, L.; Chang, C.-W.; Maynard, H. D., *Biomacromolecules* **2009,** *10* (7), 1777-1781.
[185] Oz, Y.; Arslan, M.; Gevrek, T. N.; Sanyal, R.; Sanyal, A., *ACS Appl. Mater. Interfaces.* **2016,** *8* (30), 19813-19826.
[186] Gevrek, T. N.; Bilgic, T.; Klok, H.-A.; Sanyal, A., *Macromolecules* **2014,** *47* (22), 7842-7851.

Society) and **e.** hydrogels[187] (adapted with permission from *Macromolecules* **2010**, *43* (9), 4140-4148. Copyright (2010) American Chemical Society).

5.2.3. **Thiol-ene "Click" Reaction on Materials.**

i) Low-dimensional materials.

Related to 0D materials, Zhu *et al*.[188] reported the synthesis of gold nanoparticles (AuNP) with maleimides (Figure 10a). First, they functionalized the AuNP with thiol-glycol-protected maleimide. Followed deprotection of maleimide, they attached thiol-rhodamine with the maleimide through thiol-Michael Addition. This functionalization with thiol-glycols improves the solubility in water. In addition, the post-functionalization of maleimide with different thiols (rhodamine or cysteine) are a promising template for biological applications.

[187] Kosif, I.; Park, E.-J.; Sanyal, R.; Sanyal, A., *Macromolecules* **2010,** *43* (9), 4140-4148.

[188] Zhu, J.; Waengler, C.; Lennox, R. B.; Schirrmacher, R., *Langmuir* **2012,** *28* (13), 5508-5512.

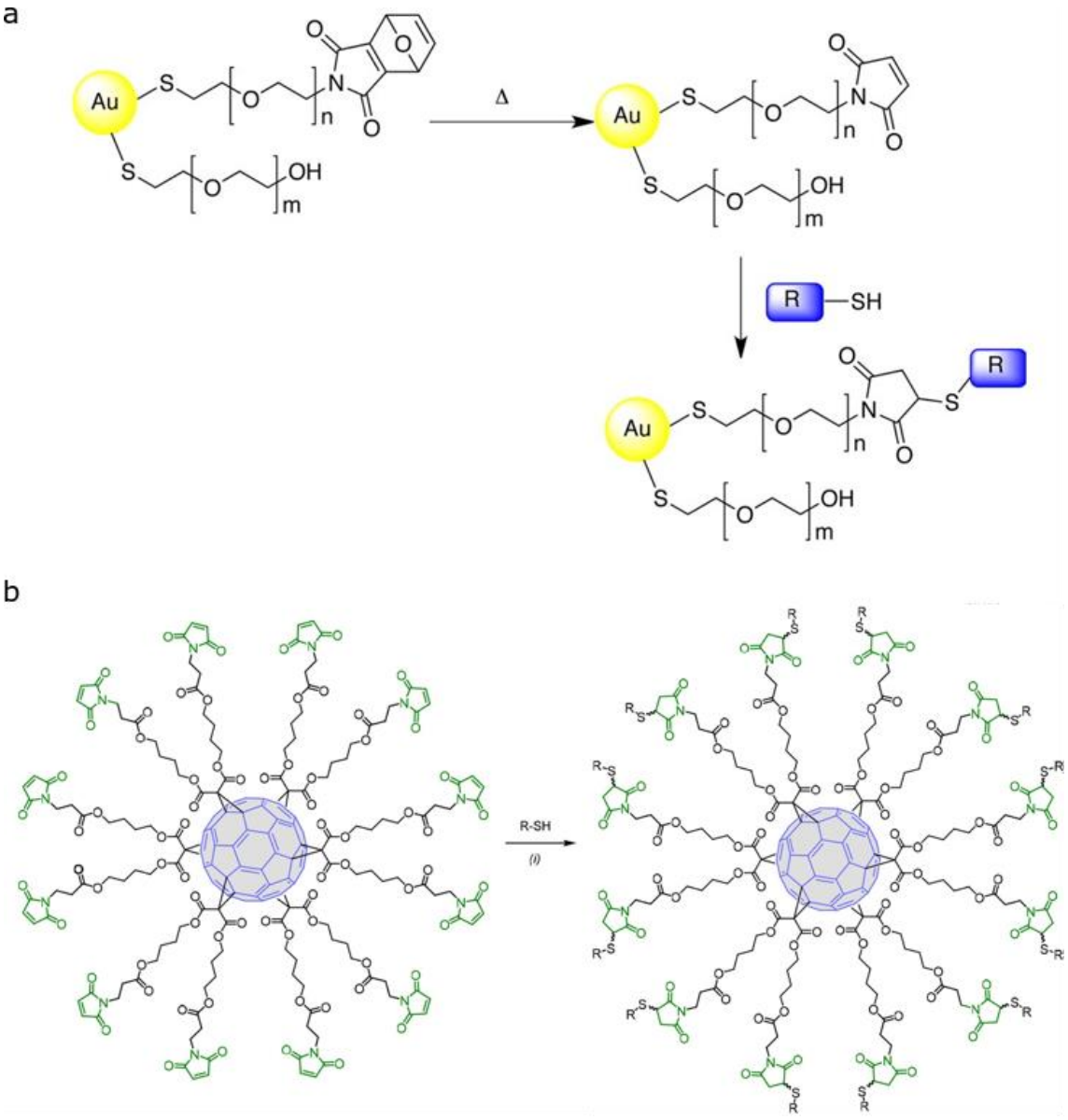

Figure 10. **a.** Functionalization of AuNP with thiols glycol-maleimide. Adapted with permission from *Langmuir* **2012,** *28* (13), 5508-5512. Copyright (2012) American Chemical Society. **b.** Symmetric hexakisadduct [60]fullerene maleimide derivatives and the thiol-Michale Addition reaction (R: PEG-thiol, alkyl thiol or cysteine methyl ester). (i): DMF, rt, 30 min. Adapted with permission from *J. Org. Chem.* **2018,** *83* (4), 1727-1736. Copyright (2018) American Chemical Society.

Another example of 0D material is the fullerene. Martín and co-workers[189] reported the synthesis of systems based on hexakisadducts of [60]fullerene through biocompatible click reactions: thiol-ene and copper-free click reactions. First, they synthesized the symmetric maleimide derivative (Figure 10b) and the post-functionalization was performed through thiol-Michael Addition. In this publication, they also synthesized an asymmetric hexakisadduct with a maleimide unit and ten cyclooctyne units in order to achieve the orthogonal click reactions. This kind of derivative could be of interest for several biological applications due to maleimide and cyclooctyne (copper-free) functional groups and these biocompatible orthogonal reactions.

Regarding examples with 1D materials, such as carbon nanotubes, there are multiple ways to functionalize them with thiol-ene reaction. For instance, the most common examples in literature are through via free radical (from thiol o disulfur bond) yielding covalent bonds S-C in the CNT.[190,191,192] On the other hand, there are examples where this methodology is not used. Gobbo *et al*.[193] performed the functionalization of thiol-modified carbon nanotubes with maleimide-AuNP through base catalysed (thiol-Michael Addition). (Figure 11a). First, they functionalized covalently CNTs through oxidation (o-CNTs) and amidation, with cysteamine, of the carboxylic acid generated from the oxidation. Then, they connected through thiol-Michael Addition CNT and AuNP.

More recently, Nagai *et al.*[194] reported a smart non-covalent functionalization of SWNT with biocompatible and stable gel layer hybrid containing maleimide groups, which can react with thiol compounds through thiol- Michael Addition. They functionalized these maleimides groups with fluorescent thiols molecules (Figure 11b). They take advantage of stability of the gel layer, such is important for in vivo biological applications. This strategy offers the possibility to target active cancer cells without losing the unique optical properties of SWNTs

[189] Ramos-Soriano, J.; *et. al. J. Org. Chem.* **2018,** *83* (4), 1727-1736.
[190] Mao, J.; Wang, Y.; Zhu, J.; Yu, J.; Hu, Z., *Appl. Surf. Sci.* **2018,** *447*, 235-243.
[191] Zabihi, O.; Ahmadi, M.; Akhlaghi bagherjeri, M.; Naebe, M., *RSC Adv.* **2015,** *5* (119), 98692-98699.
[192] Duan, Q.; Wang, Y.; Chen, S.; Miao, M.; Chen, S.; Zhang, D., *Appl. Surf. Sci.* **2019,** *486*, 144-152.
[193] Gobbo, P.; Biesinger, M. C.; Workentin, M. S., *Chem. Commun.* **2013,** *49* (27), 2831-2833.
[194] Nagai, Y.; Tsutsumi, Y.; Nakashima, N.; Fujigaya, T., *J. Am. Chem. Soc.* **2018,** *140* (27), 8544-8550.

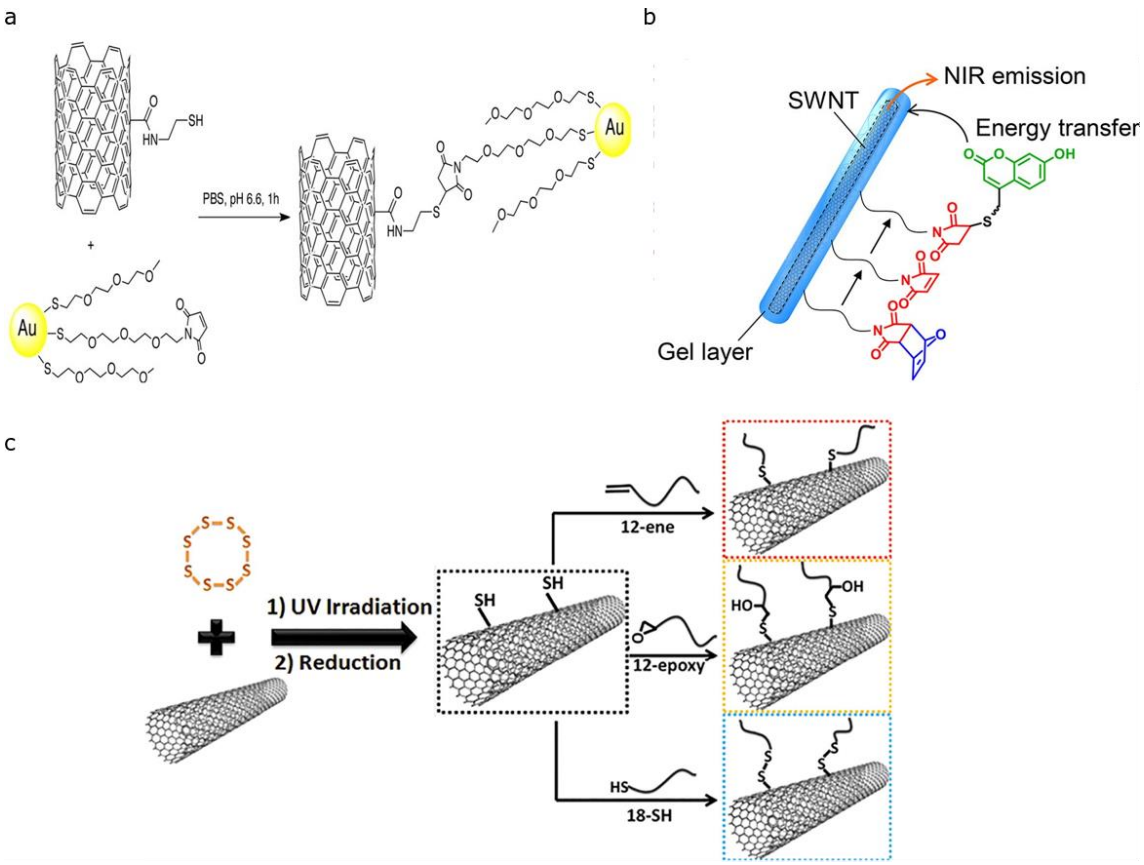

Figure 11. **a.** Covalent Functionalization of CNTs with maleimide-AuNP through thiol-Michael Addition with maleimide. **b.** Scheme of non-covalent functionalization of SWNTs with gel layer containing maleimides groups and post-functionalization with fluorescent dyes. Adapted with permission from *J. Am. Chem. Soc.* **2018,** *140* (27), 8544-8550. Copyright (2018) American Chemical Society. **c.** Scheme of functionalization of CNTs through thiol-ene click reaction.[190]

Finally, to the best of our knowledge, graphene is the only 2D material modified with thiol-ene reactions. The same as CNTs, the most commun method to functionalize graphene with thiol is by thiol-ene via free radical.[195,196] Seppala and co-workers[197] made thiol-ene click reaction between cysteamine hydrochloride and graphene oxide (GO) via free radical mechanism using AIBN as initiator (Figure 12a). On the other hand, another pathway was reported by Sanyal and co-workers[198] through non-covalent interaction

[195] Li, Y.; Bao, L.; Zhou, Q.; Ou, E.; Xu, W., *ChemistrySelect* **2017,** *2* (29), 9284-9290.
[196] Castelaín, M.; Martínez, G.; Marco, C.; Ellis, G.; Salavagione, H. J., *Macromolecules* **2013,** *46* (22), 8980-8987.
[197] Luong, N. D.; Sinh, L. H.; Johansson, L.-S.; Campell, J.; Seppälä, J., *Chem. Eur. J.* **2015,** *21* (8), 3183-3186.
[198] Oz, Y.; Barras, A.; Sanyal, R.; Boukherroub, R.; Szunerits, S.; Sanyal, A., *ACS Appl. Mater. Interfaces.* **2017,** *9* (39), 34194-34203.

between reduced graphene oxide (rGO) and maleimide-cointaining dopamine (dopa-MAL). Dopamine acts as anchor between the maleimide and rGO through hydrophobic interactions. Then, they used the thiol-maleimide chemistry which allows the facile attachment of thiol molecules via thiol-Michael Addition. They used different thiol compounds such as thiol ferrocene derivative, glutathione or cancer cell targeting cyclic peptide, c(RGDfC) (Figure 12b).

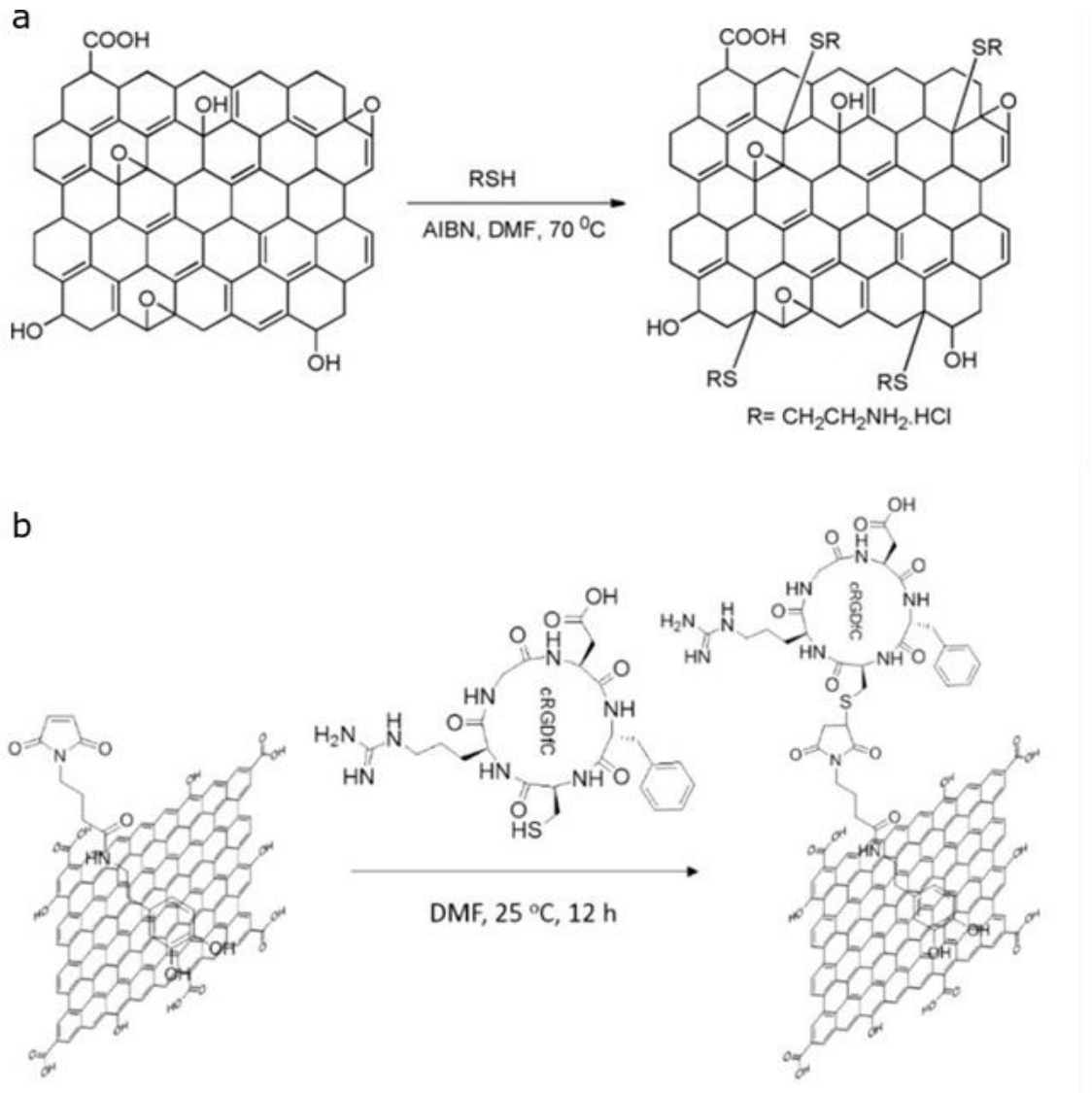

Figure 12. a. AIBN initiator of the thiol-ene click reaction for chemical modification of GO. The modified GO showed an improvement of physical properties such as dispersability. **b.** Synthesis of rGO/dopa-MAL-c(RGDfC) through thiol-ene click reaction. Adapted with permission from *ACS. Appl. Mater. Interfaces* **2017,** *9* (39), 34194-34203. Copyright (2017) American Chemical Society.

ii) Surface modification.

Yang *et al.*[199] reported the modification and functionalization of stainless steel surface. The first step is the coating of the surface with dopamine through alcohol groups. Then, the branching was performed with the attack of the amine from the dopamine to polyethyleneimine (BPEI) (Figure 13a). Finally, the poliethyleneamine layer (SS-BPEI) was functionalized with ethylene sulphide (ES) obtaining the thiol-surface modification (Figure 13a). These mercapto groups on the surface were modified with three different thiol-ene chemistries (Figure 13b): 1) with allyl derivative through thiol-ene click reaction via free radical; 2) with epoxy derivative with SN_2 ring-opening reaction and 3) acrylate derivative through thiol-Michael Addition.

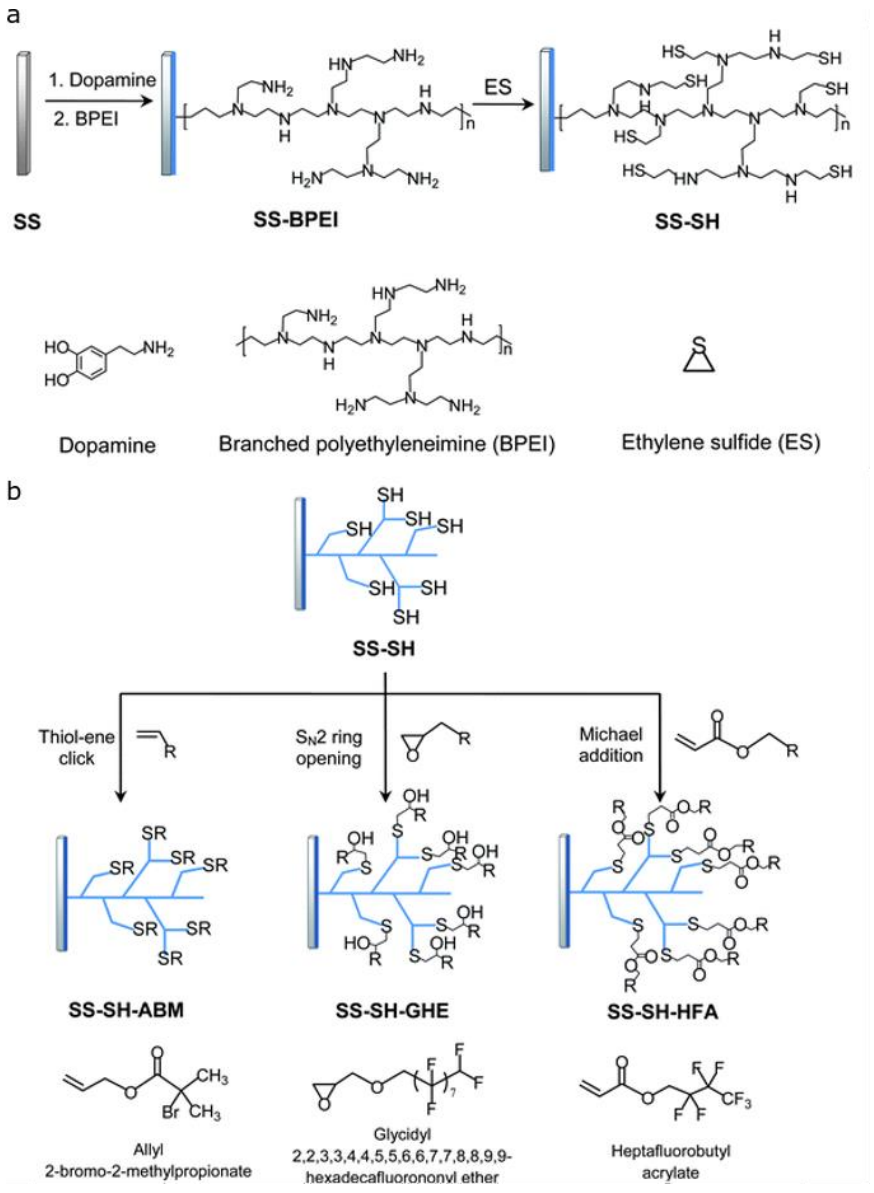

[199] Yang, W. J.; Neoh, K.-G.; Kang, E.-T.; Lay-Ming Teo, S.; Rittschof, D., *Polym. Chem.* **2013,** *4* (10), 3105-3115.

Figure 13. **a.** Surface modification of stainless steel towards obtaining post-functionalized surface with thiol. **b.** Different of thiol-ene click reaction according to the mechanism.

Another example is the construction of self-assembled monolayers (SAMs) on gold surfaces using different kinds of thiol. The general method to make SAMs involves immersing gold-coated surfaces into thiols. Mrksich and co-workers[200] reported maleimide-SAMs on gold surfaces and immobilised ligands which participate in biospecific interactions with proteins and enzymes. They immersed the gold surface into a mixture containing disulphides, one presenting a terminal maleimide group and the other presenting oligo(ethylene glycol) groups. Then, taking advantage of thiol-ene click reaction, they functionalize the maleimide with different thiols for instance peptides and thiol-mannose. The polyethylene glycol chains prevents the nonspecific adsorption of biological compounds such as proteins.

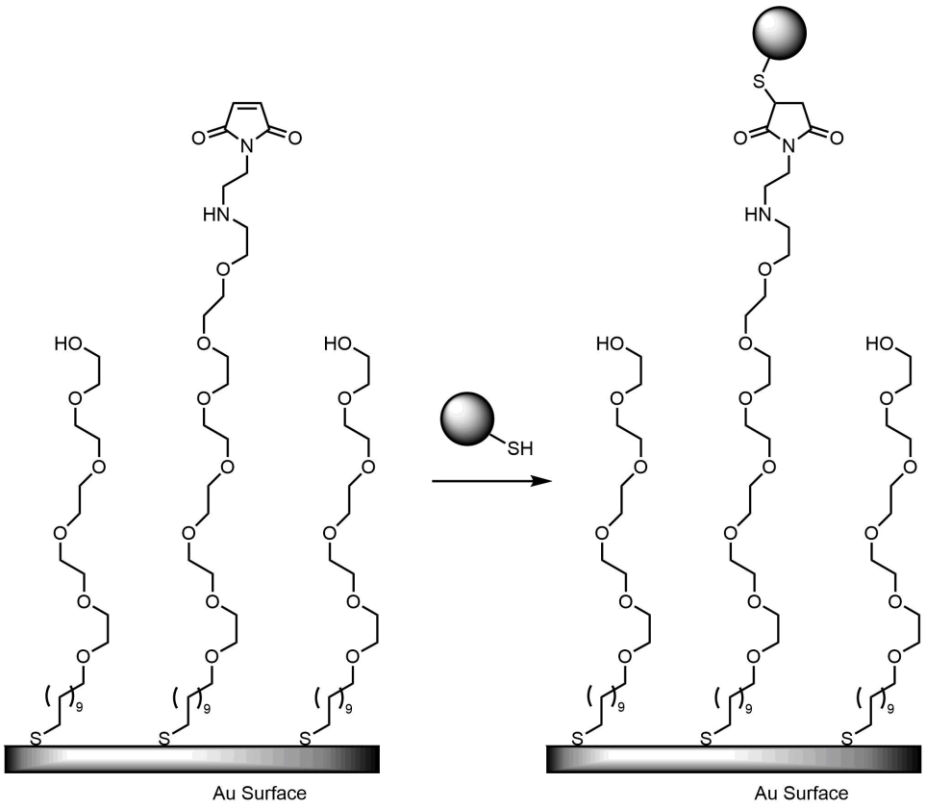

Figure 14. Coating of surface with different thiol molecules and post-functionalization via thiol-Michael Addition to maleimides. This method is useful for preparing substrates

[200] Houseman, B. T.; Gawalt, E. S.; Mrksich, M., *Langmuir* **2003,** *19* (5), 1522-1531.

for a wide range of application in basic science and biotechnology. Adapted with permission from *Langmuir* **2003,** *19* (5), 1522-1531. Copyright (2003) American Chemical Society.

6. Introduction. Transition Metal Dichalcogenides (TMDCs)

6.1. **Introduction of Layered Materials.**

Since the discovering of graphene[201] and its electronic properties, other 2D materials have garnered great interest.[202]

Layered materials are defined as solids with strong in-plane chemical bonds but weak out-of-plane, van der Waals interactions. There are many types of layered materials, which can be grouped into diverse families: hexagonal planar of graphene and boron nitride (h-BN). Transition Metal Dichalcogenides[203,204] (TMDCs; MX_2, for instance MoS_2 and WSe_2), metal halides (PbI_2), layered oxides (MnO_2) and non-planar hexagonal phosphorus, Black Phosphorus (BP) (Scheme 3).[205] One of the advantages of this materials is the abundance of some of them. For instance, graphite and MoS_2 are very abundant and easy to obtain.

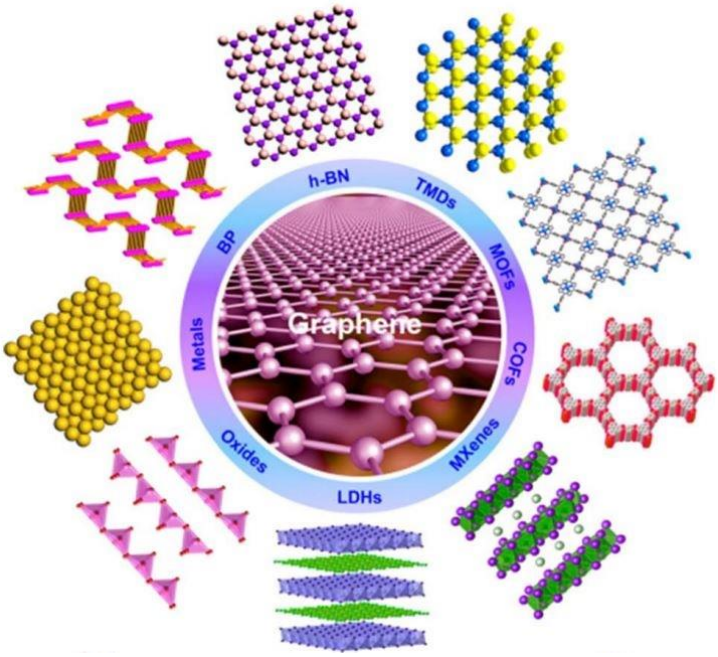

Scheme 3. Schematic of 2D layered materials.

[201] Novoselov, K. S.; Geim, A. K.; Morozov, S. V.; Jiang, D.; Zhang, Y.; Dubonos, S. V.; Grigorieva, I. V.; Firsov, A. A., *Science* **2004,** *306* (5696), 666-669.
[202] Xu, M.; Liang, T.; Shi, M.; Chen, H., *Chem. Rev.* **2013,** *113* (5), 3766-3798.
[203] Han, G. H.; Duong, D. L.; Keum, D. H.; Yun, S. J.; Lee, Y. H., *Chem. Rev.* **2018,** *118* (13), 6297-6336.
[204] Chhowalla, M.; Shin, H. S.; Eda, G.; Li, L.-J.; Loh, K. P.; Zhang, H., *Nat. Chem.* **2013,** *5*, 263.
[205] Tan, C. *et al*. *Chem. Rev.* **2017,** *117* (9), 6225-6331.

As we mentioned before, layered materials are connected by weak out of plane interactions, so this weak forces can be break easily (exfoliation) obtaining few layers or monolayer. The exfoliation improves the surface area of the material, ideal for catalytic purposes because it enhances physical properties and chemical reactivity. Also, could change the mechanical properties such as strength and resistance. However, electronic and optical properties are the most important in these materials. After exfoliation, the band gap and photoluminescence properties of some materials change dramatically,[206] for instance, the band-gap of BP is 0.3-0.5 eV and phosphorene 1.0-2.0 eV;[207] and monolayer of MoS_2 is photoluminescence and bulk material is not.[206,208]

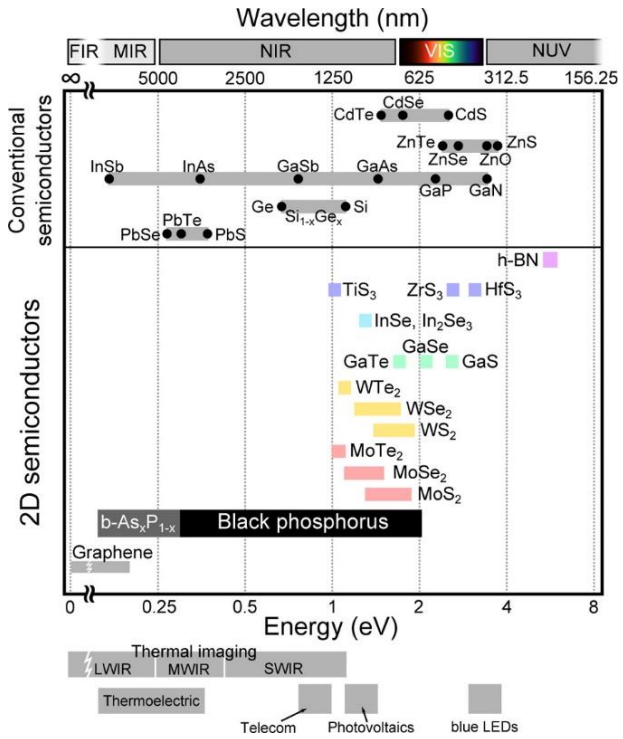

Figure 15. Comparison of the band gap for different 2D layered materials. Graphene is not semiconductor but after exfoliation, most of them are semiconductors: BP, h-BN and TMDCs such as MoS_2, WS_2, and $MoSe_2$. Reprinted with permission from *J. Phys. Chem. Lett.* **2015,** *6* (21), 4280-4291. Copyright (2015) American Chemical Society.

[206] Splendiani, A.; Sun, L.; Zhang, Y.; Li, T.; Kim, J.; Chim, C.-Y.; Galli, G.; Wang, F., *Nano Lett.* **2010,** *10* (4), 1271-1275.
[207] Castellanos-Gomez, A., *J. Phys. Chem. Lett.* **2015,** *6* (21), 4280-4291.
[208] Mak, K. F.; Lee, C.; Hone, J.; Shan, J.; Heinz, T. F., *Phys. Rev. Lett.* **2010,** *105* (13), 136805.

Nevertheless, not all characteristics of these materials are good news, they have some important disadvantages, for instance, even if some of bulk materials are easily available, the large-production of few-layers or monolayers is difficult and expensive. In addition, their properties are layer-dependent: change significantly with the number of layers; and some of exfoliated materials, such as BP, are sensitive to water and oxygen. As expected, this sensitivity when the number of layers decreases.[209]

Finally, a major focus of experimental research in recent years has concentrated on the development of experimental method to functionalize these materials[210,211] with organic molecules. This functionalization could enhance or change the properties, broaden their applications and improve their manageability too.

6.2. **Transition Metal Dichalcogenides (TMDCs).**

Transition Metal Dichalcogenides (TMDCs) are two-dimensional layered consisting of a hexagonally packed layer of a transition metal M sandwiched between two layers of chalcogenide atoms X (S , Se or Te) and interacting through strong covalent bonds, forming a MX_2 compound. In multilayer TMDCs, the single layers are connected to each other by van-der-Waals interactions[203]. One the advantages of TMDCs is their diversity. Different combinations of transition metal atom (M) with chalcogenide atoms can give rise to many possible of compounds (Figure 16b).

[209] Abellán, G.; Wild, S.; Lloret, V.; Scheuschner, N.; Gillen, R.; Mundloch, U.; Maultzsch, J.; Varela, M.; Hauke, F.; Hirsch, A., *J. Am. Chem. Soc*. **2017,** *139* (30), 10432-10440.
[210] Hirsch, A.; Hauke, F., *Angew. Chem. Int. Ed*. **2018,** *57* (16), 4338-4354.
[211] Chen, X.; McDonald, A. R., *Adv. Mater*. **2016,** *28* (27), 5738-5746.

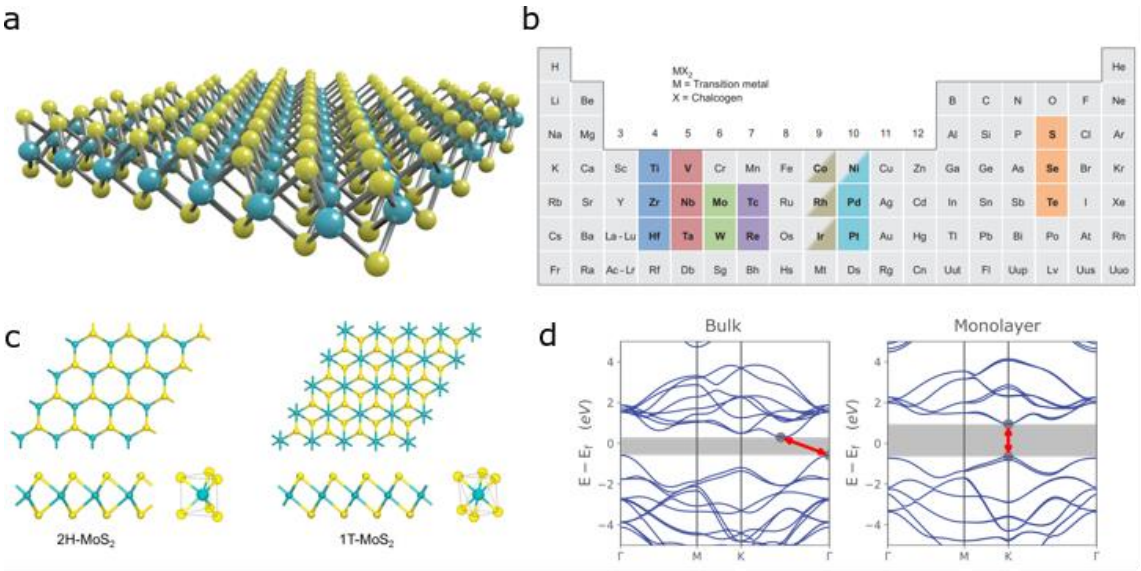

Figure 16. **a.** Monolayer of MoS_2. **b.** Periodic table with all of possibilities to form TMDCs. **c.** The two polymorphs of MoS_2: 1T and 2H. **d.** Band structure diagram (Brillouin zone) of bulk and monolayer MoS_2 showing the crossover from indirect (from Γ-point) to direct (from K-point) bandgap accompanied by a widening of the bandgap.[212]

In contrast to graphene, TMDCs exhibit a variety of stacking polymorphs because inside of an individual MX_2 monolayer the atoms can be organised in different phases, depending on the coordination of the metal atom. Most common polymorphs are 1T and 2H (Figure 16c) where the letters mean trigonal and hexagonal (respectively) and the digit indicates the number of X-M-X units in the unit cell.

The electronic properties of TMDCs[203,213,214] are diverse, starting from insulator HfS_2, semiconductors MoS_2 and WS_2, semimetals WTe_2 and $TiSe_2$, metal behaviour of NbS_2 and VSe_2. A few TMDCs such as $NbSe_2$ and TaS_2 exhibit low-temperature superconductivity. In summary, the chemistry of TMDCs compounds opens a new door to applications (such as transistors,[215,216] biomarkers,[217,218] organic solar cells[219] and

[212] Zhao, W.; Ribeiro, R. M.; Eda, G., *Acc. Chem. Res.* **2015,** *48* (1), 91-99.

[213] Wang, Q. H.; Kalantar-Zadeh, K.; Kis, A.; Coleman, J. N.; Strano, M. S., *Nat. Nanotechnol.* **2012,** *7*, 699.

[214] Mak, K. F.; Shan, J., *Nature Photonics* **2016,** *10*, 216.

[215] Radisavljevic, B.; Radenovic, A.; Brivio, J.; Giacometti, V.; Kis, A., *Nat. Nanotechnol.* **2011,** *6* (3), 147-150.

[216] Si, M.; Su, C.-J.; Jiang, C.; Conrad, N. J.; Zhou, H.; Maize, K. D.; Qiu, G.; Wu, C.-T.; Shakouri, A.; Alam, M. A.; Ye, P. D., *Nat. Nanotechnol.* **2018,** *13* (1), 24-28.

[217] Bernal, M. M.; Álvarez, L.; Giovanelli, E.; Arnáiz, A.; Ruiz-González, L.; Casado, S.; Granados, D.; Pizarro, A. M.; Castellanos-Gomez, A.; Pérez, E. M., *2D Mater.* **2016,** *3* (3), 035014.

[218] Anbazhagan, R.; Wang, H.-J.; Tsai, H.-C.; Jeng, R.-J., *RSC Adv.* **2014,** *4* (81), 42936-42941.

[219] Gu, X.; Cui, W.; Li, H.; Wu, Z.; Zeng, Z.; Lee, S.-T.; Zhang, H.; Sun, B., A *Adv. Energ. Mater.* **2013,** *3* (10), 1262-1268.

photodetectors[220,221]), new fundamental and technological pathways for inorganic 2D materials.

6.2.1. **Structure, Characteristics and Properties of MoS_2 and WS_2.**

Among all TDMCs compounds, we focus on the most abundant on Earth and the most studied, MoS_2 and WS_2, in special MoS_2. Both are semiconductors where band gap increases at the same time decreases the number of layers[208,222] (Figure 16d). Also, they have polymorphs 1T and 2H (Figure 16c). In particular in MoS_2, the electronic properties change dramatically between polymorphs:[223,224] 2H-MoS_2 is semiconductor and photoluminescence[213]. However, 1T-MoS_2 is metallic conductor.[225] A diagram of the band structure of bulk and monolayer of MoS_2 is shown in Figure 16d. At the Γ-point, the band gap transition is indirect for the bulk material. This band gap is negligible because is slower that the nonradioactive decay processes. But this indirect band gap gradually shifts to be direct for the monolayer[212]. In this point, the transitions occurs in the K-point. (Figure 16d). In general, all MoX_2 and WX_2 compounds are expected to undergo a similar indirect- to direct- band gap energy. This transition has important effects for photonics, optoelectronics and sensing applications.

Raman spectroscopy is a useful and non-destructive tool to analyse and characterize the TMDCs. In the case of MoS_2, the Raman spectrum of bulk 2H-MoS_2 has two prominent peaks:[226] an in-plane (E_{2g}) mode located around ~382 cm^{-1} and an out-of-plane (A_{1g}) mode which is located ~ 407cm^{-1} (Figure 17a). The distance of these peaks shows the grade of exfoliation and the number of layers[226]. Also, if the structure of MoS_2 is different (polymorphs 1T and 2H), the Raman spectra changes.[227] In addition, TMDCs exhibit characteristic absorption peaks. In the UV-vis spectra of MoS_2, these bands appear at 680, 610 450 and 395 nm and are referred to as A, B, C and D respectively (Figure 17b). Decreasing the number of layers, each peak from UV-vis tends to shift toward the

[220] Lopez-Sanchez, O.; Lembke, D.; Kayci, M.; Radenovic, A.; Kis, A., *Nat. Nanotechnol.* **2013,** *8*, 497.

[221] Massicotte, M. *et al*. *Nat. Nanotechnol*. **2015,** *11*, 42.

[222] Li, T.; Galli, G., *J. Phys.Chem.* **2007,** *111* (44), 16192-16196.

[223] Eda, G.; Fujita, T.; Yamaguchi, H.; Voiry, D.; Chen, M.; Chhowalla, M., *ACS Nano* **2012,** *6* (8), 7311-7317.

[224] Eda, G.; Yamaguchi, H.; Voiry, D.; Fujita, T.; Chen, M.; Chhowalla, M., Photoluminescence from Chemically Exfoliated MoS_2. *Nano Lett.* **2011,** *11* (12), 5111-5116.

[225] Wypych, F.; Schöllhorn, R., *J. Chem Soc. Chem. Commun.* **1992,** (19), 1386-1388.

[226] Lee, C.; Yan, H.; Brus, L. E.; Heinz, T. F.; Hone, J.; Ryu, S., *ACS Nano* **2010,** *4* (5), 2695-2700.

[227] Yu, Y *et al*., *Nat. Chem.* **2018,** *10* (6), 638-643.

blue, demonstrated by Coleman and co-workers.[228] In addition, the scattering effect decrease while decreases the number of layers too.

Regarding the applications of TMDCs, MoS_2 is the most used: for instance, has environmental properties,[229] such as contaminant adsorption and disinfection, and it is an attractive material for flexible field-effect transistors (FETs)[230] due to the large in-plane carrier mobility and robust mechanical properties. Furthermore, MoS_2 is used as catalyst for electrocatalytic hydrogen evolution (HER) from water[231,232] and as alternative to metal catalysis such as Pt. The catalysis is produced in the sulfur vacancies localized on all the basal plane of MoS_2. In these catalytic sides, the proton binds directly to expose Mo atoms. The catalytic sides or vacancies of S are generated during the exfoliation process or defects in the synthesis of MoS_2 by chemical vapour deposition (CVD). In addition, 1T-MoS_2 is much more active than 2H-MoS_2 for HER[227].

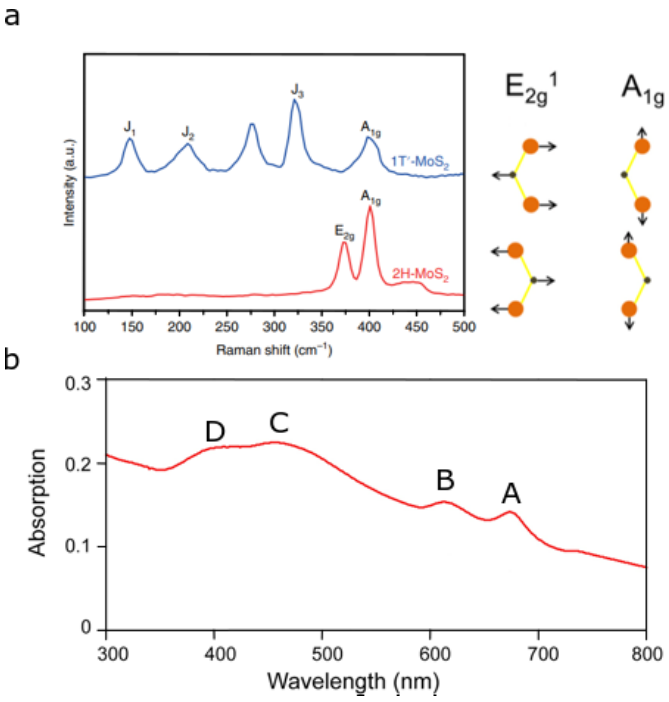

Figure 17. **a.** Comparison of Raman spectra between 1T and 2H MoS_2 polymorphs[227]. Also, the vibrations E^1_{2g} and A_{1g} from 2H-MoS_2. **b.** UV-vis of MoS_2 with A, B, C and D bands.

[228] Backes, C. *et al. Nat. Commun.* **2014,** *5* (1), 4576.
[229] Wang, Z. Mi, B., *Environ. Sci. Technol.* **2017,** *51* (15), 8229-8244.
[230] Ayari, A.; Cobas, E.; Ogundadegbe, O.; Fuhrer, M. S., *J. Appl. Phys.* **2007,** *101* (1), 014507.
[231] Li, H *et al. Nat. Mater.* **2015,** *15*, 48.
[232] Li, G.; Zhang, D.; Yu, Y.; Huang, S.; Yang, W.; Cao, L., *J. Am. Chem. Soc.* **2017,** *139* (45), 16194-16200.

Finally, about WS_2, recently Lin *et al.*[233] reported CVD-grown monolayer of 2H-WS_2 has large circular polarization (circularly polarized emission (P_{circ}) up to 60%) at 300 K. This high values are related to the lower defect densities in the structure of CVD-2H-WS_2 suggesting it is possible to control the opto-electronics properties of TMDCs with the defects of their structure.

6.2.2. **Production of ultrathin TMDCs.**

There are two methods to obtain few-layer or monolayers of TMDCs: 1) bottom up, which consists in the synthesis and growing of large-area thin layers of TMDCs and 2) top-down method, which consists in the exfoliation of TDMCs breaking the weak interactions between layers. In this part we explain different methodologies, with advantages and disadvantages:

1) *Chemical Vapour Deposition (CVD).*

CVD belongs to bottom-up methods. An example of this method is a two-step thermolysis process by dip-coating in ammonium thiomolybdates [$(NH_4)_2MoS_4$] and converting to MoS_2 by annealing at 500 °C followed by sulfurization at 1000 °C in sulfur vapour.[234] The second annealing at 1000 °C is required for improving the crystallinity.

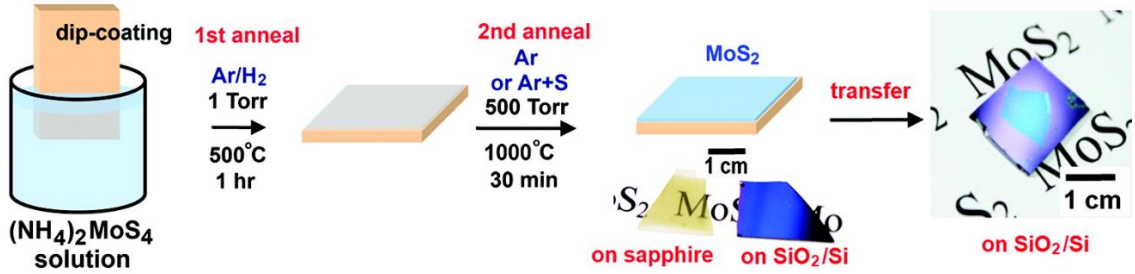

Figure 18. Process of CVD-exfoliation of MoS_2. The reaction is $(NH_4)_2MoS_4 + H_2 \rightarrow 2NH_3 + 2H_2S + MoS_2$. Adapted with permission from *Nano Lett.* **2012,** *12* (3), 1538-1544. Copyright (2012) American Chemical Society.

The advantage of this methodology is the good quality of few-layers and monolayer. On the other hand, the disadvantages are the harsh conditions, it is not a scaled-up method and it is only possible to do on a surface.

[233] Lin, W.-H.; Tseng, W.-S.; Went, C. M.; Teague, M. L.; Rossman, G. R.; Atwater, H. A.; Yeh, N.-C., *ACS Nano* **2019**.

[234] Liu, K.-K.; Zhang, W.; Lee, Y.-H.; Lin, Y.-C.; Chang, M.-T.; Su, C.-Y.; Chang, C.-S.; Li, H.; Shi, Y.; Zhang, H.; Lai, C.-S.; Li, L.-J., *Nano Lett.* **2012,** *12* (3), 1538-1544.

2) Mechanical Exfoliation.

Mechanical exfoliation is part of top-down methods: layers of TMDCs can be peeled from their bulk crystals. This method consist in putting the 2D material on a substrate with an adhesive tape. It is the best methodology to obtain the highest-quality mono-layered samples, ideal for studying properties. However, it is not a scaled-up method and it is only possible to do on a surface.

3) Chemical Exfoliation (CE).

Chemical exfoliation (top-down method) consists in the ion intercalation between layers. An example of this method is the exfoliation of MoS_2 using n-BuLi. MoS_2 reacts with n-BuLi to yield the reduced product [Li_xMoS_2]. Then, the reduce product reacts with water (reoxidazed process) causing delamination of MoS_2 monolayers and formation of hydrogen and LiOH. The product is called ce-1T-MoS_2. This is scaled-up and low-cost process but during this process the polymorph structure of MoS_2 change (2H to 1T but with an annealing at 300ºC the 2H structure is restored). Also, a mixture of different sizes of layers is obtained in the process. It is sensitive to air and are used toxic chemicals.

4) Liquid-Phase Exfoliation (LPE).[235,236]

Liquid phase exfoliation (top-down method) consists in the sonication of a suspension between the layered material and a solvent. The temperature have to be controlled in order to avoid defects in the layers. In addition, polar solvent are preferred as LPE media[235] due to the cohesive forces, such as dipole-dipole forces and hydrogen bonding among others, improve the layer separation. This method is simple, versatile, low-cost and potentially scaled-up,[237] to give large amounts of exfoliated sample. In addition, it is insensitive to air and water. However, it is necessary to find a suitable solvent and some of them are toxic. Also, different sizes are generated during the process.

[235] Backes, C.; Higgins, T. M.; Kelly, A.; Boland, C.; Harvey, A.; Hanlon, D.; Coleman, J. N., *Chem. Mater.* **2017,** *29* (1), 243-255.
[236] Coleman, J. N. *et al*. *Science* **2011,** *331* (6017), 568-571.
[237] Smith, R. J.; King, P. J.; Lotya, M.; Wirtz, C.; Khan, U.; De, S.; O'Neill, A.; Duesberg, G. S.; Grunlan, J. C.; Moriarty, G.; Chen, J.; Wang, J.; Minett, A. I.; Nicolosi, V.; Coleman, J. N., *Adv Mater.* **2011,** *23* (34), 3944-3948.

6.2.3. **Functionalization of MoS_2.**

Not only the study of intrinsic properties of these layered materials is important. Also how can we modified is a fundamental objective.[238] Through non-covalent or covalent functionalization we can change the physical/chemical properties. For instance, a non-covalent modification of MoS_2 with 2,3,5,6- tetrafluoro- 7,7,8,8-tetracyanoquinodimethane (F_4-TCNQ) permits a tunable modification of photoluminescence of a monolayer-MoS_2 via chemical-doping.[239]

Regarding the covalent functionalization of MoS_2, there are multiple methods and it is important to know which exfoliation method, organic molecules and polymorph of MoS_2 to use. Here, we present some examples of functionalization of different publications.

1) *Ligand conjugation Functionalization of 1T-MoS_2.*

Dravid and co-workers[240] reported a ligand conjugation functionalization of MoS_2 with different thiol molecules (Figure 19a). MoS_2 was chemically exfoliated using n-BuLi (ce-1T-MoS_2). In this process defects on the surface are generated in both internal edges and perimeter edges. Different thiol molecules were added to functionalize these defects. Using charged thiol molecules they could modulate the ζ-potential (Figure 19b) proving the functionalization. Also, with Fourier Transform Infrared spectroscopy (FT-IR) they found the typical peaks of thiol molecules (Figure 19c, d).With this method they obtained colloidal suspension in water stable during 21 days. In addition, using an NMe^+ thiol molecule, they can controlled the stability of the colloidal using pH.

The authors defined this procedure as covalent functionalization but the exact nature of thiol/MoS_2 interaction is unclear. It is possible that the thiol molecule is coordinating to Mo-atoms yielding a ligand coordination.

[238] Bertolazzi, S.; Gobbi, M.; Zhao, Y.; Backes, C.; Samorì, P., *Chem. Soc. Rev.* **2018,** *47* (17), 6845-6888.
[239] Mouri, S.; Miyauchi, Y.; Matsuda, K., *Nano Lett.* **2013,** *13* (12), 5944-5948.
[240] Chou, S. S.; De, M.; Kim, J.; Byun, S.; Dykstra, C.; Yu, J.; Huang, J.; Dravid, V. P., *J. Am. Chem. Soc.* **2013,** *135* (12), 4584-4587.

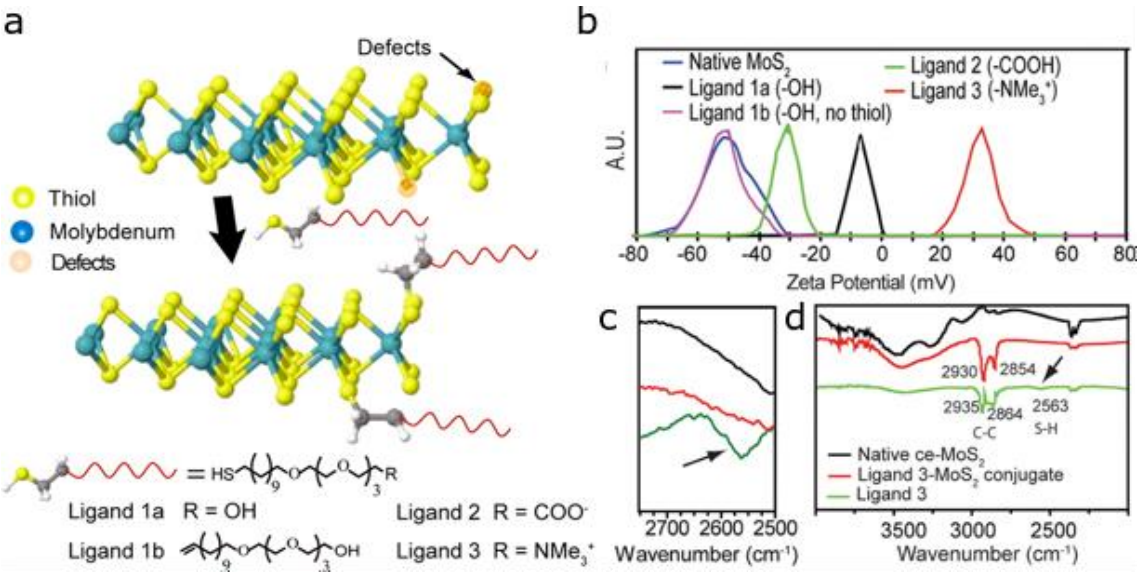

Figure 19. **a.** Scheme of ligand functionalization with thiol molecules. **b.** Dynamic Light Scattering (DLS): measurement of ζ-potential. **c.** ν(S-H) and **d.** FT-IR of the samples. Adapted with permission from *J. Am. Chem. Soc.* **2013,** *135* (12), 4584-4587. Copyright (2015) American Chemical Society.

2) *Covalent functionalization of 1T-MoS_2.*

Chhowalla and co-workers[241] reported a covalent functionalization of MoS_2 (and WS_2) using iodide molecules. They took advantages of negatives charges on the surfaces of MoS_2 after chemical exfoliation. They chemically exfoliated of MoS_2 with n-BuLi. Then, they added different iodide based electrophiles, which were attacked by these negative charges (Figure 20a). They probed this covalent functionalization with X-ray photoelectron spectroscopy (XPS) where they found a new component (Figure 20b) corresponded to S-C bond. Also appears a new component of N atom from one of molecules used. In addition, with FT-IR they found the typical signals of the product. They showed that the covalent attachment of functional groups leads to dramatic changes in the optoelectronic properties of the material.

[241] Voiry, D.; Goswami, A.; Kappera, R.; Silva, C. d. C. C. e.; Kaplan, D.; Fujita, T.; Chen, M.; Asefa, T.; Chhowalla, M., *Nat. Chem.* **2014,** *7*, 45.

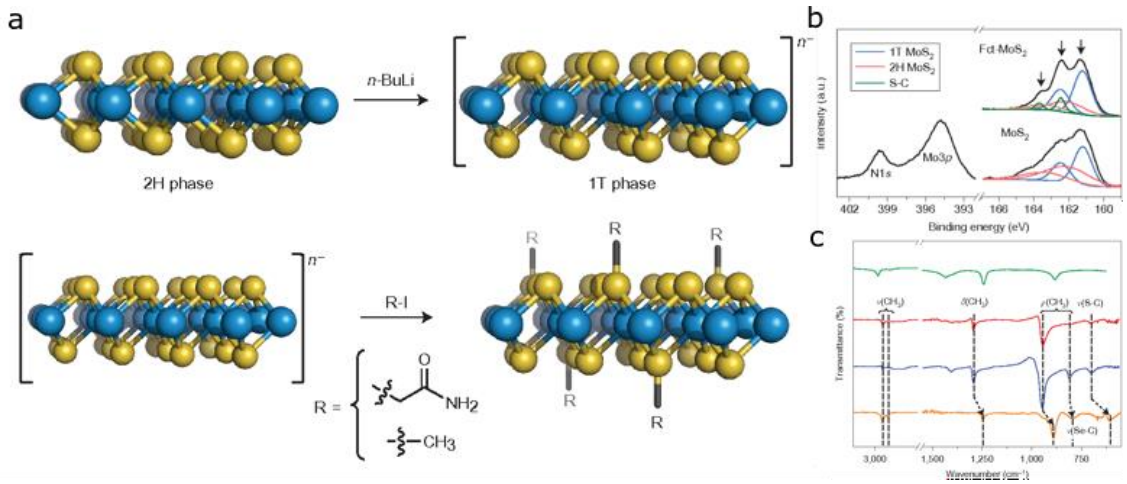

Figure 20. **a.** Scheme of the functionalization with iodide molecules. **b.** XPS measurement. **c.** FT-IR of all the samples on the publication. The red line corresponds to MoS_2 functionalized.

Other current method to functionalize MoS_2 is using diazonium salts. Knirsch *et al.*[242] reported this method beginning with a chemical exfoliation (ce-1T-MoS_2). Then, they added the electrophile aromatic diazonium salts to functionalize covalently, through negative charges on the surface of MoS_2.

Benson *et al.*[243] used the same method of functionalization but they studied the effect of the covalent functionalization and the type of ligand in the diazonium salt (electron donating or electron drawing groups) in the HER process. They showed a clearly effect in this process: first, the functionalized MoS_2 is more stable than unfuntionalized 1T-MoS_2 and secondly, the HER process works better with electron donating groups. This is a clear example of tunabling properties of MoS_2 with covalent functionalization.

3) *Functionalization of 2H-MoS_2.*

Until now, all examples of functionalization have been for ce-1T-MoS_2. It is important to remember that 1T losses all the electronic properties of 2H-MoS_2 such as semiconductor and photoluminescence (although it is possible to recover 2H-phase with an annealing at 300ºC). There are not too many examples of covalent functionalization of 2H-MoS_2.

[242] Knirsch, K. C. *et al. ACS Nano* **2015,** *9* (6), 6018-6030.

[243] Benson, E. E.; Zhang, H.; Schuman, S. A.; Nanayakkara, S. U.; Bronstein, N. D.; Ferrere, S.; Blackburn, J. L.; Miller, E. M., *J. Am. Chem. Soc.* **2018,** *140* (1), 441-450.

Backes *et al.*[244] reported a functionalization of 2H-MoS_2 exfoliated by LPE with different metal complexes. These metal complexes coordinate to sulfur atoms on the surface of MoS_2. They performed liquid-phase exfoliation of MoS_2 in 2-propanol. With this method the 2H structure is preserved. Then, they use different metal complex ($M(OAc)_2$), where M: Cu^{II}, Ni^{II} and Zn^{II}, to functionalize the S atoms. They showed that the grade of functionalization depends on the metal and occurs on the basal planes: MoS_2-$Cu(OAc)_2$ (50%) >> MoS_2-$Ni(OAc)_2$ (30%) >> MoS_2-$Zn(OAc)_2$.(10%). They demonstrated the functionalization with FT-IR, XPS and TGA.

Likewise, Chen *et al.*[245] reported another functionalization of 2H-MoS_2 through ligand functionalization with cysteine molecule. One more time, MoS_2 was exfoliated by LPE in order to conserve the 2H structure. Then, they functionalize MoS_2 with cysteine molecule by coordination of the thiol group to Mo-atoms at S-atom vacancies. Moreover, they observed disulphide products in the reaction. With several control experiments, they probed the oxidation of thiol molecule in the reaction and they proposed a mechanism where MoS_2 is mediating the conversion of thiol to disulphide releasing hydrogen from both thiols.

One last example was reported by Wang and co-workers.[246] They functionalized the basal plane of 2H-MoS_2, obtained previously by mechanical exfoliation, using aryl diazonium salts without any pre-treatments. In addition, with theory calculation and microscopy studies, they observed that the reactivity of MoS_2 increases with the defects on its structure.

[244] Backes, C.; Berner, N. C.; Chen, X.; Lafargue, P.; LaPlace, P.; Freeley, M.; Duesberg, G. S.; Coleman, J. N.; McDonald, A. R., *Angew. Chem. Int. Ed.* **2015,** *54* (9), 2638-2642.

[245] Chen, X.; Berner, N. C.; Backes, C.; Duesberg, G. S.; McDonald, A. R., *Angew. Chem. Int. Ed.* **2016,** *55* (19), 5803-5808.

[246] Chu, X. S.; Yousaf, A.; Li, D. O.; Tang, A. A.; Debnath, A.; Ma, D.; Green, A. A.; Santos, E. J. G.; Wang, Q. H., *Chem. Mater.* **2018,** *30* (6), 2112-2128.

7. Objectives

With all these premises, part of this thesis aims to functionalize of 2H-TMDCs (MoS_2 and WS_2) using thiol-ene chemistry with maleimides (thiol-Michael Addition)

The specific objectives are:

1) **Liquid-Phase exfoliation of MoS_2 and WS_2.**

2) **Functionalization of exfoliated samples with the chemistry of thiol-ene click reaction with maleimides**.

3) **Study of thiol-ene reaction between MoS_2 and maleimides.**

Chapter 3.

8. Mild Covalent Functionalization of Transition Metal Dichalcogenides with Maleimides: A “Click” Reaction for 2H-MoS_2 and WS_2

The work described in this chapter is published on *J. Am. Chem. Soc.*, **2019**, *141*, 3767.

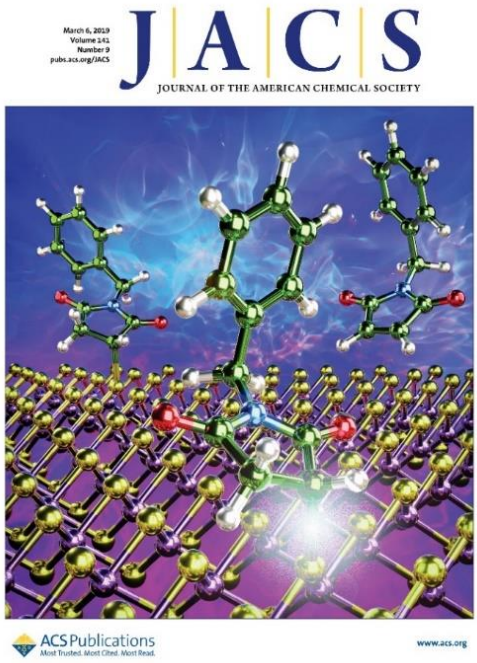

The physical properties of ultrathin transition metal dichalcogenides (2D-TMDCs) make them promising candidates as active nanomaterials for catalysis, optoelectronics, and biomedical applications. Chemical modification of TMDCs is expected to be key in modifying/adding new functions that will help make such promise a reality. We present a mild method for the modification of the basal planes of 2H-MoS_2 and WS_2. We exploit the soft nucleophilicity of sulfur to react it with maleimide derivatives, achieving covalent functionalization of 2H-TMDCs under very mild conditions. Extensive characterization proves that the reaction occurs through Michael addition. The orthogonality and versatility of the thiol−ene “click” chemistry is expected to allow the à la carte chemical manipulation of TMDCs

8.1. **Introduction**.

Transition metal dichalcogenides (TMDCs) are one of the most interesting families of lamellar materials that can be exfoliated down to bidimensional sheets of single or very few layers (2D-TMDCs).[203,213,214,247,248] The (photo)catalytic properties of 2D-TMDCs have been known for decades,[249] but their electronic properties[208,220,224,250] have brought them back to the research spotlight.[216,238,251,252,253,254]

Chemically, each sheet of a TMDC is composed of a layer of transition metal atoms (M, typically Mo or W) sandwiched between two layers of chalcogen atoms (X, typically S, Se or Te), to which they are covalently bound with MX_2 stoichiometry. These three-atom thick TMDC sheets are stacked through van der Waals forces to form the bulk material, and can be separated using mechanical[255] or liquid phase exfoliation (LPE) techniques.[217,236,256] While the mechanical exfoliation from the bulk[257] and the synthesis of monolayers (typically through chemical vapour deposition)[258] have dominated the production of individual 2D-TMDCs to study their physical properties and for the prototyping of (opto)electronic devices, LPE is a complementary approach that renders colloidal suspensions of 2D nanomaterials in much larger amounts.[237,259]

The chemical modification of TMDCs with small molecules has been explored to modify their surface properties (i.e., fine-tune colloidal properties, include specific interactions, etc.) and electronic features (i.e., improve absorption, modify band gap, etc.)[210,238].

The direct decoration with thiols is the most studied approach for the covalent modification of MoS_2.[260] Initially assumed to proceed via covalent attachment of the thiols at sulfur vacancies,[240] this interpretation has recently been called into question, and

[247] Hu, Z.; Wu, Z.; Han, C.; He, J.; Ni, Z.; Chen, W., *Chem. Soc. Rev.* **2018,** *47* (9), 3100-3128.
[248] Jariwala, D.; Sangwan, V. K.; Lauhon, L. J.; Marks, T. J.; Hersam, M. C., *ACS Nano* **2014,** *8* (2), 1102-1120.
[249] Frindt, R. F., *J. Appl. Phys.* **1966,** *37* (4), 1928-1929.
[250] Radisavljevic, B.; Radenovic, A.; Brivio, J.; Giacometti, V.; Kis, A., *Nat. Nanotechnol.* **2011,** *6*, 147.
[251] Castellanos-Gomez, A. *et al*. *Adv. Mater.* **2013,** *25* (46), 6719-6723.
[252] Castellanos-Gomez, A. *et al*. *Nano Lett.* **2013,** *13* (11), 5361-5366.
[253] Kang, K.; Xie, S.; Huang, L.; Han, Y.; Huang, P. Y.; Mak, K. F.; Kim, C.-J.; Muller, D.; Park, J., *Nature* **2015,** *520*, 656.
[254] Xie, S. *et al*. *Science* **2018,** *359* (6380), 1131-1136.
[255] Li, H.; Wu, J.; Yin, Z.; Zhang, H., *Acc. Chem. Res.* **2014,** *47* (4), 1067-1075.
[256] Cunningham, G. *et al*. *ACS Nano* **2012,** *6* (4), 3468-3480.
[257] Castellanos-Gomez, A. *et al*. *2D Mater.* **2014,** *1* (1), 011002.
[258] Lv, R.; Robinson, J. A.; Schaak, R. E.; Sun, D.; Sun, Y.; Mallouk, T. E.; Terrones, M., *Acc. Chem. Res.* **2015,** *48* (1), 56-64.
[259] Zhang, X.; Lai, Z.; Tan, C.; Zhang, H., *Angew. Chem. Int. Ed.* **2016,** *55* (31), 8816-8838.
[260] Presolski, S.; Pumera, M., *Mater. Today* **2016,** *19* (3), 140-145.

a different mechanism, involving strong physisorption of disulfides formed in situ has been proposed instead.[245] The formation of coordination bonds between metal cations and the sulfur atoms of MoS_2 has also been explored.[244,261] Finally, the nucleophilicity provided by the negative charges left over in the 1T-MoS_2 obtained after chemical exfoliation with n-BuLi has been exploited for functionalization with electrophiles, typically alkyl halides,[241] but also with aryldiazonium salts.[242]

On the other hand, maleimides are the prototypical electrophiles for sulfur-based nucleophiles, reacting through Michael addition, typically under mild conditions and orthogonally to most other functional groups. The robustness of this chemistry has been tried and tested in the biochemistry and polymer chemistry realms, where it has become part of the "click" chemistry toolbox.[167,176,262,263]
Here, we exploit the inherent soft nucleophilic character of S to functionalize 2H-MoS_2 and WS_2 covalently with maleimide derivatives at room temperature.

8.2. **Results.**

Few-layer colloids of MoS_2 and WS_2 were obtained by LPE in 2-propanol/water using an ultrasonic probe (7:3 v/v and 1 h for MoS_2; 1:1 v/v and 8 h for WS_2). This relatively mild exfoliation procedure yields colloids of the 2H polytype, as evidenced by UV−vis extinction and Raman spectroscopies, and high-resolution transmission electron microscopy (HRTEM, see below), with a majority of flakes in the few layers limit (<10 nm from AFM data), and lateral sizes in the hundreds of nanometres (100−600 nm from TEM data, see Figures S1−6). After this process, the solvent of the dispersion was changed to acetonitrile (Figure S7),[264] and *N*-benzylmaleimide or *N*-methylmaleimide, and triethylamine were added. The reaction was stirred overnight (Figure 1a). Then, the product was centrifuged and thoroughly washed with acetonitrile in order to eliminate excess reagents and physisorbed maleimide (Figure S8).

[261] Liu, Y.-T.; Tan, Z.; Xie, X.-M.; Wang, Z.-F.; Ye, X.-Y., *Chem. Asian J.* **2013,** *8* (4), 817-823.
[262] Bhatia, S. K.; Shriver-Lake, L. C.; Prior, K. J.; Georger, J. H.; Calvert, J. M.; Bredehorst, R.; Ligler, F. S., *Anal. Biochem.* **1989,** *178* (2), 408-413.
[263] Kade, M. J.; Burke, D. J.; Hawker, C. J., *J. Polym. Sci. Polym. Chem.* **2010,** *48* (4), 743-750.
[264] Giovanelli, E.; Castellanos-Gomez, A.; Pérez, E. M., *ChemPlusChem* **2017,** *82* (5), 732-741.

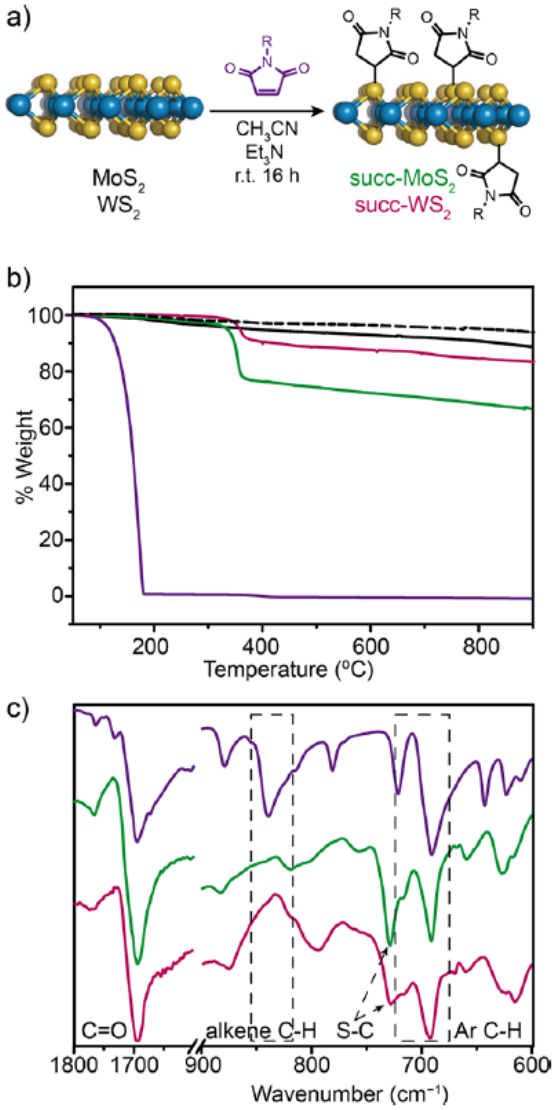

Figure 1. **a)** General scheme for the functionalization of TMDCs with maleimides (R = Bn or Me). **b)** TGA (N_2, 10 °C/min) of exfoliated MoS_2 (black solid line) and WS_2 (black dashed line), Bn-succ-MoS_2 (green), Bn-succ-WS_2 (magenta), and *N*-benzylmaleimide (purple). The colour code is identical for c). **c)** Comparison of the ATR-IR spectra of *N*-benzylmaleimide, Bn-succ-MoS_2 and Bn-succ-WS_2.

The product shows a functionalization of 24 wt % for the *N*-benzylmaleimide-functionalized MoS_2 flakes (Bn-succ-MoS_2) and 11 wt % for Bn-succ-WS_2, estimated from thermogravimetric analysis (Figure 1b). The large increase in desorption temperature of the organic material (from ca. 155 °C to ca. 320 °C) is a direct indication of covalent bonding. To prove this, we purposely prepared samples of Bn-succ-MoS_2 with a significant amount of physisorbed *N*-benzylmaleimide, where the desorption

temperature of the physisorbed and covalently attached materials are clearly distinguishable (Figure S20). The large degree of functionalization is incompatible with reaction at the edges/defect sites only, and indicates that the basal planes also undergo significant chemical modification.[241,244] Comparison of the ATR-IR spectra of the *N*-benzylmaleimide reagent, Bn-succ-MoS_2 and Bn-succ-WS_2 is conclusive with respect to the mode of functionalization. Figure 1c shows the presence of most vibrations of *N*-benzylmaleimide in both the Bn-succ-MoS_2 and Bn-succ-WS_2 samples, although significantly weaker in the latter case due to the lower degree of functionalization (see Figures S10 and S11 for full spectra). For instance, the intense carbonyl stretch appears at 1695 cm^{-1} in *N*-benzylmaleimide and at 1694 cm^{-1} in Bn-succ-MoS_2, while the aromatic C−H bending are visible at 690 and 721 cm^{-1}, and at 691 and 718 cm^{-1} in the reagent and product, respectively. Remarkably, the strong alkene C−H bending mode, at 840 cm^{-1} in the spectrum of *N*-benzylmaleimide, is completely depleted in both Bn-succ-MoS_2 and Bn-succ-WS_2. Finally, the new signals in the spectra of Bn-succ-MoS_2 (723 cm^{-1}) and Bn-succ-WS_2 (728 cm^{-1}) are assigned to the S−C stretching mode. These observations not only prove that the Bn-succ-MoS_2 and Bn-succ-WS_2 samples are functionalized covalently through a Michael addition mechanism, but also that they contain negligible amounts of physisorbed unreacted *N*-benzylmaleimide. Indeed, in Bn-succ-MoS_2 samples with physisorbed *N*-benzylmaleimide, the alkene C−H bending mode is clearly distinguishable (Figure S20). Solid-state CP-MAS-^{13}C NMR spectra of starting materials and products, and solution ^{13}C NMR spectra of adequate model compounds, are shown in Figure 2. As expected, we observe no signal from the unreacted exfoliated samples. In the *N*-benzylmaleimide spectrum, the relatively weak and sharp signal in the alkyl region, at 40.7 ppm can be unambiguously assigned to the methylene group. In the C sp^2 region, the signals between 137.0 and 125.0 ppm correspond to the phenyl and alkene carbons, and the carbonyl group is found at 171.7 ppm.

The evidence for covalent functionalization via Michael addition is unmistakable in the spectra of Bn-succ-MoS_2 and Bn-succ-WS_2. Although with our set up the CP-MAS-^{13}C NMR is not quantitative, it is qualitatively obvious that the alkyl signals increase in relative integration and show more than one chemical environment. In parallel with the increase in alkyl signals, in the aromatic-alkene region, the most deshielded signal,

corresponding to the electron-poor alkene, disappears. Comparison with the ^{13}C NMR ($CDCl_3$, 100 MHz) spectrum of the small-molecule model product of the reaction between *N*-benzylmaleimide and 1-propylthiol confirms the preceding statement. Moreover, we also tested the reaction with *N*-methylmaleimide, to avoid the possible overlapping of aromatic and alkene signals. Indeed, the disappearance of the alkene signal (at ca. 140 ppm in the starting material) is unambiguous in the case of Me-succ-MoS_2 where the region is free of any other sp^2 carbon signal. Combined with the disappearance of the alkene signal, the appearance of new methylene signals in the alkyl region is a definite proof of functionalization via Michael addition. Finally, the carbonyl signal is significantly shifted downfield (to ca. 178 ppm from ca. 175 ppm in the starting materials) and broadened in all the functionalized materials, in agreement with an attack by a sulfur nucleophile and saturation of the double bond, which results in decreased electronic density and desymmetrization of the two carbonyl groups. Again, this effect is perfectly mirrored in the soluble small-molecule models.

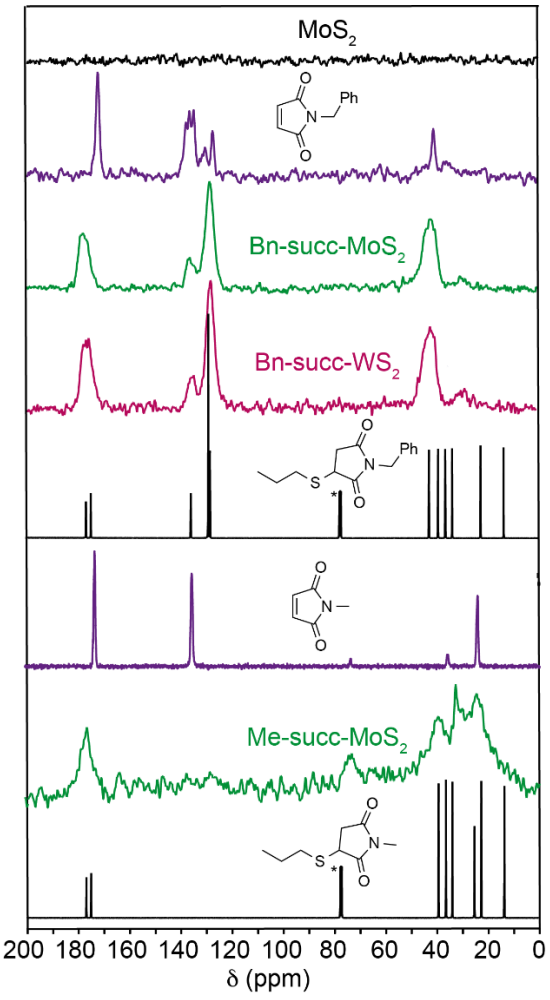

Figure 2. Comparison of the CP-MAS-^{13}C NMR (100 MHz) spectra of MoS_2, *N*-benzylmaleimide, Bn-succ-MoS_2, Bn-succ-WS_2, *N*-methylmaleimide and Me-succ-MoS_2. The solution ^{13}C NMR spectra ($CDCl_3$, 100 MHz, room temperature) of model small-molecule compounds, obtained by reaction of the corresponding maleimide and 1-propylthiol, are also shown. Solvent peaks are marked with an asterisk.

Considering that each sulfur atom in MoS_2/WS_2 is covalently bound to three Mo/W atoms, the formation of a covalent bond with the maleimide would imply the formation of a hypervalent S species with covalent bonds to three Mo/W atoms and one C atom. Such species have already been documented in the literature of soluble Mo and W clusters.[265,266,267] Alternatively, the reactivity might arise from S^- present in the structure, due to Mo vacancies created during the LPE or solvent-transfer processes.[268] To explore these hypotheses, we carried out X-ray photoemission spectroscopy (XPS) measurements.

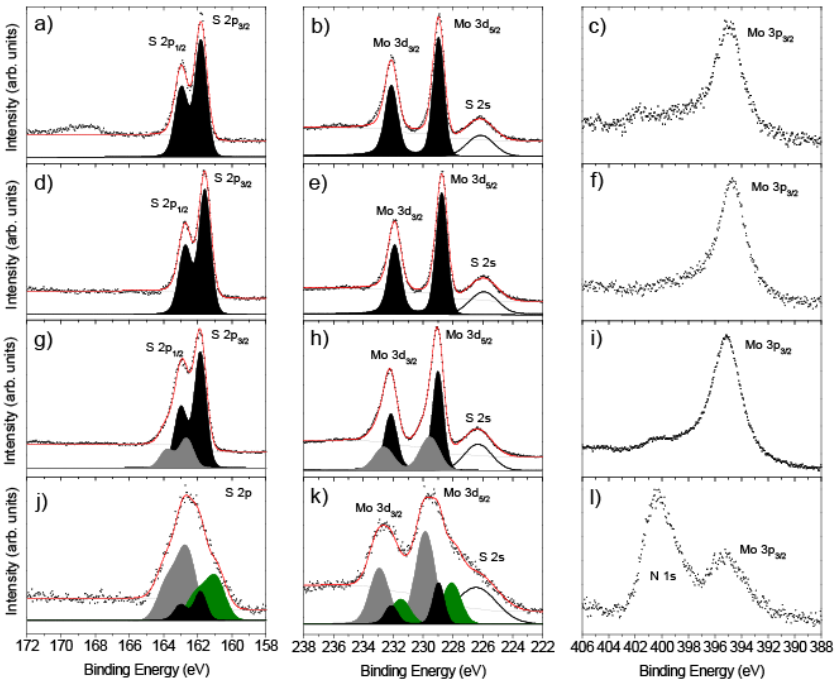

[265] Matsumoto, T.; Namiki, R.; Chang, H.-C., *Eur. J. Inorg. Chem.* **2018,** *2018* (35), 3900-3904.
[266] Gomes de Lima, M. B.; Guerchais, J. E.; Mercier, R.; Petillon, F. Y., *Organometallics* **1986,** *5* (10), 1952-1964.
[267] Ellis, J. E.; Rochfort, G. L., *Organometallics* **1982,** *1* (5), 682-689.
[268] Hai, X.; Chang, K.; Pang, H.; Li, M.; Li, P.; Liu, H.; Shi, L.; Ye, J., *J. Am. Chem. Soc.* **2016,** *138* (45), 14962-14969.

Figure 3. XPS spectra of S, Mo and N core levels for the bulk MoS_2 material **a-c)**, **d-f)** MoS_2 as obtained in 2-propanol/water. **g-i)** MoS_2 after transfer to CH_3CN. **j-l)** Bn-succ-MoS_2.

The core level of C 1s centered at 284.6 eV was used as a binding energy reference. The main results for MoS_2 are described in Figure 3, depicting the XPS core levels corresponding to the S 2p (left column), Mo 3d and S 2s (middle column), and N 1s and Mo $3p_{3/2}$ regions (right column), with their corresponding fits. In the first row, the reference powder bulk MoS_2 data is shown (Figure 3a−c). The process to change solvent from 2-propanol/water (Figure 3d−f) to CH_3CN (Figure 3g−i) already produces observable changes. Although the sharp doublet structures are maintained, the best fit requires including a second component (in gray). The origin of this component could be attributed to a different ratio of surface to bulk atoms, due to reaggregation processes, or to the partial formation of MoO_yS_z species.[269] However, the changes upon chemical functionalization (Figure 3j−l) are much more significant. To begin with, a characteristic peak for N 1s appears (Figure 3l), which can be unambiguously assigned to the maleimide fragment thanks to the comparison with the small shoulder due to residual CH_3CN in the unreacted material (Figure 3i). Furthermore, the S peak becomes significantly broader and requires a large lower energy contribution at 160.9 eV (green in Figure 3j). Likewise, the Mo signal is best fitted with a new component at 228.1 eV (green in Figure 3k). From these new components, we estimate that the functionalization is reflected in the S 2p region as a 33% of its integrated area and in the Mo 3d region as a 25%. This degree of functionalization is in good agreement with that obtained by TGA (24 wt %, i.e. 21 mol %). Similar results were obtained for WS_2 (Figure S12). These changes are consistent with the dominant mechanism for the reaction being the formation of hypervalent S, as proposed above, where the formal negative charge on the S atoms would facilitate the electron extraction.

Chemical exfoliation/functionalization of TMDCs under harsh conditions typically results in transformation of the semiconducting 2H to the metallic 1T polytype.[238] UV−vis and Raman spectroscopies, as well as HRTEM show that the

[269] Gu, J.; Aguiar, J. A.; Ferrere, S.; Steirer, K. X.; Yan, Y.; Xiao, C.; *Nat. Energy* **2017,** *2*, 16192.

semiconducting 2H nature of the TMDCs nanosheets is not altered during our functionalization protocol. For example, the Raman spectra (λ_{exc} = 532 nm) of both the pristine and functionalized samples are dominated by the characteristic E^1_{2g} and A_{1g} modes which appear only slightly shifted after functionalization (Figure S13). For comparison, covalent functionalization methods which require phase transitions result in significant changes in Raman spectroscopy.[241,242] Figure 4 shows HRTEM images of MoS_2 and WS_2 and the corresponding Bn-succ-MoS_2 and Bn-succ-WS_2 samples, where the conservation of the 2H polytype is evidenced by the hexagonal pattern in the 2D fast Fourier transforms (2D FFT, insets in Figure 4).

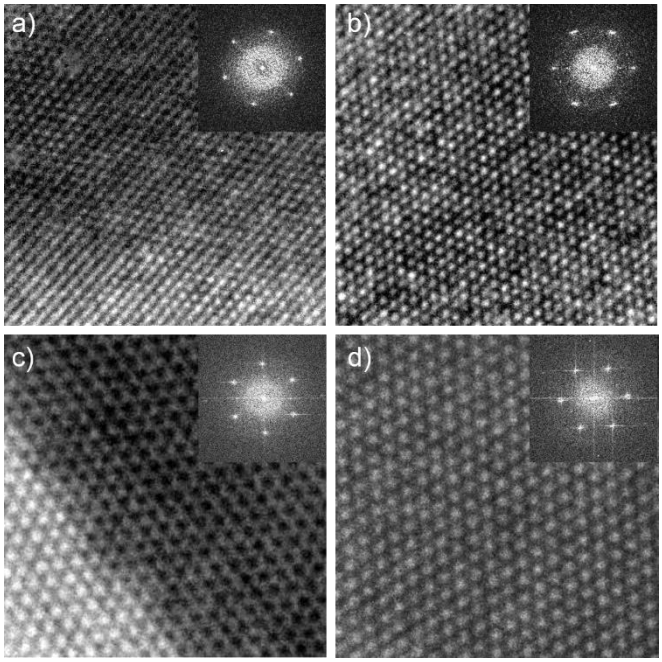

Figure 4. HRTEM micrographs of **a)** MoS_2, **b)** Bn-succ-MoS_2, **c)** WS_2 and **d)** Bn-succ-WS_2. The insets show the corresponding 2D-fast Fourier transforms.

An interesting macroscopic consequence of the chemical functionalization with organic fragments is that it brings about a noticeable increase of the stability of the colloids in nonpolar organic solvents such as $CHCl_3$, indicating a more oleophilic character of the Bn-succ-MoS_2 and Bn-succ-WS_2 surface (Figures S34 and S35).

8.3. **Conclusions.**

In summary, we develop a new strategy for the covalent functionalization of TMDCs based on the avidity of S as a soft nucleophile for soft electrophiles. In particular, we describe that 2H-MoS_2 and WS_2 can be covalently functionalized with maleimide reagents via Michael addition. The reaction occurs at room temperature, under very mild conditions that do not affect the 2H semiconducting polytype of the starting materials. Our results will allow those interested in the chemistry of TMDCs to tap into the rich toolbox of maleimide-based reagents developed to modify proteins and polymers, many even commercially available, or design à la carte reagents using well-established chemistry on the maleimide.

8.4. **Supplementary Information.**

8.4.1. **General Information.**

Materials. MoS_2 powder (<2 μm, 99%), WS_2 powder (2 μm, 99%), *N*-benzylmaleimide (99%) and triethylamine (>99%) were obtained from Sigma Aldrich. *N*-methylmaleimide (>98%) was obtained from TCI Europe and 1-propanethiol (98%) was obtained from Alfa Aesar. Solvents were purchased from Scharlau chemicals and used as received; Water was obtained from a Milli-Q filtration station ("Type 1" ultrapure water; resistivity: 18.2 MWcm at 25ºC).

Characterization methods. Analytical thin layer chromatographies (TLC) were performed using aluminium-coated Merck Kieselgel 60 F254 plates. NMR spectra were recorded on a Bruker Avance 400 (1H: 400 MHz; ^{13}C: 100 MHz) spectrometers at 298 K, using partially deuterated solvents as internal standards. Coupling constants (*J*) are denoted in Hz and chemical shifts (δ) in ppm. Solid-State CP-MAS-^{13}C Nuclear Magnetic Resonance (CP-MAS-^{13}C NMR) spectras were obtained with a Bruker AV 400 WB spectrometer. Thermogravimetric analyses (TGA) were performed using a TA Instruments TGAQ500. First, the sample was at 50ºC during 15 minutes. After that, the experiment was run with a ramp of 5 °C/min under N_2 from 50 to 1000 °C with a ramp of 10 °C/min under air from 100 to 1000 °C. Transmission electron microscopy (TEM) images were obtained with JEOL JEM 2100 microscope operated at 200 kV. Colloidal samples, exfoliated TMDCs and Bn-succ-TMDCs, were drop-cast onto 200 square mesh

copper grids covered with a carbon film. Atomic Force Microscopy (AFM) images were acquired using a JPK NanoWizard II AFM working in dynamic mode. NT-MDT NSG01 silicon cantilevers, with typical values of 5.1 N m^{-1} spring constant and 150 kHz resonant frequency, were employed under ambient conditions in air. Raman spectra were recorded with a Bruker Senterra confocal Raman microscope (Bruker Optic, Ettlingen, Germany, resolution 3- 5 cm^{-1}) by using the following parameters: objective NA 0.75, 50V; laser excitation: 532 nm, 2 mW. Colloidal samples, exfoliated TMDCs and Bn-succ-TMDCs, were drop-cast and dried onto glass slides at 50ºC. Each spectrum results from the average of ten measurements carried out in different regions distributed all over the sample. Fourier-transform infrared spectroscopy with attenuated total reflection (FT-ATR-IR) were performed with ALPHA FT-IR spectrometer of Bruker. UV-vis spectra were performed using a Cary 50 UV/Visible spectrophotometer and measured in a quartz cuvette (path length=1 cm). The colloidal stability was carried out with a suspension of exfoliated TMDCs and Bn-succ-TMDCs (0.10 mL in the case of MoS_2 and 0.15 mL of WS_2) in $CHCl_3$. It was sonicated for 2 min and transferred into a quartz cuvette (path length=1 cm). The cuvette was closed with a stopper and the extinction spectrum of the suspension was measured immediately (time zero measurement). The suspension was left at room temperature and each extinction spectrum was recorded at eight times in intervals of one hour. This process was repeated three times. The XPS measurements (X ray Photoelectron Spectroscopy) were performed under Ultra High Vacuum conditions (UHV, with a base pressure of 5×10^{-10} mbar), using a monochromatic Al Kα line as exciting photon source for core level analysis (hν = 1486.7). The emitted photoelectrons were collected in a hemispherical energy analyzer (SPHERA-U7, pass energy set to 20 eV for the XPS measurements to have a resolution of 0.6 eV) and to compensate the built up charge on the sample surface it was necessary the use of a Flood Gun (FG-500, Specs), with low energy electrons of 3 eV and 40 μA.

8.4.2. **Experimental Procedure.**

8.4.2.1. Exfoliation of TMDCs.

Liquid-phase exfoliation. MoS_2 powder (<2 μm, 99%, 1 mg/mL) was dispersed in 150 mL of a 7:3 mixture (v/v) of 2-propanol (*i*PrOH) and water,[217,264] in a 250 mL round-bottom flask further cooled down at 2.5ºC using Minichiller Huber.

WS_2 powder (2 μm, 99%, 1 mg/mL) was dispersed in 150 mL of a 1:1 mixture (v/v) of 2-propanol (*i*PrOH) and water,[270] in a 250 mL round-bottom flask further cooled down at 2.5ºC using Minichiller Huber.

The liquid-phase exfoliation (LPE) was performed by using an ultrasonic probe (Vibracell 75115, Bioblock Scientific, 500 W) immersed in the dispersion and operating at the amplitude of 40% for different hours. After sonication, the black suspension was distributed into six 50 mL conical centrifuge tubes which were centrifuged for 30 min at 1792 g (4000 rpm, Allegra X-15R Beckman Coulter centrifuge, FX6100 rotor, 20ºC). The corresponding olive-color supernatants (≈20mL) were carefully separated from the black sediment (non-exfoliated material) and collected each in another 50 mL conical centrifuge tubes for further phase transfer.

Five different experiments were carried out for each bulk powder of TMDCs, differing in the sonication time (Figure S1) (continuous ultrasound irradiation and constant temperature (2.5ºC)): 1 h, 2 h, 8 h, 16 h and 24 h. Each experiment was replicated independently.

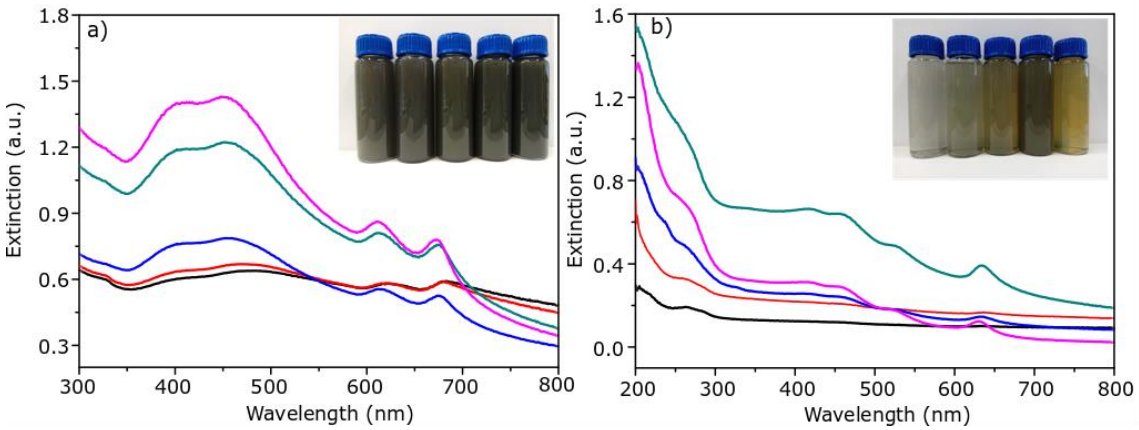

Figure S1. UV-vis spectroscopy of TMDC colloids obtained after exfoliation of TMDC powders at different times of sonication: 1h (black line), 2h (red), 8h (blue), 16h (green) and 24h (pink). **a)** MoS_2 colloids. **b)** WS_2 colloids. It was used 1.5 mL of the suspension to do the UV-vis and was added solvent until full the cuvette. (1 mL in the case of 24h of sonication). There is a blue shift while increasing the time of exfoliation.

[270] Shen, J.; He, Y.; Wu, J.; Gao, C.; Keyshar, K.; Zhang, X.; Yang, Y.; Ye, M.; Vajtai, R.; Lou, J.; Ajayan, P. M., *Nano Lett.* **2015,** *15* (8), 5449-5454.

Phase transfer of the TMDC nanosheets.[264] In a typical experiment, chloroform ($CHCl_3$) (15 mL) was added to the previously collected colloidal suspension (≈20 mL) and the mixture was rested for a few minutes. The nanosheets are located at the interface between the polar and nonpolar phases (Figure S2). Both phases were removed and the remaining nanosheets were redispersed in pure *i*PrOH (1 mL) and sonicated (Fisherbrand FB15051 bath sonicator, ultrasound frequency 37 kHz, 280 W, ultrasonic peak max. 320 W, standard sine-wave modulation). The suspension was transferred to five eppendorfs which were centrifuged (Hettich Mikro 120 centrifuge, 24-tube rotor, 14000 rpm, 18626 g, 10 min). The liquid phase was removed and the black precipitate was dispersed another time in *i*PrOH (1 mL). This procedure was repeated two times more. Finally, the exfoliated TMDCs was suspended in 5 mL of *i*PrOH and transferred to a glass vial.

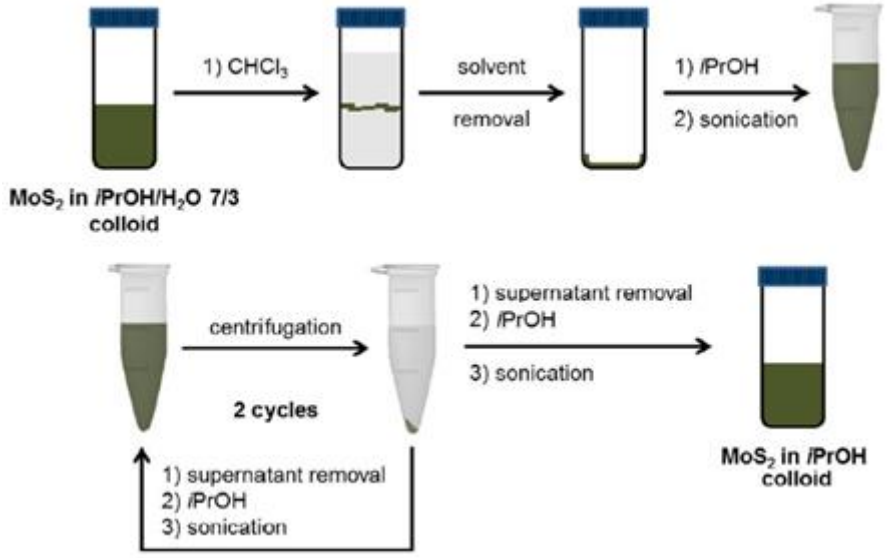

Figure S2. Phase transfer of the solvent.

Characterization of exfoliated TMDCs.

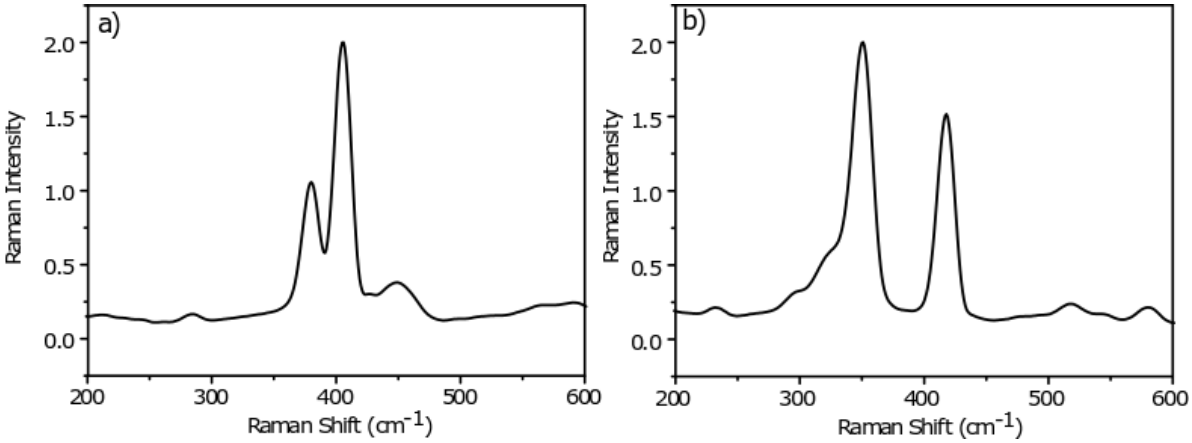

Figure S3. Raman spectroscopy (laser excitation: 532 nm) of exfoliated MoS_2 **(a)** and exfoliated WS_2 **(b).**

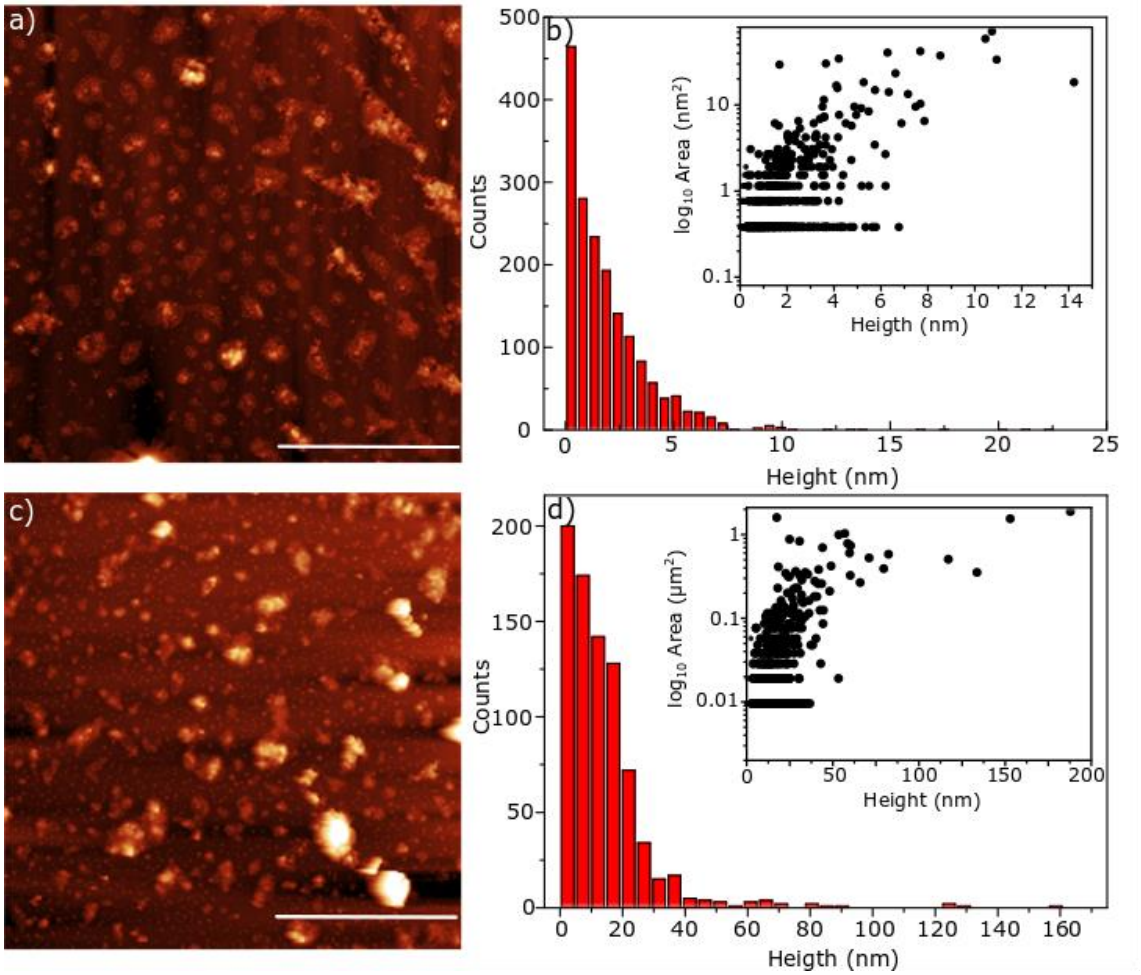

Figure S4. Atomic Force Microscopy (AFM). **a)** Image of exfoliated MoS_2. (Scale 4 μm).

b) Half value of 1730 flakes of the image. Inset: area versus height correlation of the flakes analyzed. Average value of height is less of 5 nm. **c)** Image of exfoliated WS_2. (Scale 10 μm). **d)** Average value of 812 flakes of the image. Inset: area versus height correlation of the flakes analyzed. The half value of height is less of 5 nm.

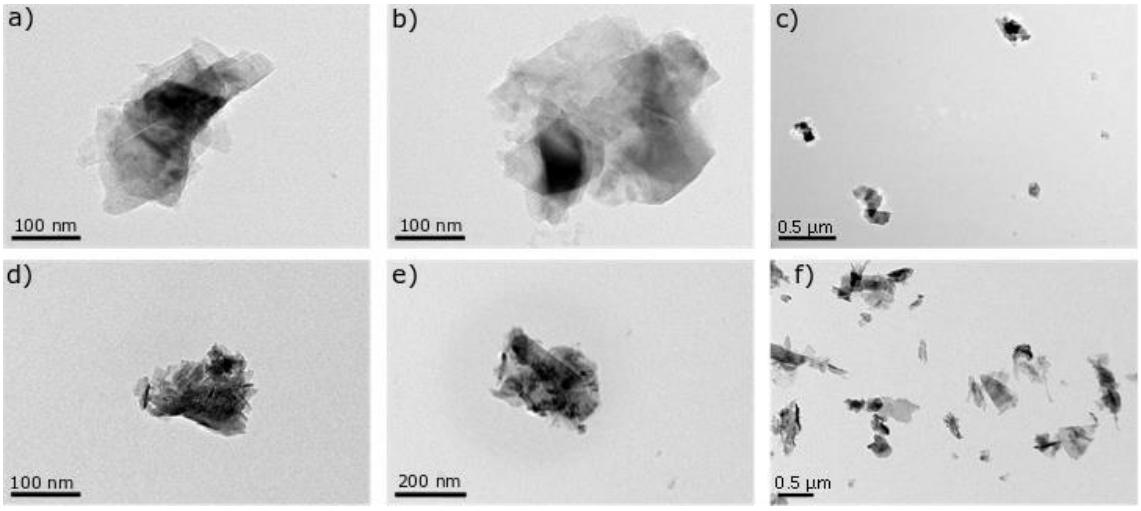

Figure S5. Transmission Electronic Microscopy (TEM) of the exfoliated flakes **a)**, **b)** and **c)** images of exfoliated MoS_2. **d)**, **e)** and **f)** images of exfoliated WS_2.

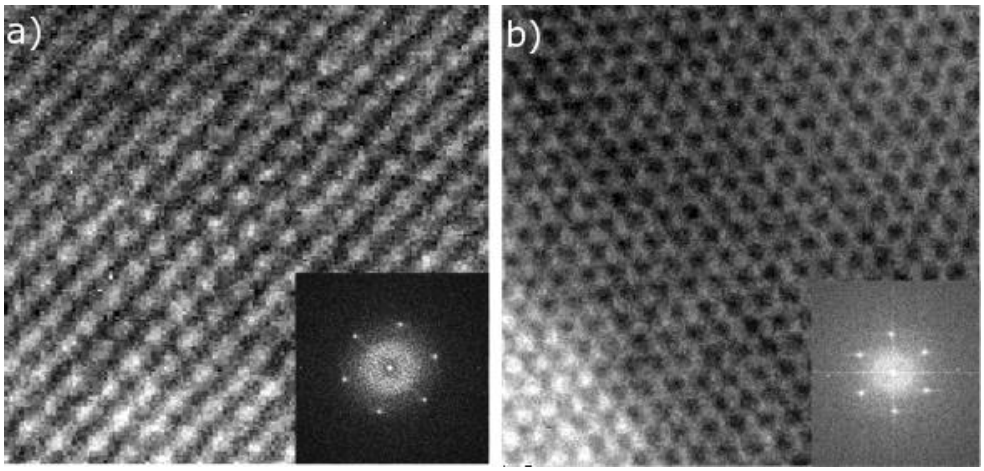

Figure S6. a) High Resolution TEM (HRTEM) of exfoliated MoS_2. Inset, FFT. **b)** HRTEM of exfoliated WS_2. Inset, FFT.

8.4.2.2. Functionalization of TMDCs.

Experimental procedure. 1 mL suspension of exfoliated TMDCs nanosheets in *i*PrOH was transferred to 2 eppendorfs and 0.25 mL of $CHCl_3$ was added in each one. The solvent mixture was sonicated for a few-seconds and the nanosheets were separated from the solvent by centrifugation (14000 rpm, 18626 g, 10 min). The resulting black precipitated was washed with *i*PrOH/$CHCl_3$ 2:1 (v/v, 1 mL per eppendorf), that is, redispersed in the solvent mixture by sonication, and then centrifuged again. This procedure was repeated 2 times more. Finally, 0.5 mL of acetonitrile (ACN) was added to each eppendorf and redispersed (Figure S7). The suspension of each eppendorf was transferred to the same glass vial to do the next step.

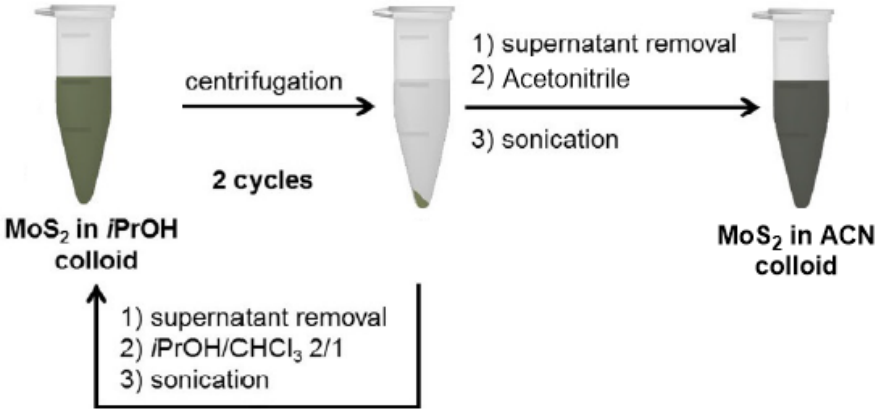

Figure S7. Solvent transfer process previous to the functionalization.

In a glass vial, 1 mL of exfoliated TMDCs nanosheets in ACN and a magnetic stir bar were added. Then, a solution of *N*-benzylmaleimide (190 mg, 1 mmol) in 1 mL of ACN (1 M) was added. Finally, 5 drops of triethylamine (Et_3N) were added to the reaction. The final mixture was stirred overnight at room temperature.

The next day the colour of the suspension was changed to red. The mixture was transferred to 2 eppendorfs (1 mL per eppendorf) and were centrifuged (14000 rpm, 18626 g, 15 min). The red liquid phase was separated from the black precipitate. Then, ACN was added (1 mL per eppendorf) for washing the non-reactive material. The mixture was dispersed by sonication and centrifuged again (14000 rpm, 18626 g, 15 min). This procedure was repeated until *N*-benzylmaleimide was disappeared in the liquid phase (each washed was checked by UV-Visible) (Figure S8). Finally, 1 mL of ACN was added

to each eppendorf and the Bn-succ-TMDCs nanosheets were dispersed. The final suspension was transferred to a glass vial.

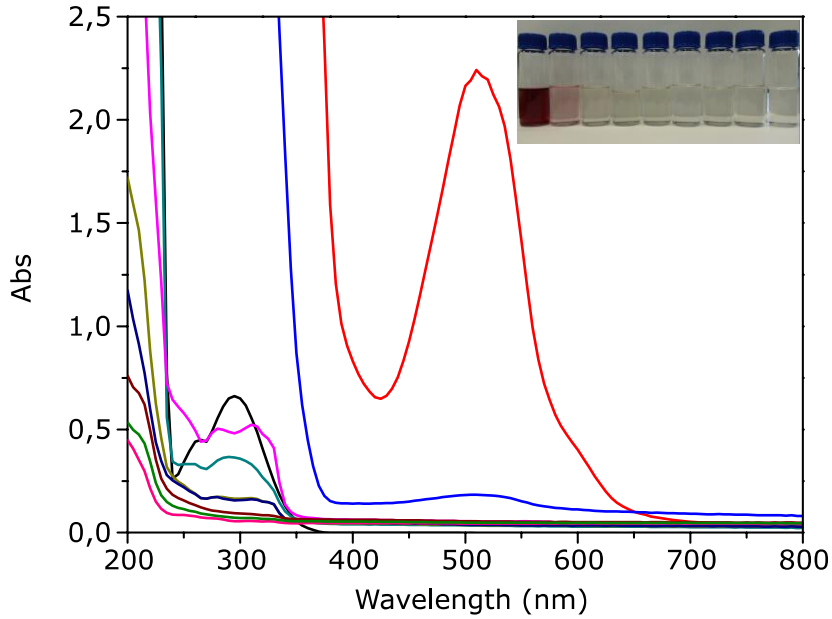

Figure S8. UV-Vis spectroscopy of washed procedure of Bn-succ-TMDCs. In this case, with eight washes was enough to clean the non-reactive material. *N*-benzylmaleimide (black line) is used as reference.

Scale-up of the reaction. In a glass vial, 5 mL of exfoliated TMDCs nanosheets in ACN and a magnetic stir bar were added. Then, *N*-benzylmaleimide (1g, 5 mmol) was added directly to the glass vial. Finally, 5 drops of triethylamine were added to the reaction. The final mixture was stirred overnight at room temperature. The washes of non-reactive material is the same that the previous section.

Characterization of Bn-succ-TMDCs.

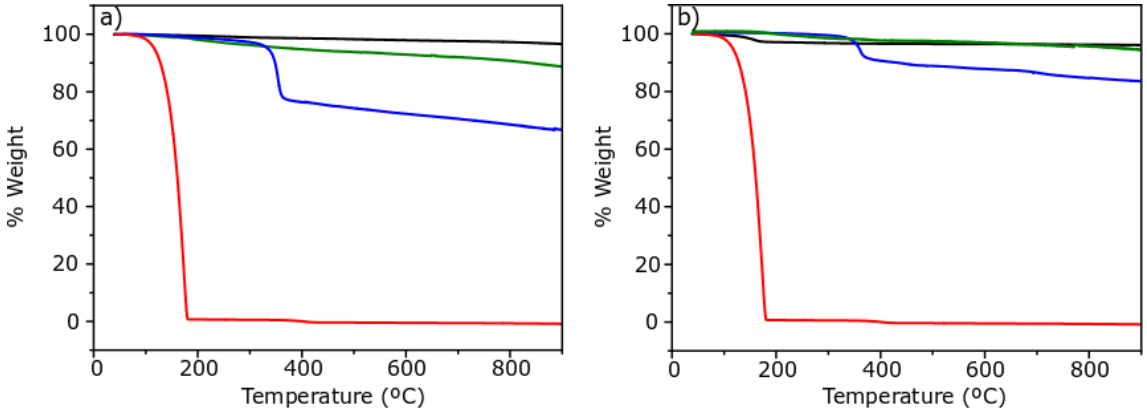

Figure S9. a) Thermogravimetric traces of MoS_2-bulk (black line), exfoliated MoS_2 (green), Bn-succ-MoS_2 (blue) and *N*-benzylmaleimide (red). **b)** WS_2-bulk (black line), exfoliated WS_2 (green), Bn-succ-WS_2 (blue) and *N*-benzylmaleimide (red).

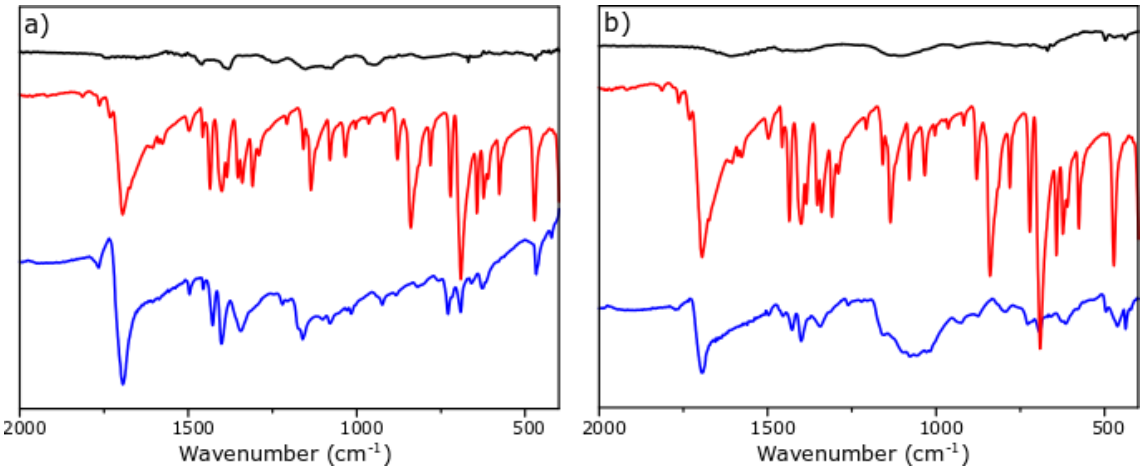

Figure S10. ATR-IR spectroscopy. **a)** Exfoliated MoS_2 (black line), *N*-benzylmaleimide (red) and Bn-succ-MoS_2 (blue). ν $(C=O)_{maleimide}$: 1695 cm^{-1}; ν $(C=O)_{Bn\text{-}succ\text{-}MoS2}$: 1694 cm^{-1}. **b)** Exfoliated WS_2 (black line), *N*-benzylmaleimide (red) and Bn-succ-WS_2 (blue). ν $(C=O)_{maleimide}$: 1695 cm^{-1}; ν $(C=O)_{Bn\text{-}succ\text{-}WS2}$: 1693 cm^{-1}.

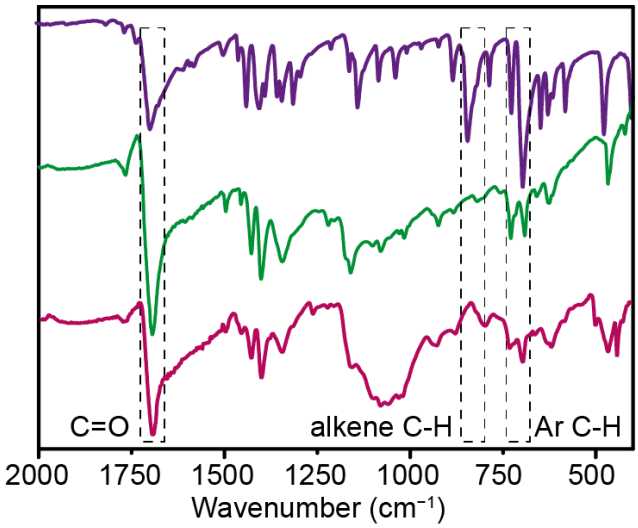

Figure S11. ATR-IR spectroscopy. Comparison between *N*-benzylmaleimide (purple line), Bn-succ-MoS_2 (green) and Bn-succ-WS_2 (magenta).

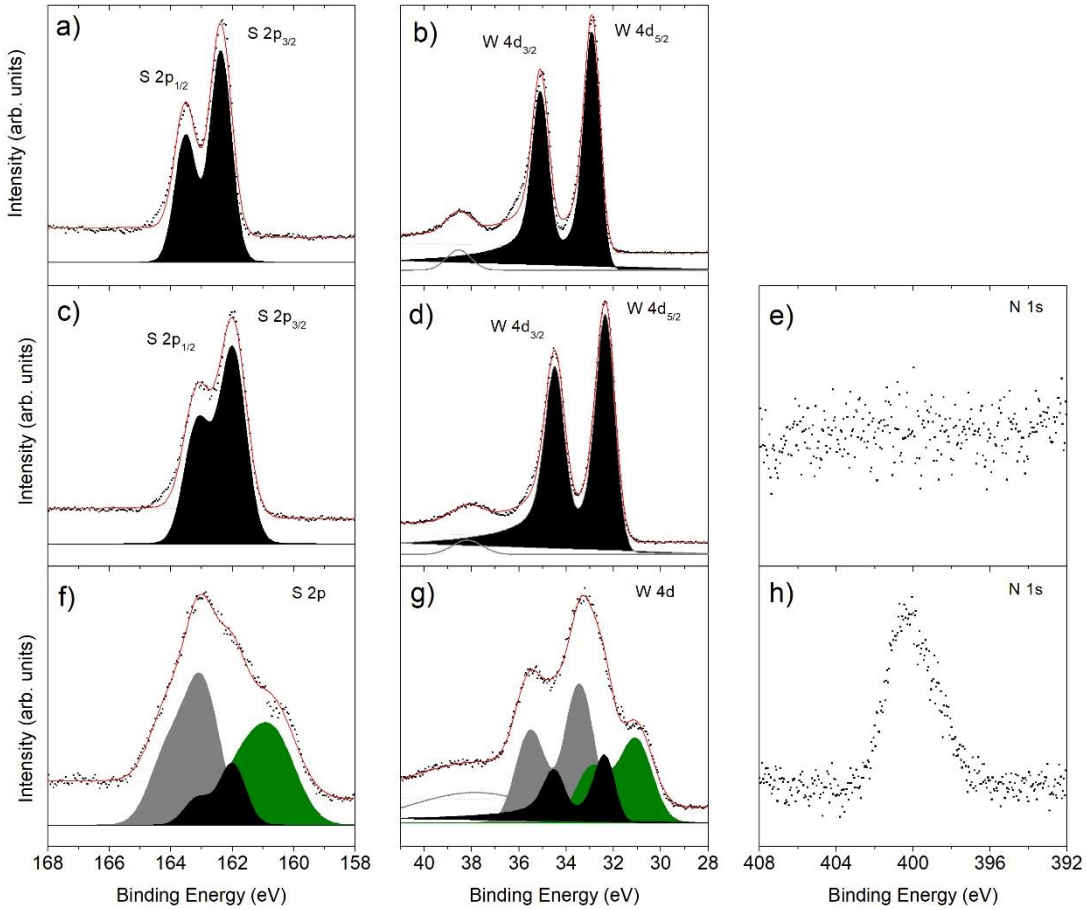

Figure S12. XPS spectra of S, W and N core levels for **a-b)** WS_2 from the bulk material, **c-e)** as obtained in 2-propanol/water (exfoliated WS_2) and **f-h)** Bn-succ-WS_2.

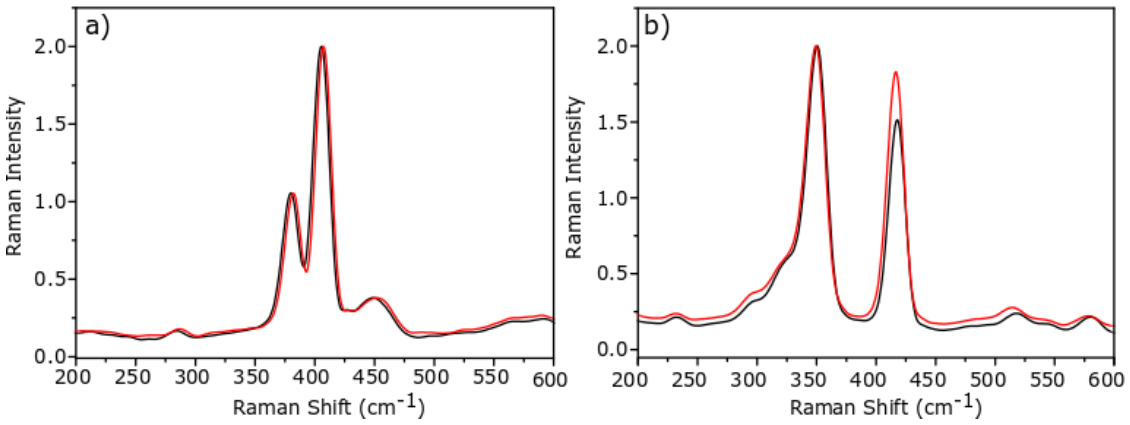

Figure S13. Raman Spectroscopy of Bn-succ-TMDCs (laser excitation: 532nm). **a)** Exfoliated MoS_2 (black line, 380 and 406 cm^{-1}) and Bn-succ-MoS_2 (red line, 382 and 408 cm^{-1}). **b)** Exfoliated WS_2 (black line, 351 and 418 cm^{-1}) and Bn-succ-WS_2 (red line, 350 and 417 cm^{-1}).

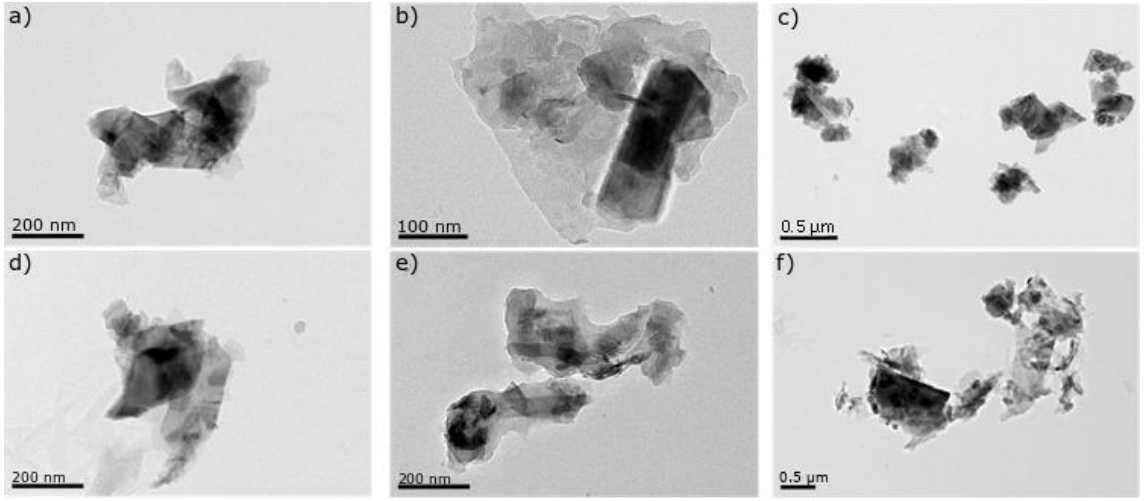

Figure S14. Transmission Electronic Microscopy (TEM) of the functionalized flakes **a)**, **b)** and **c)** images of Bn-succ-MoS_2. **d)**, **e)** and **f)** images of Bn-succ-WS_2.

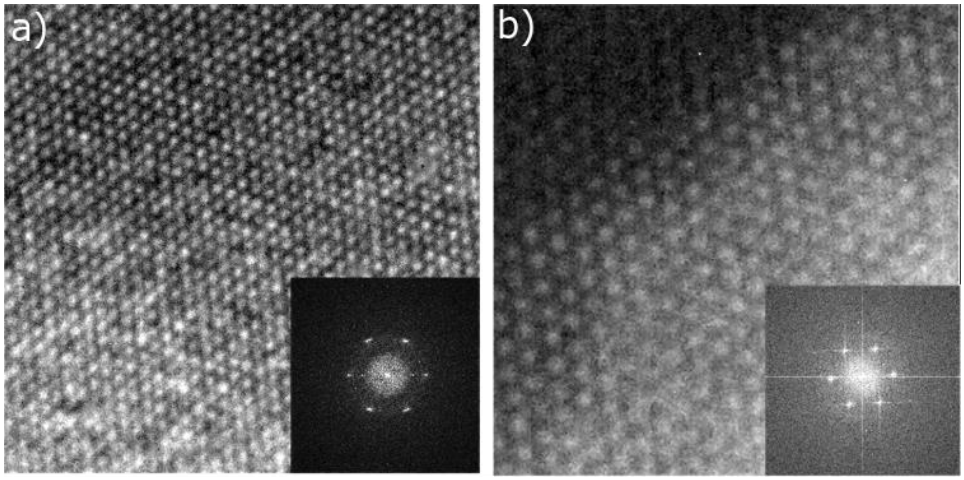

Figure S15. a) High Resolution TEM (HRTEM) of Bn-succ-MoS_2. Inset, FFT. **b)** HRTEM of Bn-succ-WS_2. Inset, FFT.

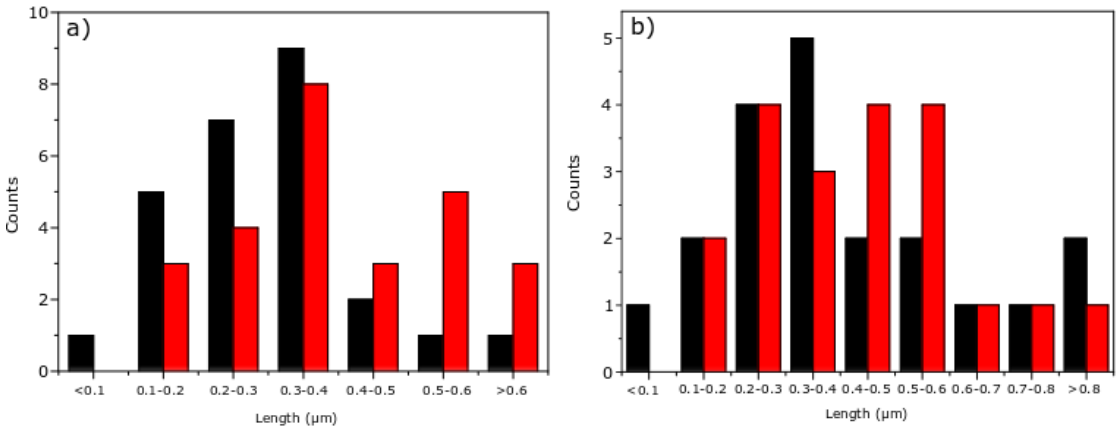

Figure S16. Analysis of length of 26 different flakes of TEM images. **a)** Exfoliated MoS_2 (black) and Bn-succ-MoS_2 (red). **b)** Exfoliated WS_2 (black) and Bn-succ-WS_2 (red).

8.4.2.3. Control experiments.

Reaction without triethylamine. In a glass vial, 1 mL of exfoliated MoS_2 in ACN and a magnetic stir bar were added. Then, a solution of *N*-benzylmaleimide (190 mg, 1 mmol) in 1 mL of ACN (1M) was added. The mixture was stirred overnight at room temperature. The next day the colour of the suspension was not changed. The procedure of washing is the same that the previous section.

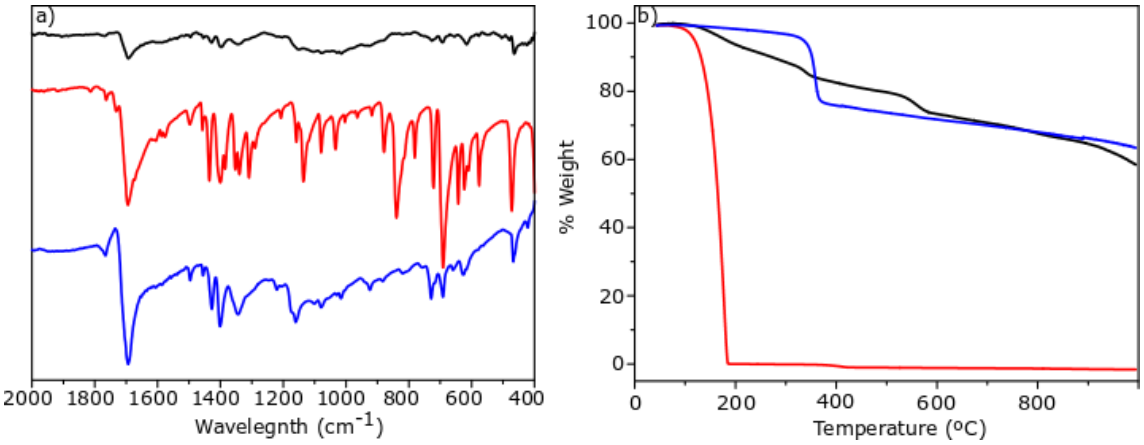

Figure S17. a) ATR-IR spectroscopy. **b)** Thermogravimetric analysis. Blank without Et_3N (black line), *N*-benzylmaleimide (red line) and Bn-succ-MoS_2 (blue).

Reaction in iPrOH/H_2O. In a glass vial, 1 mL of exfoliated MoS_2 in *i*PrOH /H_2O (7:3) and a magnetic stir bar were added. Then, a solution of *N*-benzylmaleimide (190 mg, 1 mmol) in 1 mL of *i*PrOH /H_2O (7:3) (1M) was added (it is not complete soluble). Finally, 5 drops of Et_3N were added to the reaction. The mixture was stirred overnight at room temperature. The next day the colour of the suspension was changed and all of the *N*-benzylmaleimide was dissolved. The procedure of washing is the same that the previous section.

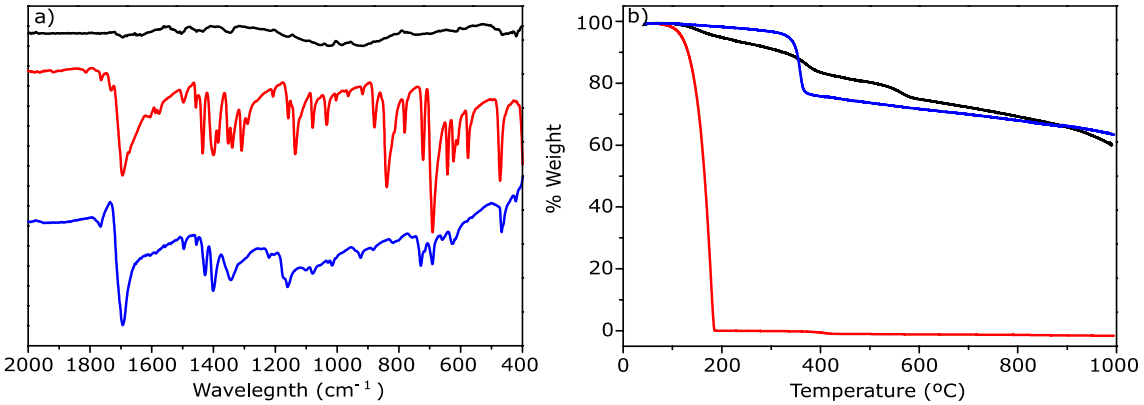

Figure S18. a) ATR-IR spectroscopy. **b)** Thermogravimetric analysis. Blank in IPA/H_2O (black line), *N*-benzylmaleimide (red line) and Bn-succ-MoS_2 (blue)**.**

Reaction in iPrOH. In a glass vial, 1 mL of exfoliated MoS_2 in *i*PrOH and a magnetic stir bar were added. Then, a solution of *N*-benzylmaleimide (190 mg, 1 mmol) in 1 mL of IPA (1M) was added (it is not soluble). Finally, 5 drops of Et_3N were added to the reaction. The mixture was stirred overnight at room temperature. The next day the colour of the suspension was changed a little. The procedure of washing is the same that the previous section.

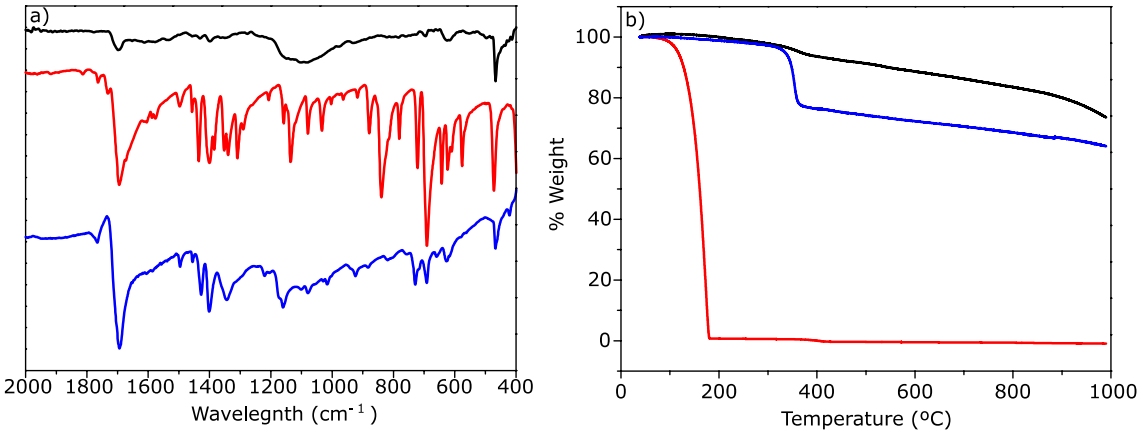

Figure S19. a) ATR-IR spectroscopy. **b)** Thermogravimetric analysis. Blank in *i*PrOH (black line), *N*-benzylmaleimide (red line) and Bn-succ-MoS_2 (blue).

Reaction without washes. In a glass vial, 1 mL of exfoliated MoS_2 in ACN and a magnetic stir bar were added. Then, a solution of *N*-benzylmaleimide (190 mg, 1 mmol) in 1 mL of ACN (1M) was added. Finally, 5 drops of Et_3N were added to the reaction.

The mixture was stirred overnight at room temperature. The next day the colour of the suspension was changed to red. The mixture of the reaction was centrifugated once: The crude was transferred to 2 eppendorfs (1 mL per eppendorf) and were centrifugated (14000 rpm, 18626 g, 15 min). The red liquid phase was separated from the black precipitate. Then, ACN was added (1 mL per eppendorf) and was transferred to a vial.

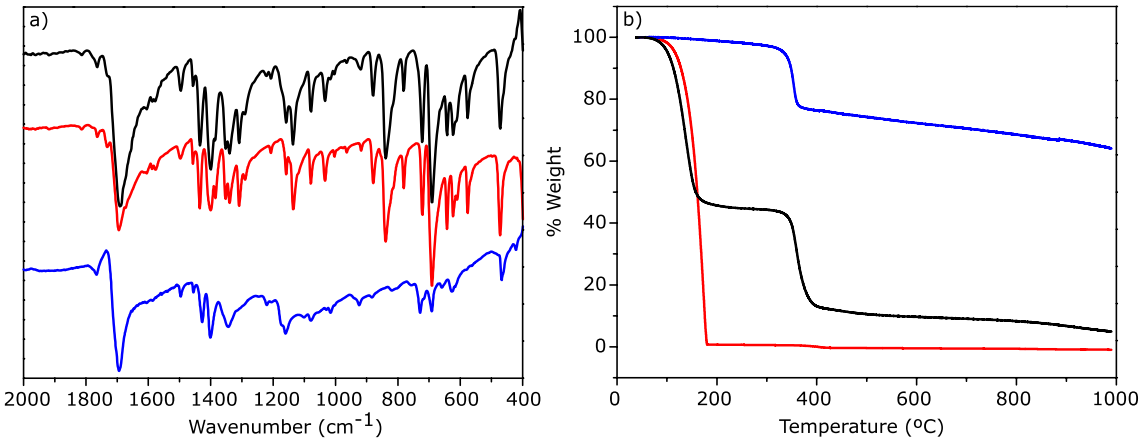

Figure S20. a) ATR-IR spectroscopy. **b)** Thermogravimetric analysis. Blank without washes (black line), *N*-benzylmaleimide (red line) and Bn-succ-MoS_2 (blue).

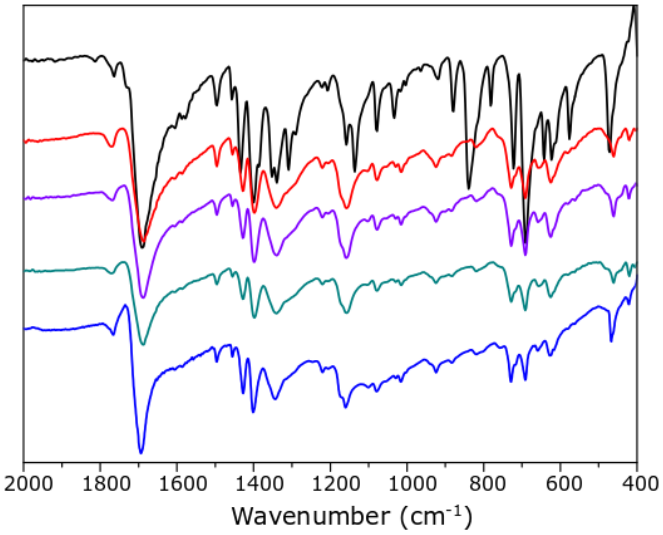

Figure S21. ATR-IR spectroscopy of the washes. Blank without washes (black line), third wash (red), sixth wash (purple), eighth wash (green) and Bn-succ-MoS_2 (blue).

Synthesis of 1-benzyl-3-(propylthio)pyrrolidine-2,5-dione.

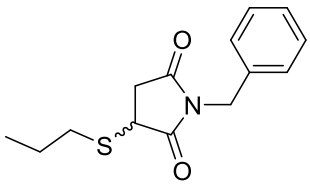

N-benzylmaleimide (200 mg, 1.07 mmol, 1 eq) was dissolved in ACN (14 mL). Then, 1-propanethiol (0.12 mL, 1.23 mmol, 1.15 eq) was added. Finally, triethylamine (0.12 mL, 0.86 mmol, 0.8 eq) was added. The reaction was turned to pink. The reaction was checked by thin-layer chromatography (TLC) (dichloromethane). When the reaction finished, the solvent was evaporated by vacuum. Then, the crude was extracted with dichloromethane and water. The organic phase was dried over Na_2SO_4 and concentrated by vacuum. The product was purified by chromatography column using DCM as eluyent. ^{1}H NMR (400 MHz, $CDCl_3$) δ 7.40 – 7.25 (m, 5H), 4.71 – 4.60 (m, 2H), 3.70 (dd, *J* = 9.1, 3.6 Hz, 1H), 3.11 (ddd, *J* = 18.7, 9.1, 1.6 Hz, 1H), 2.81 (ddd, *J* = 13.0, 8.0, 6.4 Hz, 1H), 2.67 (dd, *J* = 13.7, 6.7 Hz, 1H), 2.57 – 2.48 (m, 1H), 1.73 – 1.52 (m, 2H), 0.98 (t, *J* = 7.4 Hz, 3H). ^{13}C NMR (101 MHz, $CDCl_3$) δ 176.4, 174.5, 135.5, 128.7, 128.7, 128.0, 42.5, 39.0, 36.2, 33.5, 22.4, 13.4.

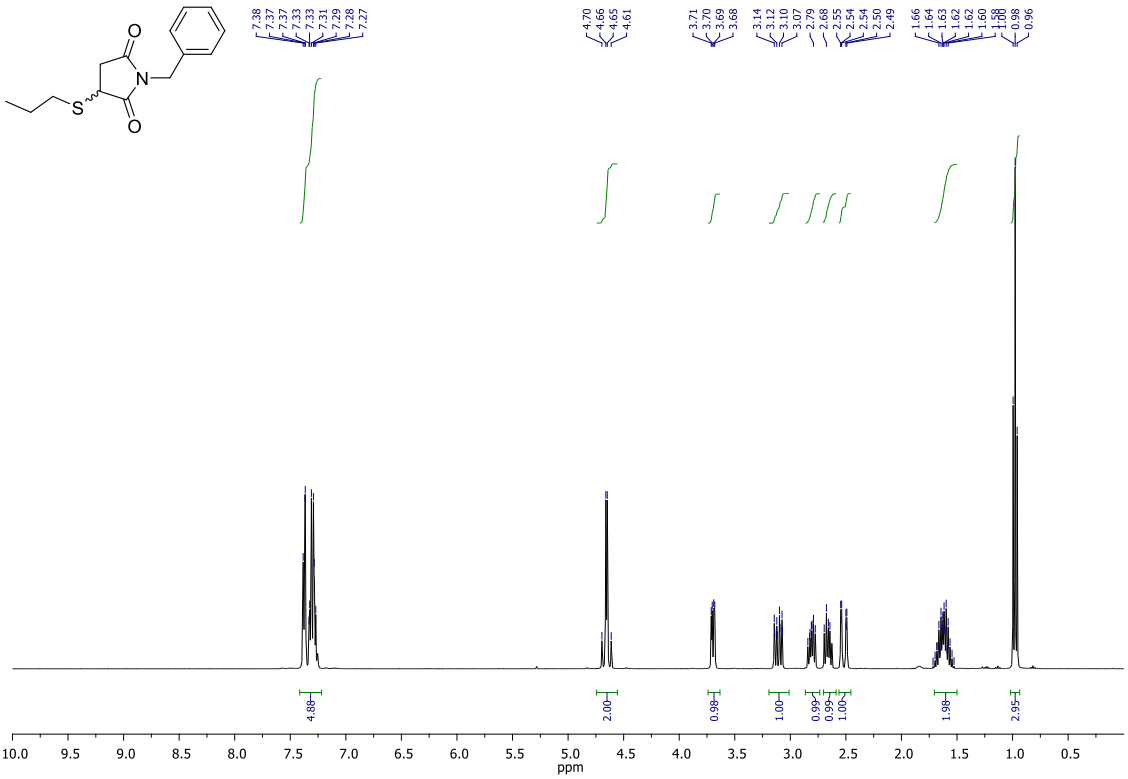

Figure S22. ^{1}H NMR of 1-benzyl-3-(propylthio)pyrrolidine-2,5-dione.

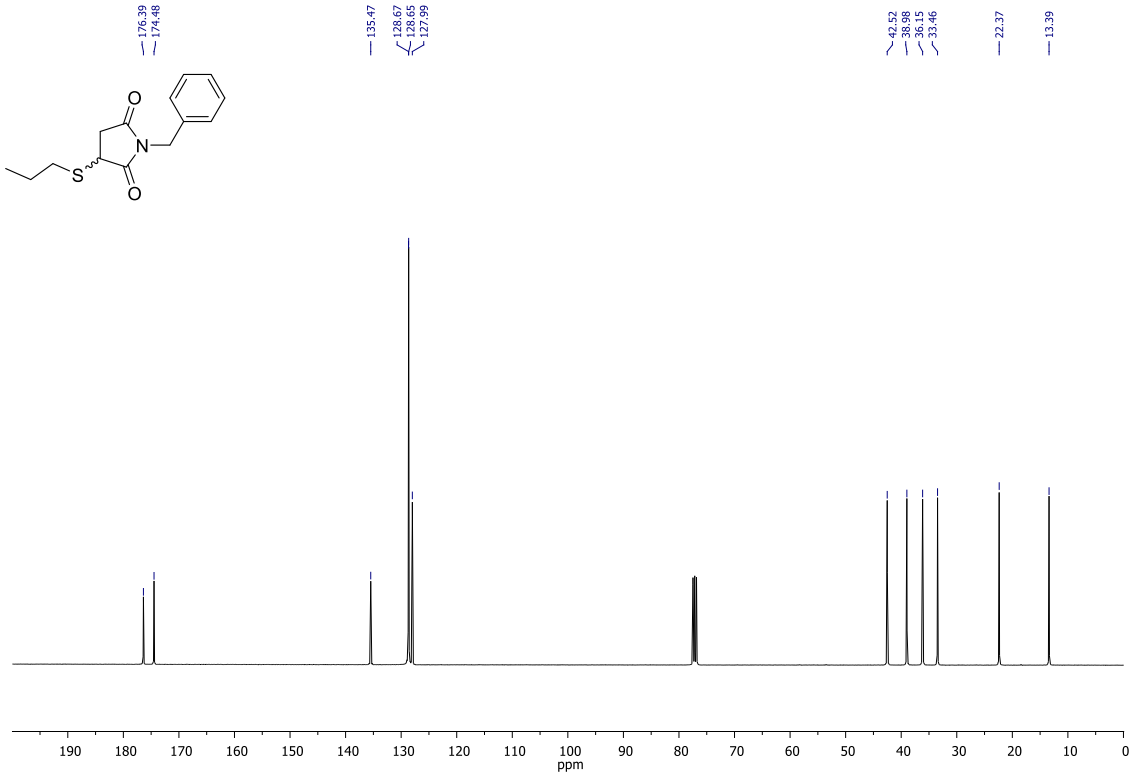

Figure S23. ^{13}C NMR of 1-benzyl-3-(propylthio)pyrrolidine-2,5-dione.

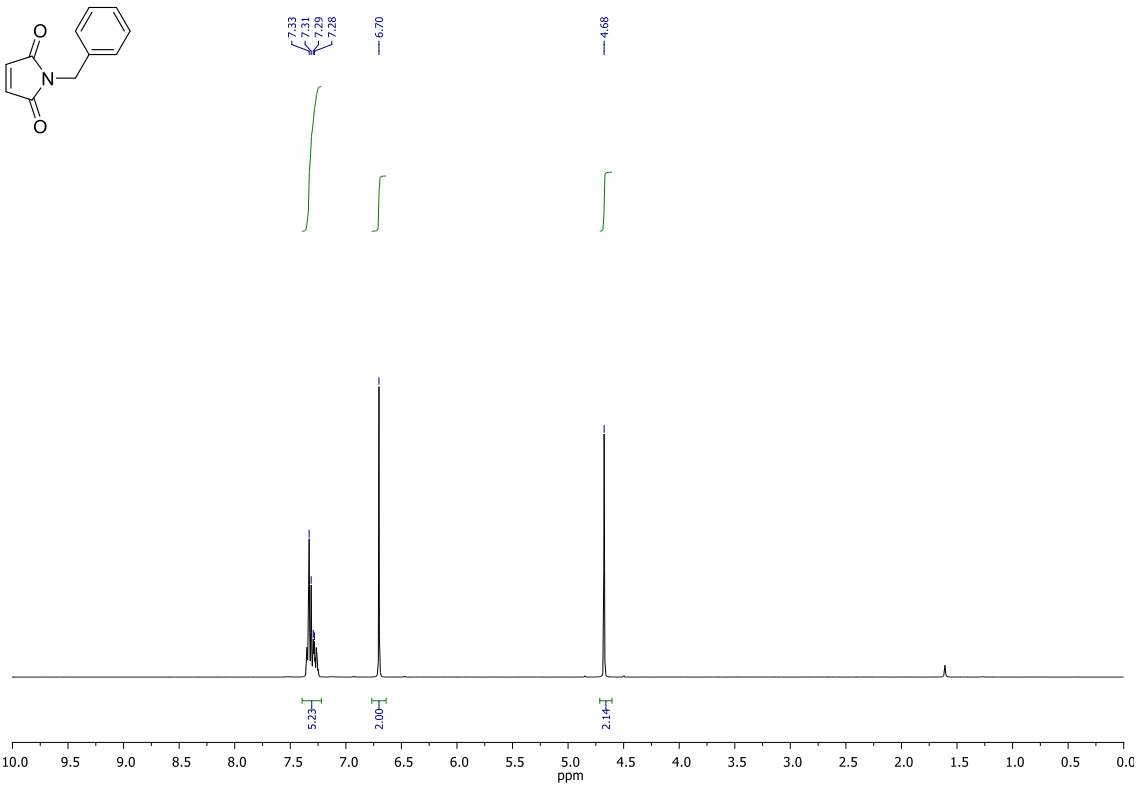

Figure S24. ^{1}H NMR of *N*-benzylmaleimide.

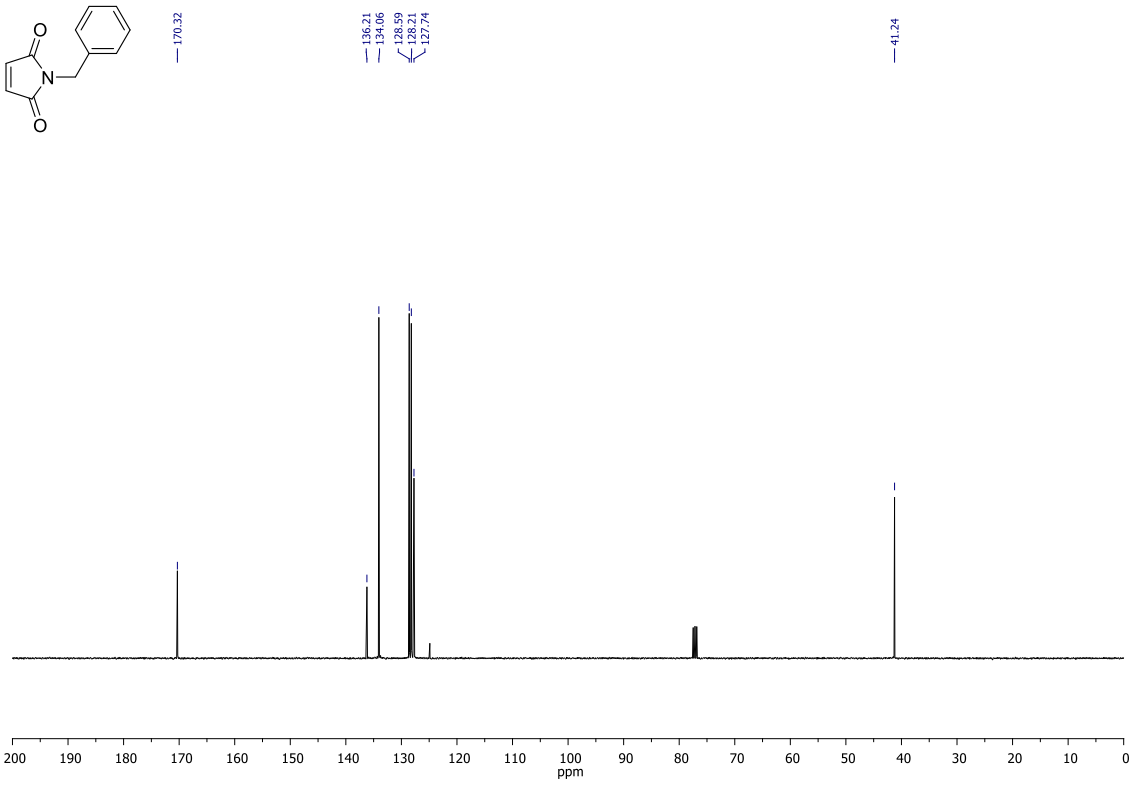

Figure S25. ^{13}C NMR of *N*-benzylmaleimide.

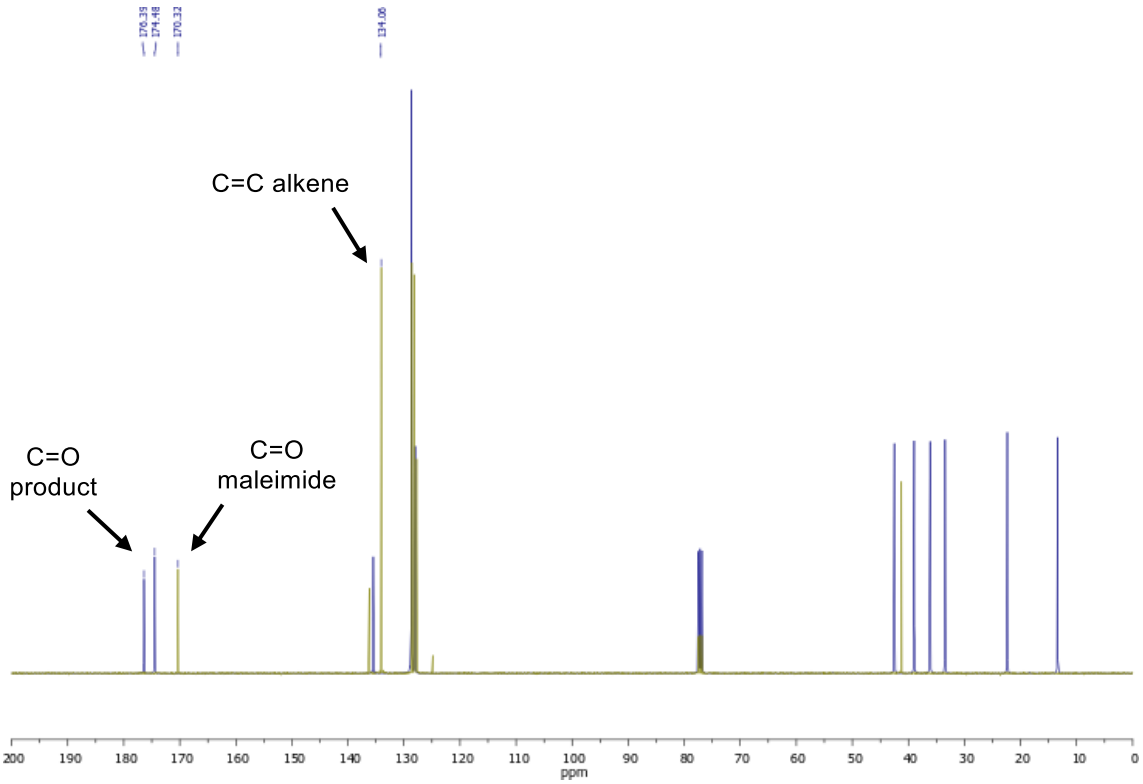

Figure S26. Comparison between ^{13}C NMR of *N*-benzylmaleimide (green spectra) and 1-benzyl-3-(propylthio)pyrrolidine-2,5-dione (blue). The double bond of *N*-benzylmaleimide (134 ppm) disappears and the C=O bond (170 ppm) is shifted downfield and appears two C=O signals (175 and 176 ppm).

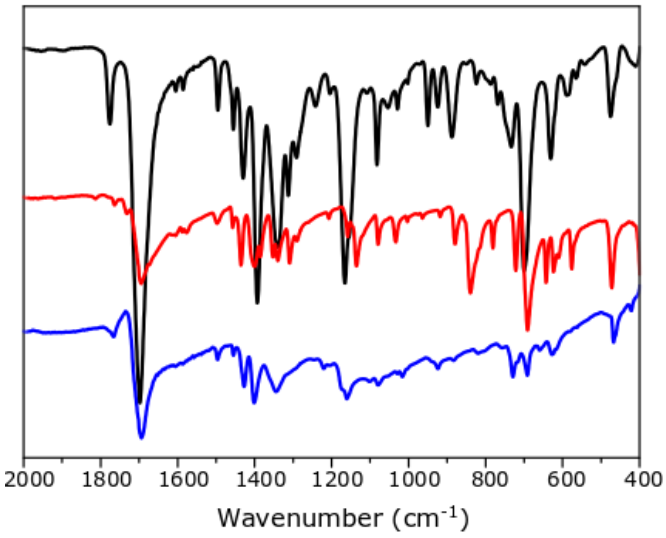

Figure S27. ATR-IR spectroscopy of 1-benzyl-3-(propylthio)pyrrolidine-2,5-dione (black line), *N*-benzylmaleimide (red) and Bn-succ-MoS_2 (blue). C-H from alkene disappears.

8.4.2.4. Reaction with N-methylmaleimide.

In a glass vial, 1 mL of exfoliated MoS_2 in ACN and a magnetic stir bar were added. Then, a solution of *N*-methylmaleimide (111 mg, 1 mmol) in 1 mL of ACN (1M) was added. Finally, 5 drops of Et_3N were added to the reaction. The mixture was stirred overnight at room temperature. The next day, the colour of the suspension was changed to red. The procedure of washing is the same that the previous section.

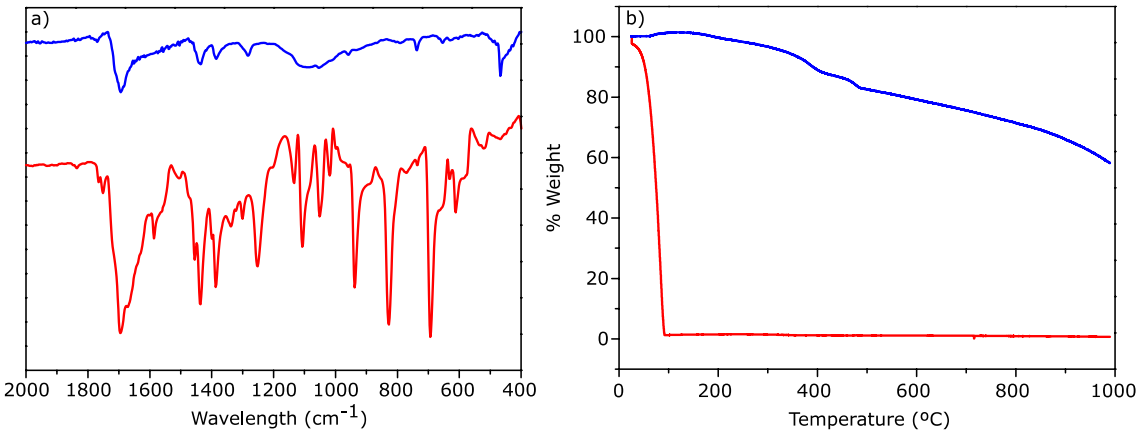

Figure S28. **a)** ATR-IR spectroscopy. **b)** Thermogravimetric analysis. Me-succ-MoS_2 (blue line), *N*-methylmaleimide (red).

Synthesis of 1-methyl-3-(propylthio)pyrrolidine-2,5-dione.

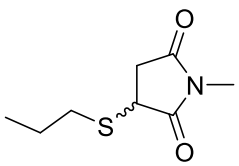

N-methylmaleimide (200 mg, 1.8 mmol, 1 eq) was dissolved in ACN (23 mL). Then, 1-propanethiol (0.20 mL, 2.1 mmol, 1.15 eq) was added. Finally, triethylamine (0.2 mL, 1.4 mmol, 0.8 eq) was added. The reaction was turned to pink. The reaction was checked by thin-layer chromatography (TLC) (dichloromethane). When the reaction finished, the solvent was evaporated by vacuum. Then, the crude was extracted with dichloromethane and water. The organic phase was dried over Na_2SO_4 and concentrated by vacuum. The product was purified by chromatography column using DCM as eluyent. ^{1}H NMR (400 MHz, $CDCl_3$) δ 3.70 (dd, *J* = 9.1, 3.7 Hz, 1H), 3.18 – 3.04 (m, 1H), 2.98 (s, 3H), 2.91 –

2.78 (m, 1H), 2.70 (m, 1H), 2.50 (dd, *J* = 18.7, 3.7 Hz, 1H), 1.76 – 1.52 (m, 2H), 0.99 (t, *J* = 7.4 Hz, 3H). ^{13}C NMR (101 MHz, $CDCl_3$) δ 176.7, 174.8, 39.1, 36.2, 33.7, 25.0, 22.3, 13.4.

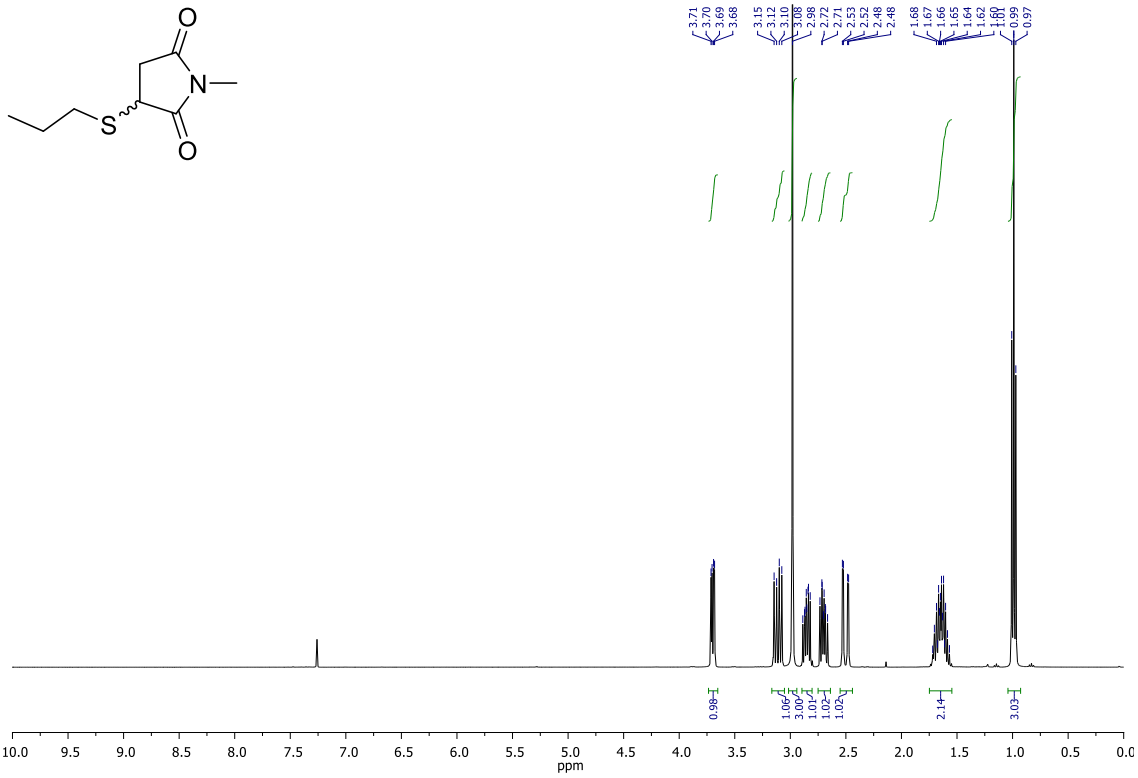

Figure S29. ^{1}H NMR of 1-methyl-3-(propylthio)pyrrolidine-2,5-dione.

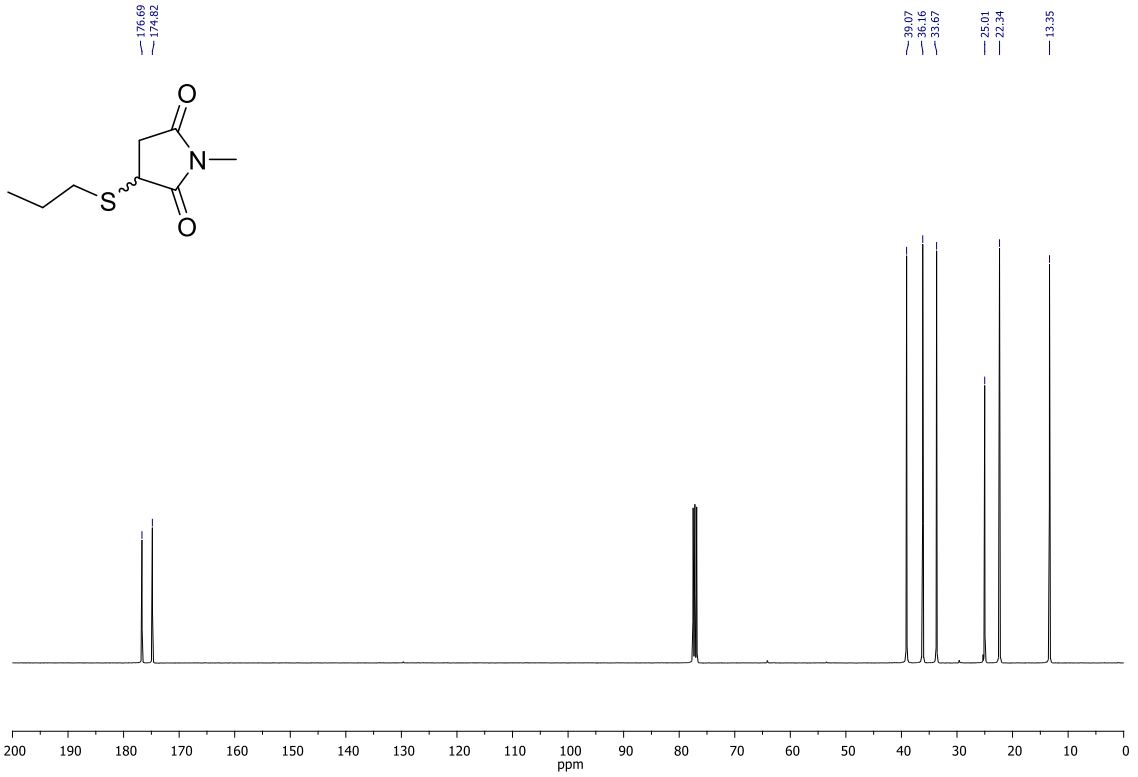

Figure S30. ^{13}C NMR of 1-methyl-3-(propylthio)pyrrolidine-2,5-dione.

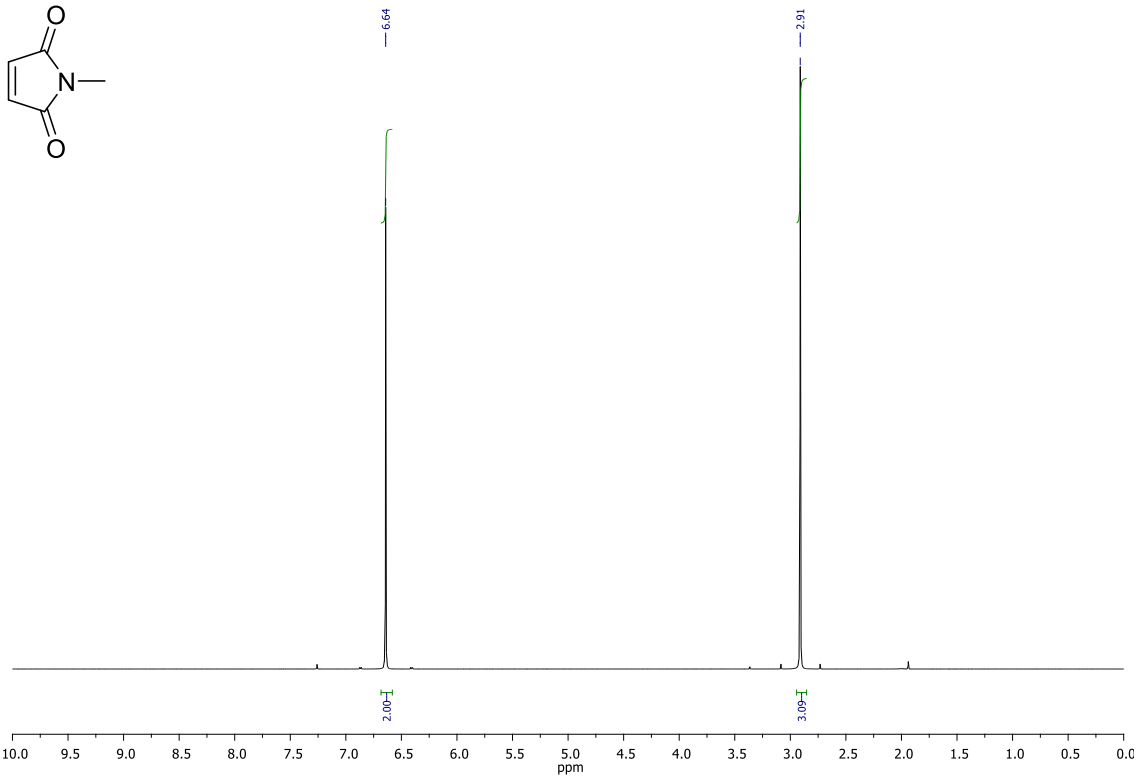

Figure S31. ^{1}H NMR of *N*-methylmaleimide.

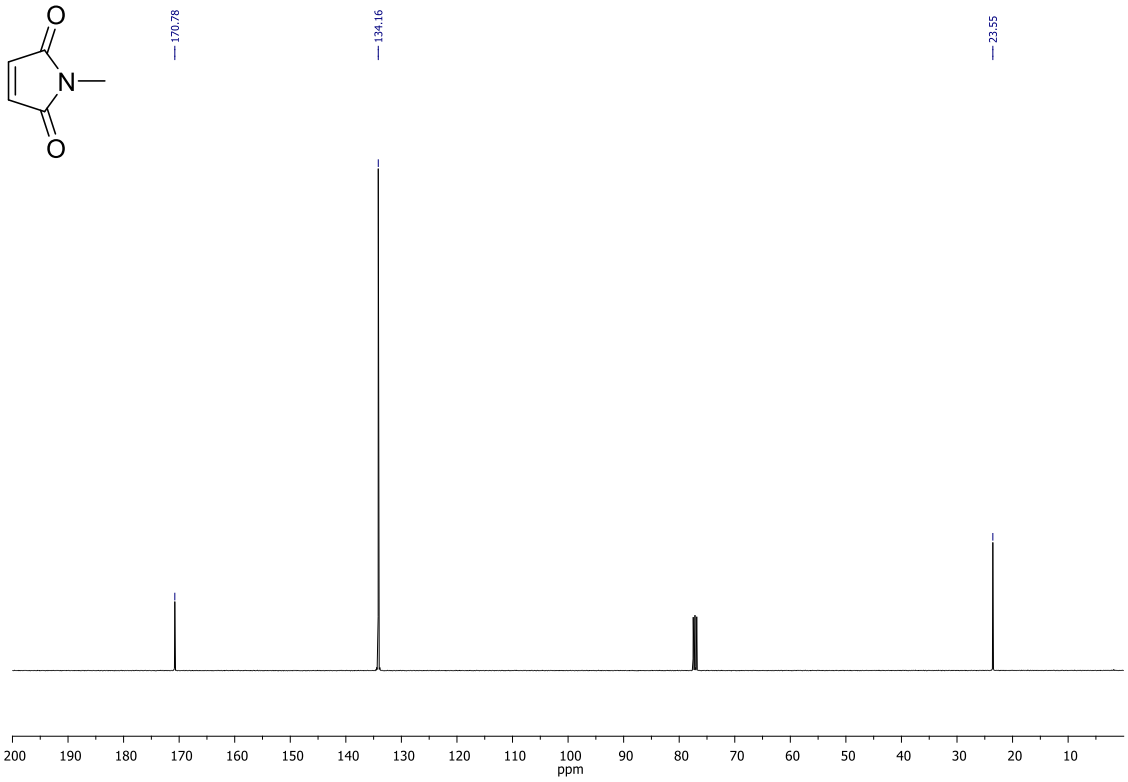

Figure S32. ^{13}C NMR of *N*-methylmaleimide.

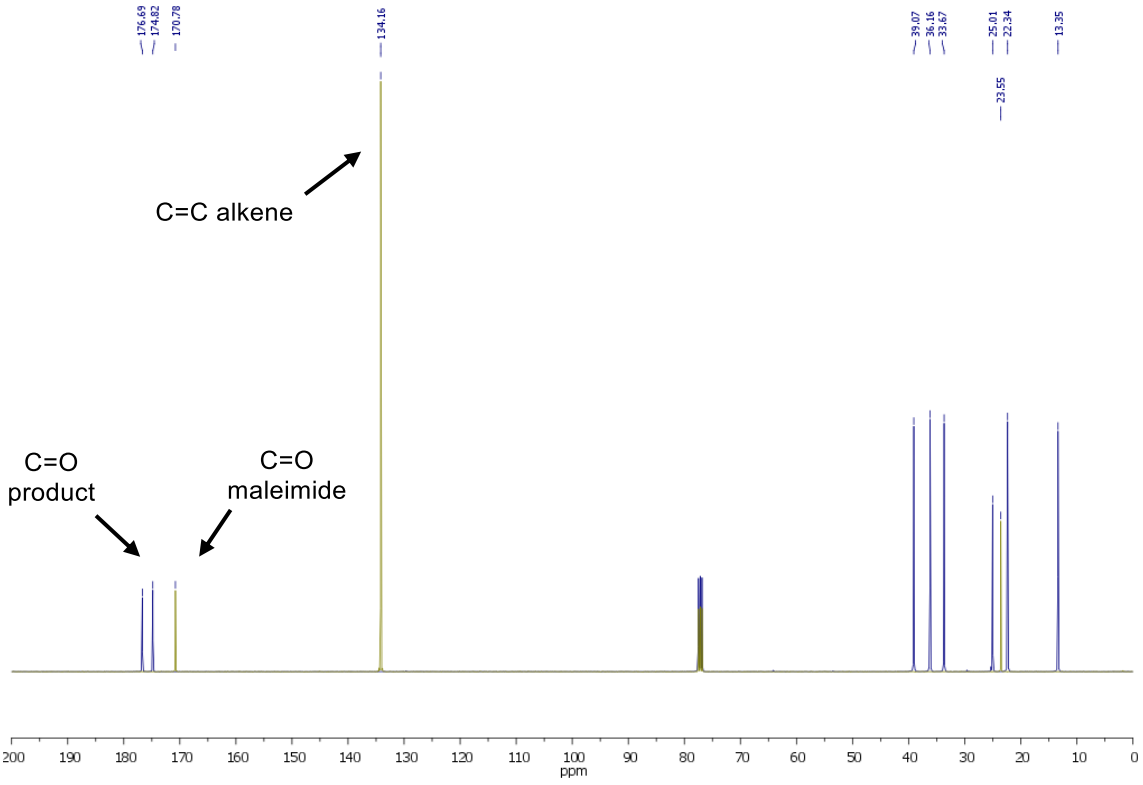

Figure S33. Comparison between ^{13}C NMR of *N*-methylmaleimide (green spectra) and 1-methyl-3-(propylthio)pyrrolidine-2,5-dione (blue). The double bond of *N*-methylmaleimide (134 ppm) disappears and the C=O bond (171 ppm) is shifted downfield and appears two C=O signals (175 and 177 ppm).

8.4.2.5. Colloidal stability experiments.

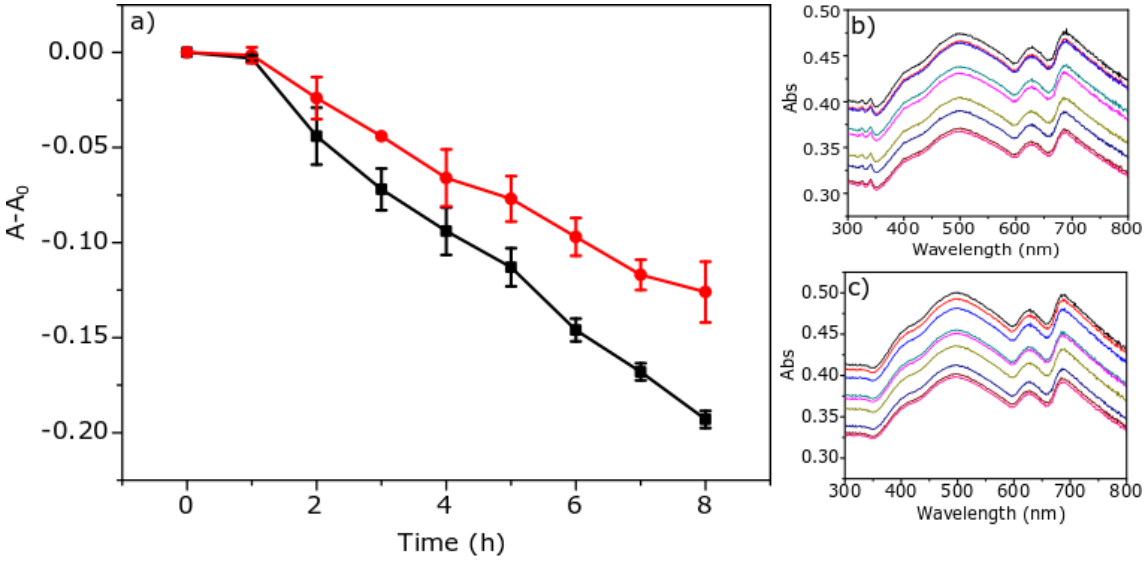

Figure S34. UV-Vis spectroscopy of colloidal stability experiments. **a)** Comparison between the colloidal stability of exfoliated MoS_2 (black line) and Bn-succ-MoS_2 (red) in $CHCl_3$. **b)** UV-Vis spectra of exfoliated MoS_2. **c)** UV-Vis spectra of Bn-succ-MoS_2.

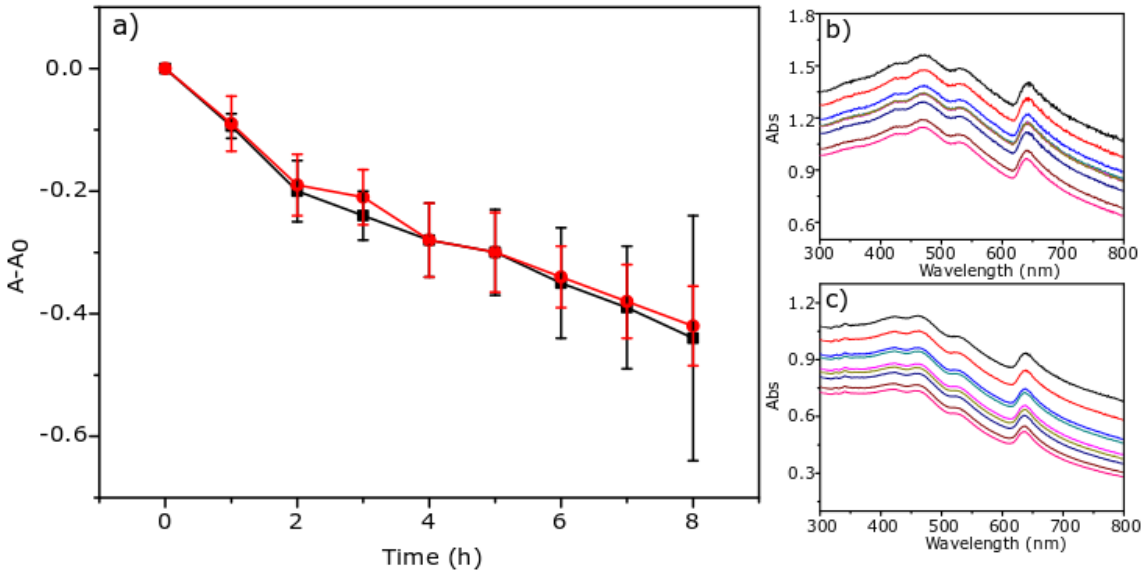

Figure S35. UV-Vis spectroscopy of colloidal stability experiments. **a)** Comparison between the colloidal stability of exfoliated WS_2 (black line) and Bn-succ-WS_2 (red) in $CHCl_3$. **b)** UV-Vis spectra of exfoliated WS_2. **c)** UV-Vis spectra of Bn-succ-WS_2.

Chapter 4.

9. Controlled Covalent Functionalization of 2H-MoS_2 with Molecular Fragments or Polymeric Adlayers

The work described in this chapter has been performed in collaboration with Aragon Nanoscience Institute (INA)[a] of Zaragoza University, Aragon, Spain. This chapter is not already published.

Ramiro Quirós-Ovies[†], Manuel Vázquez Sulleiro[†], Mariano Vera-Hidalgo, Javier Prieto, Víctor Sebastián[a], Jesús Santamaría[a], Emilio M. Pérez*

[†] These authors contributed equally to this work.

The covalent functionalization of TMDCs (MoS_2) remains a challenge, specifically the semiconducting form of MoS_2 (2H-MoS_2) is rather inert. In this work we present a complete study of the reaction of 2H-MoS_2 with maleimides via thiol-Michael Addition, previously studied by our group. We have discovered that the use or not of a base allows for different functionalization according to the type of maleimide, due to the obtaining of a polymer. The study of the reaction has been performed with different solvents, maleimides, times and temperatures.

9.1. **Introduction.**

The ever-expanding toolbox of bidimensional materials and properties offers the promise of a technological revolution.[271] Since the discovery of graphene,[201] many other bidimensional materials have been isolated and characterized.[202] Prominent examples now span the whole range of band-gaps from hexagonal boron nitride (h-BN), an insulator (band-gap ca. 5-6 eV),[272] transition metal dichalcogenides (TMDCs), which are semiconductors with band-gaps in the Vis-NIR region (1-2 eV),[258] to black phosphorus (band-gap 0.3-2 eV).[273,274]

Within this toolbox of new materials, TMDCs show well defined bandgaps that make them particularly suitable for semiconductor technology.[213,215,275] The development of reliable tools for the chemical modification of TMDCs is crucial to achieve their full technological potential.[204,210,238,276] Decoration of TMDCs materials with molecular fragments via noncovalent approaches, mostly based on dispersion/solvophobic interactions, is relatively easy and has consequently led the way towards potential applications. For example, selective chemical sensors[277,278] and enhanced photodetectors[279,280] have already been described using this strategy. Methods for the covalent modification of TMDCs are much scarcer and nearly exclusively limited to the metallic 1T phase.[241,242,281]

Several groups have described a protocol for obtaining colloidal semiconducting 2H-MoS_2 through liquid phase exfoliation from the bulk.[217,236,256,270] In our strategy, inspired by the many examples of thiol-ene chemistry in polymer chemistry and biochemistry,[167,178,263] we exploited the soft nucleophilicity of sulfur to make it react with

[271] Ferrari, A. C.; *et al. Nanoscale* **2015,** *7* (11), 4598-4810.
[272] Pakdel, A.; Bando, Y.; Golberg, D., *Chem. Soc. Revi.* **2014,** *43* (3), 934-959.
[273] Li, L.; Yu, Y.; Ye, G. J.; Ge, Q.; Ou, X.; Wu, H.; Feng, D.; Chen, X. H.; Zhang, Y., *Nat. Nanotechnol.* **2014,** *9*, 372.
[274] Castellanos-Gomez, A. *et al. 2D Mater.* **2014,** *1* (2), 025001.
[275] Yin, Z.; Li, H.; Li, H.; Jiang, L.; Shi, Y.; Sun, Y.; Lu, G.; Zhang, Q.; Chen, X.; Zhang, H., *ACS Nano* **2012,** *6* (1), 74-80.
[276] Ippolito, S.; Ciesielski, A.; Samorì, P., *Chem. Commun.* **2019,** *55* (61), 8900-8914.
[277] Chen, W. Y.; Yen, C.-C.; Xue, S.; Wang, H.; Stanciu, L. A., *ACS Appl. Mater. Interfaces.* **2019,** *11* (37), 34135-34143.
[278] Xiao, M.; Man, T.; Zhu, C.; Pei, H.; Shi, J.; Li, L.; Qu, X.; Shen, X.; Li, J., *ACS Appl. Mater. Interfaces.* **2018,** *10* (9), 7852-7858.
[279] Molina-Mendoza, A. J.; Vaquero-Garzon, L.; Leret, S.; de Juan-Fernández, L.; Pérez, E. M.; Castellanos-Gomez, A., *Chem. Commun.* **2016,** *52* (100), 14365-14368.
[280] Yu, S. H.; Lee, Y.; Jang, S. K.; Kang, J.; Jeon, J.; Lee, C.; Lee, J. Y.; Kim, H.; Hwang, E.; Lee, S.; Cho, J. H., *ACS Nano* **2014,** *8* (8), 8285-8291.
[281] Tang, Q.; Jiang, D.-e., *Chem. Mater.* **2015,** *27* (10), 3743-3748.

the prototypical soft electrophile, maleimides[282] (Figure 1). Here, we present a comprehensive study of the covalent functionalization of MoS_2 with maleimides through Michael addition. Via systematic changes to the different variables in the reaction conditions, we describe a reliable protocol for the molecular modification of MoS_2 with maleimides featuring a wide range of chemical functionalities. This reveals the formation of a covalently connected organic polymer adlayer when using increased amounts of molecular reagent in combination with a base. Therefore, the unexpected result can be useful in certain circumstances and might be common to other functionalization protocols.

9.2. **Results.**

Few-layers MoS_2 colloids were obtained through LPE in *N*-methyl-2-pyrrolidone, NMP, using an ultrasonic probe. In this case, we resorted to NMP instead of *i*PrOH-water[282] to increase the concentration of the colloids and facilitate characterization. Exfoliated MoS_2 was separated from non-exfoliated material using centrifugation. The formation of few-layer 2H-MoS_2 was proved by UV-Vis extinction, Raman spectroscopy, and X-ray Powder Diffraction (XRD) (See Figures S1-3).

The dispersion of exfoliated MoS_2 was transferred to acetonitrile (ACN), following a protocol described previously,[264] then *N*-benzylmaleimide (Bn-mal, **1**) and triethylamine (Et_3N) were added and the mixture was stirred overnight (Figure 1). The mixture was washed with ACN and *i*PrOH to remove all physisorbed Bn-mal, which was confirmed by UV-Vis of the residues (Figure S5). Moreover, TGA profiles of the mixture without any wash can clearly differentiate between physisorbed (weight loss at 170 ºC) and covalently attached maleimide (Figure S6). We first analyzed the degree of functionalization with varying degree of exfoliation, by fine-tuning the sonication conditions and centrifugation procedure, using TGA (Table S1). Unsurprisingly, we observed that for materials with a higher degree of exfoliation (those obtained with harder centrifugation conditions) a higher degree of functionalization is obtained. We also investigated the influence of the reaction time, temperature, and the relative concentration of reagents on the degree of functionalization (Table S1). The main observations that result from these studies can be summarized as follows: We note that the reaction is fast,

[282] Vera-Hidalgo, M.; Giovanelli, E.; Navío, C.; Pérez, E. M., *J. Am. Chem. Soc.* **2019,** *141* (9), 3767-3771.

nearly complete after 1h (70% functionalization by TGA, see Figure S7) and only increases to 80% after 16h. Temperature studies showed that the reaction could be performed from room temperature until reflux (Figure S8). However, the functionalization degree is reduced with increasing temperature; these results are influenced by the stability of the dispersed MoS_2, which is less stable at higher temperatures. The use of different concentrations of MoS_2 has a significant effect on the surface functionalization, following the expected tendency, that is, the more the MoS_2 solution is diluted (i.e. the larger the excess of Bn-mal) the more it is functionalized (Figure S9). Furthermore, similar variations were observed by reducing the concentration of **1** (Figure S10). Decreasing the amount of *N*-benzylmaleimide results in a lower functionalization. However, due to the small difference between 1 and 5 mmol of **1**, we conclude that we are employing a large excess of Bn-mal. In fact, a quick calculation reveals that, even under our milder conditions (entry 23, table S1), we are using 16 equivalents of Bn-mal with respect to S assuming that all sulfur atoms might be reactive, and therefore should be considered a limit at the very low end, probably of by at least an order of magnitude. In conjunction with this, we note that the degree of functionalization observed by TGA is too large to be compatible with the decoration of MoS_2 with molecular Bn-succ. We therefore decided to fully characterize a Bn-succ-MoS_2 sample, which presented a 66% weight loss in comparison with reference MoS_2, which was subjected to identical reaction and purification conditions in the absence of Bn-mal (Figure 1b). The slow decomposition of reference MoS_2 (black trace), observed between approximately 370 and 550ºC from the derivative, amounts to a total of 14% weight, and corresponds to the oxidation of MoS_2 due to the presence of air in the experiment;[283] Bn-succ-MoS_2, in contrast (orange trace), first shows the onset of a similar slow weight loss due to oxidation, which is quickly overlapped by a rapid and quantitative more significant loss (390-420 ºC) and a second rapid loss (ca. 450-550 ºC) that can be attributed to the covalently attached organic moieties. The fact that we do not observe any weight loss before 350 ºC in Bn-succ-MoS_2 confirms the absence of physisorbed Bn-mal (purple trace, compared with unwashed samples in Figure S6). ATR-FTIR of Bn-succ-MoS_2 (Figure 1c) showed conclusive evidence of functionalization, like the presence of the main vibrational modes of **1** like the carbonyl stretch (1714 cm^{-1}) and the disappearance

[283] Chu, X. S.; Li, D. O.; Green, A. A.; Wang, Q. H.,. *J. Mat. Chem.* **2017,** *5* (43), 11301-11309.

of the alkene C-H bending mode (840 cm^{-1} in **1**) and the emergence of a S-C stretching mode (728 cm^{-1}) that confirms the covalent functionalization of the material through a new S-C covalent bond.[282] X-ray photoemission spectroscopy (XPS) further confirmed the covalent attachment of **1** (Figure 1d, Figure S11-12, Table S2). As a reference, the core level of C is centered at adventitious carbon (284.8 eV). The Bn-succ-MoS_2 preserved the 2-H polymorphism. However, we find clear differences with the pristine MoS_2 and, more importantly, with the control sample experiment (*cs*-MoS_2). S 2p (162.7 eV) peak becomes broader, a new component is required for a better fitting that corresponds well to the formation of a S-C bond. N 1s peak from the succinamide core, which is absent in the control MoS_2, is clearly visible upon functionalization at 400.7 eV. The presence of new bands in the carbon region is in good agreement with new components for C=O (288.7 eV), C-S (287.0 eV) and C-N (286.0 eV). XRD and Raman spectroscopy do not present a significant shift on the signals after functionalization. (Figure S13-14).

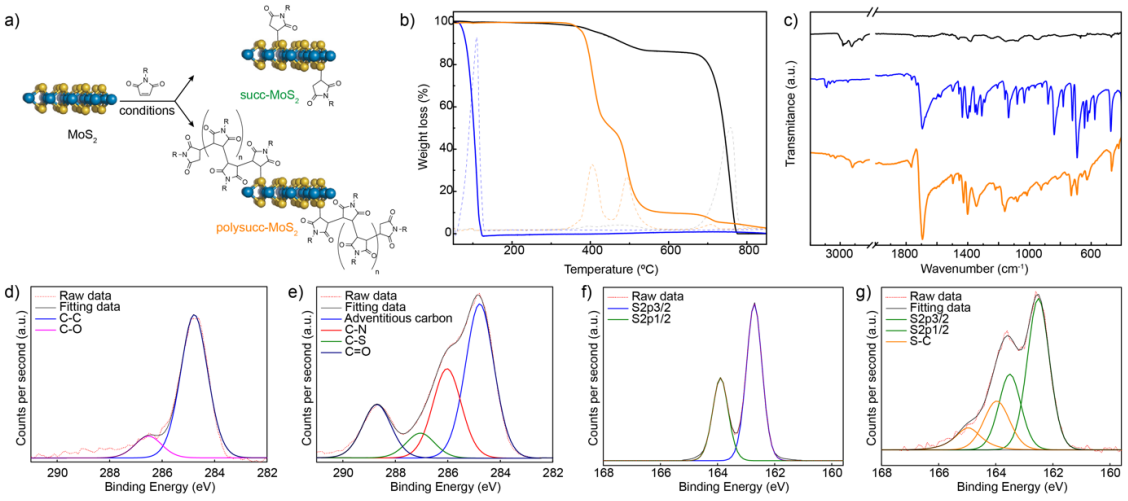

Figure 1. **a)** General scheme for different functionalization of MoS_2: succ-MoS_2 without base and Bn-succ-MoS_2 with base. **b)** TGA of bulk MoS_2 (black line), Bn-mal (blue) and Bn-succ-MoS_2 with base (orange). **c)** ATR-FTIR of bulk-MoS_2 (black line), Bn-mal (blue) and Bn-succ-MoS_2 with base (orange). **d)-g)** XPS experiments of Bn-succ-MoS_2 with base.

Some examples of high functionalization of MoS_2 are reported in the literature.[241,244,245] In this work, the large degree of functionalization shown on TGA (80 %) differs markedly from that determined by XPS (12.8 % of the S-C new component should correspond to a 23% weight loss in TGA. See Eq S1). Some studies pointed out the possibility of the homopolymerization and copolymerization of *N*-functionalized maleimides in the presence of bases.[284,285,286] To investigate if the formation of polysuccinimides of this type was feasible under our reaction conditions, we prepared a mixture of **1** (5 mmol) and Et_3N and stirred it overnight in ACN. After separation of unreacted **1**, 1.5% of the initial weight was isolated as insoluble pink powder. MALDI-TOF analysis confirmed the formation of a polymer with a periodic repetition of 187 Da, which corresponds perfectly to the succinimide fragments of polysucc (Figure 1a). The formation of a Gaussian envelope from 2 to 10 kDa with a maximum peak at 4890 corresponds to 26 units of homopolymer, (Figure S15). Furthermore, ^{1}H NMR experiments confirm the disappearance of the alkene signals, and the appearance of signals, at 4.61 and 4.40, that can be attributed to the new aliphatic protons. Moreover, all signals appear broadened, which is characteristic of the formation of high-molecular weight species (Figure S16).

The strong evidence of formation of S-C bond (IR and XPS) presented above suggests that MoS_2 is functionalized covalently with polysucc, rather than physisorption of the polymer after formation in solution. A functionalization with polysucc will also be consistent with the large weight loss observed by TGA. AFM and STEM micrographs also support this hypothesis. In AFM we observe that the polysucc-MoS_2 flakes present roughness of a height of 15 nm, with phase contrast very similar to that of the pure polysucc (Figure S17). With the element sensitive resolution of STEM, we confirm that we do not find self-standing polymer particles, but rather MoS_2 flakes surrounded by amorphous organic matter (Figure 2).

[284] Haas, H. C.; MacDonald, R. L., *J.Polymer Science: Polym. Chem. Ed.* **1973,** *11* (2), 327-343.
[285] Kojima, K.; Yoda, N.; Marvel, C. S., *J. Polym. Sci.: Polym. Chem.* **1966,** *4* (5), 1121-1134.
[286] Abel, B. A.; McCormick, C. L., *Macromolecules* **2016,** *49* (17), 6193-6202.

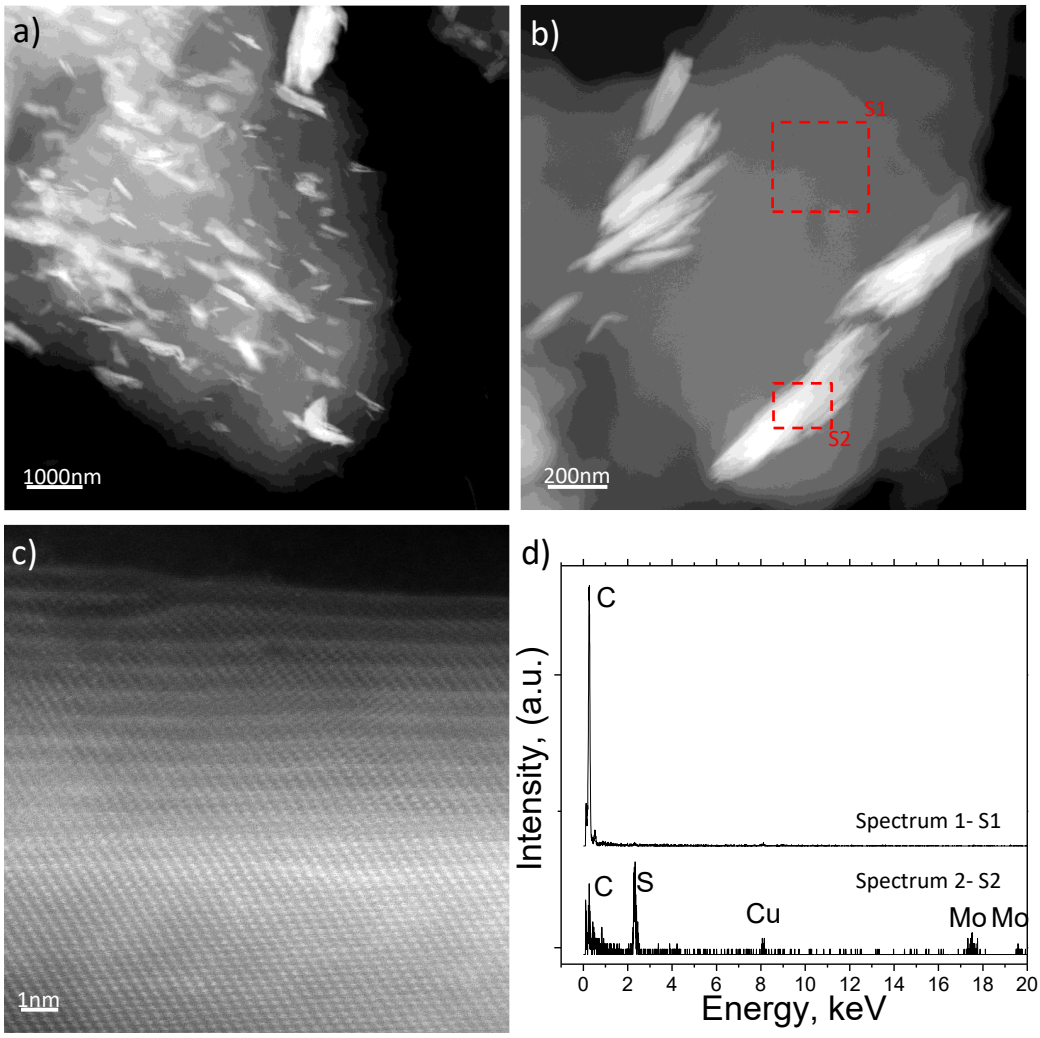

Figure 2. **a-c)** High-angle annular-dark-field scanning transmission electron microscopy (HAADF-STEM) images at different magnifications of polysucc-MoS_2 flakes. An organic layer with a less bright contrast than MoS_2 flakes was observed. **d)** Energy Dispersive X-Ray Spectroscopy analysis of dashed-red line areas in b).

We note that grafting polymers onto the surface of 2D materials can be useful to decorate them with multiple functional groups, for instance to enhance binding to biomolecules for biosensing purposes,[287,288,289] but is typically not the desired outcome when reacting molecules with nanomaterials.[290] We therefore studied how to control/prevent polymerization to obtain exclusively molecular functionalization. In this

[287] Kalantar-zadeh, K.; Ou, J. Z., *ACS Sensors* **2016,** *1* (1), 5-16.
[288] Pumera, M.; Loo, A. H., *TrAC Trend. Anal. Chem.* **2014,** *61*, 49-53.
[289] Zhang, W.; Zhang, P.; Su, Z.; Wei, G., S *Nanoscale* **2015,** *7* (44), 18364-18378.
[290] Greenwood, J. *et al. ACS Nano* **2015,** *9* (5), 5520-5535.

case, doing away with the base was sufficient. Figure 3 shows the characterization of Bn-succ-MoS_2. The weight loss of *f*-MoS_2 (**1**) observed by TGA dropped considerably, to 5.5% wt (Figure 3a). This is more in line with what can be expected for a rather effective surface reaction considering our degree of exfoliation. Again, we do not observe any weight loss before 300 ºC meaning physisorbed **1** was successfully removed during the washing step. In accordance with the lower amount of organic material, ATR-IR showed less intense signals of the material. However, the new C-S stretching mode (728 cm^{-1}) and carbonyl stretch (1714 cm^{-1}) are clearly observed (Figure 3b). XPS of *f*-MoS_2(**1**) present a broadband at the S 2p peak requiring a new component (6.8 %) for the fitting that can correspond to S-C bond (orange, Figure 3c). Analysis of the C region is particularly informative: components for C=O (288.7 eV), C-S (287.0 eV) and C-N (285.9 eV) are again needed for the correct fitting, but in this case, the relative intensity of the C=O and C-N components with respect to C-S is much smaller (0.25:0.50:0.77) in accordance with molecular functionalization (Figure 3d). Finally, N 1s peak that is not visible in the control sample and is observed in the surface of the Bn-succ-MoS_2 material (Figure S12). The weight loss observed in TGA is the same in the control sample and its corresponding pristine material in both experiments: with and without Et_3N (Figure S18).

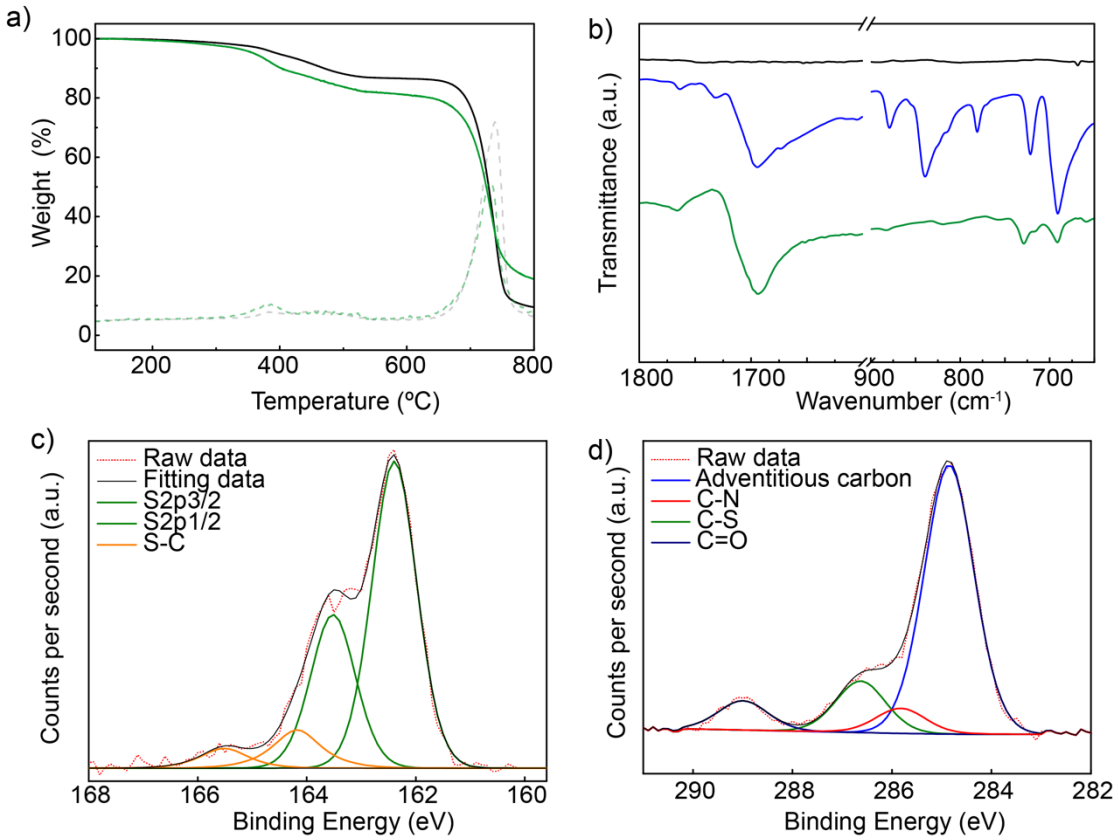

Figure 3. Characterization of succ-MoS_2 without base. **a)** TGA of MoS_2 (black line) and succ-MoS2 (green). **b)** ATR-FTIR of bulk-MoS_2 (black line), Bn-mal (blue) and Bn-succ-MoS_2 (orange). **c)** and **d)** XPS measuments.

Lastly, we decided to test the scope and flexibility of these reaction conditions. To begin with, we performed the reaction at different concentration of **1** (0.1 to 5 mmol). The functionalized MoS_2 showed a significant variation of the functionalization by TGA from 1.9 % to 5.6 %. (Figure S19). This seems to be the upper limit for molecular functionalization. In fact, when the reaction was left stirring for one month under otherwise identical conditions, we obtained a very similar degree of functionalization (5.5 % wt comparing it with its *p*-MoS_2) (See Figure S20).

The tolerance for different solvents was also investigated by performing the reaction in different solvents. (See Table S3, Figure S21-22). Dichloromethane (8 %) and chloroform (6 %) both showed higher functionalization degree by TGA compared to ACN. However, the slope of the loss is not as well defined as in ACN (Figure S21), which

might indicate that some physisorbed **1** is still present, even after the washings. When the reaction was carried out in DMF we found 7 % of organic material, comparable with ACN, but with a more tedious cleaning of the material. Remarkably, ATR-IR confirmed the presence of the C-S stretching in all solvents. (Figure S22).

With the optimal reaction and purification conditions already determined, we tested the scope of the reaction using 10 different maleimides (Figure 4), some of which were intentionally selected to be used as chemical handles for further modification (5-10). Within experimental error, and considering the different molecular weights, we observe similar degrees of functionalization (See Figures S21-22) for all the maleimides: 1-10 %, except **6**, which shows a much larger loading of organic material (16%). We explain this result noting that **6** features an aniline that probably acts as a base catalyst in the formation of a homopolymer.

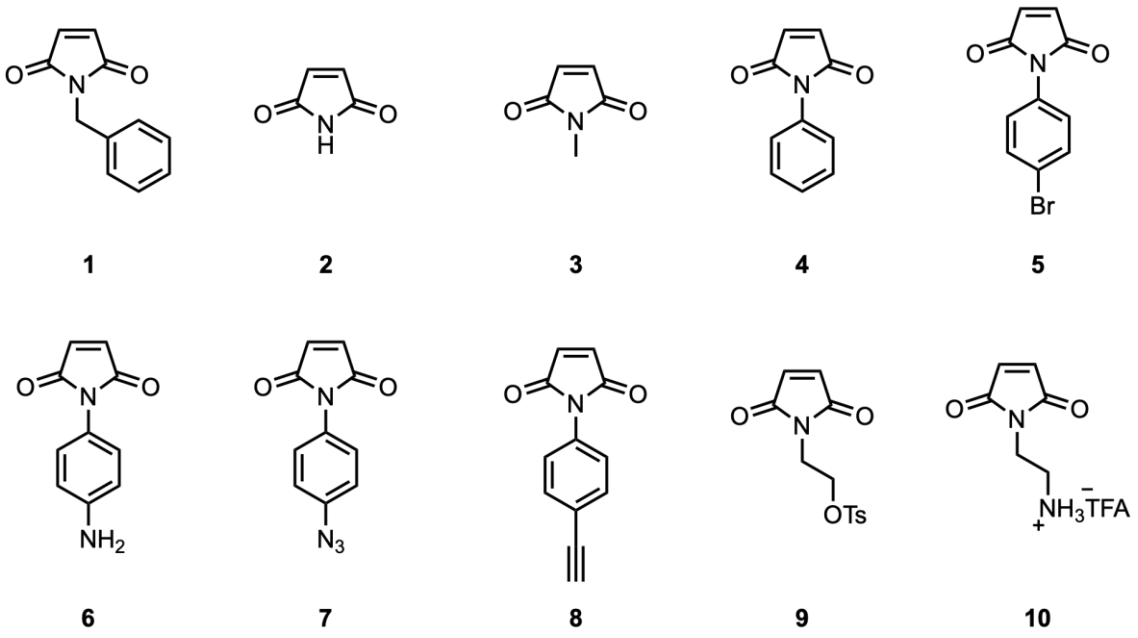

Figure 4. Maleimide scope used for the covalent functionalization of MoS_2.

f-MoS_2(**n**)	Weight loss (%)	ν (C=O)	ν (C-S)
f-MoS_2(**1**)	5.5 ± 0.7	1714	728
f-MoS_2(**2**)	6.2 ± 1.5	1714	728
f-MoS_2(**3**)	1.1 ± 0.3	1702	728
f-MoS_2(**4**)	1.8 ± 1.1	1698	728
f-MoS_2(**5**)	7.5 ± 0.7	1704	731
f-MoS_2(**6**)	15.8 ± 0.8	1714	731
f-MoS_2(**7**)	2 ± 3.4	1714	----
f-MoS_2(**8**)	6.8 ± 2.8	1694	728
f-MoS_2(**9**)	12.5 ± 3.5	1714	731
f-MoS_2(**10**)	8.6 ± 3.1	1698	728

9.3. **Conclusions.**

In summary, we present a thorough study of covalent functionalization of 2H-MoS_2 with maleimides via thiol-Michael Addition. We explore changes in reagents, stoichiometries, concentrations, solvents, and temperature and report the following main finding: The use of a base (Et_3N) promotes formation of a polymeric maleimide adlayer, which is covalentely attached to MoS_2. In the absence of a base, the functionalization stops at the molecular monolayer. Both pathways of covalent functionalization were demonstrated by a full characterization: XPS, TGA and IR, among others. In addition, the 2H polytype is preserved again demonstrating the mild conditions of the reaction. Finally, a scope of the reaction has been performed showing the great versatility of the reaction due to the wide range of maleimides used. To conclude, the thiol-ene click reaction is a powerful tool of functionalization MoS_2 and derivatives.

9.4. **Supporting Information**

9.4.1. **General Information**

Materials. MoS_2 powder (99%) was obtained from Sigma Aldrich. *N*-Methylmaleimide (>98%), *N*-Phenylmaleimide (>98%), *N*-Benzylmaleimide (>98%),

4,4'-Bismaleimido-diphenylmethane and Bis (3-ethyl-5- methyl-4- maleimidophenyl) methane were obtained from TCI Europe. *N*-(4-Bromophenyl) maleimide was obtained from Alfa Aesar and *N*-(Aminophenyl) maleimide was obtained from Apollo Scientific. Solvents were purchased from Scharlab Chemicals S. L. and used as received; water was obtained from a Milli-Q filtration station ("Type 1" ultrapure water; resistivity: 18.2 MΩ·cm at 25 ºC).

Characterization Methods. The extinction spectra were measured in a quartz cuvette (path length = 1 cm) with a Cary 50 UV/Visible spectrophotometer. Each suspension was briefly sonicated and transferred to a quartz cuvette (path length = 1 cm). The cuvette was closed with a stopper and the extinction spectrum of the suspension was measured immediately (time zero measurement). All thermogravimetric analyses were performed in a Q500 Instrument. The general procedure consisted of a fast heating ramp to 100 ºC, followed by a 30' isothermal. Then, a ramp of 10 ºC/min to 1000 ºC is carried out and, finally, the system was allowed to gradually cool to 50 ºC, with a last isothermal of 5 min. The data sampling interval is 0.50 s/pt. The experiments were performed both in nitrogen and air. If not specified, the experiments are normally run under air. Raman Spectroscopy of bulk MoS_2, exfoliated MoS_2 and functionalized MoS_2 powders were scratched and supported onto glass slides. Raman Spectroscopy was carried out in a Senterra Raman Spectrometer confocal Raman microscope (Bruker Optic, Ettlingen, Germany, resolution 3-5 cm^{-1}) using the following parameters: laser excitation: 532 nm, 2 mW; scanning: 1", 5 coadditions; objective NA 0.75, 50V. The standard procedure consisted of scanning 20 points, randomly selected, over different areas of the material. Exfoliating the sample renders thinner layers of the materials. The thinner the layers are, the closer must appear both maximums in the Raman spectrum. Infrared spectra with attenuated total reflection (ATR-IR) were performed with a Bruker ALPHA FT-IR spectrometer. All experiments were carried out employing 24 scans. XPS (X-ray Photoelectron Spectroscopy) measurements were performed under Ultra High Vacuum conditions (UHV, with a base pressure of 5×10-10 mbar), using a monochromatic Al Kα line as exciting photon source for core level analysis (hν = 1486.7 eV). The emitted photoelectrons were collected in a hemispherical energy analyzer (SPHERA-U7, pass energy set to 20 eV for the XPS measurements to have a resolution of 0.6 eV) and to compensate the built up charge on the sample surface it was necessary the use of a Flood

Gun (FG-500, Specs), with low energy electrons of 3 eV and 40 µA. Transmission Electron Microscopy images of the MoS_2 flakes after the exfoliation (pristine, *p*-MoS_2) and after the functionalization (*f*-MoS_2) are obtained to check the changes in the general structure of the sample. Bulk MoS_2, exfoliated MoS_2 and functionalized MoS_2 were drop-casted onto 200 square mesh copper grids covered with a carbon film. They were observed using a JEOL JEM 2100 microscope operated at 200 kV.

9.4.2. **Experimental Procedure.**

Liquid-phase Exfoliation. 1 mg/mL dispersion of MoS_2 (200 mg) NMP (200mL) was prepared in a 250 mL round-bottom flask. The mixture was sonicated (Vibracell 75115 (VC 505 / VC 750)-Bioshock Scientific) during 1 hour, operating at the amplitude of 40%, without pulse and using an ice bath to prevent the heating of the dispersion. Afterwards, the black dispersion was divided into six falcon eppendorfs and centrifuged for 30' at 2000 rpm (Allegra X-15R Beckman Coulter centrifuge, FX6100 rotor, 20 ºC). Then, the supernatant was separated from the black sediment (non-exfoliated) by decanting and then it was filtered in a membrane filtration system (Omnipore 0.45 µm PTFE membrane filters, 45 mm in diameter). The membrane with the retained exfoliated MoS_2 was dispersed in acetonitrile and filtered again. This re-dispersion process was repeated three times with 60 mL of acetonitrile (ACN) and three times with 60 mL of isopropyl alcohol (*i*PrOH).

Functionalization procedure of MoS_2. 6 mg of exfoliated MoS_2 in 10 mL of ACN was added in a 20mL vial. Then, the suspension was sonicated few seconds. Finally, the maleimide derivative was added and the reaction was stirring 16h at rt. After that, the dispersion was filtered through Omnipore 0.45 µm PTFE membrane filters, 25 mm in diameter. In order to wash the sample, the material was redispersed in 20 mL of ACN, and filtered. This process is repeated three times with ACN and three times more with *i*PrOH.

Quantification of the functionalization.

Eq S1

$$\text{W.loss (\%)} = \frac{\text{X} \cdot \text{MW(Moiety attached)}}{\text{X[MW(Moiety attached)} + \text{MW}(MoS_2)] + (1 - \text{X}) \cdot \text{MW}(MoS_2)} \cdot 100$$

$$X = \text{Percentage of modified sulfur atoms; W. loss} = \text{Weight loss}$$

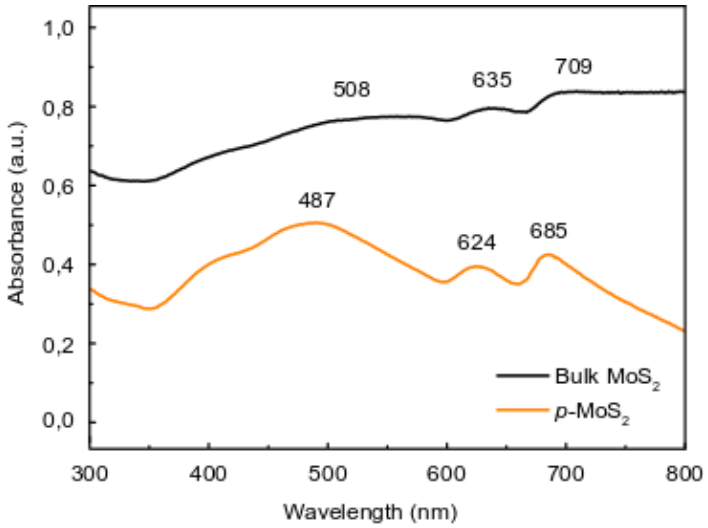

Figure S1. UV-Vis spectra of exfoliated MoS_2 and bulk material.

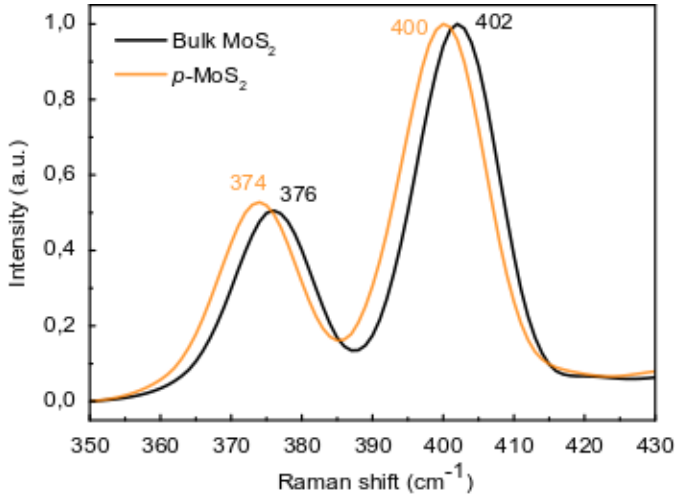

Figure S2. Raman spectra of exfoliated MoS_2 and bulk material.

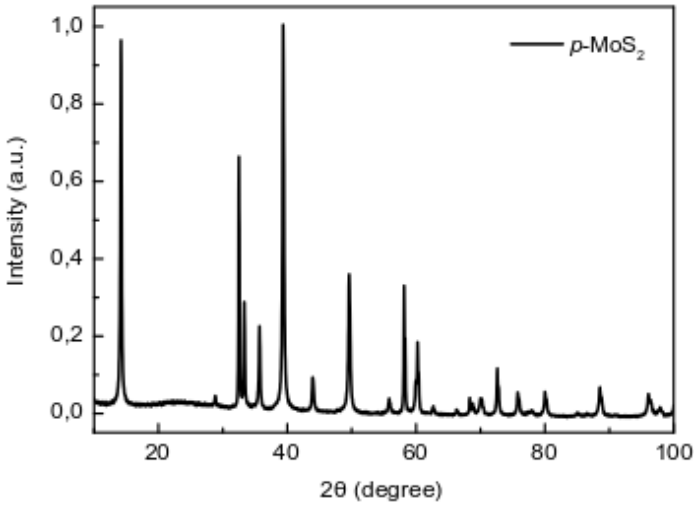

Figure S3. XRD of exfoliated MoS_2.

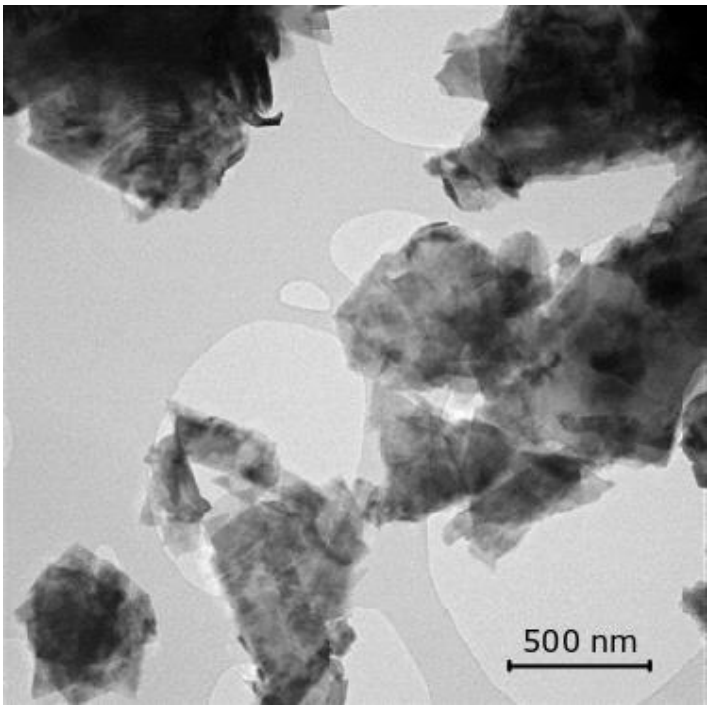

Figure S4. TEM of exfoliated MoS_2.

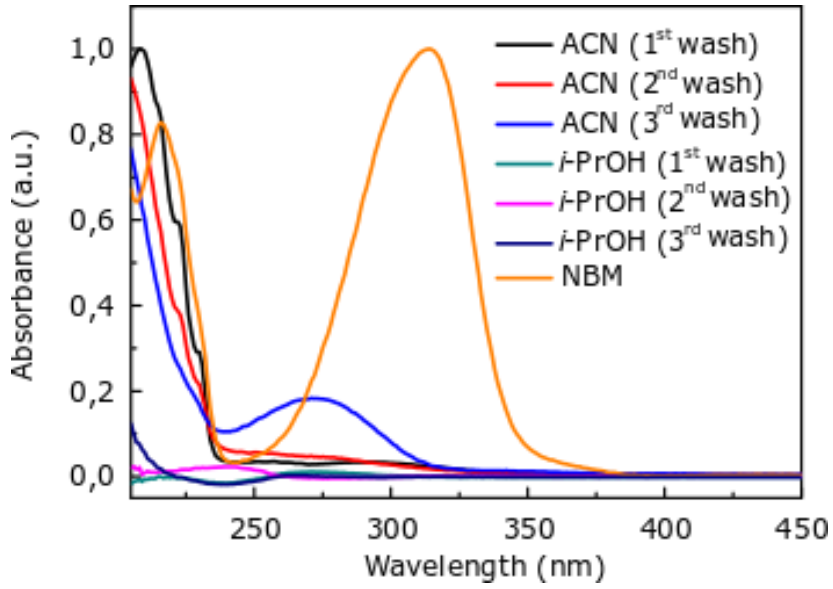

Figure S5. UV-Vis spectra of the washings of the functionalization reaction.

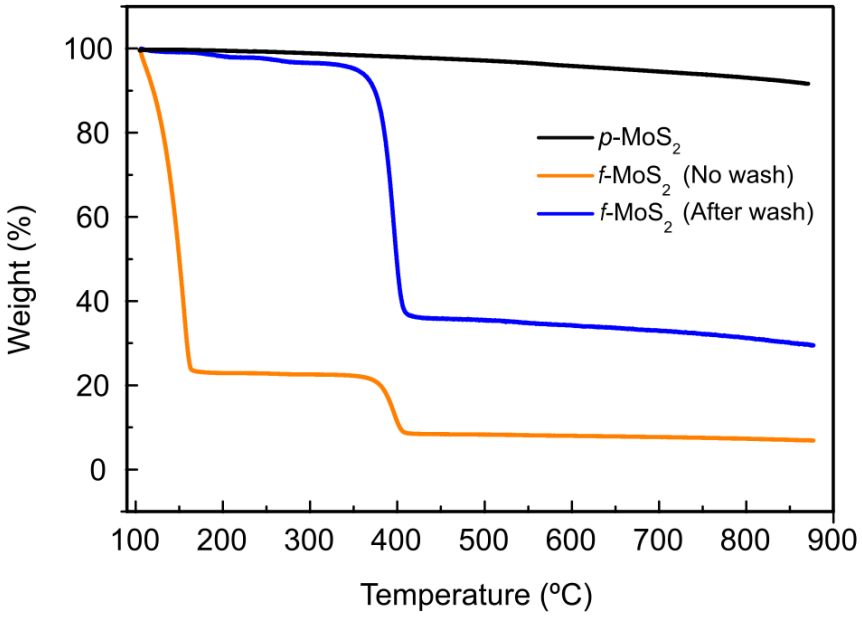

Figure S6. TGA of exfoliated material (black line), unwashed Bn-succ-MoS_2 (*f*-MoS_2) (orange line) and washed Bn-succ-MoS_2 (blue line). In all cases using base in the reaction. Performed under N_2.

Table S1. Analysis of the reactivity in the covalent functionalization of MoS_2 in presence of benzyl maleimide and base.

Entry	Solvent	Sonication	Centrifugation	Reaction solvent	W. MoS_2	W. NBM	Time	T^o	W. loss (%)
1	*i*PrOH /H_2O (7:3)	1h, 40%	4000 rpm, 30’	ACN	5	468 mg (2.5 mmol)	16 h	r.t.	24[a]
2	*i*PrOH /H_2O (7:3)	16h, 40%	4000 rpm, 30’	ACN	5	468 mg (2.5 mmol)	16 h	r.t.	-[b]
3	*i*PrOH /H_2O (7:3)	24h, 40%	4000 rpm, 30’	ACN	5	468 mg (2.5 mmol)	16 h	r.t.	-[b]
4	*i*PrOH /H_2O (7:3)	1h, 40%	4000 rpm, 30’	NMP	5	468 mg (2.5 mmol)	16 h	r.t.	0
5	NMP	4h, 23%	-[c]	ACN	5	468 mg (2.5 mmol)	16 h	r.t.	0
6	NMP	4h, 23%	-[d]	ACN	5	468 mg (2.5 mmol)	16 h	r.t.	0
7	NMP	4h, 23%	-	NMP	1000	935 mg (5 mmol)	4h	0 ^{o}C	0[e]

8	NMP	1h, 40%	4000 rpm, 30’	ACN	5	468 mg (2.5 mmol)	16 h	r.t.	90
9	NMP	1h, 40%	4000 rpm, 30’	ACN/ NMP (1%)	5	468 mg (2.5 mmol)	16 h	r.t.	0
10	NMP	1h, 40%	4000 rpm, 30’	ACN/ NMP (50%)	5	468 mg (2.5 mmol)	16 h	r.t.	0
11	NMP	1h, 40%	2000 rpm, 30’	ACN	5	468 mg (2.5 mmol)	16 h	r.t.	80
12	NMP	1h, 40%	500 rpm, 30’	ACN	5	468 mg (2.5 mmol)	16 h	r.t.	60
13	NMP	1h, 40%	2000 rpm, 30’	PhCN	5	468 mg (2.5 mmol)	16 h	r.t.	60
14	NMP	1h, 40%	2000 rpm, 30’	THF	5	468 mg (2.5 mmol)	16 h	r.t.	0
15	NMP	1h, 40%	2000 rpm, 30’	DMF	5	468 mg (2.5 mmol)	16 h	r.t.	0
16	NMP	1h, 40%	2000 rpm, 30’	$CHCl_3$	5	468 mg (2.5 mmol)	16 h	r.t.	0

17	NMP	1h, 40%	2000 rpm, 30’	Toluene	5	468 mg (2.5 mmol)	16 h	r.t.	0
18	NMP	1h, 40%	2000 rpm, 30’	ACN	2	468 mg (2.5 mmol)	16 h	r.t.	90
19	NMP	1h, 40%	2000 rpm, 30’	ACN	10	468 mg (2.5 mmol)	16 h	r.t.	59
20	NMP	1h, 40%	2000 rpm, 30’	ACN	20	468 mg (2.5 mmol)	16 h	r.t.	31
21	NMP	1h, 40%	2000 rpm, 30’	ACN	5	9 mg (0.05 mmol)	16 h	r.t.	0
22	NMP	1h, 40%	2000 rpm, 30’	ACN	5	94 mg (0.5 mmol)	16 h	r.t.	11
23	NMP	1h, 40%	2000 rpm, 30’	ACN	5	187 mg (1 mmol)	16 h	r.t.	27
24	NMP	1h, 40%	2000 rpm, 30’	ACN	5	935 mg (5 mmol)	16 h	r.t.	90
25	NMP	1h, 40%	2000 rpm, 30’	ACN	5	468 mg (2.5 mmol)	1 h	r.t.	66

26	NMP	1h, 40%	2000 rpm, 30’	ACN	5	468 mg (2.5 mmol)	2 h	r.t.	72
27	NMP	1h, 40%	2000 rpm, 30’	ACN	5	468 mg (2.5 mmol)	4 h	r.t.	78
28	NMP	1h, 40%	2000 rpm, 30’	ACN	5	468 mg (2.5 mmol)	8 h	r.t.	80
29	NMP	1h, 40%	2000 rpm, 30’	ACN	5	468 mg (2.5 mmol)	16 h	50 ºC	85
30	NMP	1h, 40%	2000 rpm, 30’	ACN	5	468 mg (2.5 mmol)	16 h	82 ºC	65

[a]Previous work at the group. [b]The amount of exfoliated MoS_2 of one single exfoliation process is not enough to carry out the functionalization reaction. [c]Decanted overnight. [d]Decanted for 48 h. [e]Sonication and maleimide reaction were performed at the same time.

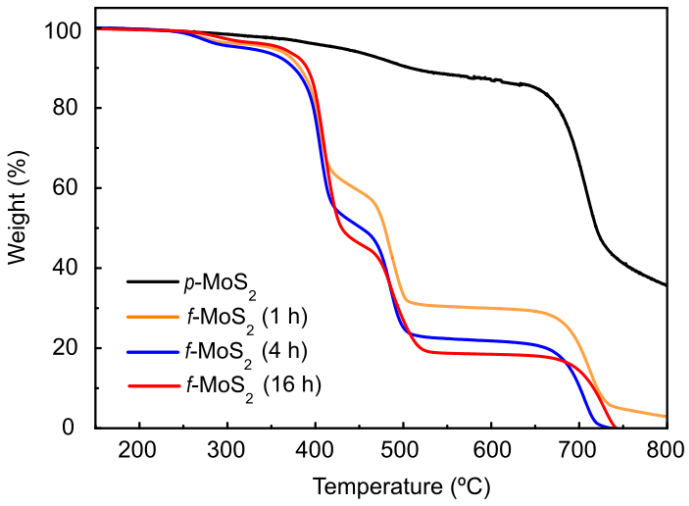

Figure S7. TGA profiles regarding time of reaction.

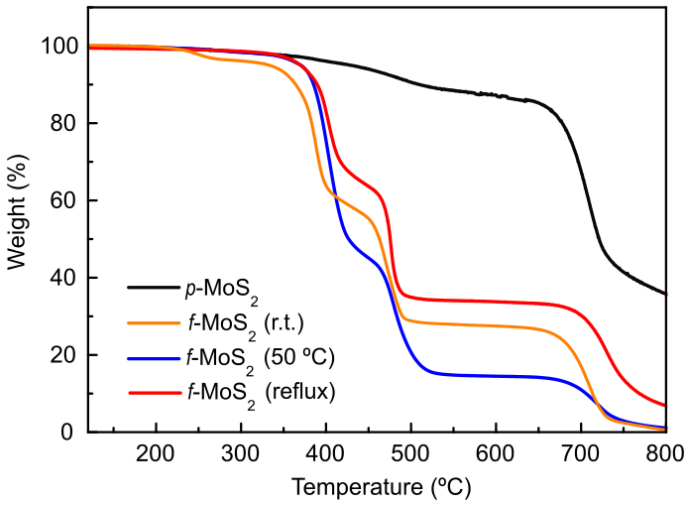

Figure S8. TGA profiles regarding temperature of reaction.

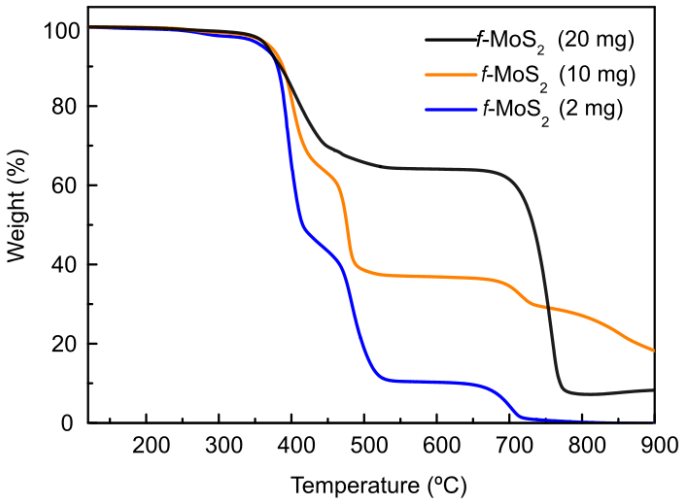

Figure S9. TGA profiles regarding the mass of exfoliated MoS_2 added to the reaction.

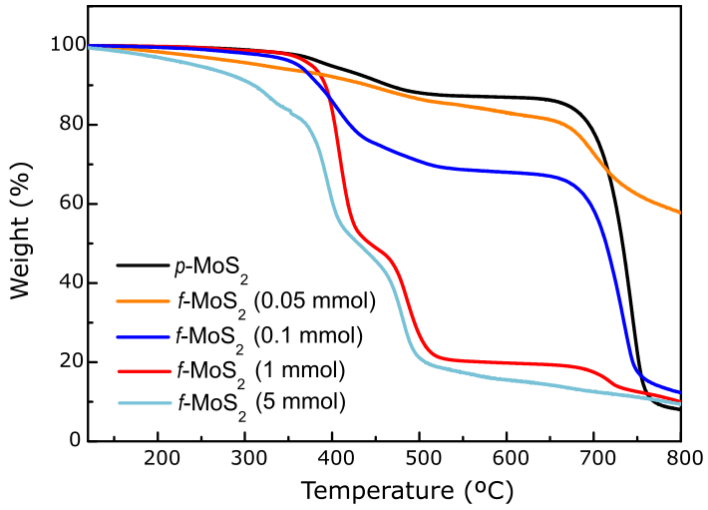

Figure S10. TGA profiles regarding the amount of maleimide added to the reaction

Table S2. Atomic percentages of XPS survey spectra of different modified MoS_2.

Materials	**Core level**	**Binding Energy (eV)**	**Atomic %**
succ-MoS_2	O 1s	532.8	37.8
	N 1s	400.7	0.3
	C 1s	284.8	51.0
	Mo 3d	229.8	3.5
	S 2p	162.4	7.4
f-MoS_2(**5**)	O 1s	532.7	22.0
	N 1s	400.8	1.2
	C 1s	284.8	54.8
	Mo 3d	229.6	6.7
	S 2p	162.5	14.0
	Br 3d	**71.1**	**1.3**

Pristine MoS_2	O 1s	532.4	7.8
	C 1s	284.8	43.8
	Mo 3d	229.9	15.6
	S 2p	162.7	32.8
polysucc-MoS_2	O 1s	532.40	13.4
	N 1s	400.70	6.1
	C 1s	284.80	78.4
	Mo 3d	229.70	0.6
	S 2p	162.60	1.5
cs-MoS_2	O 1s	533.4	12.8
	C 1s	284.8	32.4
	Mo 3d	229.9	17.1
	S 2p	162.7	37.7

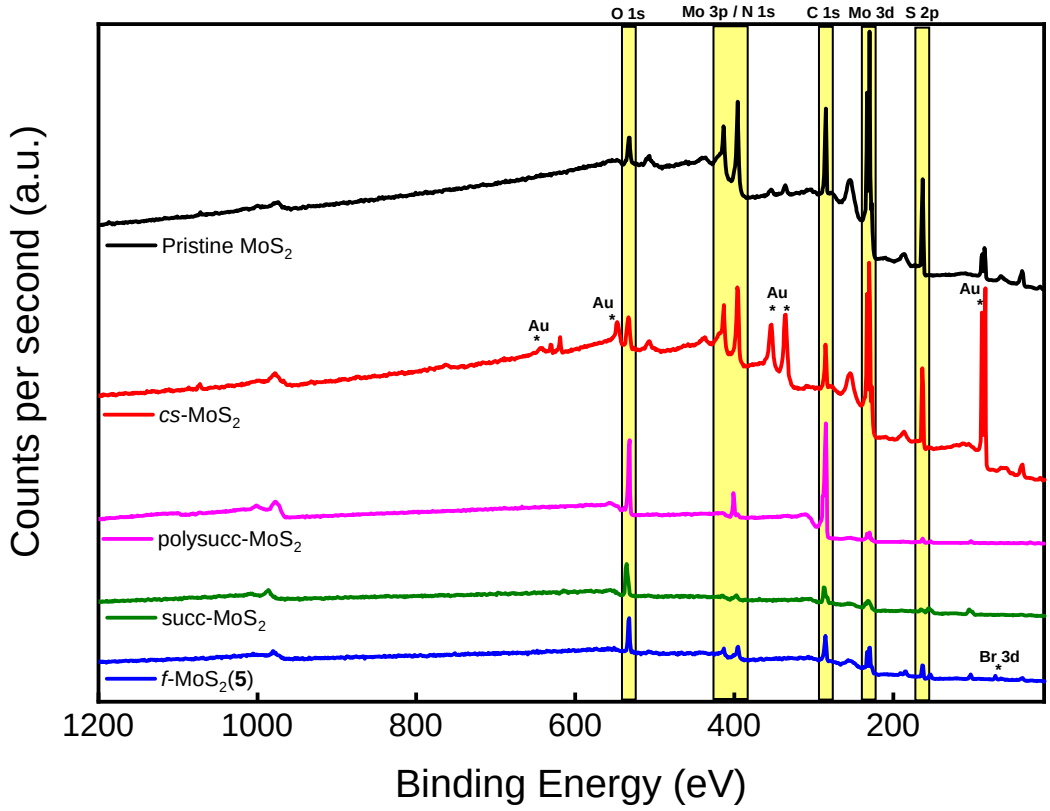

Figure S11. XPS survey spectra of different modified MoS_2.

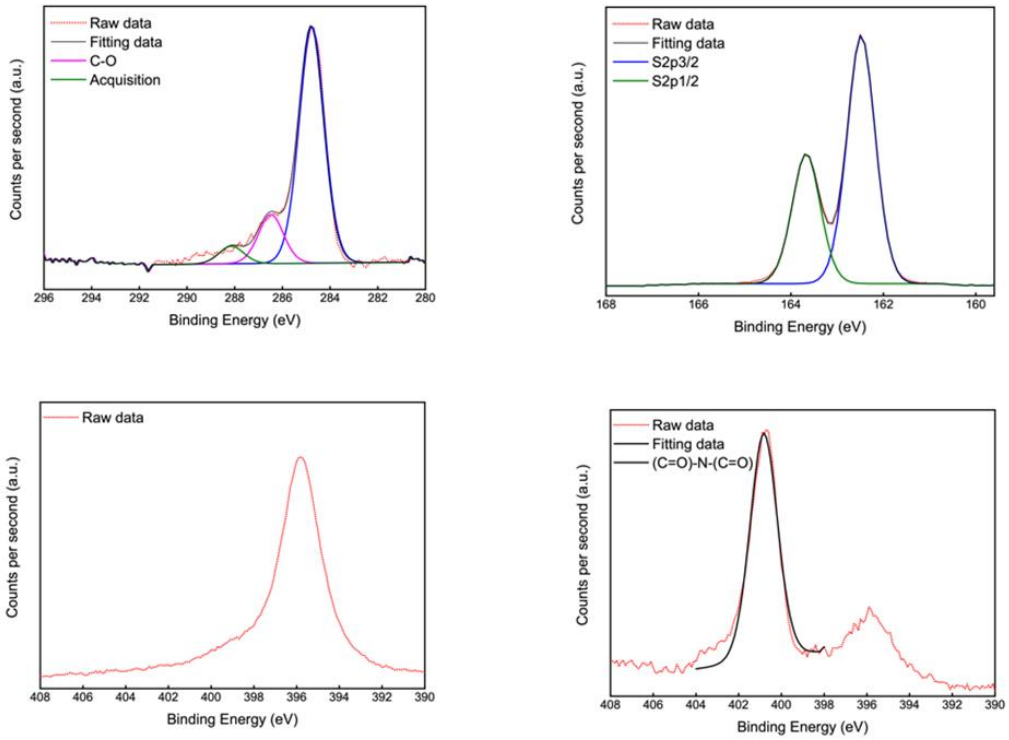

Figure S12. XPS analysis of pristine, control sample, and Bn-succ-MoS_2 with base with **1**. Core levels of C 1s and S 2p of the control sample (up) and N 1s comparison between control sample (bottom-left) and Bn-succ-MoS_2 with base (bottom-right).

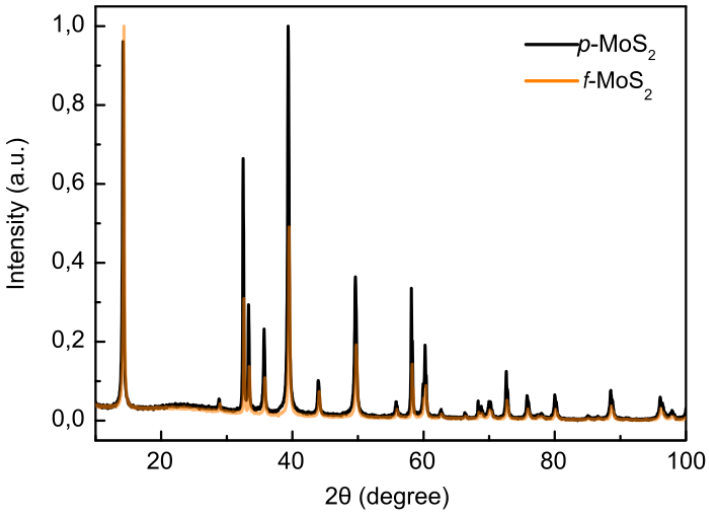

Figure S13. XRD exfoliated MoS_2 and Bn-succ-MoS_2 with base.

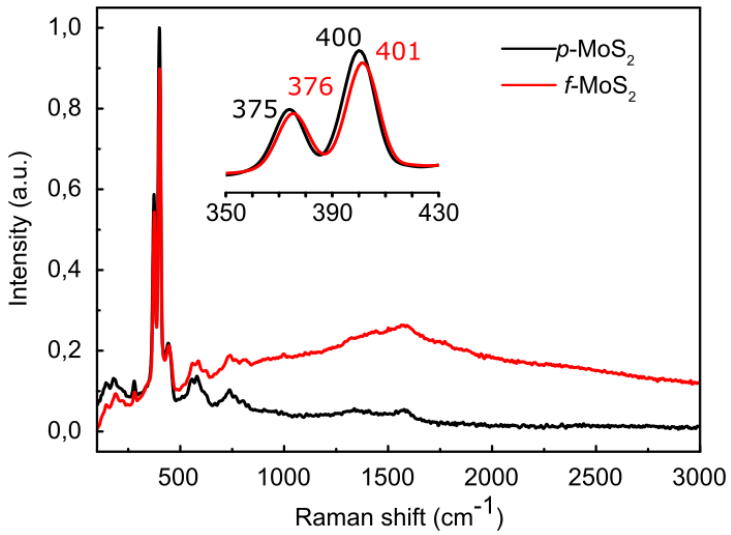

Figure S14. Raman spectra of exfoliated MoS_2 and Bn-succ-MoS_2.

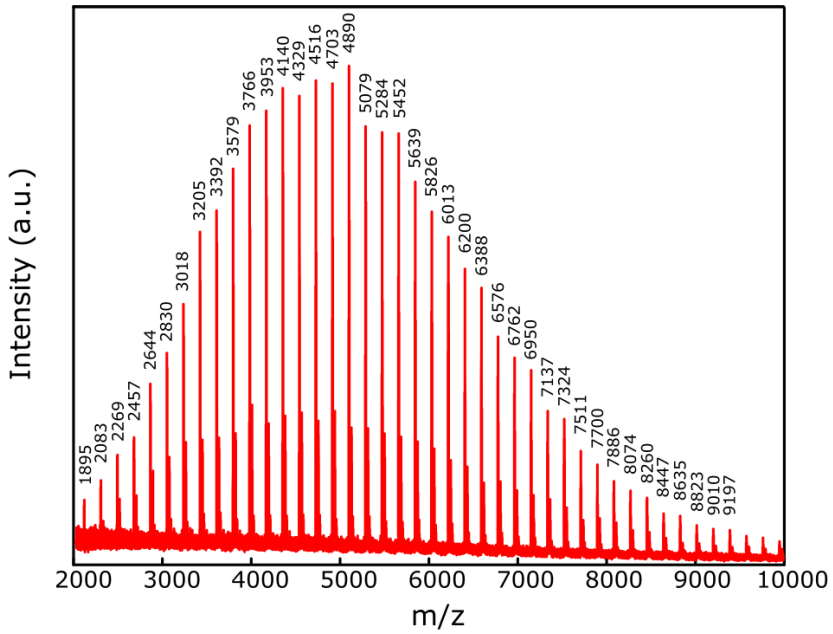

Figure S15. MALDI of the polymer formation from the reaction of Bn-succ-MoS_2 with base.

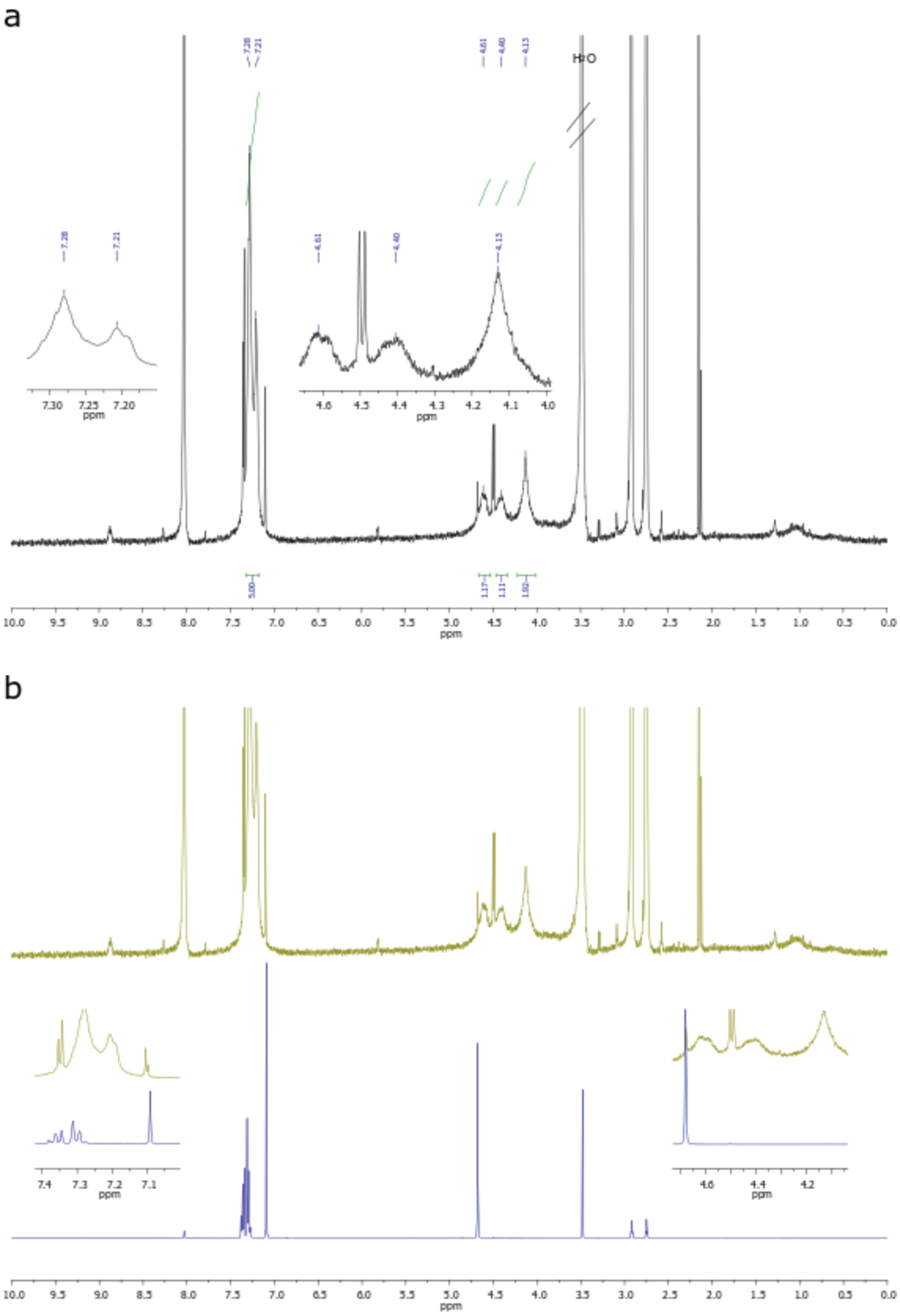

Figure S16. a) ^{1}HNMR spectrum (400 MHz, DMF-d^{7}) of subproduct of *N*-benzylmaleimide from Bn-succ-MoS_2 reaction with base. The new signals are ^{1}H NMR

(400 MHz, DMF) δ 7.24 (m, 5H), 4.61 (s, 1H), 4.40 (s, 1H), 4.13 (s, 1H). **b)** Comparison between the ^{1}H NMR spectra (400 MHz, DCM-d^7) of *N*-benzylmaleimide (blue) and subproduct of the reaction (green): new signals appear which correspond with the polymerization of the maleimide. However, in the same spectra it is possible to observe a remaining of alkene and CH_2-benzyl of the starting material but with a little shift.

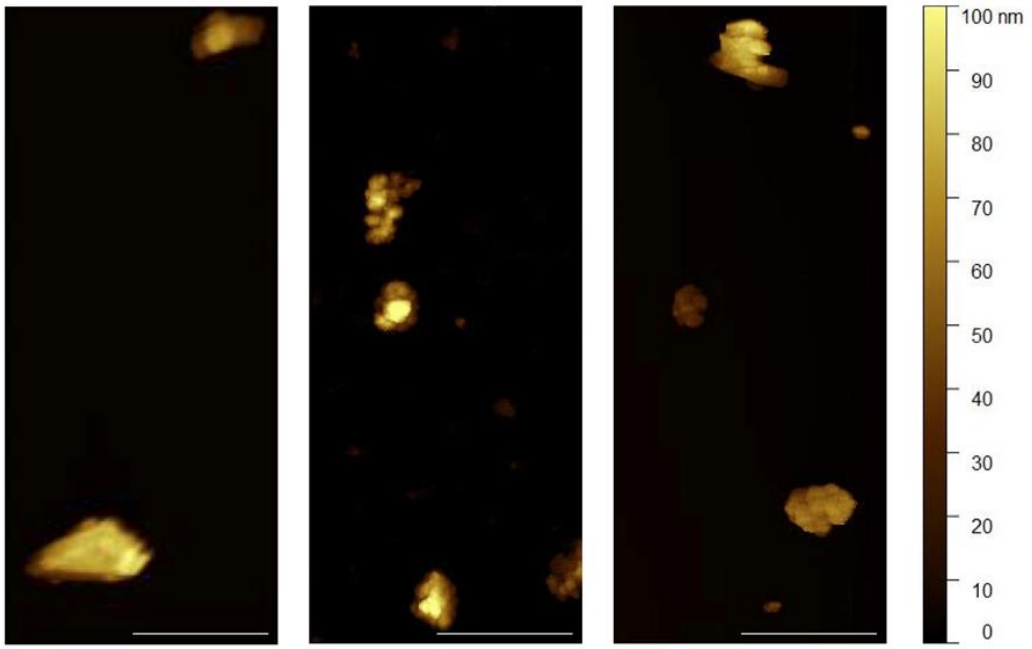

Figure S17. AFM images of *p*-MoS_2 (left) Bn-succ-MoS_2 with base (mid) and succ-MoS_2 without base (right). Scale bar 1 µm.

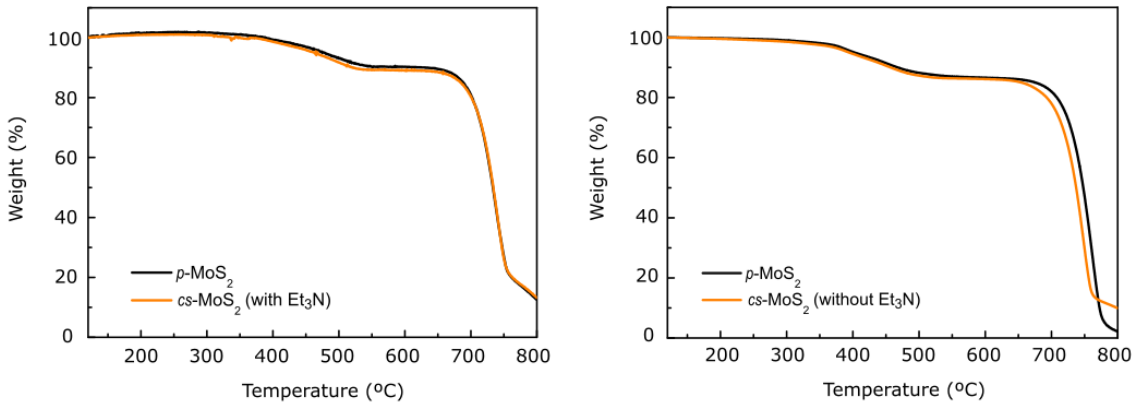

Figure S18. TGA profiles of *p*-MoS_2 and *cs*-MoS_2 (control sample experiment with the same conditions of the functionalization but not adding an organic moiety) with and without Et_3N.

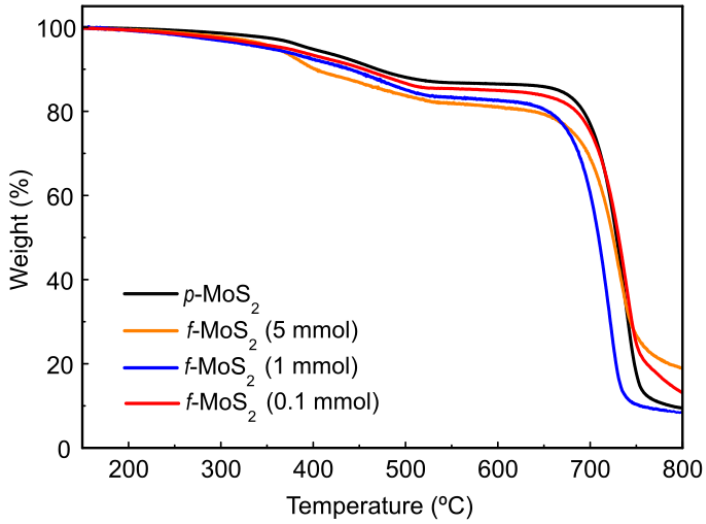

Figure S19. TGA profiles regarding the amount of maleimide added to the reaction.

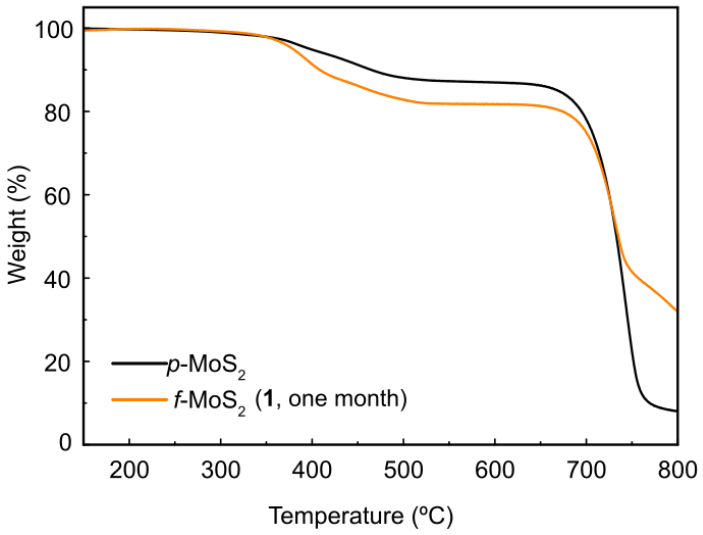

Figure S20. TGA profile of one-month reaction.

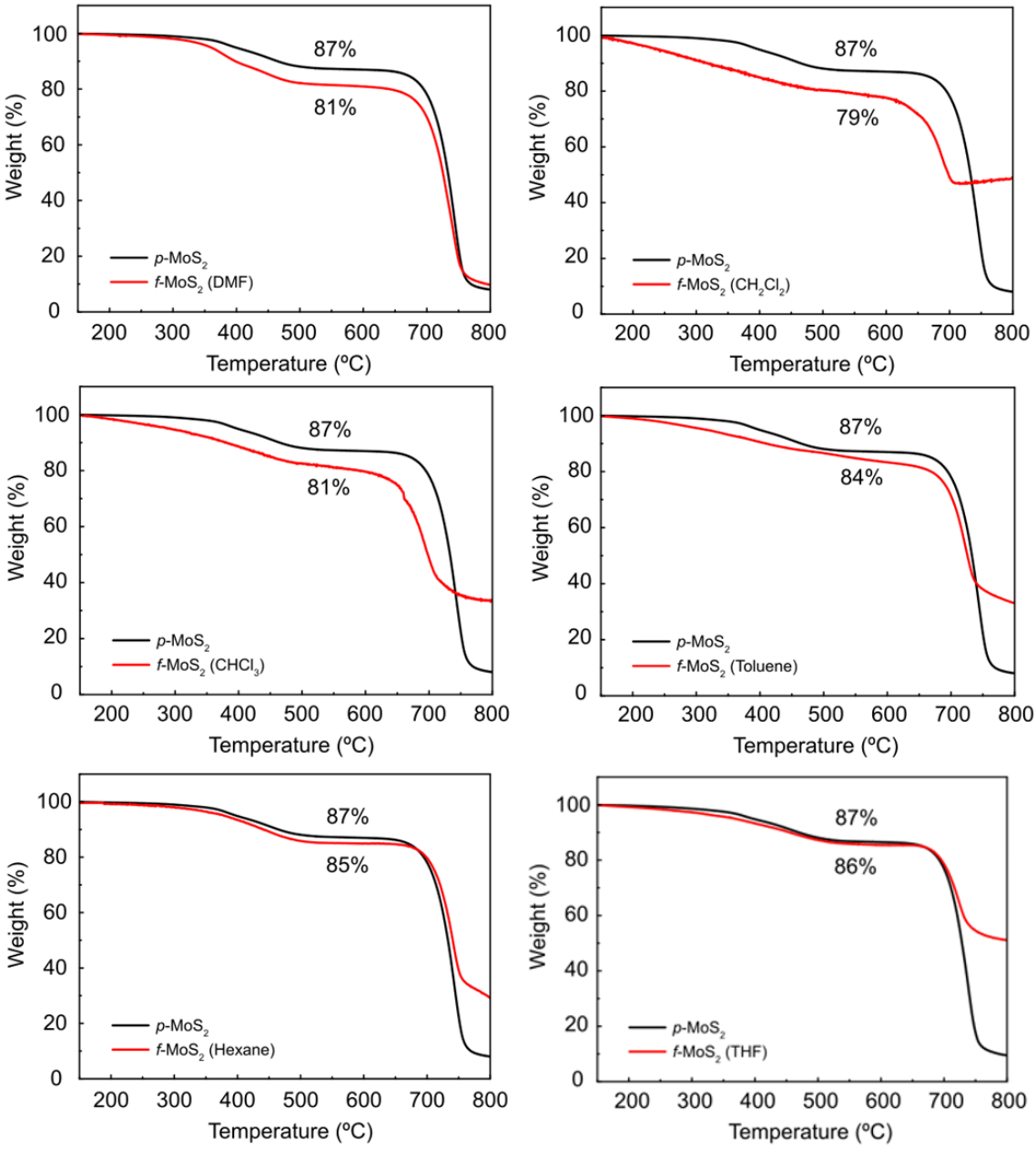

Figure S21. TGA of MoS_2 functionalization of **1** using different solvents.

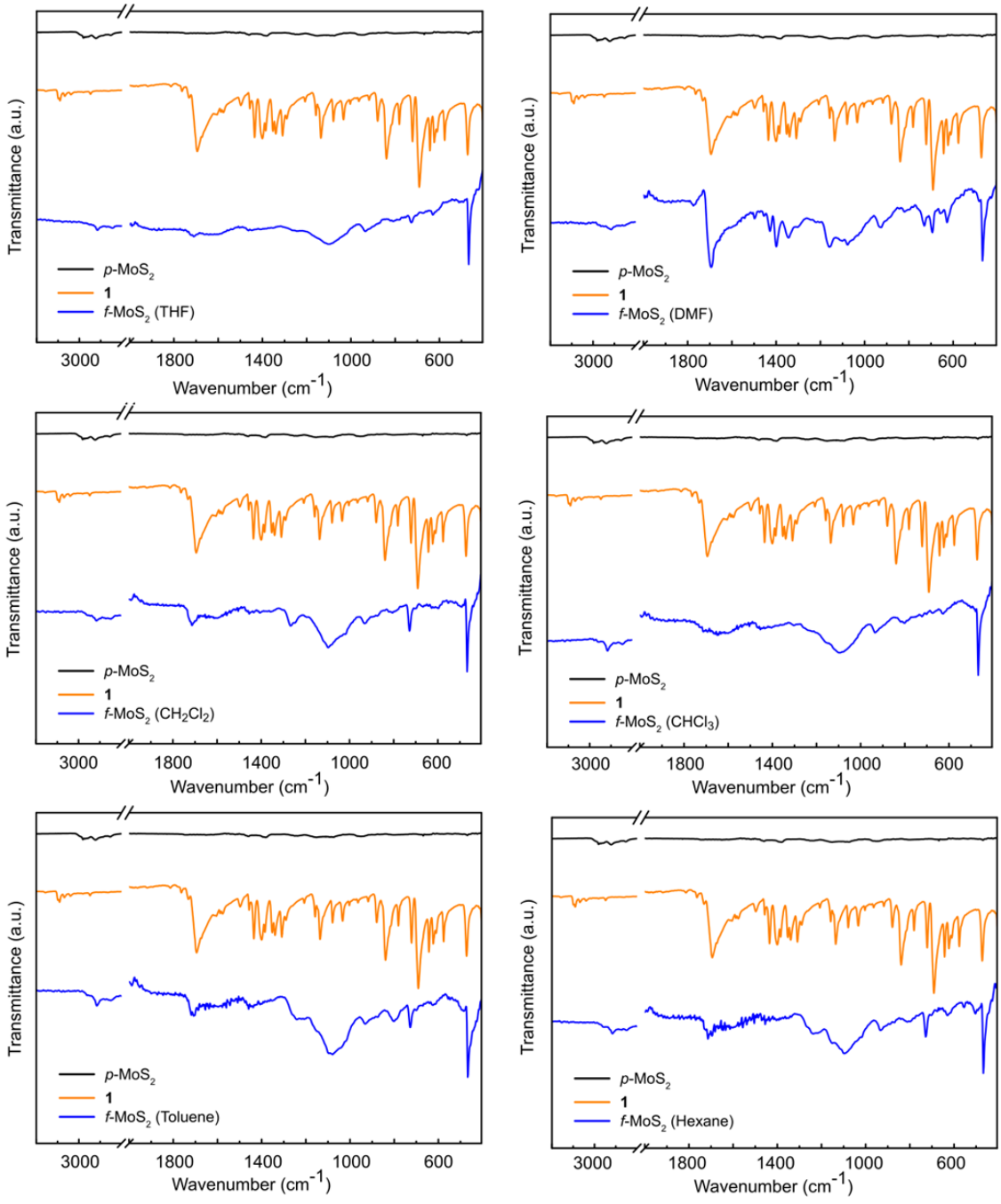

Figure S22. ATR-IR of MoS_2 functionalization of **1** using different solvents.

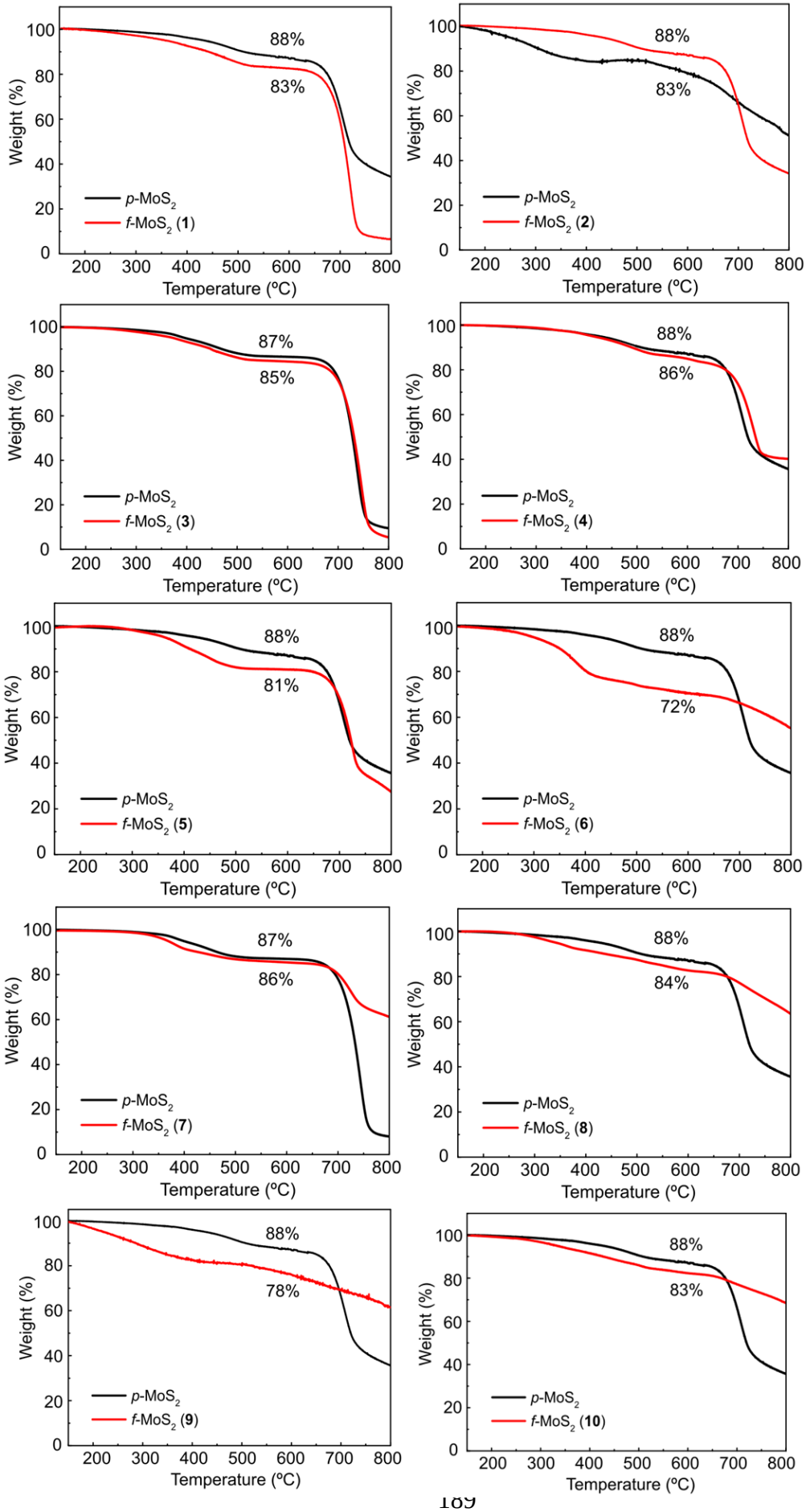
Weight (%)
Temperature (ºC)
88%
83%
p-MoS2
f-MoS2 (1)
f-MoS2 (2)
87%
85%
f-MoS2 (3)
86%
f-MoS2 (4)
81%
f-MoS2 (5)
72%
f-MoS2 (6)
f-MoS2 (7)
84%
f-MoS2 (8)
78%
f-MoS2 (9)
f-MoS2 (10)

Figure S23. TGA of MoS_2 functionalization using different maleimides.

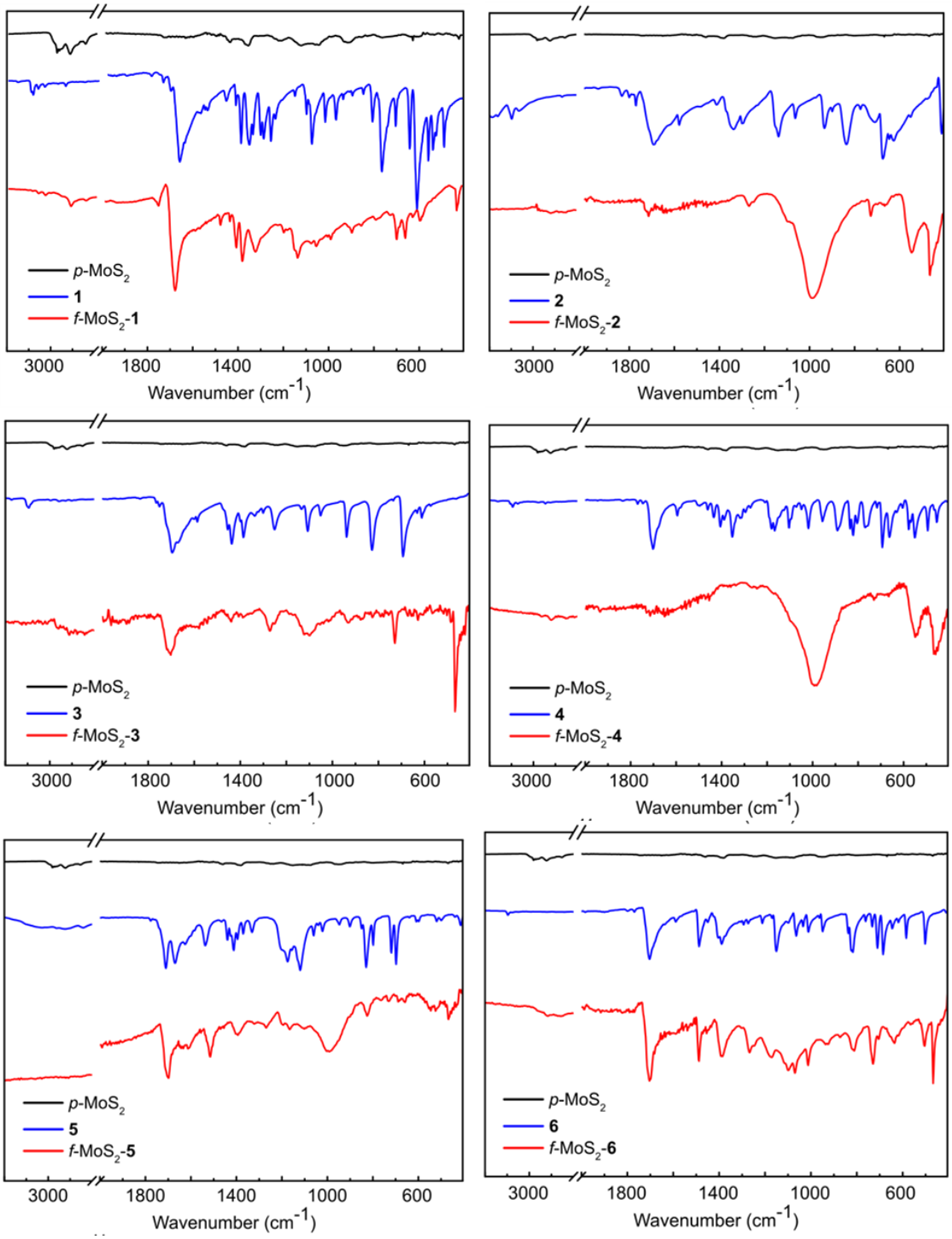

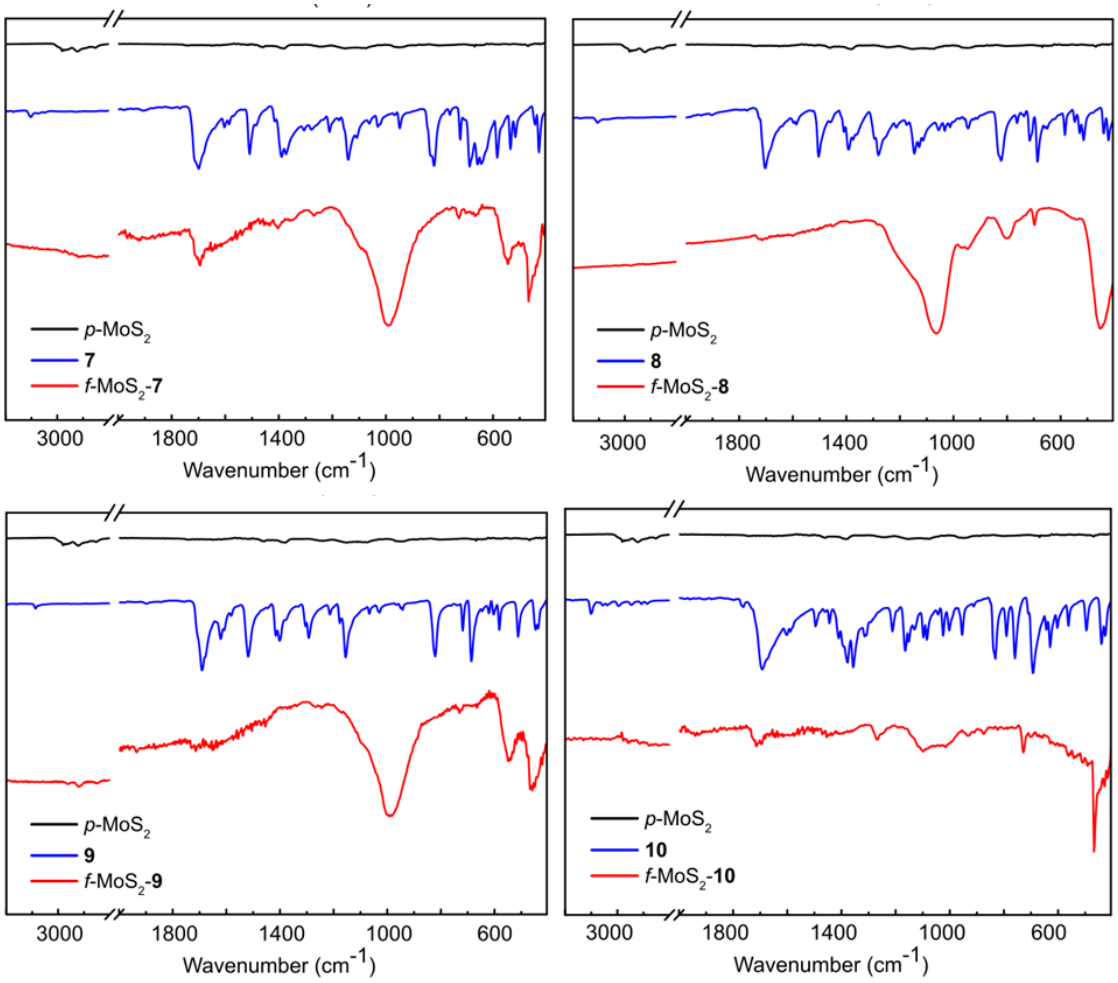

Figure S24. ATR-IR of MoS_2 functionalization using different maleimides.

Table S3.

Entry	**Solvent**	**Weight loss (%)**	**ν C=O** (cm^{-1})	**ν C-S** (cm^{-1})
1	THF	1	1708	726
2	DMF	7	1696	731
3	CH_2Cl_2	8	1714	728
4	$CHCl_3$	6	-	-
5	Toluene	3	1720, 1706	728
6	Hexane	2	1714, 1696	728

9.4.3. **Synthesis of Maleimide Derivatives.**

*Synthesis of 1-(4-azidophenyl)-1H-pyrrole-2,5-dione (**7**).*[291]

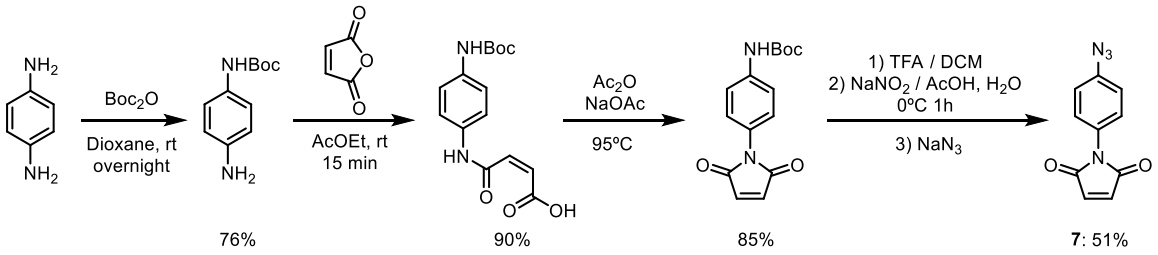

The synthesis of compound **7** was done following the procedure of Carrié et al, *Chem. Commun.*, **2014**, *50*, 9387-9389.

*Synthesis of 1-(4-ethynylphenyl)-1H-pyrrole-2,5-dione (**8**).*[292]

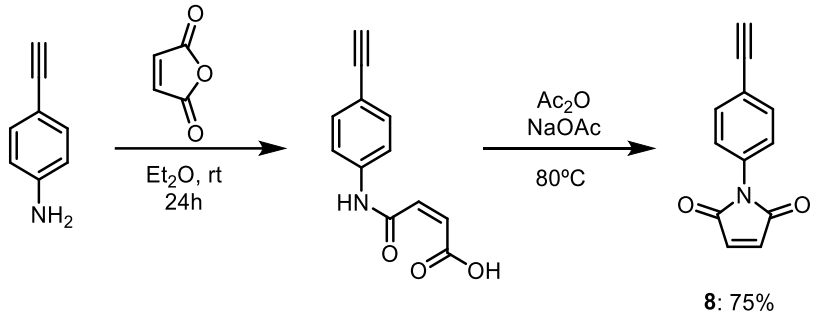

The synthesis of compound **8** was done following the procedure of Itou W., Hagiwara T., *Reactive and Functional Polymers*, **2016**, *101*, 70-74.

*Synthesis of 1-(2-hydroxyethyl)-1H-pyrrole-2,5-dione (**11**).*[293]

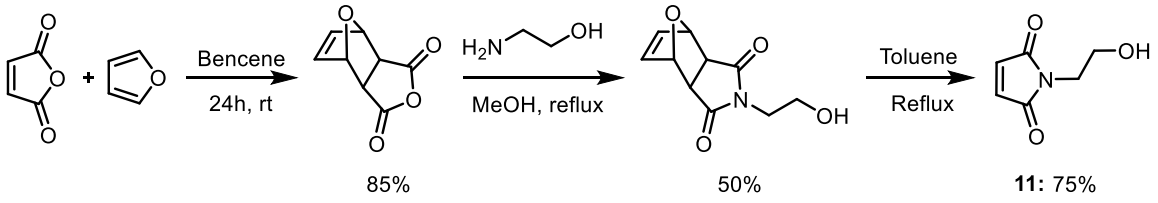

The synthesis of compound **11** was done following the procedure of Heath et al, *Macromolecules*, **2008**, *41*, 719.

[291] Carrié, H.; Tran, D. T.; Rousseau, S.; Chaignepain, S.; Schmitter, J.-M.; Deffieux, D.; Quideau, S., *Chem. Commun.* **2014,** *50* (66), 9387-9389.

[292] Itou, W.; Hagiwara, T., *React. Funct. Polym.* **2016,** *101*, 70-74.

[293] Heath, W. H.; Palmieri, F.; Adams, J. R.; Long, B. K.; Chute, J.; Holcombe, T. W.; Zieren, S.; Truitt, M. J.; White, J. L.; Willson, C. G., *Macromolecules* **2008,** *41* (3), 719-726.

*Synthesis of 1-(2-hydroxyethyl)-1H-pyrrole-2,5-dione (**9**).*

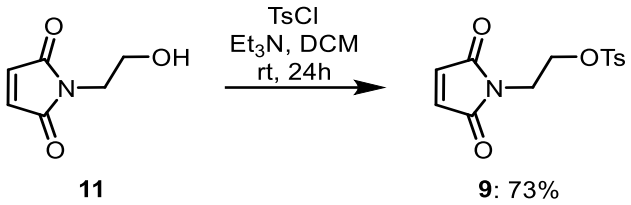

Compound **11** (1.62 g, 11.5 mmol, 1 eq) was dissolved in DCM (115 mL) and Et_3N (3.7 mL, 26.5 mmol, 2 eq) was added. Then, the solution was cooled at 0ºC within an ice bath. TsCl (2.63 g, 13.8 mmol, 1.2 eq) was added in one portion and the reaction was allowed to stir at rt for 24h. The next day, the reaction was extracted with DCM/H_2O three times and the organic phase was dried over anhydrous Na_2SO_4 and concentrated under reduced pressure. The purification of the compound was performed with a column chromatography on silica gel using DCM as eluent. Its spectroscopic data were in concordance with those described in the literature (*J. Med. Chem.* **1971**, *14*, 873-878).

*Synthesis of 2-(2,5-dioxo-2,5-dihydro-1H-pyrrol-1-yl)ethan-1-aminium (**10**).*[294]

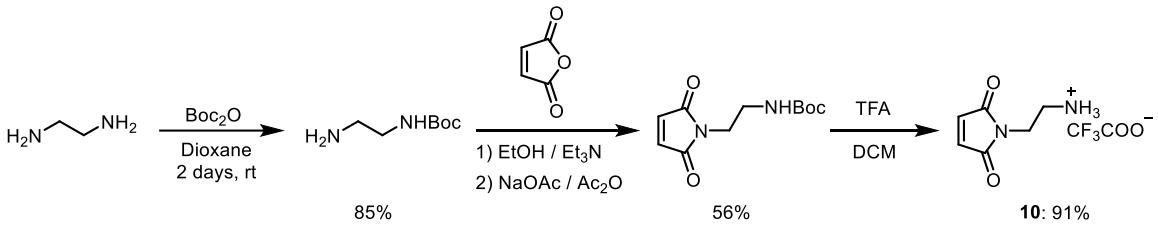

The synthesis of compound **10** was done following the procedure of Tang, F. et al, *Org. Biomol. Chem.*, **2016**, *14*, 9501-9518.

[294] Tang, F.; Yang, Y.; Tang, Y.; Tang, S.; Yang, L.; Sun, B.; Jiang, B.; Dong, J.; Liu, H.; Huang, M.; Geng, M.-Y.; Huang, W., *Org. Biomol. Chem.* **2016,** *14* (40), 9501-9518.

CONCLUSIONES

1) En el *capítulo 1* hemos mostrado que la encapsulación dentro macrociclos mediante enlace mecánico (MINT) de dopaje tipo n o p es una estrategia válida para la regulación de la actividad catalítica de SWNTs. Hemos elegido como prueba de concepto la reducción de nitro arenos. El efecto electrónico de los macrociclos en la actividad catalítica es claramente predominante: mac- exTTF electrón dador acelera la reacción, mac- AQ electrón aceptor la ralentiza y el mac-pyr electrónicamente neutro posee una actividad similar a los SWNTs. Finalmente, MINTs son catalizadores estables que pueden ser reciclados.

2) En el *capítulo 2* hemos explorado el estudio de MINT-AQ como un método eficiente de inmovilización de AQ que retiene las propiedades electroquímicas de la molécula. La estrategia MINT puede resolver el problema de disolución-inestabilidad de moléculas orgánicas físicamente absorbidas tras la reducción electroquímica. Además, se ha realizado una prueba de concepto para aplicaciones electroquímicas de MINT en la reacción de reducción de oxígeno. Una mejora de la producción de H_2O_2 en sistemas MINT-AQ respecto a las pruebas control de SWNT y AQ@SWNT.

3) En el *capítulo 3* hemos desarrollado una nueva estrategia de funcionalización covalente de TMDCs basados en la avidez del S como nucleófilo suave con electrófilos suaves. En particular, hemos descrito que 2H-MoS_2 y WS_2 pueden ser funcionalizados covalentemente con maleimidas vía Adición de Michael. La reacción ocurre en condiciones suaves donde no afecta la estructura semiconductora 2H de los materiales de partida.

4) En el *capítulo 4* hemos llevado a cabo un estudio completo de la funcionalización covalente con maleimidas via tiol- Adicion de Michael, previamente descrito en el *capítulo 3*. En estas condiciones de reacción hemos descubierto que, si se usa base o no, MoS_2 se funcionaliza con diferentes compuestos: con un polímero o

molecula aislada, respectivamente. Con un estudio completo de la reacción y caracterización, hemos visto que la reacción funciona en diferentes disolventes, con un amplio abanico de maleimidas y en diferentes temperaturas, siendo la mas óptima a temperatura ambiente. Este estudio demuestra de nuevo la funcionalizacion covalente de MoS_2 y su gran versatilidad, cuyo origen es debido a la reaccion click tiol-eno.

CONCLUSIONS

1) In *chapter 1* we have shown that encapsulation within p- or n-doping macrocycles through mechanical bond (MINT) is a valid strategy for the regulation of the catalytic activity of SWNTs. We have chosen the reduction of nitroaromatic compounds as a test. The electronic effect of the macrocycles on the catalytic activity is clearly predominant: electron-donating mac- exTTF lead to a higher activity, electron-accepting mac-AQ slow the reaction rates and the electronically neutral mac-pyr show similar activity to pristine SWNTs. Finally, MINTs are stable catalysts that can be recycled.

2) In the *chapter 2* we explored the study of MINT-AQ as efficient way of immobilization of AQ while retaining the electrochemical properties of the pristine molecule. MINT strategy could solve the problem of dissolution-instability of physically adsorbed organic molecules upon electrochemical reduction. Further, a proof of concept for electrocatalytic application of MINT-AQ towards oxygen reduction was explored. An improvement in H_2O_2 production rate in MINT-AQ systems with respect to control samples of SWNT and AQ@SWNT.

3) In the *chapter 3* we have developed a new strategy for the covalent functionalization of TMDCs based on the avidity of S as a soft nucleophile for soft electrophiles. In particular, we have describe that 2H-MoS_2 and WS_2 can be covalently functionalized with maleimide reagents via Michael addition. The reaction occurs under very mild conditions that do not affect the 2H semiconducting polytype of the starting materials.

4) In the *chapter 4* we have described a complete study of covalent functionalization of MoS_2 with maleimides via thiol-Michael Addition, previously described in the *chapter 3*. Under these reaction conditions we have discovered that, if a base is used or not, MoS_2 is functionalized with different compounds: a polymer or

isolated molecules, respectively. With a complete study of the reaction and characterization we have seen that the reaction works in different solvents, with a wide range of maleimides and different temperatures. This study demonstrates again the covalent functionalization of MoS_2 and their versatility whose origin is due to the Thiol-ene click reaction.

REFERENCES

1. Iijima, S., Helical microtubules of graphitic carbon. *Nature* **1991,** *354* (6348), 56-58.
2. Iijima, S.; Ichihashi, T., Single-shell carbon nanotubes of 1 nm diameter. *Nature* **1993,** *363* (6430), 603-605.
3. Odom, T. W.; Huang, J.-L.; Kim, P.; Lieber, C. M., Atomic structure and electronic properties of single-walled carbon nanotubes. *Nature* **1998,** *391* (6662), 62-64.
4. Javey, A.; Guo, J.; Wang, Q.; Lundstrom, M.; Dai, H., Ballistic carbon nanotube field-effect transistors. *Nature* **2003,** *424* (6949), 654-657.
5. Berber, S.; Kwon, Y.-K.; Tománek, D., Unusually High Thermal Conductivity of Carbon Nanotubes. *Phys. Rev. Lett.* **2000,** *84* (20), 4613-4616.
6. Tans, S. J.; Devoret, M. H.; Dai, H.; Thess, A.; Smalley, R. E.; Geerligs, L. J.; Dekker, C., Individual single-wall carbon nanotubes as quantum wires. *Nature* **1997,** *386* (6624), 474-477.
7. Cao, L.; Meziani, M. J.; Sahu, S.; Sun, Y.-P., Photoluminescence Properties of Graphene versus Other Carbon Nanomaterials. *Acc. Chem. Res.* **2013,** *46* (1), 171-180.
8. Singh, P.; Campidelli, S.; Giordani, S.; Bonifazi, D.; Bianco, A.; Prato, M., Organic functionalisation and characterisation of single-walled carbon nanotubes. *Chem. Soc. Rev.* **2009,** *38* (8), 2214-2230.
9. Zhao, Y.-L.; Stoddart, J. F., Noncovalent Functionalization of Single-Walled Carbon Nanotubes. *Acc. Chem. Res.* **2009,** *42* (8), 1161-1171.
10. Dai, H., Carbon Nanotubes: Synthesis, Integration, and Properties. *Acc. Chem. Res.* **2002,** *35* (12), 1035-1044.
11. Rao, R.; Pint, C. L.; Islam, A. E.; Weatherup, R. S.; Hofmann, S.; Meshot, E. R.; Wu, F.; Zhou, C.; Dee, N.; Amama, P. B.; Carpena-Nuñez, J.; Shi, W.; Plata, D. L.; Penev, E. S.; Yakobson, B. I.; Balbuena, P. B.; Bichara, C.; Futaba, D. N.; Noda, S.; Shin, H.; Kim, K. S.; Simard, B.; Mirri, F.; Pasquali, M.; Fornasiero, F.; Kauppinen, E. I.; Arnold, M.; Cola, B. A.; Nikolaev, P.; Arepalli, S.; Cheng, H.-M.; Zakharov, D. N.; Stach, E. A.; Zhang, J.; Wei, F.; Terrones, M.; Geohegan, D. B.; Maruyama, B.; Maruyama, S.; Li, Y.; Adams, W. W.; Hart, A. J., Carbon Nanotubes and Related Nanomaterials: Critical Advances and Challenges for Synthesis toward Mainstream Commercial Applications. *ACS Nano* **2018,** *12* (12), 11756-11784.
12. Appenzeller, J., Carbon Nanotubes for High-Performance Electronics—Progress and Prospect. *Proceedings of the IEEE* **2008,** *96* (2), 201-211.
13. Marcaccio, M.; Paolucci, F., *Making and exploiting fullerenes, graphene, and carbon nanotubes*. Springer: 2014.
14. LeMieux, M. C.; Roberts, M.; Barman, S.; Jin, Y. W.; Kim, J. M.; Bao, Z., Self-Sorted, Aligned Nanotube Networks for Thin-Film Transistors. *Science* **2008,** *321* (5885), 101-104.

15. Avouris, P.; Chen, Z.; Perebeinos, V., Carbon-based electronics. *Nat. Nanotechnol.* **2007,** *2* (10), 605-615.
16. Shulaker, M. M.; Hills, G.; Patil, N.; Wei, H.; Chen, H.-Y.; Wong, H. S. P.; Mitra, S., Carbon nanotube computer. *Nature* **2013,** *501*, 526.
17. De Volder, M. F. L.; Tawfick, S. H.; Baughman, R. H.; Hart, A. J., Carbon Nanotubes: Present and Future Commercial Applications. *Science* **2013,** *339* (6119), 535-539.
18. Aurand, E. R.; Usmani, S.; Medelin, M.; Scaini, D.; Bosi, S.; Rosselli, F. B.; Donato, S.; Tromba, G.; Prato, M.; Ballerini, L., Nanostructures to Engineer 3D Neural-Interfaces: Directing Axonal Navigation toward Successful Bridging of Spinal Segments. *Adv. Funct. Mater.* **2018,** *28* (12), 1700550.
19. Kwon, O. S.; Song, H. S.; Park, T. H.; Jang, J., Conducting Nanomaterial Sensor Using Natural Receptors. *Chem. Rev.* **2019,** *119* (1), 36-93.
20. Schroeder, V.; Savagatrup, S.; He, M.; Lin, S.; Swager, T. M., Carbon Nanotube Chemical Sensors. *Chem. Rev.* **2019,** *119* (1), 599-663.
21. Melchionna, M.; Marchesan, S.; Prato, M.; Fornasiero, P., Carbon nanotubes and catalysis: the many facets of a successful marriage. *Catal. Sci. Technol.* **2015,** *5* (8), 3859-3875.
22. Dai, L.; Xue, Y.; Qu, L.; Choi, H.-J.; Baek, J.-B., Metal-Free Catalysts for Oxygen Reduction Reaction. *Chem. Rev.* **2015,** *115* (11), 4823-4892.
23. Gavrel, G.; Jousselme, B.; Filoramo, A.; Campidelli, S., Supramolecular Chemistry of Carbon Nanotubes. In *Making and Exploiting Fullerenes, Graphene, and Carbon Nanotubes*, Marcaccio, M.; Paolucci, F., Eds. Springer Berlin Heidelberg: Berlin, Heidelberg, 2014; pp 95-126.
24. Pérez, E. M.; Martín, N., π–π interactions in carbon nanostructures. *Chem. Soc. Rev.* **2015,** *44* (18), 6425-6433.
25. Tuncel, D., Non-covalent interactions between carbon nanotubes and conjugated polymers. *Nanoscale* **2011,** *3* (9), 3545-3554.
26. Zheng, M.; Jagota, A.; Semke, E. D.; Diner, B. A.; McLean, R. S.; Lustig, S. R.; Richardson, R. E.; Tassi, N. G., DNA-assisted dispersion and separation of carbon nanotubes. *Nat. Mater.* **2003,** *2*, 338.
27. Chen, R. J.; Zhang, Y.; Wang, D.; Dai, H., Noncovalent Sidewall Functionalization of Single-Walled Carbon Nanotubes for Protein Immobilization. *J. Am. Chem. Soc.* **2001,** *123* (16), 3838-3839.
28. Naotoshi, N.; Yasuhiko, T.; Hiroto, M., Water-Soluble Single-Walled Carbon Nanotubes via Noncovalent Sidewall-Functionalization with a Pyrene-Carrying Ammonium Ion. *Chem. Lett.* **2002,** *31* (6), 638-639.
29. Fagan, J. A., Aqueous two-polymer phase extraction of single-wall carbon nanotubes using surfactants. *Nanoscale Adv.* **2019,** *1* (9), 3307-3324.
30. Moore, V. C.; Strano, M. S.; Haroz, E. H.; Hauge, R. H.; Smalley, R. E.; Schmidt, J.; Talmon, Y., Individually Suspended Single-Walled Carbon Nanotubes in Various Surfactants. *Nano Lett.* **2003,** *3* (10), 1379-1382.

31. Delgado, J. L.; de la Cruz, P.; Urbina, A.; López Navarrete, J. T.; Casado, J.; Langa, F., The first synthesis of a conjugated hybrid of C_{60}–fullerene and a single-wall carbon nanotube. *Carbon* **2007,** *45* (11), 2250-2252.
32. Pompeo, F.; Resasco, D. E., Water Solubilization of Single-Walled Carbon Nanotubes by Functionalization with Glucosamine. *Nano Lett.* **2002,** *2* (4), 369-373.
33. Baker, S. E.; Cai, W.; Lasseter, T. L.; Weidkamp, K. P.; Hamers, R. J., Covalently Bonded Adducts of Deoxyribonucleic Acid (DNA) Oligonucleotides with Single-Wall Carbon Nanotubes: Synthesis and Hybridization. *Nano Lett.* **2002,** *2* (12), 1413-1417.
34. Baskaran, D.; Mays, J. W.; Zhang, X. P.; Bratcher, M. S., Carbon Nanotubes with Covalently Linked Porphyrin Antennae: Photoinduced Electron Transfer. *J. Am. Chem. Soc.* **2005,** *127* (19), 6916-6917.
35. Cosnier, S.; Holzinger, M., Design of carbon nanotube-polymer frameworks by electropolymerization of SWCNT-pyrrole derivatives. *Electrochim. Acta* **2008,** *53* (11), 3948-3954.
36. Mickelson, E. T.; Huffman, C. B.; Rinzler, A. G.; Smalley, R. E.; Hauge, R. H.; Margrave, J. L., Fluorination of single-wall carbon nanotubes. *Chem. Phys. Lett.* **1998,** *296* (1), 188-194.
37. Hu, H.; Zhao, B.; Hamon, M. A.; Kamaras, K.; Itkis, M. E.; Haddon, R. C., Sidewall Functionalization of Single-Walled Carbon Nanotubes by Addition of Dichlorocarbene. *J. Am. Chem. Soc.* **2003,** *125* (48), 14893-14900.
38. Guldi, D. M.; Marcaccio, M.; Paolucci, D.; Paolucci, F.; Tagmatarchis, N.; Tasis, D.; Vázquez, E.; Prato, M., Single-Wall Carbon Nanotube–Ferrocene Nanohybrids: Observing Intramolecular Electron Transfer in Functionalized SWNTs. *Angew. Chem. Int. Ed.* **2003,** *42* (35), 4206-4209.
39. Delgado, J. L.; de la Cruz, P.; Langa, F.; Urbina, A.; Casado, J.; López Navarrete, J. T., Microwave-assisted sidewall functionalization of single-wall carbon nanotubes by Diels–Alder cycloaddition. *Chem. Commun.* **2004,** (15), 1734-1735.
40. Coleman, K. S.; Bailey, S. R.; Fogden, S.; Green, M. L. H., Functionalization of Single-Walled Carbon Nanotubes via the Bingel Reaction. *J. Am. Chem. Soc.* **2003,** *125* (29), 8722-8723.
41. Ying, Y.; Saini, R. K.; Liang, F.; Sadana, A. K.; Billups, W. E., Functionalization of Carbon Nanotubes by Free Radicals. *Org. Lett.* **2003,** *5* (9), 1471-1473.
42. Pénicaud, A.; Poulin, P.; Derré, A.; Anglaret, E.; Petit, P., Spontaneous Dissolution of a Single-Wall Carbon Nanotube Salt. *J. Am. Chem. Soc.* **2005,** *127* (1), 8-9.
43. Schirowski, M.; Abellán, G.; Nuin, E.; Pampel, J.; Dolle, C.; Wedler, V.; Fellinger, T.-P.; Spiecker, E.; Hauke, F.; Hirsch, A., Fundamental Insights into the Reductive Covalent Cross-Linking of Single-Walled Carbon Nanotubes. *J. Am. Chem. Soc.* **2018,** *140* (9), 3352-3360.
44. Leigh, D. A., Genesis of the Nanomachines: The 2016 Nobel Prize in Chemistry. *Angew. Chem. Int. Ed.* **2016,** *55* (47), 14506-14508.

45. Stoddart, J. F., Mechanically Interlocked Molecules (MIMs)—Molecular Shuttles, Switches, and Machines (Nobel Lecture). *Angew. Chem. Int. Ed.* **2017,** *56* (37), 11094-11125.
46. Sauvage, J.-P., From Chemical Topology to Molecular Machines (Nobel Lecture). *Angew. Chem. Int. Ed.* **2017,** *56* (37), 11080-11093.
47. Feringa, B. L., The Art of Building Small: From Molecular Switches to Motors (Nobel Lecture). *Angew. Chem. Int. Ed.* **2017,** *56* (37), 11060-11078.
48. Xu, Y.; Kaur, R.; Wang, B.; Minameyer, M. B.; Gsänger, S.; Meyer, B.; Drewello, T.; Guldi, D. M.; von Delius, M., Concave–Convex π–π Template Approach Enables the Synthesis of [10]Cycloparaphenylene–Fullerene [2]Rotaxanes. *J. Am. Chem. Soc.* **2018,** *140* (41), 13413-13420.
49. Barrejón, M.; Mateo-Alonso, A.; Prato, M., Carbon Nanostructures in Rotaxane Architectures. *Eur. J. Org. Chem.* **2019,** *2019* (21), 3371-3383.
50. Diehl, M. R.; Steuerman, D. W.; Tseng, H.-R.; Vignon, S. A.; Star, A.; Celestre, P. C.; Stoddart, J. F.; Heath, J. R., Single-Walled Carbon Nanotube Based Molecular Switch Tunnel Junctions. *ChemPhysChem* **2003,** *4* (12), 1335-1339.
51. Pérez, E. M., Putting Rings around Carbon Nanotubes. *Chem. Eur. J.* **2017,** *23* (52), 12681-12689.
52. López-Moreno, A.; Pérez, E. M., Pyrene-based mechanically interlocked SWNTs. *Chem. Commun.* **2015,** *51* (25), 5421-5424.
53. Leret, S.; Pouillon, Y.; Casado, S.; Navío, C.; Rubio, Á.; Pérez, E. M., Bimodal supramolecular functionalization of carbon nanotubes triggered by covalent bond formation. *Chem. Sci.* **2017,** *8* (3), 1927-1935.
54. de Juan, A.; Pouillon, Y.; Ruiz-González, L.; Torres-Pardo, A.; Casado, S.; Martín, N.; Rubio, Á.; Pérez, E. M., Mechanically Interlocked Single-Wall Carbon Nanotubes. *Angew. Chem. Int. Ed.* **2014,** *53* (21), 5394-5400.
55. de Juan-Fernández, L.; Münich, P. W.; Puthiyedath, A.; Nieto-Ortega, B.; Casado, S.; Ruiz-González, L.; Pérez, E. M.; Guldi, D. M., Interfacing porphyrins and carbon nanotubes through mechanical links. *Chem. Sci.* **2018,** *9* (33), 6779-6784.
56. de Juan, A.; López-Moreno, A.; Calbo, J.; Ortí, E.; Pérez, E. M., Determination of association constants towards carbon nanotubes. *Chem. Sci.* **2015,** *6* (12), 7008-7014.
57. Dias, E. L.; Nguyen, S. T.; Grubbs, R. H., Well-Defined Ruthenium Olefin Metathesis Catalysts: Mechanism and Activity. *J. Am. Chem. Soc.* **1997,** *119* (17), 3887-3897.
58. Miki, K.; Saiki, K.; Umeyama, T.; Baek, J.; Noda, T.; Imahori, H.; Sato, Y.; Suenaga, K.; Ohe, K., Unique Tube–Ring Interactions: Complexation of Single-Walled Carbon Nanotubes with Cycloparaphenyleneacetylenes. *Small* **2018,** *14* (26), 1800720.
59. López-Moreno, A.; Nieto-Ortega, B.; Moffa, M.; de Juan, A.; Bernal, M. M.; Fernández-Blázquez, J. P.; Vilatela, J. J.; Pisignano, D.; Pérez, E. M., Threading through Macrocycles Enhances the Performance of Carbon Nanotubes as Polymer Fillers. *ACS Nano* **2016,** *10* (8), 8012-8018.

60. Blanco, M.; Álvarez, P.; Blanco, C.; Jiménez, M. V.; Fernández-Tornos, J.; Pérez-Torrente, J. J.; Oro, L. A.; Menéndez, R., Enhanced Hydrogen-Transfer Catalytic Activity of Iridium N-Heterocyclic Carbenes by Covalent Attachment on Carbon Nanotubes. *ACS Catal.* **2013,** *3* (6), 1307-1317.
61. Reuillard, B.; Ly, K. H.; Rosser, T. E.; Kuehnel, M. F.; Zebger, I.; Reisner, E., Tuning Product Selectivity for Aqueous CO_2 Reduction with a Mn(bipyridine)-pyrene Catalyst Immobilized on a Carbon Nanotube Electrode. *J. Am. Chem. Soc.* **2017,** *139* (41), 14425-14435.
62. Sgobba, V.; Guldi, D. M., Carbon nanotubes—electronic/electrochemical properties and application for nanoelectronics and photonics. *Chem. Soc. Rev.* **2009,** *38* (1), 165-184.
63. Hijazi, I.; Bourgeteau, T.; Cornut, R.; Morozan, A.; Filoramo, A.; Leroy, J.; Derycke, V.; Jousselme, B.; Campidelli, S., Carbon Nanotube-Templated Synthesis of Covalent Porphyrin Network for Oxygen Reduction Reaction. *J. Am. Chem. Soc.* **2014,** *136* (17), 6348-6354.
64. Murakami, N.; Miyake, H.; Tajima, T.; Nishikawa, K.; Hirayama, R.; Takaguchi, Y., Enhanced Photosensitized Hydrogen Production by Encapsulation of Ferrocenyl Dyes into Single-Walled Carbon Nanotubes. *J. Am. Chem. Soc.* **2018,** *140* (11), 3821-3824.
65. Tran, P. D.; Le Goff, A.; Heidkamp, J.; Jousselme, B.; Guillet, N.; Palacin, S.; Dau, H.; Fontecave, M.; Artero, V., Noncovalent Modification of Carbon Nanotubes with Pyrene-Functionalized Nickel Complexes: Carbon Monoxide Tolerant Catalysts for Hydrogen Evolution and Uptake. *Angew. Chem. Int. Ed.* **2011,** *50* (6), 1371-1374.
66. Li, F.; Zhang, B.; Li, X.; Jiang, Y.; Chen, L.; Li, Y.; Sun, L., Highly Efficient Oxidation of Water by a Molecular Catalyst Immobilized on Carbon Nanotubes. *Angew. Chem. Int. Ed.* **2011,** *50* (51), 12276-12279.
67. Kramer, W. W.; McCrory, C. C. L., Polymer coordination promotes selective CO_2 reduction by cobalt phthalocyanine. *Chem. Sci.* **2016,** *7* (4), 2506-2515.
68. Rosser, T. E.; Windle, C. D.; Reisner, E., Electrocatalytic and Solar-Driven CO_2 Reduction to CO with a Molecular Manganese Catalyst Immobilized on Mesoporous TiO_2. *Angew. Chem. Int. Ed.* **2016,** *55* (26), 7388-7392.
69. Maurin, A.; Robert, M., Catalytic CO_2-to-CO conversion in water by covalently functionalized carbon nanotubes with a molecular iron catalyst. *Chem. Commun.* **2016,** *52* (81), 12084-12087.
70. Lin, S.; Diercks, C. S.; Zhang, Y.-B.; Kornienko, N.; Nichols, E. M.; Zhao, Y.; Paris, A. R.; Kim, D.; Yang, P.; Yaghi, O. M.; Chang, C. J., Covalent organic frameworks comprising cobalt porphyrins for catalytic CO_2 reduction in water. *Science* **2015,** *349* (6253), 1208-1213.
71. Mirkhalaf, F.; Tammeveski, K.; Schiffrin, D. J., Substituent effects on the electrocatalytic reduction of oxygen on quinone-modified glassy carbon electrodes. *Phys. Chem. Chem. Phys.* **2004,** *6* (6), 1321-1327.

72. Campos-Martin, J. M.; Blanco-Brieva, G.; Fierro, J. L. G., Hydrogen Peroxide Synthesis: An Outlook beyond the Anthraquinone Process. *Angew. Chem. Int. Ed.* **2006,** *45* (42), 6962-6984.
73. Werner, D.; Apaydin, D. H.; Portenkirchner, E., An Anthraquinone/Carbon Fiber Composite as Cathode Material for Rechargeable Sodium-Ion Batteries. *Batteries Supercaps* **2018,** *1* (4), 160-168.
74. Wielend, D.; Apaydin, D. H.; Sariciftci, N. S., Anthraquinone thin-film electrodes for reversible CO_2 capture and release. *J. Mater. Chem.* **2018,** *6* (31), 15095-15101.
75. Gong, Z.; Zhang, G.; Wang, S., Electrochemical Reduction of Oxygen on Anthraquinone/Carbon Nanotubes Nanohybrid Modified Glassy Carbon Electrode in Neutral Medium. *J. Chem.* **2013,** *2013*, 9.
76. Alberts, B., *Molecular Biology of the Cell*. CRC Press: 2017.
77. Zhou, M.; Wang, H.-L.; Guo, S., Towards high-efficiency nanoelectrocatalysts for oxygen reduction through engineering advanced carbon nanomaterials. *Chem. Soc. Rev.* **2016,** *45* (5), 1273-1307.
78. Shi, H.; Shen, Y.; He, F.; Li, Y.; Liu, A.; Liu, S.; Zhang, Y., Recent advances of doped carbon as non-precious catalysts for oxygen reduction reaction. *J. Mater. Chem.* **2014,** *2* (38), 15704-15716.
79. Schaetz, A.; Zeltner, M.; Stark, W. J., Carbon Modifications and Surfaces for Catalytic Organic Transformations. *ACS Catal.* **2012,** *2* (6), 1267-1284.
80. Yu, D.; Nagelli, E.; Du, F.; Dai, L., Metal-Free Carbon Nanomaterials Become More Active than Metal Catalysts and Last Longer. *J. Phys. Chem. Lett.* **2010,** *1* (14), 2165-2173.
81. Shui, J.; Wang, M.; Du, F.; Dai, L., N-doped carbon nanomaterials are durable catalysts for oxygen reduction reaction in acidic fuel cells. *Sci. Adv.* **2015,** *1* (1), e1400129.
82. Zhang, S.; Kang, P.; Ubnoske, S.; Brennaman, M. K.; Song, N.; House, R. L.; Glass, J. T.; Meyer, T. J., Polyethylenimine-Enhanced Electrocatalytic Reduction of CO_2 to Formate at Nitrogen-Doped Carbon Nanomaterials. *J. Am. Chem. Soc.* **2014,** *136* (22), 7845-7848.
83. Lee, W. J.; Maiti, U. N.; Lee, J. M.; Lim, J.; Han, T. H.; Kim, S. O., Nitrogen-doped carbon nanotubes and graphene composite structures for energy and catalytic applications. *Chem. Commun.* **2014,** *50* (52), 6818-6830.
84. Zhao, Y.; Yang, L.; Chen, S.; Wang, X.; Ma, Y.; Wu, Q.; Jiang, Y.; Qian, W.; Hu, Z., Can Boron and Nitrogen Co-doping Improve Oxygen Reduction Reaction Activity of Carbon Nanotubes? *J. Am. Chem. Soc.* **2013,** *135* (4), 1201-1204.
85. Martínez-Periñán, E.; de Juan, A.; Pouillon, Y.; Schierl, C.; Strauss, V.; Martín, N.; Rubio, Á.; Guldi, D. M.; Lorenzo, E.; Pérez, E. M., The mechanical bond on carbon nanotubes: diameter-selective functionalization and effects on physical properties. *Nanoscale* **2016,** *8* (17), 9254-9264.
86. Larsen, J. W.; Freund, M.; Kim, K. Y.; Sidovar, M.; Stuart, J. L., Mechanism of the carbon catalyzed reduction of nitrobenzene by hydrazine. *Carbon* **2000,** *38* (5), 655-661.

87. Anaya-Plaza, E.; Oliva, M. M.; Kunzmann, A.; Romero-Nieto, C.; Costa, R. D.; de la Escosura, A.; Guldi, D. M.; Torres, T., Quaternized Pyridyloxy Phthalocyanines Render Aqueous Electron-Donor Carbon Nanotubes as Unprecedented Supramolecular Materials for Energy Conversion. *Adv. Funct. Mater.* **2015,** *25* (48), 7418-7427.
88. Mollahosseini, M.; Karunaratne, E.; Gibson, G. N.; Gascón, J. A.; Papadimitrakopoulos, F., Fullerene-Assisted Photoinduced Charge Transfer of Single-Walled Carbon Nanotubes through a Flavin Helix. *J. Am. Chem. Soc.* **2016,** *138* (18), 5904-5915.
89. Blanco, V.; Leigh, D. A.; Marcos, V.; Morales-Serna, J. A.; Nussbaumer, A. L., A Switchable [2]Rotaxane Asymmetric Organocatalyst That Utilizes an Acyclic Chiral Secondary Amine. *J. Am. Chem. Soc.* **2014,** *136* (13), 4905-4908.
90. Marcos, V.; Stephens, A. J.; Jaramillo-Garcia, J.; Nussbaumer, A. L.; Woltering, S. L.; Valero, A.; Lemonnier, J.-F.; Vitorica-Yrezabal, I. J.; Leigh, D. A., Allosteric initiation and regulation of catalysis with a molecular knot. *Science* **2016,** *352* (6293), 1555-1559.
91. Zhu, K.; Baggi, G.; Vukotic, V. N.; Loeb, S. J., Reversible mechanical protection: building a 3D "suit" around a T-shaped benzimidazole axle. *Chem. Sci.* **2017,** *8* (5), 3898-3904.
92. Chamberlain, T. W.; Biskupek, J.; Skowron, S. T.; Markevich, A. V.; Kurasch, S.; Reimer, O.; Walker, K. E.; Rance, G. A.; Feng, X.; Müllen, K.; Turchanin, A.; Lebedeva, M. A.; Majouga, A. G.; Nenajdenko, V. G.; Kaiser, U.; Besley, E.; Khlobystov, A. N., Stop-Frame Filming and Discovery of Reactions at the Single-Molecule Level by Transmission Electron Microscopy. *ACS Nano* **2017,** *11* (3), 2509-2520.
93. Sumanasekera, G. U.; Allen, J. L.; Fang, S. L.; Loper, A. L.; Rao, A. M.; Eklund, P. C., Electrochemical Oxidation of Single Wall Carbon Nanotube Bundles in Sulfuric Acid. *J. Phys. Chem.* **1999,** *103* (21), 4292-4297.
94. Skákalová, V.; Kaiser, A. B.; Dettlaff-Weglikowska, U.; Hrnčariková, K.; Roth, S., Effect of Chemical Treatment on Electrical Conductivity, Infrared Absorption, and Raman Spectra of Single-Walled Carbon Nanotubes. *J. Phys. Chem.* **2005,** *109* (15), 7174-7181.
95. Lee, J. E.; Ahn, G.; Shim, J.; Lee, Y. S.; Ryu, S., Optical separation of mechanical strain from charge doping in graphene. *Nat. Commun.* **2012,** *3*, 1024.
96. Dresselhaus, M. S.; Jorio, A.; Hofmann, M.; Dresselhaus, G.; Saito, R., Perspectives on Carbon Nanotubes and Graphene Raman Spectroscopy. *Nano Lett.* **2010,** *10* (3), 751-758.
97. Wu, S.; Wen, G.; Wang, J.; Rong, J.; Zong, B.; Schlögl, R.; Su, D. S., Nitrobenzene reduction catalyzed by carbon: does the reaction really belong to carbocatalysis? *Catal. Sci. Technol.* **2014,** *4* (12), 4183-4187.
98. Calbo, J.; López-Moreno, A.; de Juan, A.; Comer, J.; Ortí, E.; Pérez, E. M., Understanding Noncovalent Interactions of Small Molecules with Carbon Nanotubes. *Chem. Eur. J.* **2017,** *23* (52), 12909-12916.

99. Canevet, D.; Gallego, M.; Isla, H.; de Juan, A.; Pérez, E. M.; Martín, N., Macrocyclic Hosts for Fullerenes: Extreme Changes in Binding Abilities with Small Structural Variations. *J. Am. Chem. Soc.* **2011,** *133* (9), 3184-3190.
100. Grimme, S., Semiempirical GGA-type density functional constructed with a long-range dispersion correction. *J. Comput. Chem.* **2006,** *27* (15), 1787-1799.
101. Yanai, T.; Tew, D. P.; Handy, N. C., A new hybrid exchange–correlation functional using the Coulomb-attenuating method (CAM-B3LYP). *Chem. Phys. Lett.* **2004,** *393* (1), 51-57.
102. Binkley, J. S.; Pople, J. A.; Hehre, W. J., Self-consistent molecular orbital methods. 21. Small split-valence basis sets for first-row elements. *J. Am. Chem. Soc.* **1980,** *102* (3), 939-947.
103. Boys, S. F.; Bernardi, F., The calculation of small molecular interactions by the differences of separate total energies. Some procedures with reduced errors. *Mol. Phys.* **1970,** *19* (4), 553-566.
104. Rao, C. N. R.; Voggu, R., Charge-transfer with graphene and nanotubes. *Mater. Today* **2010,** *13* (9), 34-40.
105. Bachilo, S. M.; Strano, M. S.; Kittrell, C.; Hauge, R. H.; Smalley, R. E.; Weisman, R. B., Structure-Assigned Optical Spectra of Single-Walled Carbon Nanotubes. *Science* **2002,** *298* (5602), 2361-2366.
106. Gao, Y.; Ma, D.; Wang, C.; Guan, J.; Bao, X., Reduced graphene oxide as a catalyst for hydrogenation of nitrobenzene at room temperature. *Chem. Commun.* **2011,** *47* (8), 2432-2434.
107. Etacheri, V.; Marom, R.; Elazari, R.; Salitra, G.; Aurbach, D., Challenges in the development of advanced Li-ion batteries: a review. *Energ. Environ. Sci.* **2011,** *4* (9), 3243-3262.
108. Häupler, B.; Wild, A.; Schubert, U. S., Carbonyls: Powerful Organic Materials for Secondary Batteries. *Adv. Energ. Mater.* **2015,** *5* (11), 1402034.
109. Alotto, P.; Guarnieri, M.; Moro, F., Redox flow batteries for the storage of renewable energy: A review. *Renew. Sustain. Energ. Rev.* **2014,** *29*, 325-335.
110. González, A.; Goikolea, E.; Barrena, J. A.; Mysyk, R., Review on supercapacitors: Technologies and materials. *Renew. Sustain. Energ. Rev.* **2016,** *58*, 1189-1206.
111. Dalle, K. E.; Warnan, J.; Leung, J. J.; Reuillard, B.; Karmel, I. S.; Reisner, E., Electro- and Solar-Driven Fuel Synthesis with First Row Transition Metal Complexes. *Chem. Rev.* **2019,** *119* (4), 2752-2875.
112. Kalyanasundaram, K.; Graetzel, M., Artificial photosynthesis: biomimetic approaches to solar energy conversion and storage. *Curr. Opin. Biotech.* **2010,** *21* (3), 298-310.
113. Eftekhari, A., Electrocatalysts for hydrogen evolution reaction. *Int. J. Hydrog. Energ.* **2017,** *42* (16), 11053-11077.
114. Safizadeh, F.; Ghali, E.; Houlachi, G., Electrocatalysis developments for hydrogen evolution reaction in alkaline solutions – A Review. *Int. J. Hydrog. Energ.* **2015,** *40* (1), 256-274.

115. Apaydin, D. H.; Schlager, S.; Portenkirchner, E.; Sariciftci, N. S., Organic, Organometallic and Bioorganic Catalysts for Electrochemical Reduction of CO_2. *ChemPhysChem* **2017,** *18* (22), 3094-3116.
116. Aresta, M., *Carbon dioxide recovery and utilization*. Springer Science & Business Media: 2013.
117. Benson, E. E.; Kubiak, C. P.; Sathrum, A. J.; Smieja, J. M., Electrocatalytic and homogeneous approaches to conversion of CO_2 to liquid fuels. *Chem. Soc. Rev.* **2009,** *38* (1), 89-99.
118. Aresta, M., *Carbon dioxide as chemical feedstock*. Wiley Online Library: 2010; Vol. 416.
119. Nocera, D. G., The Artificial Leaf. *Acc. Chem. Res.* **2012,** *45* (5), 767-776.
120. Berardi, S.; Drouet, S.; Francàs, L.; Gimbert-Suriñach, C.; Guttentag, M.; Richmond, C.; Stoll, T.; Llobet, A., Molecular artificial photosynthesis. *Chem. Soc. Rev.* **2014,** *43* (22), 7501-7519.
121. Francke, R.; Schille, B.; Roemelt, M., Homogeneously Catalyzed Electroreduction of Carbon Dioxide—Methods, Mechanisms, and Catalysts. *Chem. Rev.* **2018,** *118* (9), 4631-4701.
122. Martinez, U.; Komini Babu, S.; Holby, E. F.; Zelenay, P., Durability challenges and perspective in the development of PGM-free electrocatalysts for the oxygen reduction reaction. *Curr. Opin. Electrochem.* **2018,** *9*, 224-232.
123. Fukuzumi, S., Artificial photosynthesis for production of hydrogen peroxide and its fuel cells. *Biochim. Biophys. Acta.* **2016,** *1857* (5), 604-611.
124. Rosser, T. E.; Gross, M. A.; Lai, Y.-H.; Reisner, E., Precious-metal free photoelectrochemical water splitting with immobilised molecular Ni and Fe redox catalysts. *Chem. Sci.* **2016,** *7* (7), 4024-4035.
125. Hammouche, M.; Lexa, D.; Savéant, J. M.; Momenteau, M., Catalysis of the electrochemical reduction of carbon dioxide by iron("0") porphyrins. *J. Electroanal. Chem. Interf. Electrochem.* **1988,** *249* (1), 347-351.
126. Steinlechner, C.; Roesel, A. F.; Oberem, E.; Päpcke, A.; Rockstroh, N.; Gloaguen, F.; Lochbrunner, S.; Ludwig, R.; Spannenberg, A.; Junge, H.; Francke, R.; Beller, M., Selective Earth-Abundant System for CO_2 Reduction: Comparing Photo- and Electrocatalytic Processes. *ACS Catal.* **2019,** *9* (3), 2091-2100.
127. Coskun, H.; Aljabour, A.; De Luna, P.; Farka, D.; Greunz, T.; Stifter, D.; Kus, M.; Zheng, X.; Liu, M.; Hassel, A. W.; Schöfberger, W.; Sargent, E. H.; Sariciftci, N. S.; Stadler, P., Biofunctionalized conductive polymers enable efficient CO_2 electroreduction. *Sci. Adv.* **2017,** *3* (8), e1700686.
128. Yu, H.; Shang, L.; Bian, T.; Shi, R.; Waterhouse, G. I. N.; Zhao, Y.; Zhou, C.; Wu, L.-Z.; Tung, C.-H.; Zhang, T., Nitrogen-Doped Porous Carbon Nanosheets Templated from g-C_3N_4 as Metal-Free Electrocatalysts for Efficient Oxygen Reduction Reaction. *Adv. Mater.* **2016,** *28* (25), 5080-5086.
129. Dey, S.; Mondal, B.; Chatterjee, S.; Rana, A.; Amanullah, S.; Dey, A., Molecular electrocatalysts for the oxygen reduction reaction. *Nat. Rev. Chem.* **2017,** *1*, 0098.
130. Warczak, M.; Gryszel, M.; Jakešová, M.; Đerek, V.; Głowacki, E. D., Organic semiconductor perylenetetracarboxylic diimide (PTCDI) electrodes for

electrocatalytic reduction of oxygen to hydrogen peroxide. *Chem. Commun.* **2018,** *54* (16), 1960-1963.

131. Jakešová, M.; Apaydin, D. H.; Sytnyk, M.; Oppelt, K.; Heiss, W.; Sariciftci, N. S.; Głowacki, E. D., Hydrogen-Bonded Organic Semiconductors as Stable Photoelectrocatalysts for Efficient Hydrogen Peroxide Photosynthesis. *Adv. Funct. Mater.* **2016,** *26* (29), 5248-5254.
132. Goor, G.; Glenneberg, J.; Jacobi, S., Hydrogen peroxide. *Ullmann's encyclopedia of industrial chemistry* **2000**.
133. Sarapuu, A.; Helstein, K.; Vaik, K.; Schiffrin, D. J.; Tammeveski, K., Electrocatalysis of oxygen reduction by quinones adsorbed on highly oriented pyrolytic graphite electrodes. *Electrochim. Acta* **2010,** *55* (22), 6376-6382.
134. Tammeveski, K.; Kontturi, K.; Nichols, R. J.; Potter, R. J.; Schiffrin, D. J., Surface redox catalysis for O_2 reduction on quinone-modified glassy carbon electrodes. *J. Electroanal. Chem.* **2001,** *515* (1), 101-112.
135. Vaik, K.; Mäeorg, U.; Maschion, F. C.; Maia, G.; Schiffrin, D. J.; Tammeveski, K., Electrocatalytic oxygen reduction on glassy carbon grafted with anthraquinone by anodic oxidation of a carboxylate substituent. *Electrochim. Acta* **2005,** *50* (25), 5126-5131.
136. P. M. Hoang, S. H., and B. Lionel Funt, Preparation and Properties of Electrodes Modified by Polymeric Films with Pendant Anthraquinone Groups. *J. Electrochem. Soc.* **1985,** *132* (9), 2129-2133.
137. Mooste, M.; Kibena-Põldsepp, E.; Matisen, L.; Tammeveski, K., Oxygen Reduction on Anthraquinone Diazonium Compound Derivatised Multi-walled Carbon Nanotube and Graphene Based Electrodes. *Electroanal.* **2017,** *29* (2), 548-558.
138. Lee, M.; Hong, J.; Kim, H.; Lim, H.-D.; Cho, S. B.; Kang, K.; Park, C. B., Organic Nanohybrids for Fast and Sustainable Energy Storage. *Adv. Mater.* **2014,** *26* (16), 2558-2565.
139. Bourourou, M.; Elouarzaki, K.; Lalaoui, N.; Agnès, C.; Le Goff, A.; Holzinger, M.; Maaref, A.; Cosnier, S., Supramolecular Immobilization of Laccase on Carbon Nanotube Electrodes Functionalized with (Methylpyrenylaminomethyl)anthraquinone for Direct Electron Reduction of Oxygen. *Chem. Eur. J.* **2013,** *19* (28), 9371-9375.
140. Weigl, S.; Bretterbauer, K.; Hesser, G.; Schöfberger, W.; Paulik, C., Synthesis, characterization, and description of influences on the stabilizing activity of antioxidant-functionalized multi-walled carbon nanotubes. *Carbon* **2015,** *81*, 305-313.
141. Constanze, L.; Huzil, J. T.; Marina, V. I.; Marianna, F., Non-Covalent Functionalization of Carbon Nanotubes with Surfactants for Pharmaceutical Applications - A Critical Mini-Review. *Drug Delivery Lett.* **2011,** *1* (1), 45-57.
142. Belin, T.; Epron, F., Characterization methods of carbon nanotubes: a review. *Mater. Sci. Eng.* **2005,** *119* (2), 105-118.

143. Zhang, W.; Shaikh, A. U.; Tsui, E. Y.; Swager, T. M., Cobalt Porphyrin Functionalized Carbon Nanotubes for Oxygen Reduction. *Chem. Mater.* **2009**, *21* (14), 3234-3241.
144. Blanco, M.; Nieto-Ortega, B.; de Juan, A.; Vera-Hidalgo, M.; López-Moreno, A.; Casado, S.; González, L. R.; Sawada, H.; González-Calbet, J. M.; Pérez, E. M., Positive and negative regulation of carbon nanotube catalysts through encapsulation within macrocycles. *Nat. Commun.* **2018,** *9* (1), 2671.
145. Lehn, J., Supramolecular chemistry. *Science* **1993,** *260* (5115), 1762-1763.
146. Huang, F.; Anslyn, E. V., Introduction: Supramolecular Chemistry. *Chem. Rev.* **2015,** *115* (15), 6999-7000.
147. Liu, Z.; Nalluri, S. K. M.; Stoddart, J. F., Surveying macrocyclic chemistry: from flexible crown ethers to rigid cyclophanes. *Chem. Soc. Rev.* **2017,** *46* (9), 2459-2478.
148. Amabilino, D. B.; Gale, P. A., Supramolecular chemistry anniversary. *Chem. Soc. Rev.* **2017,** *46* (9), 2376-2377.
149. Kassem, S.; van Leeuwen, T.; Lubbe, A. S.; Wilson, M. R.; Feringa, B. L.; Leigh, D. A., Artificial molecular motors. *Chem. Soc. Rev.* **2017,** *46* (9), 2592-2621.
150. Stoddart, J. F., Molecular Machines. *Acc. Chem. Res.* **2001,** *34* (6), 410-411.
151. Babaei, A.; Connor, P. A.; McQuillan, A. J.; Umapathy, S., UV-Visible Spectrooelectrochemistry of the Reduction Products of Anthraquinone in Dimethylformamide Solutions: An Advanced Undergraduate Experiment. *J. Chem. Educ.* **1997,** *74* (10), 1200.
152. J. Revenga, F. R. a. J. T., Study of the Redox Behavior of Anthraquinone in Aqueous Medium. *J. Electrochem. Soc.* **1994,** *141* (2), 330-333.
153. Vikkisk, M.; Kruusenberg, I.; Joost, U.; Shulga, E.; Kink, I.; Tammeveski, K., Electrocatalytic oxygen reduction on nitrogen-doped graphene in alkaline media. *Appl. Catal. Environ.* **2014,** *147*, 369-376.
154. Qu, J.; Shen, Y.; Qu, X.; Dong, S., Electrocatalytic Reduction of Oxygen at Multi-Walled Carbon Nanotubes and Cobalt Porphyrin Modified Glassy Carbon Electrode. *Electroanal.* **2004,** *16* (17), 1444-1450.
155. Kruusenberg, I.; Alexeyeva, N.; Tammeveski, K.; Kozlova, J.; Matisen, L.; Sammelselg, V.; Solla-Gullón, J.; Feliu, J. M., Effect of purification of carbon nanotubes on their electrocatalytic properties for oxygen reduction in acid solution. *Carbon* **2011,** *49* (12), 4031-4039.
156. Šljukić, B.; Banks, C. E.; Compton, R. G., An overview of the electrochemical reduction of oxygen at carbon-based modified electrodes. *J. Iran. Chem. Soc.* **2005,** *2* (1), 1-25.
157. G. Su, Y. W. a. M. G., Direct Colorimetric Detection of Hydrogen Peroxide Using 4-Nitrophenyl Boronic Acid or Its Pinacol Ester. *Am. J. Anal. Chem.* **2011,** *2* (8), 879-884.
158. Apaydin, D. H.; Seelajaroen, H.; Pengsakul, O.; Thamyongkit, P.; Sariciftci, N. S.; Kunze-Liebhäuser, J.; Portenkirchner, E., Photoelectrocatalytic Synthesis of Hydrogen Peroxide by Molecular Copper-Porphyrin Supported on Titanium Dioxide Nanotubes. *ChemCatChem* **2018,** *10* (8), 1793-1797.

159. Bard, A. J.; Faulkner, L. R., Fundamentals and applications. *Electrochem. Methods* **2001,** *2*, 482.
160. Kolb, H. C.; Finn, M. G.; Sharpless, K. B., Click Chemistry: Diverse Chemical Function from a Few Good Reactions. *Angew. Chem. Int. Ed.* **2001,** *40* (11), 2004-2021.
161. Iha, R. K.; Wooley, K. L.; Nyström, A. M.; Burke, D. J.; Kade, M. J.; Hawker, C. J., Applications of Orthogonal "Click" Chemistries in the Synthesis of Functional Soft Materials. *Chem. Rev.* **2009,** *109* (11), 5620-5686.
162. Tunca, U., Click and Multicomponent Reactions Work Together for Polymer Chemistry. *Macromol. Chem. Phys.* **2018,** *219* (16), 1800163.
163. Collman, J. P.; Devaraj, N. K.; Eberspacher, T. P. A.; Chidsey, C. E. D., Mixed Azide-Terminated Monolayers: A Platform for Modifying Electrode Surfaces. *Langmuir* **2006,** *22* (6), 2457-2464.
164. Xu, Z.; Bratlie, K. M., Click Chemistry and Material Selection for in Situ Fabrication of Hydrogels in Tissue Engineering Applications. *ACS Biomater. Sci. Eng.* **2018,** *4* (7), 2276-2291.
165. Lamping, S.; Buten, C.; Ravoo, B. J., Functionalization and Patterning of Self-Assembled Monolayers and Polymer Brushes Using Microcontact Chemistry. *Acc. Chem. Res.* **2019,** *52* (5), 1336-1346.
166. Candan, O. A.; Durmaz, H.; Hizal, G.; Tunca, U., Quadruple click reactions for the synthesis of cysteine-terminated linear multiblock copolymers. *J. Polym. Sci. Polym. Chem.* **2012,** *50* (14), 2863-2870.
167. Hoyle, C. E.; Bowman, C. N., Thiol–Ene Click Chemistry. *Angew. Chem. Int. Ed.* **2010,** *49* (9), 1540-1573.
168. Nair, D. P.; Podgórski, M.; Chatani, S.; Gong, T.; Xi, W.; Fenoli, C. R.; Bowman, C. N., The Thiol-Michael Addition Click Reaction: A Powerful and Widely Used Tool in Materials Chemistry. *Chem. Mater.* **2014,** *26* (1), 724-744.
169. Lowe, A. B., Thiol–ene "click" reactions and recent applications in polymer and materials synthesis: a first update. *Polym. Chem.* **2014,** *5* (17), 4820-4870.
170. Mather, B. D.; Viswanathan, K.; Miller, K. M.; Long, T. E., Michael addition reactions in macromolecular design for emerging technologies. *Prog. Polym. Sci.* **2006,** *31* (5), 487-531.
171. Hoyle, C. E.; Lowe, A. B.; Bowman, C. N., Thiol-click chemistry: a multifaceted toolbox for small molecule and polymer synthesis. *Chem. Soc. Rev.* **2010,** *39* (4), 1355-1387.
172. Sinha, A. K.; Equbal, D., Thiol−Ene Reaction: Synthetic Aspects and Mechanistic Studies of an Anti-Markovnikov-Selective Hydrothiolation of Olefins. *Asian J. Org. Chem.* **2019,** *8* (1), 32-47.
173. Jonkheijm, P.; Weinrich, D.; Köhn, M.; Engelkamp, H.; Christianen, P. C. M.; Kuhlmann, J.; Maan, J. C.; Nüsse, D.; Schroeder, H.; Wacker, R.; Breinbauer, R.; Niemeyer, C. M.; Waldmann, H., Photochemical Surface Patterning by the Thiol-Ene Reaction. *Angew. Chem.* **2008,** *120* (23), 4493-4496.

174. Göbel, R.; Hesemann, P.; Friedrich, A.; Rothe, R.; Schlaad, H.; Taubert, A., Modular Thiol–Ene Chemistry Approach towards Mesoporous Silica Monoliths with Organically Modified Pore Walls. *Chem. Eur. J.* **2014,** *20* (52), 17579-17589.
175. Stolz, R. M.; Northrop, B. H., Experimental and Theoretical Studies of Selective Thiol–Ene and Thiol–Yne Click Reactions Involving N-Substituted Maleimides. *J. Org. Chem.* **2013,** *78* (16), 8105-8116.
176. Northrop, B. H.; Frayne, S. H.; Choudhary, U., Thiol–maleimide "click" chemistry: evaluating the influence of solvent, initiator, and thiol on the reaction mechanism, kinetics, and selectivity. *Polym. Chem.* **2015,** *6* (18), 3415-3430.
177. Oz, Y.; Sanyal, A., The Taming of the Maleimide: Fabrication of Maleimide-Containing 'Clickable' Polymeric Materials. *Chem. Rec.* **2018,** *18* (6), 570-586.
178. Ravasco, J. M. J. M.; Faustino, H.; Trindade, A.; Gois, P. M. P., Bioconjugation with Maleimides: A Useful Tool for Chemical Biology. *Chem. Eur. J.* **2019,** *25* (1), 43-59.
179. Sanyal, A., Diels–Alder Cycloaddition-Cycloreversion: A Powerful Combo in Materials Design. *Macromol. Chem. Phys.* **2010,** *211* (13), 1417-1425.
180. Gandini, A.; Carvalho, A. J. F.; Trovatti, E.; Kramer, R. K.; Lacerda, T. M., Macromolecular materials based on the application of the Diels–Alder reaction to natural polymers and plant oils. *Eur. J. Lipid Sci. Technol.* **2018,** *120* (1), 1700091.
181. Koehler, K. C.; Anseth, K. S.; Bowman, C. N., Diels–Alder Mediated Controlled Release from a Poly(ethylene glycol) Based Hydrogel. *Biomacromolecules* **2013,** *14* (2), 538-547.
182. Renault, K.; Fredy, J. W.; Renard, P.-Y.; Sabot, C., Covalent Modification of Biomolecules through Maleimide-Based Labeling Strategies. *Bioconjugate Chem.* **2018,** *29* (8), 2497-2513.
183. Harper, J. C.; Polsky, R.; Wheeler, D. R.; Brozik, S. M., Maleimide-Activated Aryl Diazonium Salts for Electrode Surface Functionalization with Biological and Redox-Active Molecules. *Langmuir* **2008,** *24* (5), 2206-2211.
184. Bays, E.; Tao, L.; Chang, C.-W.; Maynard, H. D., Synthesis of Semitelechelic Maleimide Poly(PEGA) for Protein Conjugation By RAFT Polymerization. *Biomacromolecules* **2009,** *10* (7), 1777-1781.
185. Oz, Y.; Arslan, M.; Gevrek, T. N.; Sanyal, R.; Sanyal, A., Modular Fabrication of Polymer Brush Coated Magnetic Nanoparticles: Engineering the Interface for Targeted Cellular Imaging. *ACS Appl. Mater. Interfaces.* **2016,** *8* (30), 19813-19826.
186. Gevrek, T. N.; Bilgic, T.; Klok, H.-A.; Sanyal, A., Maleimide-Functionalized Thiol Reactive Copolymer Brushes: Fabrication and Post-Polymerization Modification. *Macromolecules* **2014,** *47* (22), 7842-7851.
187. Kosif, I.; Park, E.-J.; Sanyal, R.; Sanyal, A., Fabrication of Maleimide Containing Thiol Reactive Hydrogels via Diels−Alder/Retro-Diels−Alder Strategy. *Macromolecules* **2010,** *43* (9), 4140-4148.
188. Zhu, J.; Waengler, C.; Lennox, R. B.; Schirrmacher, R., Preparation of Water-Soluble Maleimide-Functionalized 3 nm Gold Nanoparticles: A New Bioconjugation Template. *Langmuir* **2012,** *28* (13), 5508-5512.

189. Ramos-Soriano, J.; Reina, J. J.; Illescas, B. M.; Rojo, J.; Martín, N., Maleimide and Cyclooctyne-Based Hexakis-Adducts of Fullerene: Multivalent Scaffolds for Copper-Free Click Chemistry on Fullerenes. *J. Org. Chem.* **2018,** *83* (4), 1727-1736.
190. Mao, J.; Wang, Y.; Zhu, J.; Yu, J.; Hu, Z., Thiol functionalized carbon nanotubes: Synthesis by sulfur chemistry and their multi-purpose applications. *Appl. Surf. Sci.* **2018,** *447*, 235-243.
191. Zabihi, O.; Ahmadi, M.; Akhlaghi bagherjeri, M.; Naebe, M., One-pot synthesis of aminated multi-walled carbon nanotube using thiol-ene click chemistry for improvement of epoxy nanocomposites properties. *RSC Adv.* **2015,** *5* (119), 98692-98699.
192. Duan, Q.; Wang, Y.; Chen, S.; Miao, M.; Chen, S.; Zhang, D., Functionalized carbon nanotube films by thiol-ene click reaction. *Appl. Surf. Sci.* **2019,** *486*, 144-152.
193. Gobbo, P.; Biesinger, M. C.; Workentin, M. S., Facile synthesis of gold nanoparticle (AuNP)–carbon nanotube (CNT) hybrids through an interfacial Michael addition reaction. *Chem. Commun.* **2013,** *49* (27), 2831-2833.
194. Nagai, Y.; Tsutsumi, Y.; Nakashima, N.; Fujigaya, T., Synthesis of Single-Walled Carbon Nanotubes Coated with Thiol-Reactive Gel via Emulsion Polymerization. *J. Am. Chem. Soc.* **2018,** *140* (27), 8544-8550.
195. Li, Y.; Bao, L.; Zhou, Q.; Ou, E.; Xu, W., Functionalized Graphene Obtained via Thiol-Ene Click Reactions as an Efficient Electrochemical Sensor. *ChemistrySelect* **2017,** *2* (29), 9284-9290.
196. Castelaín, M.; Martínez, G.; Marco, C.; Ellis, G.; Salavagione, H. J., Effect of Click-Chemistry Approaches for Graphene Modification on the Electrical, Thermal, and Mechanical Properties of Polyethylene/Graphene Nanocomposites. *Macromolecules* **2013,** *46* (22), 8980-8987.
197. Luong, N. D.; Sinh, L. H.; Johansson, L.-S.; Campell, J.; Seppälä, J., Functional Graphene by Thiol-ene Click Chemistry. *Chem. Eur. J.* **2015,** *21* (8), 3183-3186.
198. Oz, Y.; Barras, A.; Sanyal, R.; Boukherroub, R.; Szunerits, S.; Sanyal, A., Functionalization of Reduced Graphene Oxide via Thiol–Maleimide "Click" Chemistry: Facile Fabrication of Targeted Drug Delivery Vehicles. *ACS Appl. Mater. Interfaces* **2017,** *9* (39), 34194-34203.
199. Yang, W. J.; Neoh, K.-G.; Kang, E.-T.; Lay-Ming Teo, S.; Rittschof, D., Stainless steel surfaces with thiol-terminated hyperbranched polymers for functionalization via thiol-based chemistry. *Polym. Chem.* **2013,** *4* (10), 3105-3115.
200. Houseman, B. T.; Gawalt, E. S.; Mrksich, M., Maleimide-Functionalized Self-Assembled Monolayers for the Preparation of Peptide and Carbohydrate Biochips. *Langmuir* **2003,** *19* (5), 1522-1531.
201. Novoselov, K. S.; Geim, A. K.; Morozov, S. V.; Jiang, D.; Zhang, Y.; Dubonos, S. V.; Grigorieva, I. V.; Firsov, A. A., Electric Field Effect in Atomically Thin Carbon Films. *Science* **2004,** *306* (5696), 666-669.
202. Xu, M.; Liang, T.; Shi, M.; Chen, H., Graphene-Like Two-Dimensional Materials. *Chem. Rev.* **2013,** *113* (5), 3766-3798.

203. Han, G. H.; Duong, D. L.; Keum, D. H.; Yun, S. J.; Lee, Y. H., van der Waals Metallic Transition Metal Dichalcogenides. *Chem. Rev.* **2018,** *118* (13), 6297-6336.
204. Chhowalla, M.; Shin, H. S.; Eda, G.; Li, L.-J.; Loh, K. P.; Zhang, H., The chemistry of two-dimensional layered transition metal dichalcogenide nanosheets. *Nat. Chem.* **2013,** *5*, 263.
205. Tan, C.; Cao, X.; Wu, X.-J.; He, Q.; Yang, J.; Zhang, X.; Chen, J.; Zhao, W.; Han, S.; Nam, G.-H.; Sindoro, M.; Zhang, H., Recent Advances in Ultrathin Two-Dimensional Nanomaterials. *Chem. Rev.* **2017,** *117* (9), 6225-6331.
206. Splendiani, A.; Sun, L.; Zhang, Y.; Li, T.; Kim, J.; Chim, C.-Y.; Galli, G.; Wang, F., Emerging Photoluminescence in Monolayer MoS_2. *Nano Lett.* **2010,** *10* (4), 1271-1275.
207. Castellanos-Gomez, A., Black Phosphorus: Narrow Gap, Wide Applications. *J. Phys. Chem. Lett.* **2015,** *6* (21), 4280-4291.
208. Mak, K. F.; Lee, C.; Hone, J.; Shan, J.; Heinz, T. F., Atomically Thin MoS_2: A New Direct-Gap Semiconductor. *Phys. Rev. Lett.* **2010,** *105* (13), 136805.
209. Abellán, G.; Wild, S.; Lloret, V.; Scheuschner, N.; Gillen, R.; Mundloch, U.; Maultzsch, J.; Varela, M.; Hauke, F.; Hirsch, A., Fundamental Insights into the Degradation and Stabilization of Thin Layer Black Phosphorus. *J. Am. Chem. Soc.* **2017,** *139* (30), 10432-10440.
210. Hirsch, A.; Hauke, F., Post-Graphene 2D Chemistry: The Emerging Field of Molybdenum Disulfide and Black Phosphorus Functionalization. *Angew. Chem. Int. Ed.* **2018,** *57* (16), 4338-4354.
211. Chen, X.; McDonald, A. R., Functionalization of Two-Dimensional Transition-Metal Dichalcogenides. *Adv. Mater.* **2016,** *28* (27), 5738-5746.
212. Zhao, W.; Ribeiro, R. M.; Eda, G., Electronic Structure and Optical Signatures of Semiconducting Transition Metal Dichalcogenide Nanosheets. *Acc. Chem. Res.* **2015,** *48* (1), 91-99.
213. Wang, Q. H.; Kalantar-Zadeh, K.; Kis, A.; Coleman, J. N.; Strano, M. S., Electronics and optoelectronics of two-dimensional transition metal dichalcogenides. *Nat. Nanotechnol.* **2012,** *7*, 699.
214. Mak, K. F.; Shan, J., Photonics and optoelectronics of 2D semiconductor transition metal dichalcogenides. *Nature Photonics* **2016,** *10*, 216.
215. Radisavljevic, B.; Radenovic, A.; Brivio, J.; Giacometti, V.; Kis, A., Single-layer MoS_2 transistors. *Nat. Nanotechnol.* **2011,** *6* (3), 147-150.
216. Si, M.; Su, C.-J.; Jiang, C.; Conrad, N. J.; Zhou, H.; Maize, K. D.; Qiu, G.; Wu, C.-T.; Shakouri, A.; Alam, M. A.; Ye, P. D., Steep-slope hysteresis-free negative capacitance MoS_2 transistors. *Nat. Nanotechnol.* **2018,** *13* (1), 24-28.
217. Bernal, M. M.; Álvarez, L.; Giovanelli, E.; Arnáiz, A.; Ruiz-González, L.; Casado, S.; Granados, D.; Pizarro, A. M.; Castellanos-Gomez, A.; Pérez, E. M., Luminescent transition metal dichalcogenide nanosheets through one-step liquid phase exfoliation. *2D Mater.* **2016,** *3* (3), 035014.

218. Anbazhagan, R.; Wang, H.-J.; Tsai, H.-C.; Jeng, R.-J., Highly concentrated MoS_2 nanosheets in water achieved by thioglycolic acid as stabilizer and used as biomarkers. *RSC Adv.* **2014,** *4* (81), 42936-42941.
219. Gu, X.; Cui, W.; Li, H.; Wu, Z.; Zeng, Z.; Lee, S.-T.; Zhang, H.; Sun, B., A Solution-Processed Hole Extraction Layer Made from Ultrathin MoS_2 Nanosheets for Efficient Organic Solar Cells. *Adv. Energ. Mater.* **2013,** *3* (10), 1262-1268.
220. Lopez-Sanchez, O.; Lembke, D.; Kayci, M.; Radenovic, A.; Kis, A., Ultrasensitive photodetectors based on monolayer MoS_2. *Nat. Nanotechnol.* **2013,** *8*, 497.
221. Massicotte, M.; Schmidt, P.; Vialla, F.; Schädler, K. G.; Reserbat-Plantey, A.; Watanabe, K.; Taniguchi, T.; Tielrooij, K. J.; Koppens, F. H. L., Picosecond photoresponse in van der Waals heterostructures. *Nat. Nanotechnol.* **2015,** *11*, 42.
222. Li, T.; Galli, G., Electronic Properties of MoS_2 Nanoparticles. *J. Phys.Chem.* **2007,** *111* (44), 16192-16196.
223. Eda, G.; Fujita, T.; Yamaguchi, H.; Voiry, D.; Chen, M.; Chhowalla, M., Coherent Atomic and Electronic Heterostructures of Single-Layer MoS_2. *ACS Nano* **2012,** *6* (8), 7311-7317.
224. Eda, G.; Yamaguchi, H.; Voiry, D.; Fujita, T.; Chen, M.; Chhowalla, M., Photoluminescence from Chemically Exfoliated MoS_2. *Nano Lett.* **2011,** *11* (12), 5111-5116.
225. Wypych, F.; Schöllhorn, R., 1T-MoS_2, a new metallic modification of molybdenum disulfide. *J. Chem. Soc. Chem. Commun.* **1992,** (19), 1386-1388.
226. Lee, C.; Yan, H.; Brus, L. E.; Heinz, T. F.; Hone, J.; Ryu, S., Anomalous Lattice Vibrations of Single- and Few-Layer MoS_2. *ACS Nano* **2010,** *4* (5), 2695-2700.
227. Yu, Y.; Nam, G.-H.; He, Q.; Wu, X.-J.; Zhang, K.; Yang, Z.; Chen, J.; Ma, Q.; Zhao, M.; Liu, Z.; Ran, F.-R.; Wang, X.; Li, H.; Huang, X.; Li, B.; Xiong, Q.; Zhang, Q.; Liu, Z.; Gu, L.; Du, Y.; Huang, W.; Zhang, H., High phase-purity 1T′-MoS_2- and 1T′-$MoSe_2$-layered crystals. *Nat. Chem.* **2018,** *10* (6), 638-643.
228. Backes, C.; Smith, R. J.; McEvoy, N.; Berner, N. C.; McCloskey, D.; Nerl, H. C.; O'Neill, A.; King, P. J.; Higgins, T.; Hanlon, D.; Scheuschner, N.; Maultzsch, J.; Houben, L.; Duesberg, G. S.; Donegan, J. F.; Nicolosi, V.; Coleman, J. N., Edge and confinement effects allow in situ measurement of size and thickness of liquid-exfoliated nanosheets. *Nat. Commun.* **2014,** *5* (1), 4576.
229. Wang, Z.; Mi, B., Environmental Applications of 2D Molybdenum Disulfide (MoS_2) Nanosheets. *Environ. Sci. Technol.* **2017,** *51* (15), 8229-8244.
230. Ayari, A.; Cobas, E.; Ogundadegbe, O.; Fuhrer, M. S., Realization and electrical characterization of ultrathin crystals of layered transition-metal dichalcogenides. *J. Appl. Phys.* **2007,** *101* (1), 014507.
231. Li, H.; Tsai, C.; Koh, A. L.; Cai, L.; Contryman, A. W.; Fragapane, A. H.; Zhao, J.; Han, H. S.; Manoharan, H. C.; Abild-Pedersen, F.; Nørskov, J. K.; Zheng, X., Activating and optimizing MoS_2 basal planes for hydrogen evolution through the formation of strained sulfur vacancies. *Nat. Mater.* **2015,** *15*, 48.

232. Li, G.; Zhang, D.; Yu, Y.; Huang, S.; Yang, W.; Cao, L., Activating MoS_2 for pH-Universal Hydrogen Evolution Catalysis. *J. Am. Chem. Soc.* **2017,** *139* (45), 16194-16200.
233. Lin, W.-H.; Tseng, W.-S.; Went, C. M.; Teague, M. L.; Rossman, G. R.; Atwater, H. A.; Yeh, N.-C., Nearly 90% Circularly Polarized Emission in Monolayer WS_2 Single Crystals by Chemical Vapor Deposition. *ACS Nano* **2019**.
234. Liu, K.-K.; Zhang, W.; Lee, Y.-H.; Lin, Y.-C.; Chang, M.-T.; Su, C.-Y.; Chang, C.-S.; Li, H.; Shi, Y.; Zhang, H.; Lai, C.-S.; Li, L.-J., Growth of Large-Area and Highly Crystalline MoS_2 Thin Layers on Insulating Substrates. *Nano Lett.* **2012,** *12* (3), 1538-1544.
235. Backes, C.; Higgins, T. M.; Kelly, A.; Boland, C.; Harvey, A.; Hanlon, D.; Coleman, J. N., Guidelines for Exfoliation, Characterization and Processing of Layered Materials Produced by Liquid Exfoliation. *Chem. Mater.* **2017,** *29* (1), 243-255.
236. Coleman, J. N.; Lotya, M.; O'Neill, A.; Bergin, S. D.; King, P. J.; Khan, U.; Young, K.; Gaucher, A.; De, S.; Smith, R. J.; Shvets, I. V.; Arora, S. K.; Stanton, G.; Kim, H.-Y.; Lee, K.; Kim, G. T.; Duesberg, G. S.; Hallam, T.; Boland, J. J.; Wang, J. J.; Donegan, J. F.; Grunlan, J. C.; Moriarty, G.; Shmeliov, A.; Nicholls, R. J.; Perkins, J. M.; Grieveson, E. M.; Theuwissen, K.; McComb, D. W.; Nellist, P. D.; Nicolosi, V., Two-Dimensional Nanosheets Produced by Liquid Exfoliation of Layered Materials. *Science* **2011,** *331* (6017), 568-571.
237. Smith, R. J.; King, P. J.; Lotya, M.; Wirtz, C.; Khan, U.; De, S.; O'Neill, A.; Duesberg, G. S.; Grunlan, J. C.; Moriarty, G.; Chen, J.; Wang, J.; Minett, A. I.; Nicolosi, V.; Coleman, J. N., Large-Scale Exfoliation of Inorganic Layered Compounds in Aqueous Surfactant Solutions. *Adv. Mater.* **2011,** *23* (34), 3944-3948.
238. Bertolazzi, S.; Gobbi, M.; Zhao, Y.; Backes, C.; Samorì, P., Molecular chemistry approaches for tuning the properties of two-dimensional transition metal dichalcogenides. *Chem. Soc. Rev.* **2018,** *47* (17), 6845-6888.
239. Mouri, S.; Miyauchi, Y.; Matsuda, K., Tunable Photoluminescence of Monolayer MoS_2 via Chemical Doping. *Nano Lett.* **2013,** *13* (12), 5944-5948.
240. Chou, S. S.; De, M.; Kim, J.; Byun, S.; Dykstra, C.; Yu, J.; Huang, J.; Dravid, V. P., Ligand Conjugation of Chemically Exfoliated MoS_2. *J. Am. Chem. Soc.* **2013,** *135* (12), 4584-4587.
241. Voiry, D.; Goswami, A.; Kappera, R.; Silva, C. d. C. C. e.; Kaplan, D.; Fujita, T.; Chen, M.; Asefa, T.; Chhowalla, M., Covalent functionalization of monolayered transition metal dichalcogenides by phase engineering. *Nat. Chem.* **2014,** *7*, 45.
242. Knirsch, K. C.; Berner, N. C.; Nerl, H. C.; Cucinotta, C. S.; Gholamvand, Z.; McEvoy, N.; Wang, Z.; Abramovic, I.; Vecera, P.; Halik, M.; Sanvito, S.; Duesberg, G. S.; Nicolosi, V.; Hauke, F.; Hirsch, A.; Coleman, J. N.; Backes, C., Basal-Plane Functionalization of Chemically Exfoliated Molybdenum Disulfide by Diazonium Salts. *ACS Nano* **2015,** *9* (6), 6018-6030.
243. Benson, E. E.; Zhang, H.; Schuman, S. A.; Nanayakkara, S. U.; Bronstein, N. D.; Ferrere, S.; Blackburn, J. L.; Miller, E. M., Balancing the Hydrogen Evolution

Reaction, Surface Energetics, and Stability of Metallic MoS_2 Nanosheets via Covalent Functionalization. *J. Am. Chem. Soc.* **2018,** *140* (1), 441-450.

244. Backes, C.; Berner, N. C.; Chen, X.; Lafargue, P.; LaPlace, P.; Freeley, M.; Duesberg, G. S.; Coleman, J. N.; McDonald, A. R., Functionalization of Liquid-Exfoliated Two-Dimensional 2H-MoS_2. *Angew. Chem. Int. Ed.* **2015,** *54* (9), 2638-2642.
245. Chen, X.; Berner, N. C.; Backes, C.; Duesberg, G. S.; McDonald, A. R., Functionalization of Two-Dimensional MoS_2: On the Reaction Between MoS_2 and Organic Thiols. *Angew. Chem. Int. Ed.* **2016,** *55* (19), 5803-5808.
246. Chu, X. S.; Yousaf, A.; Li, D. O.; Tang, A. A.; Debnath, A.; Ma, D.; Green, A. A.; Santos, E. J. G.; Wang, Q. H., Direct Covalent Chemical Functionalization of Unmodified Two-Dimensional Molybdenum Disulfide. *Chem. Mater.* **2018,** *30* (6), 2112-2128.
247. Hu, Z.; Wu, Z.; Han, C.; He, J.; Ni, Z.; Chen, W., Two-dimensional transition metal dichalcogenides: interface and defect engineering. *Chem. Soc. Rev.* **2018,** *47* (9), 3100-3128.
248. Jariwala, D.; Sangwan, V. K.; Lauhon, L. J.; Marks, T. J.; Hersam, M. C., Emerging Device Applications for Semiconducting Two-Dimensional Transition Metal Dichalcogenides. *ACS Nano* **2014,** *8* (2), 1102-1120.
249. Frindt, R. F., Single Crystals of MoS_2 Several Molecular Layers Thick. *J. Appl. Phys.* **1966,** *37* (4), 1928-1929.
250. Radisavljevic, B.; Radenovic, A.; Brivio, J.; Giacometti, V.; Kis, A., Single-layer MoS_2 transistors. *Nat. Nanotechnol.* **2011,** *6*, 147.
251. Castellanos-Gomez, A.; van Leeuwen, R.; Buscema, M.; van der Zant, H. S. J.; Steele, G. A.; Venstra, W. J., Single-Layer MoS_2 Mechanical Resonators. *Adv. Mater.* **2013,** *25* (46), 6719-6723.
252. Castellanos-Gomez, A.; Roldán, R.; Cappelluti, E.; Buscema, M.; Guinea, F.; van der Zant, H. S. J.; Steele, G. A., Local Strain Engineering in Atomically Thin MoS_2. *Nano Lett.* **2013,** *13* (11), 5361-5366.
253. Kang, K.; Xie, S.; Huang, L.; Han, Y.; Huang, P. Y.; Mak, K. F.; Kim, C.-J.; Muller, D.; Park, J., High-mobility three-atom-thick semiconducting films with wafer-scale homogeneity. *Nature* **2015,** *520*, 656.
254. Xie, S.; Tu, L.; Han, Y.; Huang, L.; Kang, K.; Lao, K. U.; Poddar, P.; Park, C.; Muller, D. A.; DiStasio, R. A.; Park, J., Coherent, atomically thin transition-metal dichalcogenide superlattices with engineered strain. *Science* **2018,** *359* (6380), 1131-1136.
255. Li, H.; Wu, J.; Yin, Z.; Zhang, H., Preparation and Applications of Mechanically Exfoliated Single-Layer and Multilayer MoS_2 and WSe_2 Nanosheets. *Acc. Chem. Res.* **2014,** *47* (4), 1067-1075.
256. Cunningham, G.; Lotya, M.; Cucinotta, C. S.; Sanvito, S.; Bergin, S. D.; Menzel, R.; Shaffer, M. S. P.; Coleman, J. N., Solvent Exfoliation of Transition Metal Dichalcogenides: Dispersibility of Exfoliated Nanosheets Varies Only Weakly between Compounds. *ACS Nano* **2012,** *6* (4), 3468-3480.

257. Castellanos-Gomez, A.; Buscema, M.; Molenaar, R.; Singh, V.; Janssen, L.; van der Zant, H. S. J.; Steele, G. A., Deterministic transfer of two-dimensional materials by all-dry viscoelastic stamping. *2D Mater.* **2014,** *1* (1), 011002.
258. Lv, R.; Robinson, J. A.; Schaak, R. E.; Sun, D.; Sun, Y.; Mallouk, T. E.; Terrones, M., Transition Metal Dichalcogenides and Beyond: Synthesis, Properties, and Applications of Single- and Few-Layer Nanosheets. *Acc. Chem. Res.* **2015,** *48* (1), 56-64.
259. Zhang, X.; Lai, Z.; Tan, C.; Zhang, H., Solution-Processed Two-Dimensional MoS_2 Nanosheets: Preparation, Hybridization, and Applications. *Angew. Chem. Int. Ed.* **2016,** *55* (31), 8816-8838.
260. Presolski, S.; Pumera, M., Covalent functionalization of MoS_2. *Mater. Today* **2016,** *19* (3), 140-145.
261. Liu, Y.-T.; Tan, Z.; Xie, X.-M.; Wang, Z.-F.; Ye, X.-Y., Processable and Robust MoS_2 Paper Chemically Cross-Linked with Polymeric Ligands by the Coordination of Divalent Metal Ions. *Chem. Asian J.* **2013,** *8* (4), 817-823.
262. Bhatia, S. K.; Shriver-Lake, L. C.; Prior, K. J.; Georger, J. H.; Calvert, J. M.; Bredehorst, R.; Ligler, F. S., Use of thiol-terminal silanes and heterobifunctional crosslinkers for immobilization of antibodies on silica surfaces. *Anal. Biochem.* **1989,** *178* (2), 408-413.
263. Kade, M. J.; Burke, D. J.; Hawker, C. J., The power of thiol-ene chemistry. *J. Polym. Sc.Polym. Chem.* **2010,** *48* (4), 743-750.
264. Giovanelli, E.; Castellanos-Gomez, A.; Pérez, E. M., Surfactant-Free Polar-to-Nonpolar Phase Transfer of Exfoliated MoS_2 Two-Dimensional Colloids. *ChemPlusChem* **2017,** *82* (5), 732-741.
265. Matsumoto, T.; Namiki, R.; Chang, H.-C., Tuning the Electron Acceptability of the $[Mo_6S_8]$ Cluster Core by Decorating It with Methyl Groups on the Face-Bridging μ^3-Sulfides. *Eur. J. Inorg. Chem.* **2018,** *2018* (35), 3900-3904.
266. Gomes de Lima, M. B.; Guerchais, J. E.; Mercier, R.; Petillon, F. Y., Reactions of bimetallic group VI (6) complexes. 3. Synthesis, characterization and reactivity of dimeric molybdenum(III) and tungsten(III) compounds with bridging thiolate ligands. A molybdenum-95 NMR study on dinuclear molybdenum complexes. Crystal structure of $[Mo_2^{III}(.eta.5\text{-}C_5H_5)_2(SMe)_3(CO)_2]Br.cntdot.H_2O$. *Organometallics* **1986,** *5* (10), 1952-1964.
267. Ellis, J. E.; Rochfort, G. L., Synthesis and characterization of zerovalent polynuclear metal carbonyl compounds of chromium, molybdenum, and tungsten. X-ray crystal structure of $[Me_4N]_3[W_3(CO)_9(.mu.\text{-}OC_2H_5)(.mu.3\text{-}OC_2H_5)_2]$. *Organometallics* **1982,** *1* (5), 682-689.
268. Hai, X.; Chang, K.; Pang, H.; Li, M.; Li, P.; Liu, H.; Shi, L.; Ye, J., Engineering the Edges of MoS_2 (WS_2) Crystals for Direct Exfoliation into Monolayers in Polar Micromolecular Solvents. *J. Am. Chem. Soc.* **2016,** *138* (45), 14962-14969.
269. Gu, J.; Aguiar, J. A.; Ferrere, S.; Steirer, K. X.; Yan, Y.; Xiao, C.; Young, James L.; Al-Jassim, M.; Neale, N. R.; Turner, J. A., A graded catalytic–protective layer for an efficient and stable water-splitting photocathode. *Nat. Energy* **2017,** *2*, 16192.

270. Shen, J.; He, Y.; Wu, J.; Gao, C.; Keyshar, K.; Zhang, X.; Yang, Y.; Ye, M.; Vajtai, R.; Lou, J.; Ajayan, P. M., Liquid Phase Exfoliation of Two-Dimensional Materials by Directly Probing and Matching Surface Tension Components. *Nano Lett.* **2015,** *15* (8), 5449-5454.
271. Ferrari, A. C.; Bonaccorso, F.; Fal'ko, V.; Novoselov, K. S.; Roche, S.; Bøggild, P.; Borini, S.; Koppens, F. H. L.; Palermo, V.; Pugno, N.; Garrido, J. A.; Sordan, R.; Bianco, A.; Ballerini, L.; Prato, M.; Lidorikis, E.; Kivioja, J.; Marinelli, C.; Ryhänen, T.; Morpurgo, A.; Coleman, J. N.; Nicolosi, V.; Colombo, L.; Fert, A.; Garcia-Hernandez, M.; Bachtold, A.; Schneider, G. F.; Guinea, F.; Dekker, C.; Barbone, M.; Sun, Z.; Galiotis, C.; Grigorenko, A. N.; Konstantatos, G.; Kis, A.; Katsnelson, M.; Vandersypen, L.; Loiseau, A.; Morandi, V.; Neumaier, D.; Treossi, E.; Pellegrini, V.; Polini, M.; Tredicucci, A.; Williams, G. M.; Hee Hong, B.; Ahn, J.-H.; Min Kim, J.; Zirath, H.; van Wees, B. J.; van der Zant, H.; Occhipinti, L.; Di Matteo, A.; Kinloch, I. A.; Seyller, T.; Quesnel, E.; Feng, X.; Teo, K.; Rupesinghe, N.; Hakonen, P.; Neil, S. R. T.; Tannock, Q.; Löfwander, T.; Kinaret, J., Science and technology roadmap for graphene, related two-dimensional crystals, and hybrid systems. *Nanoscale* **2015,** *7* (11), 4598-4810.
272. Pakdel, A.; Bando, Y.; Golberg, D., Nano boron nitride flatland. *Chem. Soc. Revi.* **2014,** *43* (3), 934-959.
273. Li, L.; Yu, Y.; Ye, G. J.; Ge, Q.; Ou, X.; Wu, H.; Feng, D.; Chen, X. H.; Zhang, Y., Black phosphorus field-effect transistors. *Nat. Nanotechnol.* **2014,** *9*, 372.
274. Castellanos-Gomez, A.; Vicarelli, L.; Prada, E.; Island, J. O.; Narasimha-Acharya, K. L.; Blanter, S. I.; Groenendijk, D. J.; Buscema, M.; Steele, G. A.; Alvarez, J. V.; Zandbergen, H. W.; Palacios, J. J.; van der Zant, H. S. J., Isolation and characterization of few-layer black phosphorus. *2D Mater.* **2014,** *1* (2), 025001.
275. Yin, Z.; Li, H.; Li, H.; Jiang, L.; Shi, Y.; Sun, Y.; Lu, G.; Zhang, Q.; Chen, X.; Zhang, H., Single-Layer MoS_2 Phototransistors. *ACS Nano* **2012,** *6* (1), 74-80.
276. Ippolito, S.; Ciesielski, A.; Samorì, P., Tailoring the physicochemical properties of solution-processed transition metal dichalcogenides via molecular approaches. *Chem. Commun.* **2019,** *55* (61), 8900-8914.
277. Chen, W. Y.; Yen, C.-C.; Xue, S.; Wang, H.; Stanciu, L. A., Surface Functionalization of Layered Molybdenum Disulfide for the Selective Detection of Volatile Organic Compounds at Room Temperature. *ACS Appl. Mater. Interfaces.* **2019,** *11* (37), 34135-34143.
278. Xiao, M.; Man, T.; Zhu, C.; Pei, H.; Shi, J.; Li, L.; Qu, X.; Shen, X.; Li, J., MoS_2 Nanoprobe for MicroRNA Quantification Based on Duplex-Specific Nuclease Signal Amplification. *ACS Appl. Mater. Interfaces* **2018,** *10* (9), 7852-7858.
279. Molina-Mendoza, A. J.; Vaquero-Garzon, L.; Leret, S.; de Juan-Fernández, L.; Pérez, E. M.; Castellanos-Gomez, A., Engineering the optoelectronic properties of MoS_2 photodetectors through reversible noncovalent functionalization. *Chem. Commun.* **2016,** *52* (100), 14365-14368.
280. Yu, S. H.; Lee, Y.; Jang, S. K.; Kang, J.; Jeon, J.; Lee, C.; Lee, J. Y.; Kim, H.; Hwang, E.; Lee, S.; Cho, J. H., Dye-Sensitized MoS_2 Photodetector with Enhanced Spectral Photoresponse. *ACS Nano* **2014,** *8* (8), 8285-8291.

281. Tang, Q.; Jiang, D.-e., Stabilization and Band-Gap Tuning of the 1T-MoS_2 Monolayer by Covalent Functionalization. *Chem. Mater.* **2015,** *27* (10), 3743-3748.
282. Vera-Hidalgo, M.; Giovanelli, E.; Navío, C.; Pérez, E. M., Mild Covalent Functionalization of Transition Metal Dichalcogenides with Maleimides: A "Click" Reaction for 2H-MoS_2 and WS_2. *J. Am. Chem. Soc.* **2019,** *141* (9), 3767-3771.
283. Chu, X. S.; Li, D. O.; Green, A. A.; Wang, Q. H., Formation of MoO_3 and WO_3 nanoscrolls from MoS_2 and WS_2 with atmospheric air plasma. *J. Mat. Chem.* **2017,** *5* (43), 11301-11309.
284. Haas, H. C.; MacDonald, R. L., Maleimide polymers. I. A polymeric color reaction. *J.Polymer Science: Polym. Chem. Ed.* **1973,** *11* (2), 327-343.
285. Kojima, K.; Yoda, N.; Marvel, C. S., Base-catalyzed polymerization of maleimide and some derivatives and related unsaturated carbonamides. *J. Polym. Sci.: Polym. Chem.* **1966,** *4* (5), 1121-1134.
286. Abel, B. A.; McCormick, C. L., "One-Pot" Aminolysis/Thiol–Maleimide End-Group Functionalization of RAFT Polymers: Identifying and Preventing Michael Addition Side Reactions. *Macromolecules* **2016,** *49* (17), 6193-6202.
287. Kalantar-zadeh, K.; Ou, J. Z., Biosensors Based on Two-Dimensional MoS_2. *ACS Sensors* **2016,** *1* (1), 5-16.
288. Pumera, M.; Loo, A. H., Layered transition-metal dichalcogenides (MoS_2 and WS_2) for sensing and biosensing. *TrAC Trend. Anal. Chem.* **2014,** *61*, 49-53.
289. Zhang, W.; Zhang, P.; Su, Z.; Wei, G., Synthesis and sensor applications of MoS_2-based nanocomposites. *Nanoscale* **2015,** *7* (44), 18364-18378.
290. Greenwood, J.; Phan, T. H.; Fujita, Y.; Li, Z.; Ivasenko, O.; Vanderlinden, W.; Van Gorp, H.; Frederickx, W.; Lu, G.; Tahara, K.; Tobe, Y.; Uji-i, H.; Mertens, S. F. L.; De Feyter, S., Covalent Modification of Graphene and Graphite Using Diazonium Chemistry: Tunable Grafting and Nanomanipulation. *ACS Nano* **2015,** *9* (5), 5520-5535.
291. Carrié, H.; Tran, D. T.; Rousseau, S.; Chaignepain, S.; Schmitter, J.-M.; Deffieux, D.; Quideau, S., New affinity-based probes for capturing flavonoid-binding proteins. *Chem. Commun.* **2014,** *50* (66), 9387-9389.
292. Itou, W.; Hagiwara, T., Synthesis and polymerization of N-(4-ethynylphenyl)maleimide as a novel monomer with two polymerizable and modifiable groups. *React. Funct. Polym.* **2016,** *101*, 70-74.
293. Heath, W. H.; Palmieri, F.; Adams, J. R.; Long, B. K.; Chute, J.; Holcombe, T. W.; Zieren, S.; Truitt, M. J.; White, J. L.; Willson, C. G., Degradable Cross-Linkers and Strippable Imaging Materials for Step-and-Flash Imprint Lithography. *Macromolecules* **2008,** *41* (3), 719-726.
294. Tang, F.; Yang, Y.; Tang, Y.; Tang, S.; Yang, L.; Sun, B.; Jiang, B.; Dong, J.; Liu, H.; Huang, M.; Geng, M.-Y.; Huang, W., One-pot N-glycosylation remodeling of IgG with non-natural sialylglycopeptides enables glycosite-specific and dual-payload antibody–drug conjugates. *Org. Biomol. Chem*. **2016**, *14* (40), 9501-9518.